
**DUBLIN CITY UNIVERSITY**

**SCHOOL OF ELECTRONIC ENGINEERING**


# Self-Powered, Sustainable E-textiles for Wearable Devices in the Internet of Things


**by**

**Sanjaya Dinuwan Gunawardhana Karnasooriya Ragalage, MSc**


**December 2025**

**A thesis submitted in fulfilment of the requirements for the degree of Doctor of Philosophy**

**(PhD)**

**from**


**Dublin City University**

**School of Electronic Engineering**

**Supervised by : Dr. Shirley Coyle, Prof. Tomas Ward**

**DECLARATION**

I hereby certify that this material, which I now submit for assessment on the programme of study leading to the award of Doctor of Philosophy is entirely my own work, and that I have exercised reasonable care to ensure that the work is original and have conformed to the regulations on the use and declaration of Generative AI, and does not to the best of my knowledge breach any law of copyright, and has not been taken from the work of others save and to the extent that such work has been cited and acknowledged within the text of my work.

Signed : Sanjaya Dinuwan Gunawardhana Karnasooriya Ragalage

ID No: 21266343 Date: 12/12/2025

## REPORTING OF GEN AI TOOL USE IN RESEARCH THESES

| | |
|---|---|
| **Tools:** | ***ChatGPT 4.0, 5.0, Grammarly from Jul 2025 to Sep 2025*** |
| **Outputs:** | I used ChatGPT and Grammarly to improve the clarity and academic writing style with grammar throughout the thesis.<br>Also, ChatGPT has been used to improve some parts of the codes generated in appendix C,D,E,F,I, and J |
| **Prompts:** | I asked ChatGPT to "Improve this text grammar, academic style while maintaining flow with previous paragraph".<br>To improve the appendix codes after generating the primary code, I asked ChatGPT " can you assist with converting this code to show changing frequency(or amplitude) while maintaining fixed amplitude (or frequency) for a given interval (ex: 1 to 5 Hz frequency with 5 mm amplitude and 5s time for each frequency) in a same graph" |
| **Iterations:** | Mostly once for some parts of the thesis where a better flow is required. After a prompt was generated each and every part was carefully read and manually edited to fill the gaps while maintaining the correct theoretical background supported with literature.<br>For codes, sometimes a few iterations (2 to 3 times) were required to improve the final version as required. All codes are manually checked line by line and validated by running each block. |
| **Critical Reflection:** | As a non-native English speaker, the role of Gen AI has been vital with assisting to improve the clarity and grammar in some parts of the thesis to develop a high quality and academically sound thesis. Furthermore, the use of Gen AI to improve the codes has assisted to focus more on the core objectives of the project while meeting the deadlines and delivering high impacted outputs. |

**Tiomanta do na cáiníocóirí in Éirinn, a raibh a bhflaithiúlacht dofheicthe ní hamháin mar thacaíocht don obair seo ach a thug seans dom freisin fás, foghlaim agus mo bhrionglóidí a shaothrú.**

**Dedicated to the taxpayers of Ireland, whose unseen generosity not only supported this work but also gave me the chance to grow, learn, and pursue my dreams.**

**ACKNOWLEDGEMENT**

I express my sincere gratitude to my supervisor, Dr. Shirley Coyle, for providing me with her invaluable guidance and encouragement throughout this project. I would also like to extend my appreciation to her for her patience, wisdom, and unwavering support during times when I found the project challenging. Her willingness to go above and beyond to assist me with my project was commendable. Dr. Coyle also ensured that I had access to all the necessary resources and continued to check in on me to see if I required any further assistance. Her unwavering support was instrumental in my success, and I am grateful for her contributions to my project.

I wish to express my gratitude to my secondary supervisor, Prof. Tomas Ward, for his invaluable guidance and insightful suggestions that helped enhance various aspects of my project. Our cordial conversations provided me with fresh perspectives and enabled me to approach my PhD research from a more nuanced angle. Also, whenever I talked with him the encouragement, he gave to me was one of the biggest inspiration for me to move forward with highly competitive research area.

I would like to show my kind gratitude towards Prof Suresh C. Pillai as my external examiner for providing valuable insights to further improve my thesis. His comments mean a lot to me and are invaluable to the progress of my research. I would like to express my kind gratitude to Prof. Stephen Daniels, the head of the School of Electronic Engineering for his kind guidance as my transfer report examiner and internal examiner. His guidance and suggestions has been a tremendous support to align and improve the quality of my research work. Also, I wish to express my gratitude for Dr. Marissa Condon for organizing a smooth viva examination as the committee chair.

I would like to express my kind gratitude for Insight Research Ireland Research Centre for Data Analysis for the scholarship and kind assistance throughout my PhD journey. All the management and assistance staff from the research institute has gone above and beyond to make my journey a successful one. Without your support this would be just a mere dream.

I would like to express my gratitude to Dr. Garrett McGuinness, the head of school of Mechanical Engineering for his invaluable support and guidance in the technique of electrospinning. His assistance and access to the laboratory set up have enabled me to conduct my experiments with ease and efficiency beyond my expectations.

I am fortunate to have the support of a highly skilled team from University College Dublin Prof Brian Rodriguez and Dr. Waseem Wani and Tyndall national institute comprising Dr. Brendan O'Flynn and Dr. Roy Simorangkir (currently serves as an assistant professor at Durham University, UK). Their expertise has been instrumental in shaping my perspectives on product development and commercialization, which will undoubtedly prove invaluable in the future.

I would like to thank, School of Electronic Engineering and School of Mechanical Engineering technical staff for bearing me with their always busy schedules. I would like to express my gratitude towards my esteemed colleagues, Luz and Sonal, for their unwavering support and attentive ear during both my triumphs and struggles.

Finally, I wanted to extend my sincere gratitude to my wife, Asanka, for her unwavering love, support, and encouragement throughout my journey. I also thank my family for their constant presence and support whenever I needed it. I hope I made you all proud. I appreciated everyone’s care and thoughtfulness throughout last 4 years and I would like to express a deep gratitude to all of you.

## RESEARCH OUTPUTS

### Journal Publications

**Gunawardhana K. R. S. D**., Simorangkir R. B. V. B., McGuinness G. B., Rasel M. S., Colorado L. A. M, Baberwal S. S., Ward T. E., O'Brian B., Coyle S. M., The potential of electrospinning and textile engineering to enable the realisation of the energy-autonomous wearable wireless sensing systems. ACS Nano, 2024, https://doi.org/10.1021/acsnano.3c09077 **(Lead Author)**

**Gunawardhana, K. R. Sanjaya D**., Zhou Fang, Garrett B. McGuinness, Luz Alejandra Magre Colorado, Sonal Santosh Baberwal, Waseem Ahmad Wani, Brian J. Rodriguez, Robert O'Connor, Ciara Smullen, Tomás E. Ward, and Shirley M. Coyle. 2025. "Innovative Self-Powered Sensing: Potential of Fabrigami and Electrospun Nanofibre-Based Triboelectric Nanogenerator for Joint Biomechanics Monitoring." Wiley Small e06363. https://doi.org/10.1002/smll.202506363. **(Lead Author)**

Santosh Baberwal, Sonal, Luz Alejandra Magre, **Gunawardhana, K. R. Sanjaya D**, Michael Parkinson, Tomás Ward, and Shirley Coyle. 2024. "Motor Imagery with Cues in Virtual Reality, Audio and Screen." Journal of Neural Engineering 21(5):056020. https://doi.org/10.1088/1741-2552/ad775e **(Co-Author)**

### Patent

"Fabrigami Sensor" by **Sanjaya Dinuwan Gunawardhana Karnasooriya Ragalage,** Zhou Fang, Garrett B McGuinness, Shirley M Coyle (**UK patent filled no. 2505562.5)**

### Conference papers

**Karnasooriya Ragalage, Sanjaya D. G.**, Hamza Qadeer, Garrett B. McGuinness, Tomas E. Ward, and Shirley M. Coyle. 2024. "Self-Powered Breath Monitoring Using Electrospun Biodegradable and Biocompatible Textile Sensors." Pp. 1–4 in 2024 IEEE 20th International Conference on Body Sensor Networks (BSN). IEEE. **(Lead Author)**

K. R. Sanjaya D. Gunawardhana, Garret. B. McGuinness, Tomás E. Ward, Shirley M. Coyle., Flexible, biocompatible, and self-powered wearable gait monitoring and tactile sensing using parallelly electrospun CA and PVDF membranes., at 8th International Conference on Electrospinning 2024 at AGH University of Krakow, Krakow, Poland, 25-28th June 2024. (Lead Author)

Saunders, N.; **Gunawardhana, K. R. S. D.;** Magre Colorado, L.A.; Baberwal, S.S.; Coyle, S. Hit the Ground Running—Wearable Sensors to Measure Foot Plantar Pressure. Eng. Proc. 2023, 30, 6. https://doi.org/10.3390/engproc2023030006 **(Corresponding Author)**

Baberwal S.S.; Magre L. A.; **Gunawardhana K. R. S. D.**; Ward T.; Coyle S. "Protocol design and testing to investigate Motor Imagery training using cues in different mediums: A pilot study," in 2023 20th International Conference on Electrical Engineering, Computing Science and Automatic Control (CCE), Institute of Electrical and Electronics Engineers (IEEE), Dec. 2023, pp. 1–6. Doi: 10.1109/CCE60043.2023.10332874 **(Co-Author)**

Coulter, Ruairi, **K. R. Sanjaya. Dinuwan Gunawardhana**, and Shirley Coyle. 2024. "Design and Development of a Nylon Based Actuator for Use in a Soft Robotic Glove." Pp. 168–72 in 2024 International Conference on the Challenges, Opportunities, Innovations and Applications in Electronic Textiles, E-Textiles 2024. Institute of Electrical and Electronics Engineers Inc. **(Corresponding Author)**

Magre Colarado L. A.; Baberwal S.S; **Gunawardhana K. R. S. D;** Moran K. ; Coyle S. "Understanding Barriers in Physical Engagement: Prototyping an Exergame for Anterior Cruciate Ligament Rehabilitation" 2025 IEEE Int. Work. Sport. Technol. Res., pp. 162–167, Oct. 2025, Doi: 10.1109/STAR66750.2025.11264789.**(Co-Author)**

**Posters**

**Gunawardhana KRSD**, McGuinness G, Ward T, Coyle S, Wearable self-powered sensors and e-textiles for healthcare applications, National Centre for Sensor Research (NCSR) research day, held at Dublin City University (16/05/2022)

**Gunawardhana KRSD**, McGuinness G, Ward T, Coyle S, Electrospinning: a potential candidate for in situ wearable energy harvesting, communication and self-powered sensing, Insight smart surrounding showcase, held at the Helix, Dublin City University (17/10/2022)

Saunders, N.; **Gunawardhana, K.R.S.D**.; Magre Colorado, L.A.; Baberwal, S.S.; Coyle, S. Hit the Ground Running—Wearable Sensors to Measure Foot Plantar Pressure, presented at E Textile 2022, Nottingham, UK, https://e-textilesconference.com/poster-presentations-3/

**Gunawardhana KRSD**, Coyle S, Electrospinning for comfortably wearable self-powered healthcare monitoring system, Research on walls competition organized by graduate studies office Dublin City University (27/09/2023)

**Demonstrations**

Presented self-powered smart insole and breath sensor, Scientific Plenary, Insight SFI centre for data analytics, Galway, Ireland, 17/10/2023.

Presented pressure sensor Hit the Ground Running—Wearable Sensors to Measure Foot Plantar Pressure., industry focused event, Navigating Data-Driven Futures, Insight SFI centre for data analytics, The Helix, Dublin City University, 15/11/2023.

**Presentations**

Towards optimized wearable self-powered sensing – presented at Sensors PRI meeting organized by Insight SFI centre for data analytics (14/04/2022)

Self-Powered Sustainable E-Textiles for Wearable Devices in the Internet of Things- presented at International Summer School and conference on Smart Textiles, Niederrhein University of Applied Sciences, Mönchengladbach, Germany (4$^{th}$ to 8$^{th}$ September 2023)

**Gunawardhana K.R.S.D.,** Self-Powered, Sustainable E-textiles for Truly Wearable Devices in the Internet of Things, Faculty of Textile and Clothing Technology, University of Applied Sciences, , Mönchengladbach, Germany, (On 20$^{th}$ June 2024 Honorarium speech for the research institute)

**TABLE OF CONTENT**

**LIST OF ABREVIATIONS**

| | |
|---|---|
| AA | Acetic Acid |
| AATCC | American Association of Textile Chemists and Colourists |
| ADC | Analog to Digital Converter |
| Ag-CA | Silver Nanoparticles doped Cellulose Acetate |
| ASTM | American Society for Testing and Materials |
| BLE | Bluetooth |
| CA | Cellulose Acetate |
| CNT | Carbon Nanotubes |
| CPD | Contact Potential Difference |
| DDEF | Distance dependence Electric Field |
| DMF | Dimethylformamide |
| DSSC | Dye Sensitized Solar Cells |
| EDLC | Electric Double-Layer Capacitors |
| EDS | Energy-Dispersive X-ray Spectroscopy |
| EEG | Evaporative Energy Generation |
| F(β) | percentage of β phase |
| FA | Formic Acid |
| FTIR | Fourier-Transform Infrared Spectroscopy |
| IEC | International Electrotechnical Commission |
| IPC | Institute of Printed Circuits |
| $I_{SC}$ | Short Circuit Current |
| ISO | International Organization for Standardization |
| JBM | Joint Biomechanics Monitoring |
| KPFM | Kelvin Probe Force Microscopy |
| MW | Molecular Weight |
| MWCNT | multi-walled carbon nanotubes |
| OSC | Organic Solar Cells |
| PA | Polyamide |
| PAN | Polyacrylonitrile |
| PANI | Polyaniline |
| PCB | Printed Circuit Board |
| PCE | Power Conversion Efficiency |
| PCL | Polycaprolactone |
| PDMS | Polydimethylsiloxane |
| PEDOT | Poly (3,4-(ethylenedioxy) thiophene) |
| PEDOT | Poly (3,4-(ethylenedioxy) thiophene) |
| PENG | Piezoelectric Nanogenerator |
| PI | Polyimide |
| PLA | Poly Lactic Acid |
| PP | Polypyrrole |
| PSC | Perovskite Solar Cells |
| PSC | Perovskite Solar Cells |
| PTFE | polytetrafluoroethylene |
| PU | Polyurethane |

| | |
|---|---|
| PVA | Poly Vinyl Alcohol |
| PVDF | Poly(vinylidene fluoride) |
| PVDF-HFP | Poly(vinylidene fluoride-hexafluoropropylene) |
| PVDF-TrFE | Polyvinylidene fluoride-trifluoroethylene |
| PVP | Polyvinylpyrrolidone |
| $Q_{SC}$ | Charge Density |
| SEHG | Solar Energy Harvesting |
| SEM | Scanning Electron Microscope |
| SPI | Serial Peripheral Interface |
| TBAB | tetra butyl ammonium bromide |
| TCD | Tip to Collector Distance |
| TEG | Thermoelectric Energy Generation |
| TENG | Triboelectric Nanogenerator |
| TRL | Technology Readiness Level |
| $V_{OC}$ | Open Circuit Voltage |
| XPS | X-ray Photoelectron Spectroscopy |
| XRD | X-ray diffraction analysis |

**TABLE OF FIGURES**

## LIST OF TABLES

## ABSTRACT

### Self-Powered, Sustainable E-textiles for Wearable Devices in the Internet of Things

**Sanjaya Dinuwan Gunawardhana Karnasooriya Ragalage**

With the advancement technologies/themes such as artificial intelligence, 5G/6G communications and the Internet of Things, body-worn electronic devices for continuous lifestyle monitoring have become increasingly prevalent. However, the use of Li-ion batteries as the primary power source for these devices raises concerns regarding carbon emissions and e-waste generation. Triboelectric nanogenerators (TENG) offer a promising alternative by converting body movements into electrical signals, thereby reducing or eliminating the use of batteries. Due to their high response and self-powering ability, TENGs are well-suited for monitoring joint biomechanics in applications such as home rehabilitation and sports injury prevention. This research focuses on developing sustainable and sensitive TENG-based sensors for monitoring joint biomechanics, emphasizing innovations in material engineering with electrospinning and structural design to accurately detect parameters like joint angle, speed and movement frequency.

A comprehensive literature review identified limitations in current wearable TENGs and highlighted opportunities for combining electrospun membranes with origami-inspired, "fabrigami" architectures for fabric-based sensor development. Initial studies on electrospun cellulose acetate (CA) and polycaprolactone (PCL) have demonstrated biodegradability, but with limited sensing performance. Subsequent optimization, involving the replacement of PCL with polyvinylidene difluoride (PVDF), improved pressure sensitivity and durability.

Further enhancement was achieved by incorporating silver nanoparticles (AgNPs) into CA fibres, improving charge-trapping ability, fibre morphology, and mechanical strength. The optimized Ag–CA/PVDF TENG exhibited a high-pressure sensitivity of 11.7 V $kPa^{-1}$, with a fast response and stable durability, making it suitable for precise biomechanical monitoring. For the first time, integration into a fabrigami structure enabled lightweight, practically wearable, real-time knee motion sensing, accurately capturing joint angles, speed, and frequency, with wireless data transmission via a compact circuit.

This research demonstrates a synergistic strategy combining electrospun material optimization with fabrigami structural design, demonstrating a pathway toward self-powered, wireless, and highly sensitive wearable systems for rehabilitation, sports performance, and healthcare monitoring.

# CHAPTER 1

## 1. INTRODUCTION

### 1.1. Motivation

Rapid advances in wearable technology have influenced many industries, including healthcare, sports, safety, environmental monitoring, space exploitation, soft robotics, transportation and industrial sensing. Biomechanical measurements are important in assessing human health and performance by providing quantitative analysis of human kinematics. Assessing joint biomechanics is relevant for healthcare where movement is affected by conditions such as osteoarthritis or during recovery from injury or medical procedures such as knee surgery or hip replacement. Assessing joint biomechanics (JBM) following knee or elbow injuries and surgeries may assist in tailoring personalised recovery and treatment plans. Beyond clinical applications, assessing biomechanics is fundamental to sports science, as well as comprehending and evaluating body mechanics in order to refine techniques, thereby enhancing athletic performance while at the same time reducing injury risks[1].

Technological advancements have greatly enhanced the accuracy of biomechanical assessments while transitioning from basic goniometers to advanced motion capture systems. Modern motion-capturing systems now provide detailed data on the angles, speed, and frequency of human movements, which are crucial for therapeutic and performance-enhancement applications. However, they come with significant drawbacks, including the need for a substantial financial investment in their purchase, operation, and maintenance. Additionally, these systems require considerable processing power and must be set up in a controlled environment. Furthermore, limiting their portability and versatility for use in different settings makes them challenging to use for the improvement of users' day to day activities[2]. Wearable technology, which has the flexibility for daily use, can gather useful physiological and biomechanical data. However, the increasing uptake in such devices calls

for innovative means of powering them, leading to a need for energy-autonomous wearable wireless sensing systems providing continuous and reliable monitoring capabilities without requiring external power sources or frequent battery replacements[3–7]. While early wearable sensors focused mainly on simple sensing functions, such as heart rate, respiration, body movement and step counting,[6,8,9] recent developments have enabled more sophisticated functionalities (e.g., real-time multiple physiological parameters monitoring, motion tracking, machine learning augmented brain computer interfaces, and ambient environmental sensing).

Recent developments in sensor technology have introduced Triboelectric Nanogenerator (TENG) as a promising alternative for assessing human joint movement[3,10–12]. TENGs use the triboelectric effect to generate electrical signals from mechanical motion, offering unique advantages such as high sensitivity, lightweight, flexibility, and easy integration over traditional systems. Unlike advanced motion capture systems, TENGs provide a more accessible and cost-effective solution for wearable applications in both clinical, home and athletic environments [7] .

Since Z. L. Wang's research group first introduced the concept in 2012, significant advancements have been made in TENG technology, particularly in wearable applications for detecting basic human activities, such as gait analysis[13], hand and finger movement detection[14,15], body gesture recognition[16], physical exercise monitoring[17,18], heart rate monitoring[19], and respiratory monitoring[20]. In recent years, experimental studies have explored the use of TENGs for upper and lower limb rehabilitation[21], muscle function recovery[22], pulmonary rehabilitation[23], and other applications, including neck injury rehabilitation caused by poor posture, accidents, or prolonged computer use[10,12]. Pandey et al. highlight that despite their precision, efficiency, and sensitivity for wearable JBM and rehabilitation applications, TENGs still face significant challenges[12].

# CHAPTER 1

The characteristics of the human body, such as its shape, comfort requirements, and safety concerns, present challenges to the development of wireless sensing systems for JBM monitoring applications. To assure comfort and wearability, wearable devices must be flexible, lightweight, breathable, biocompatible, and capable of conforming to the contours of the human body[3]. Many TENG-based sensors used for rehabilitation are currently bulky and heavy, which hinders their practicality for real-world use[21,24]. Moreover, the accurate detection of low-frequency, low-force movements, crucial for capturing detailed parameters like speed, frequency, and joint angles, remains an underexplored area in the context of TENG sensors. Furthermore, these devices require robust and reliable fabrication techniques for scalable production while maintaining high performance and functionality. This necessitates the exploration of different materials and manufacturing approaches to meet these requirements and enable seamless implementation of the systems on the human body[25].

Researchers have been experimenting with a range of materials and manufacturing techniques to address these requirements in developing TENG based wearable wireless sensing systems. Materials reported to date include traditional polymers, advanced metallic and functional materials, and processes like lithography, casting, printing, and chemical and mechanical modifications[26–29]. While these methods typically deliver satisfactory electrical and sensing performance, there are still challenges to overcome with regards to the wearer's comfort during everyday body movements. In particular, enhancing flexibility and breathability is essential for achieving long-term comfort. To create practically wearable devices, experts are exploring advanced nanofabrication techniques and textile engineering concepts for improving scalability[30]. Techniques that are compatible with large-scale textile manufacturing processes are essential to bring these concepts beyond the lab and into feasible production lines.

One approach is to use nanofabrication techniques to integrate sensing and electrical properties into fibres and fabrics. Among these methods, electrospinning has emerged as a plausible candidate for human in vitro and in vivo applications[31,32]. Interestingly, the electrospinning technique offers a multitude of benefits over other film processing methods by creating a micro/nano porous fibre structure for the development of energy-autonomous wearable sensing systems. It allows for multiple fibre alignments, customizable porosity targeting flat and asymmetric surfaces[33], and boasts a high surface-to-volume ratio for sustainable manufacturing.[34] Its molecular-level alignment reduces the need for post-processing techniques, such as in-situ formation of piezoelectric properties in Poly(vinylidene difluoride) (PVDF) and its copolymers[35–37]. Additionally, it enables multi-component nanofabrication in a single micro/nanoscale step[38,39]. Compared to other techniques such as photolithography, chemical vapor deposition and inductive couple plasma etching, electrospinning is more cost-effective and efficient, making it a plausible choice among the scientific community[40]. Furthermore, electrospun nanofibres can be easily formed into yarn via twisting and braiding techniques and then converted or attached to fabrics through weaving, knitting, or embroidery, making it an ideal method for integrating with the current textile manufacturing processes[41,42]. All of these factors contribute to the positive impact of electrospinning, making it the preferred choice for a variety of applications.

Integration of such nano fabrication layers to achieve higher functionality and maintain the conformal shape of the body is a challenging process. Having mechanical robust while maintaining contact separation movements (described in section 2.3 modes of TENG) required innovative structural design approaches. Origami, an ancient Japanese art form centred on the meticulous folding of paper to craft detailed shapes, has long been esteemed for its blend of simplicity and intricate design. Initially practiced for ceremonial purposes, origami has transformed into a contemporary method for investigating geometry and

engineering principles[43]. Expanding on this tradition, fabrigami has emerged as an inventive adaptation, utilizing the same folding methods with pliable, resilient fabrics[44]. This advancement facilitates the creation of adaptable, long-lasting structures with potential applications in fields like soft robotics[45–47], wearable technology[48,49], and adaptive materials[50,51].

This thesis aims to bridge this gap by integrating nanofabricated TENG-based layers with fabrigami-inspired textile structures to develop energy-autonomous, flexible, and conformal sensing systems for joint biomechanics monitoring. This approach combines the sensitivity of TENGs, the scalability of electrospinning, and the adaptability of fabrigami to overcome current limitations in wearable sensing technologies.

### 1.2. Problem Statement

Although TENG based systems provide a wide range of benefits to improve the JBM monitoring there are some significant areas to further improve the quality and market readiness of such systems.

- Many are bulky, rigid, or heavy, reducing comfort and wearability.
- The accurate detection of low-frequency and low-force joint movements, vital for rehabilitation and performance assessment, is still underdeveloped.
- Existing fabrication methods for integrating nano-functional layers into textiles often compromise conformality, robustness, and scalability.
- Mechanical durability and adaptive structural design remain unmet challenges for long-term, real-world applications.
- Measuring speed, joint angle and frequency of movements are vital for home rehabilitation systems and systems with such level of detail capturing is still under investigation.

Thus, there is a clear research gap: the lack of scalable, energy-autonomous, and conformal wearable sensing systems that integrate nanofabricated functional layers with adaptive textile architectures for reliable and comfortable joint biomechanics monitoring.

# CHAPTER 2

## 2. LITERATURE REVIEW

**Publication status: Published as a journal paper**

**Part of this chapter published as a journal paper in ACS Nano**

Gunawardhana, K. R. S., Simorangkir, R. B. V. B., Mcguinness, G. B., Rasel, M. S., Colorado, L. A. M., Baberwal, S. S., Ward, T. E., O'flynn, B., & Coyle, S. M. (2024). The Potential of Electrospinning to Enable the Realization of Energy-Autonomous Wearable Sensing Systems. ACS Nano, 18(4), 2649–2684. https://doi.org/10.1021/ACSNANO.3C09077

# CHAPTER 2

## 2.1. Introduction

In addition to advanced sensing functionalities, the potential to harnessing energy from the surrounding environment has been addressed in order to provide longer and more continuous operation while wirelessly transmitting data and information[16,52]. IDTechEx reported that the market for wearable sensors is expanding at a compound annual growth rate of 5%, with a projected value of USD 7.2 billion by 2035[53]. This demonstrates the increasing demand for wearable technologies across multiple industries, which will require advance energy-autonomous systems in order to comply with sustainability targets. The ability to eliminate or reduce the need for battery replacements in wearable devices would greatly enhance their convenience, usability and sustainability, thereby making them more appealing to consumers and industries. To meet this demand, next-generation wearable systems must be designed as fully energy-autonomous platforms rather than relying on conventional battery-powered architectures.

Creating energy-autonomous wearable wireless sensing systems involves the integration of several essential building blocks (Figure 1). Such blocks include i) energy harvesters, ii) energy storage devices, iii)sensors, iv) communication modules, and v)processing units[54]. Energy harvesters are responsible for converting ambient energy sources into electrical energy that can be used to power the wearable device. The ambient energy may be harvested from sources including solar(Organic Solar Cell (OSC), Perovskite Solar Cell (PSC), Dye Sensitized Solar Cell (DSSC))[55], mechanical(Piezoelectric Nanogenerator (PENG), TENG)[56], or thermal energy[57]. The energy storage devices, such as batteries, supercapacitors and hybrid systems store the harvested energy for use when ambient energy is unavailable[58]. This ensures the continuous operation of the wearable device. Sensors play a crucial role in collecting data from the surroundings, looking inwards at physiological signals from the wearer's body and outwards at data emanating from the environmental

conditions around the wearer. Moreover, these data provide useful information about the wearer's status for various applications in health, lifestyle, safety, work and provide additional input methods for human machine interfacing.

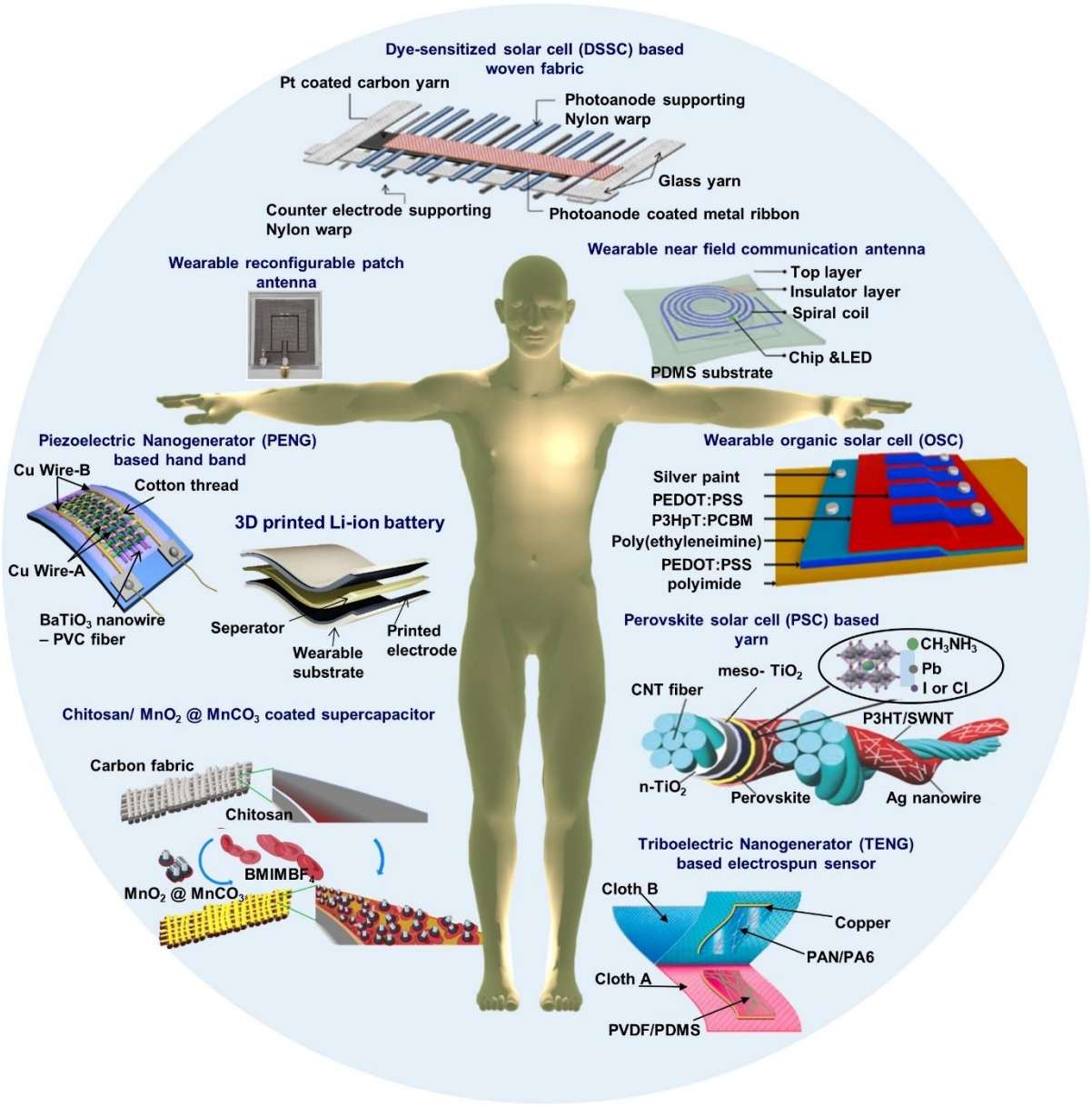


Figure 1: Examples of recent developments in energy autonomous wireless sensing devices including wearable energy harvesting, self-powered sensing, energy storage and communication devices.

(PENG – reprinted from ref[59] and OSC – reprinted from ref[60] with permission Copyright©2015 Elsevier B.V., PSC– reprinted from ref[61] with permission

Importantly, the performance of wearable sensors is often constrained by the choice of materials and fabrication strategies, which directly impact sensitivity, durability, and power generation. Addressing these challenges has drawn increasing attention to nanostructured materials and advanced fabrication techniques such as electrospinning. Some of the advantages of using electrospinning for fabricating wearable electronics can be summarized as follows.

**Fibre-based structure:** Electrospinning enables the fabrication of ultrafine/intricate three-dimensional fibre networks with diameters ranging from nanometres to micrometres. These fibres can be easily collected as nonwoven mats or aligned into patterns with desirable wearable properties, such as breathability[67–69], washability[70], biocompatibility[67], stretchability, and flexibility[71]. These fibres can serve as construction blocks for a variety of components, including sensors, electrodes, and energy storage elements[41]. In particular, due to the ultrafine fabrication nature, electrospinning can produce breathable, washable, transparent and flexible graphene-based electrodes[72] which is comparatively cost effective compared with Ag or Au based nanostructured electrodes. The high surface area-to-volume ratio of electrospun fibres provides enhanced sensitivity for sensing applications and efficient charge storage for energy-related devices[73].

**Controllability of properties:** The process can be easily modified to control the fibre morphology, composition, and alignment. By adjusting the spinning parameters and using different materials, it is possible to create fibres with tailored properties such as high porosity, high surface area, tensile strength and elastic modulus[34,42,55,74–76]. Furthermore, advances in some electrospinning techniques such as needleless electrospinning, wet electrospinning and blow electrospinning have provided higher output targeting lower manufacturing time[38,77–81]. This versatility renders electrospinning suitable for a wide range of wearable electronic applications[34,42,55,74,76].

**Integration with flexible substrates:** Wearable electronics require flexible and conformable substrates to ensure comfort and functionality. Electrospinning can be performed directly onto flexible substrates, including yarns, fabrics and polymer films, without requiring complex processing steps. The resulting electrospun fibres can conform to the substrate's surface, allowing for seamless integration with textiles, apparel, and even directly onto the human body. This conformability enhances the comfort and wearability of the electronic devices[42,82]. Selecting suitable filler materials[83], using bicomponent[84] or multicomponent electrospinning techniques[85] and introducing further processing methods[86], flexibility, elasticity and other related mechanical properties can be further enhanced.

**Multifunctionality:** Electrospinning allows for the incorporation of various functional materials into the fibres. By combining different polymers, nanoparticles, or even biological molecules, electrospun fibres can exhibit multiple functionalities such as conductivity, biocompatibility and biodegradability. This multifunctionality makes electrospinning an attractive technique for fabricating complex, integrated wearable electronic systems. [34,42,55,74,76,87]

To date, there have been some review papers written in the context of electrospinning technology and its implementation. For example, Xue et al. comprehensively reviewed the process of electrospinning nanofibres, methods and applications[73]. Recently Zhi et al.[42], Babu et al.[34] and Joshi et al.[88] have provided comprehensive reviews on the use of electrospinning in piezoelectric, triboelectric and supercapacitor based wearable devices, respectively. Gunawardhana et al. provided an in-depth review of how electrospinning contributes to the development of different building blocks in wearable, wireless, energy autonomous devices and considers how to integrate them using traditional textile engineering techniques[7]. In addition to the improvement of energy harvesting, energy storage, sensing and transmission, equal attention has been given to the mechanical and aesthetic performance improvements using different fabrication techniques.

Among these building blocks, sensing stands out as particularly critical, as it forms the direct interface between the wearer and the digital environment. However, for sensing data to be useful, it must be seamlessly transmitted to external devices such as smartphones or laptops for storage, analysis, and real-time feedback. This highlights the importance of coupling sensors with lightweight communication modules and efficient processing units[25,89]. TENGs operates through contact electrification and electrostatic induction, where charges are transferred via an external electrode and subsequently through a load, generating a detectable signal. The sensitivity and accuracy of TENG-based sensors are significantly influenced by the triboelectric substrate. Advancements in substrate design are crucial for optimizing sensor performance, including improvements in surface morphology and material composition to enhance the triboelectric effect[90]. Additionally, optimizing the efficiency of charge transfer between the triboelectric layers is essential for maximizing electrical output[91,92], requiring careful consideration of interface properties and material interactions. Furthermore, ensuring effective mechanical movement between the

triboelectric layers is crucial, as it directly impacts the energy conversion efficiency[93]. Collectively, these factors are vital in advancing the performance of TENG-based sensors.

This chapter is structured into seven interconnected sections to establish this research's theoretical and technological foundation. It begins with an overview of electrospinning technology, detailing its historical development, working mechanisms, material systems, and advanced techniques enabling nanostructured, flexible substrate development. The second section explores how electrospun materials have been employed in energy-autonomous wearable sensing systems, with a particular emphasis on TENGs, while also referring to related applications in piezoelectric, thermoelectric, and solar energy harvesting. Section three introduces the structural design principles of origami and its transformation into fabrigami, fabric-based folding systems that offer unique advantages for wearable integration. The fourth section delves into the synergy between electrospinning and fabrigami, focusing on material and structural considerations for enabling foldable, functional textiles. Section five reviews the development of fabrigami-enabled TENGs and their relevance in monitoring joint biomechanics, emphasizing mechanical adaptability, anatomical conformity, and energy autonomy. Section six addresses system-level integration strategies, including textile-based fabrication, wireless communication, and sustainable power management. Finally, section seven outlines current testing protocols for evaluating wearable technologies and discusses emerging research challenges and future opportunities in the field of electrospun fabrigami systems.

## 2.2. Electrospinning technique

### 2.2.1. Brief history

Electrospinning can be categorized as a form of electrostatic spraying. Electrostatic spraying applies a small charge to an aerosolized droplet before it separates from the nozzle. Electrospinning utilizes this approach to produce continuous fibres through jet formation.

The fibre properties are determined by the viscosity and viscoelastic properties of the polymer material.[73] Although the history of electrospinning dates back to the early 1600s, it was not popular until 1902 that Mortan and Cooley filed multiple patents for the electrospinning process.[41] In 1938, the Soviet Union began using the commercially available electrospun product to capture aerosol particles. Between 1964 and 1969, Geoffrey Ingram Taylor conducted a series of experiments to mathematically understand the cone-shape polymer droplet under applied high voltage.[41,94] In 1996, Reneker et al. reported the possibility of producing nanofibres using the electrospinning technique, attracting the interest of scientists worldwide as a promising nanofabrication technique.[95]

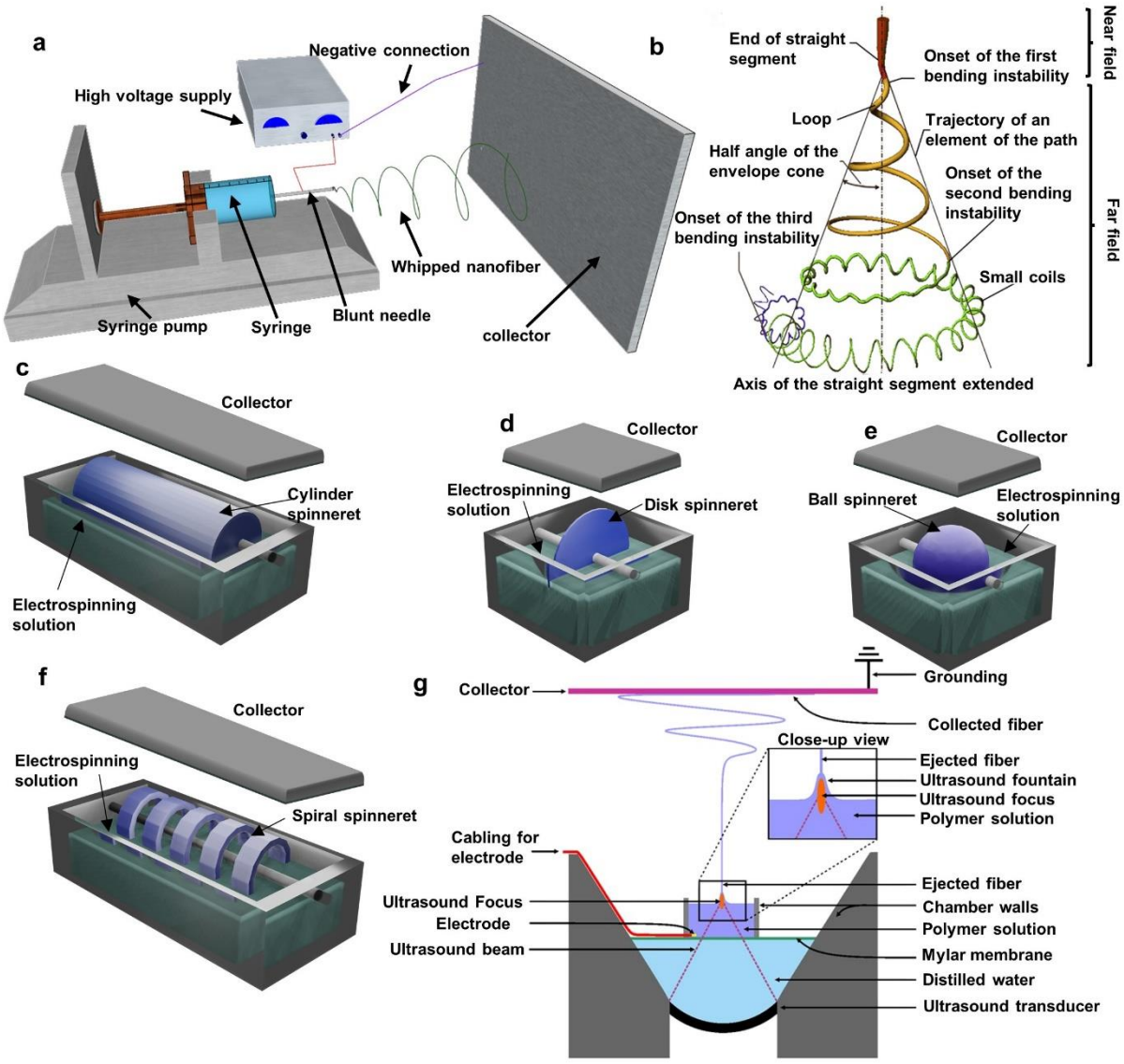

Figure 2: Principle and evolution of electrospinning technique.

a) Basic electrospinning set-up, b) Electrospinning whipping action reprinted from ref[73,96] With permission Copyright©2019 and copyright©2006, American Chemical Society, Needleless electrospinning with rotating, c) Cylinder, d) Disk, e) Ball and f) Spiral techniques (c, d, e and f are adapted from ref[97].), g) Ultrasound enhanced electrospinning technique use with polymer chamber reprinted from ref.[98] published with CC BY Copyright©2018 The Authors. Published by Springer Nature. Whole figure copied from ref [7] published with CC BY Copyright©2024, The Authors.

### 2.2.2. Operating principle

A basic electrospinning setup consists of three main parts: the jet formation mechanism, the collection mechanism, and the high voltage source[99] (Figure 2a). Typically, the jet formation mechanism comprises a polymer-loaded syringe with a blunt needle tip. The majority of materials used in electrospinning are organic polymers. The possibility to dissolve some of these polymers in an appropriate solvent meets the lead requirement for implementing the solvent/solution-based electrospinning process.[73] Certain polymer materials have high chemical resistance, which has led to the development of a technique called melt electrospinning. This technique involves melting the polymer and using it for melt-blowing and spinning bonding to produce nanofibres. The polymer is compressed through this needle using a controlled mechanism. The high voltage applied between the needle tip and collector causes charges to accumulate around the tip and the polymer droplet. When the electrostatic repulsion force created by accumulated charges exceeds the surface tension defined for a particular polymer type, nanofibres begin to attract towards the collector, followed by solidification and deposition in a randomly oriented way.[99,100] Initially, the repulsive force converts the polymer droplet into a cone-like shape, commonly referred to as Tayler's cone. Even though the jet is formulated as a straight line, it undergoes

rigorous whipping due to bending instabilities (Figure 2b). Solution parameters, process parameters, and ambient environmental parameters have a significant impact on the performance of the electrospinning process.[101] The effects of each parameter on nanofibres formation are summarized in Table 1.

In 1969, Taylor derived an equation to approximately determine the critical voltage ($V_k$ kV) required to overcome the surface tension in a given material.[102]

$$V_k = \frac{4H^2}{L^2}\left(ln\left(\frac{2L}{R}\right) - 1.5\right)(1.3\pi RT)(0.09) \quad \text{(E1)}$$

In Equation 1, H (cm) is the distance between the needle tip (or spinneret) and the collector, L(cm) is length of the needle (or spinneret), R (cm) is the outer radius of the needle, and T (Dyn/cm) is the surface tension of the polymer material. Based on this equation, there is a proportional relationship between the surface tension and the critical voltage at the jet formation. The value of 1.3 was determined using the assumption that the cone has a semi-vertical angle with a value of 49.30 (2 cos (49.3) =1.3). Factor 0.09 was inserted to get the outcome in kV. Viscoelastic properties of the polymer material should ensure that the continuous fibre surpasses the Rayleigh limit after the near field region.[73,103] It is worth noting that one of the important phenomena in nanofibre formation is radial charge repulsion, which allows for whipping action.

Table 1: Effect of solution, process and ambient environment parameters for the electrospun nanofibres.

| Parameter | Effect on the nanofibres |
|---|---|
| Solution parameters | |
| Solvent evaporation rate | Determines the solidification rate. Mainly affected in solution electrospinning. Clogging at the needle might occur when the |

| | |
|---|---|
| | volatility is very high. Low evaporation causes wet fibres to form at the collector, resulting in solvent patches.[73] |
| Solvent dielectric constant | Influences the magnitude of electrostatic repulsion at the jet; the higher the dielectric constant, the higher the applied voltage required for stable jetting. A higher dielectric constant reduces the inter-fibre spacing.[104] |
| Solubility | High solubility is always favourable for preparing fine fibres.[99] |
| Polymer type | Determines the selection of molecular weight, viscosity, solution type and concentration, as well as the process parameters. |
| Polymer concentration | Determines the consistency of the formulated fibre network depending on the type of material and its molecular weight. If the concentration is too low, the fibres tend to either discontinue or merge.<br>For instance, Poly Vinyl Alcohol(PVA)- 5 wt.% resulted in beaded fibres, 15 wt.% resulted in uniform fibre, 25 wt.% resulted in coarse non-uniform fibre[105]<br>Polyamide (PA)6- 6 wt.% resulted in droplets, 15 wt.% resulted in merged fibres, 25 wt.% in smooth fibres[106]<br>If the concentration is too low, electro spraying is prominent with discontinuous, merged or bearded fibres. In needleless electrospinning techniques, a very high concentration completely halts the electrospinning process.[82]<br>In CA nanofibres, the tensile strength, break strain, and initial modulus increase with increasing concentration.[107] |

| | |
|---|---|
| Viscosity | Depending on material type, solvent type and concentration decreasing viscosity and surface tension results in thinner fibres.<br>High viscosity complicates the ejection process. A minimum viscosity is always necessary for chain entanglement[108] |
| Molecular weight | Affects the viscosity of the polymer solution.[109] Low molecular weight and limited chain entanglements produce nanofibres with beaded structure; the fibre diameter increases with molecular weight.[105] |
| Conductivity | If the solution is completely insulating, electrospinning is not possible. High conductivity reduces the diameter of fibres.[99]<br>The Taylor cone will not develop if the conductivity is too high.[73] |
| Process parameters | |
| Applied voltage | Sufficient voltage is required to compensate for the repulsive force caused by surface tension. Average fibre diameter decreases as the voltage is increased further. Additionally, the change of α to β phase while high voltage is rapid, which favours energy harvesting applications. Further increasing voltage results in beads and fibre breaks due to increased drawing stress.[109]<br>In needleless electrospinning, high voltage reduces fibre diameter and increases fibre production rate.[82] |
| Needle gauge | Affects the diameter of the fibres. Additionally, different gauges can result in multiple jets.[34] |

| | |
|---|---|
| Spinneret types | Conventional method - Blunt needle<br>Advanced developments- needleless; cylinder, ball, porous tube, disk, coil, cone, stepped pyramid, wire frame, cleft, bead chain, bowl, slit[31] (See section 1.4) |
| Flow rate | A high flow rate results in higher fibre production and coarser fibres, however an excessively high flow rate results in droplets without the formation of fibres. Flow rates lower than the critical value (value which produces the jet with usual Taylor cone), on the other hand, cause congestion at the needle tip with an unstable jet, branching splitting, and flattened fibres.[82] |
| Collector design | Variations in collector design and its effects:<br>Metal plate collector: A simple architecture to achieve uniform morphology[99]<br>Double plate collector: better alignment than metal plate collector<br>Circular electrode collector: High productivity with easy separation of membranes<br>Rotating cylinder: Fibre alignment is high with reduced diameter and high physical properties. Further, increase the β phase of materials such as PVDF which is favourable in energy harvesting and self-powered sensing applications.<br>Rotating disk collector: Highly aligned nanofibres with enhanced β Phase.[109] |

| | |
|---|---|
| | There are some other techniques such as liquid bath, guide wire, rotating wire drum and conveyor,[31,110] which can be used to produce nanofibres in continuous uniform operation. |
| Tip to collector distance (TCD) | Mainly affects the evaporation process; the higher the distance, the higher the evaporation and stretching. However, over the optimum value, electric field intensity decreases. Additionally, a higher value will prevent the deposition of fibres onto the collector. A lower distance will result in a denser structure.[109] In needleless electrospinning, short distances provide interconnected nanofibres with outstanding mechanical properties.[82] |
| Ambient environment parameters | |
| Relative humidity | Low humidity is preferable for uniform morphology.[99] |
| Temperature | Increasing the temperature increases the rate of solvent volatilization and decreases viscosity and surface tension, resulting in the formation of small diameter fibres.[109] |

### 2.2.3. Materials

In literature dimethylformamide (DMF),[107,111] dimethylacetamide,[107] certain alcohols,[73] formic acid, dichloromethane,[112] tetrahydrofuran,[107] chloroform,[113] acetone,[114] hexa-fluor isopropanol,[100] dimethyl sulfoxide[115] and methane sulfonic acid[116] are widely used as solvents for electrospinning. Despite the fact that water is not a favourable solvent for electrospinning due to its high dielectric constant, PVA electrospinning is generally carried out using deionized water.[73,117] Furthermore, a wider variety of biodegradable and biocompatible polymers can be electrospun targeting wearable electronic applications. By utilizing electrospinning, it is possible to enhance the mechanical properties of

biodegradable materials, including increased flexibility, stretchability and breathability when compared to film-based substrates.[118] Table 2 summarizes the use of different materials for electrospinning, mainly in wearable contexts, which is the focus of this chapter. Different electrospinning techniques for improving the performance related with wearable applications using these materials have been detailed in the sections below.

Table 2: Prominent electrospinning materials in energy autonomous sensing systems.

| Application | Mechanism | Electrospinnable layer | Electrospinning materials |
|---|---|---|---|
| Energy Harvester | TENG, TENG self-powered sensors | Triboelectric layer | PVDF,[109] Polyimide(PI),[119] polyvinylidene fluoride-trifluoro ethylene (PVDF-TrFE), and Poly(vinylidene fluoride-hexafluoropropylene) (PVDF-HFP),[120] Poly Lactic Acid (PLA), CA, PA6, PA66, MXene[34] |
| | | Electrode layer | Poly (3,4-(ethylenedioxy) thiophene) (PEDOT), Carbon nanotubes(CNT)[3,34] |
| | PENG, PENG self-powered sensors | Piezoelectric layer | PVDF, PVDF-TRFE, PVDF-HFP, Polyacrylonitrile (PAN), Cellulose, PLA[121] |

| | | | |
|---|---|---|---|
| | | Electrode layer | PEDOT, CNT, Polyaniline (PANI)[42] |
| | DSSC | Electrode layer | Pt, ZnO, ZnO-$TiO_2$ |
| | | Supporting materials | PLA, PVDF and PVA, Polyvinylpyrrolidone ( PVP), CA $Cu(In_{1-x}, Ga_x)Se_2$, $Cu_2ZnSnS_4$, and $Cu_2ZnSnSSe_4$[122] |
| | OSC | Electrode layer | PAN, PANI[123] |
| | | Functional/Supporting material | poly(methyl methacrylate),[124] Polycaprolactone(PCL), poly(3-hexylthiophene):phenyl-C61-butyric acid methyl ester (P3HT:PCBM)[125] |
| | PSC | Supporting material for perovskite layer | PVP,[126] PI, Polyurethane (PU)[127] |
| Storage | Supercapacitors | Supporting material for electrolyte layer | PLA, PVDF and PVA[128] |
| | | Electrode layer | PEDOT, PANI, Polypyrrole (PP), Carbon nanofibres (CNF)[88] |

| | | | |
|---|---|---|---|
| | Li-ion batteries | Electrode layer | PEDOT: PSS, Polydopamine, PP, carbon nanofiller reinforced cellulose[88] |
| | | Supporting material | PLA, PVDF and PVA |

### 2.2.4. Advanced electrospinning techniques

Centrifugal spinning has been employed for over half a century to fabricate glass nanofibres by regulating parameters such as the radius of the orifice, angular velocity of the spinneret, distance from the centre of the orifice to the collector, polymer-related parameters and environmental conditions. Centrifugal electrospinning is an advanced architecture that applies an electrostatic field to the traditional centrifugal spinning technique. Experimental results demonstrate that the production rate of centrifugal electrospinning is twelve times that of conventional electrospinning systems with low polymer concentration.[38] In addition, centrifugal electrospinning promotes an exceptional improvement in mechanical performance and, in conjunction with melt electrospinning, can produce ultra-fine fibre for high-rate supercapacitors.[38,129]

Earlier advances in electrospinning technology indicate that multi-nozzle electrospinning and multicomponent electrospinnable nozzles result in increased throughput and enable functional material developments.[38,39] Using a multi-nozzle electrospinning technique and moving collector apparatus, such as rotating drum, mandrel or belt, it is possible to develop highly oriented nanofibre architectures with high mechanical qualities for wearable applications. In addition, multicomponent techniques can produce bilateral conductive and nonconductive surface samples necessary for energy harvesting, storage and communication devices.[38,39]

Even though traditional needle-based electrospinning is a simple and versatile nanofabrication technique, low production yield, needle clogging, and limited capacity have limited its practical applications.[32] Moreover, the rapidly growing wearable electronics market necessitates a higher production rate, mandating alternative electrospinning techniques. Needleless electrospinning is a popular method, which uses a widely open liquid surface with a specially developed spinneret that is partially submerged in the electrospinning solution. As spinnerets for needleless electrospinning, cylinders (Figure 2c), disks (Figure 2d), balls (Figure 2e), springs (Figure 2f), coils, wires, rods, and spirals are increasingly popular. All these spinnerets can create a thin polymer layer on their surface as a result of rotation-induced agitation. Based on the intensity of the electric field, a conical spike is formed towards the collector, resulting in multiple polymer jets. Some experiments provide evidence that ball and disk spinnerets have good control over fibre diameter and productivity, whereas changing the electric field in ring and coil spinnerets leads to thinner fibres with a large surface area.[38]

In 2016, Laidmäe et al. filed a patent for an ultrasound enhanced electrospinning technique (Figure 2g).[98] This method used a focused and highly intense ultrasound to create an ultrasonic fountain when a precursor solution was placed on a mylar (electrically insulating and acoustically conducting) membrane. Controlling ultrasound parameters and maintaining sufficient electric field towards the collector can control the gradients of mechanical properties, giving greater prospects for future wearable electronic devices.[98,130]

Typically, electrospinning falls within a flow rate range of 4-10 μL/min, which presents challenges for scaling up production. However, blow spinning is a promising and relatively unexplored method that can inject fibres at a much higher rate of 200 μL/min. This technique leverages gas pressure to propel the polymer onto the surface, similar to melt spinning, and combines it with the polymer dissolution process used in solution electrospinning.[77,78] Blow

spinning has shown promise in producing micro-scale fibres for wearable electronic applications.[131]

Mostly, electrospun membranes feature tightly packed small pore sizes formed from small diameter nanofibres. However, by transitioning from traditional solid collectors to grounded liquid baths (using a nonsolvent of electrospun polymer), it becomes possible to achieve liquid phase collection with specific functionalities, such as high porosity with 3D morphology.[132,133] This method, known as wet electrospinning, is an area that has been relatively unexplored in wearable electronic applications. Nonetheless, evidence suggests that the 3D morphology of this technique facilitates rapid access to electrolytes in energy storage devices, resulting in faster charge-discharge times and higher storage capacity.[79–81]

## 2.3. Electrospinning in mechanical self-powered systems

This section discusses the application of electrospinning techniques to manufacture textile compatible materials for energy harvesting and self-powered sensing functionalities. Section 2.3.1. provides an introduction and working principle information related to the TENG technique with theoretical models. Section 2.3.2 and section 2.3.3. explore the use of electrospinning for mechanical energy harvesting and self-powered sensing, respectively, using triboelectric technique. Section 2.3.4. summarizes the use of electrospinning in other building blocks; Piezoelectric, solar, thermal and evaporative energy harvesting, wearable storage devices and communication devices.

### 2.3.1. Introduction to TENG and operation principle

Movement from the human body is a pertinent energy source for powering wearable sensors. For instance, the ankle, arm, knee, shoulder, elbow, and fingers movement can produce 66.8 W, 60 W, 36.4 W, 2.2 W, 2.1 W, and 6.9 W-19 mW of energy, respectively.[134] The two most widely used methods of wearable energy harvesting are based on piezoelectric and

triboelectric principles/ TENG and PENG devices, shown in Figure 3a, b respectively. These are pioneering mechanical energy harvesting and self-powered sensing techniques which can convert irregular and low-frequent human movements into electricity. The conversion of mechanical motion into electrical power/signals can be described by Maxwell's equations of displacement current.[135,136] PENG is a concept that was developed in 2006 by Wang's research group, which works on the stress state and electrical polarization of a specific piezoelectric material.[137–139] Several years later, Fan, Tian and Wang developed the TENG in 2012 based on contact electrification and electrostatic induction.[140] A recent survey shows that over 6000 scientists worldwide are working on TENG research, which as a rapidly evolving research area making it a promising method for wearable electronics power/sensing.[135] Furthermore, based on material selection, architecture, fabrication technique, and power management methods, the power conversion efficiency and peak power outputs of piezoelectric and triboelectric devices can be adjusted.[141,142] Additionally, utilizing the electrospinning technique to create hybrid PENG and TENG devices offers advantages due to the natural polarization of certain materials. This results in increased power generation and sensitivity compared to other manufacturing methods.[143,144]

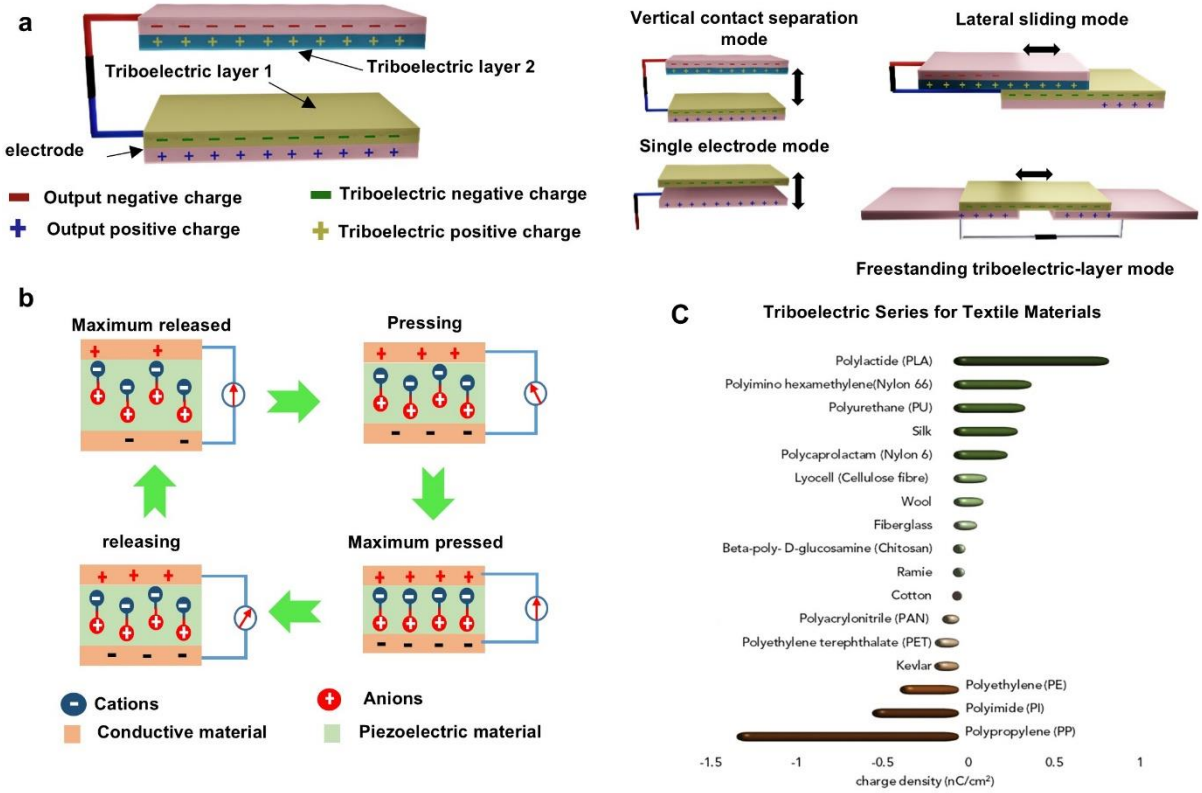


Figure 3: Principle and working mechanism of mechanical energy harvesting techniques.

a) Schematic of TENG and main working modes, b) Working mechanism of PENG, adapted from ref[145]. copied from ref [7] published with CC BY Copyright©2024, The Authors.c) Triboelectric series for textile materials copied from ref [3] published with CC BY NC ND Copyright©2020, The Authors.

Triboelectric nanogenerators function through triboelectrification and electrostatic induction, resulting in a relative movement of two charged surfaces. Even though the exact process of triboelectrification is still unclear[135], evidence claims that it occurs primarily through electrons,[146] charged materials,[147] ions, or a combination of all factors.[148] In addition, Ko et al. examined the electron transfer mechanism of the triboelectrification process and concluded that there is a positive relationship with the potential interface barrier, and stuck charges are the foundation for triboelectric charge separation.[149] A triboelectric series has been developed based on an empirical classification to identify the positively and negatively charged materials,[150] e.g., materials such as wood or nylon are at one end of the

scale with a tendency to positively charged while PDMS, PVDF and silicone rubber has a tendency to become negative. There are a number of publications quantifying the triboelectric series,[150] and in one previous publication by Gunawardhana et al, an adjusted triboelectric series is presented related to wearable materials(Figure 3c).[3] A TENG device typically uses two materials that are well separated from each other within the triboelectric series, targeting higher charge separation. There are different set-ups for arranging the materials within the TENG devices to ensure the interaction between these materials generates energy, including contact-separation, lateral sliding mode, freestanding electrode mode and single electrode mode. TENG contact separation mode (Figure 3a) is the most common architecture. Using this traditional architecture, the TENG device has two distinct nonconductive (or one conductive and the other nonconductive) materials attached to electrodes which are connected to an external load (Figure 3a). The triboelectric materials undergo close contact and separation movements, resulting in charge separation due to the triboelectric effect. Repetition of relative moment of the materials can induce charge to the attached electrodes, creating electron flow from one electrode to the other through the external load. When the TENG's triboelectric materials are in contact with each other the electrons flow goes in one direction, then when the triboelectric materials separate the electrons flow in the opposite direction, resulting in an alternating current flow. Selection and fabrication of suitable materials further apart in the triboelectric series, as well as the improvement of the electrostatic induction process, are the pioneering research topics related to this technique.[3]

In an effort to understand the generation of charge within nanogenerators, in 2017 Wang proposed that the current output can be explained using Maxwell's displacement current theory.[151]

$$J_D = \frac{\partial D}{\partial t} = \varepsilon_0 \frac{\partial E}{\partial t} + \frac{\partial P}{\partial t} \qquad \text{(E2)}$$

In Equation 2, $J_D$ is the displacement current density of the displacement field D for time t, E is the electric field, $\varepsilon_0$ is the permittivity of the dielectric material, and P is the polarisation field. In this equation, while the term $\varepsilon_0 \frac{\partial E}{\partial t}$ provides vital information regarding electromagnetic waves in wireless communication, $\frac{\partial P}{\partial t}$ is directly related to the output current of nanogenerator devices.[135,151] In addition, the PENG and TENG devices are referred to as capacitive induction devices[152]. For TENG, mechanical motion between triboelectric substrates modulates the capacitance between electrodes in response to a fixed triboelectric surface creating high impedance energy harvesting device.[151] Similarly for PENG, while the initial conversion relies on the piezoelectric effect to generate a potential difference, the device's, external electrical characteristics are often modelled as a voltage source in series with an internal capacitance.[153] A parallel plate capacitor model was developed for contact separation mode TENG architecture to explain the relationship between voltage (V), charge (Q) and layer separation of nanogenerator (x), which is known as the V-Q-x relationship.[151,154]

$$V = -\frac{1}{C}Q + V_{OC} \qquad \text{(E3)}$$

In equation E3; C indicates overall capacitance while $V_{OC}$ indicates the open circuit voltage of nanogenerator devices. Dharmasena et al. developed a distance-dependence electric field (DDEF) model to overcome the limitations of the parallel plate model, such as the complexity of the polarisation of dielectric layers, electric field behaviour inside the parallel plates and induction behaviour of the output charges in electrodes.[134,155] This model was developed considering the finite dimension of the charged surfaces and the perpendicular distance (y) from the charged surface. According to the DDEF method, the overall electric field ($E_Z$) generated from such a charged surface with a surface charge density of σ, permittivity of ε along with the dimensions of width (W) and Length (L) can be defined as,

$$E_Z = \frac{\sigma}{\pi\varepsilon} arctan\left[\frac{\frac{L}{W}}{2\left(\frac{y}{W}\right)\sqrt{4\left(\frac{y}{W}\right)^2+\left(\frac{L}{W}\right)^2+1}}\right] \quad \text{(E4)}$$

The DDEF model can be used not only for charged surfaces, but also be used to analyse the output behaviour of the electrodes. Concurrently, DDEF can predict the power output behaviour of the TENG devices. Furthermore, Dharmasena et al. examined the effect of the power output with material parameters, such as triboelectric charge density and dielectric constant, and structural parameters, such as layer thickness and surface area. Theoretical results were conclusive that triboelectric charging has a quadratic relationship with the power output, thus determining charge density as a critical factor in TENG power optimization.[134] This implies that an increase in surface area and a reduction of the thickness of the TENG layer are favourable for higher power generation in TENG devices. Also, increasing the surface area reduces the internal impedance, and maintaining a sufficient thickness is crucial to stabilise the accumulation of triboelectric charges. Electrospinning can be used in TENG devices to increase the surface contact area, thus increasing charge density and resulting in high power output. In addition, due to the nature of nanofabrication the thickness of the layers produced by electrospinning can be controlled, which is favourable for high power generation.

### 2.3.2. Electrospinning-enabled TENGs for energy harvesting

Electrospinning can manufacture single triboelectric surfaces or composite-based device architectures to create TENG devices.[34] Kim et al. have investigated the possibility of developing TENG devices using PI nanofibres in a one-step electrospinning process (Figure 4a). In this experiment, the PI layer was used as the tribonegative layer, while aluminium was used as the tribopositive layer. Initially, this set-up demonstrated an open circuit voltage ($V_{OC}$) of 66.1 V and short circuit current ($I_{SC}$) of 1.68 μA while using commercial PI films. Subsequently, the commercial PI film was replaced with screen-printed PI film which

resulted in a reduction $V_{OC}$ to 45.6 V and $I_{SC}$ to 1.61 µA. Conversely, electrospun PI nanofibre film demonstrated a significantly higher $V_{OC}$ of 366 V and $I_{SC}$ of 6.52 µA, thereby increasing the performance of the TENG device. SEM images reveal that the surface of commercially produced PI film and screen printing is flat and has a lower surface area compared to electrospun samples. It is worth noting that there were no noticeable differences in the static electricity of all three samples, therefore, it is the increase in surface area that is attributed to being the main factor in creating higher surface charges and greater electrostatic induction which ultimately leads to higher output power.[119]

The choice of materials is an important factor in the design of TENG devices. Ferroelectric polymers, namely PVDF, PVDF-TrFE, and PVDF-HFP, are widely used in electrospinning-based TENG devices given their high fluorine content which contributes to high electron affinity resulting in tribonegative surfaces.[100] Lee et al. have published a comprehensive review on the progress of PVDF as a functional material in TENG energy harvesting and self-powered sensing.[120] To summarize their findings, besides having a high electron affinity, utilizing various electrospinning arrangements can enhance both the physical and electrical qualities of the PVDF fibres produced. Wang et al. have developed TENG using PVDF (tribonegative) and PA6 (tribopositive) with balanced physical and electrical performance using parallel nanofibre arrangement acquired through electrospinning (Figure 4b). During electrospinning, PVDF was collected through a rotary collector targeting parallel arrangement by changing the rotation speed. The high speed of the drum reduced the fibre diameter and increased the tensile strength in a longitudinal direction. In addition, under 2 Hz impact frequency with separation of 4 mm, the resulting TENG demonstrated $V_{OC}$ of 164 V, $I_{SC}$ of 392 nA and power density of 129.46 $mWm^{-2}$, which was significantly stable for 100,000 cycles.[156] Furthermore, Song et al. observed that increasing the arrangement of electrospun nanofibres in parallel way can improve the forward polarised dipoles in PVDF, thus increasing $V_{OC}$, $I_{SC}$, and power density 0.5, 2.6 and 2.2 times, respectively. The

occurrence of this phenomenon is highly likely when the charge produced by the piezoelectric feature of PVDF nanofibres aligns with the charge generated by friction. As a result, the surface polarization is significantly increased.[157]

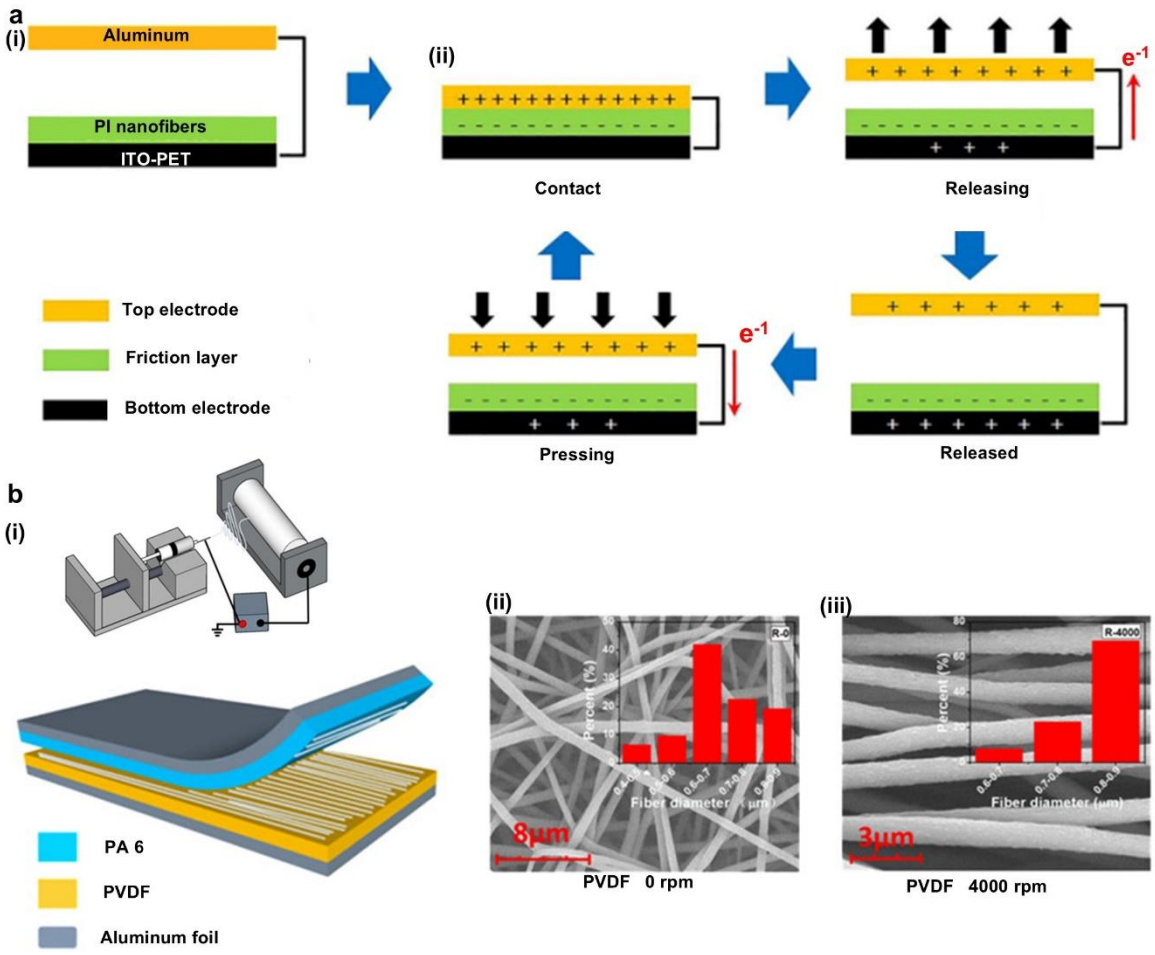


Figure 4: Using electrospinning single and dual triboelectric layer modification for energy harvesting applications.

a) Schematic of PI nanofibre and aluminium-based TENG reprinted from ref.[119] published with CC BY Copyright©2020 The Authors., b) Ordered electrospun sample schematic, SEM images of 0 and 4000 rpm rotary collector based nanofibres, (i), (ii), and (iii), respectively, reprinted from ref[156] with permission Copyright©2020, American Chemical Society

In addition to pristine material electrospinning, functional filler materials[158] have been used along with electrospinning precursors to improve the performance of TENG devices. For example, Sun et al. have published a flexible TENG architecture with $MoS_2$/CNT (MC)

loaded 12% PVDF electrospun nanofibres (tribonegative) and nylon fabric as a positive layer (Figure 5a). Kelvin probe force microscope results compared with PVDF nanofibres and MC loaded PVDF nanofibres shows that MC can improve the surface potential of PVDF nanofibres enhancing electrical performances. The 0.3% MC loaded PVDF has resulted in $V_{OC}$ of 300 V and $I_{SC}$ of 11.5 μA under 50 N contact and separation force with 1.5 Hz frequency. Furthermore, 134 mW $m^{-2}$ power density was achieved through a load resistor of 100 MΩ resistor and could charge a 10 μF capacitor in 44 s. Contrary to these findings, a further increase of MC content creates a conductive network creating leakage current, thus neutralizing some charges in the surface. Moreover, proving that there needs to be sufficient thickness for charge accumulation and transfer, performance increased when the thickness increased from 0.04 to 0.08 mm (Figure 5a (i, ii)). In contrast, further increases beyond this thickness reduced the performance as given in the DDEF model which was previously discussed. However, the device output was stable over 3000 cycles, and after six months of exposure to normal indoor humidity and temperature, 30% performance was retained.[159]

Aside from MC, MXene materials can be used as a filler material, providing excellent electromagnetic interference shielding, high electrochemical activity and excellent volumetric capacitance properties favourable for TENG applications.[160] When MXene is used as thin films, there are some challenges to overcome, including low flexibility, a highly brittle nature, and surface roughness. However, electrospinning fabrication can solve these problems by maintaining nanoscale surface roughness, enhancing frictional contact, and increasing surface-to-volume ratio, thus improving flexibility. Sardana et al. developed a wearable real-time gas monitoring system using Mxene nanofibres (30% Mxene/PVA Negative) and 19% CA solution (positive) (Figure 5b). The device (with dimension 3 × 3 cm2) could generate a maximum voltage of 140 V, current of 92 μA and power ~1.361 $Wm^{-2}$ through a 2 MΩ load resistor. High tribonegativity and conductive nature of MXene has significantly reduced the internal impedance of the triboelectric layers by creating higher

outputs. Targeting real-world applications, along with a suitable power management system attached to a shoe insole, the device successfully powered MXene/$TiO_2$/CNFs heterojunction-based sensor for $NH_3$ detection[161] Figure 5b (ii)).

Electrospinning can be used to develop highly conductive, porous and flexible electrodes suitable for wearable TENG devices. For instance, Qin et al. demonstrated a composite TENG using Janus structured with PLA, PVDF NHF nanofibre as triboelectric surfaces, and PEDOT to achieve conductivity with respective layers (Figure 5c(i)). The conductivity of PEDOT-PLA nanofibres and PEDOT-PVDF NHF was recorded as ~2.63 mS $cm^{-1}$ and ~66.67 mS $cm^{-1}$, respectively. The device was ultra-lightweight (2 × 2 cm2 sample with 25.8 mg) and demonstrated $V_{OC}$ of 140 V, $I_{SC}$ of 3.8 μA, a charge of 48 nC and peak power of 0.75 mW through 150 MΩ under periodic contact and separation movement. In addition, the device could be used to light up 50 commercial LED lights and identify the throat swallowing and gripping action of the human wrist.[162] Furthermore, Janus-structured electrospinning creates a breathable, lightweight, and flexible structure that is comfortable to wear. It also improves adhesion between conductive and triboelectric layers while reducing delamination.

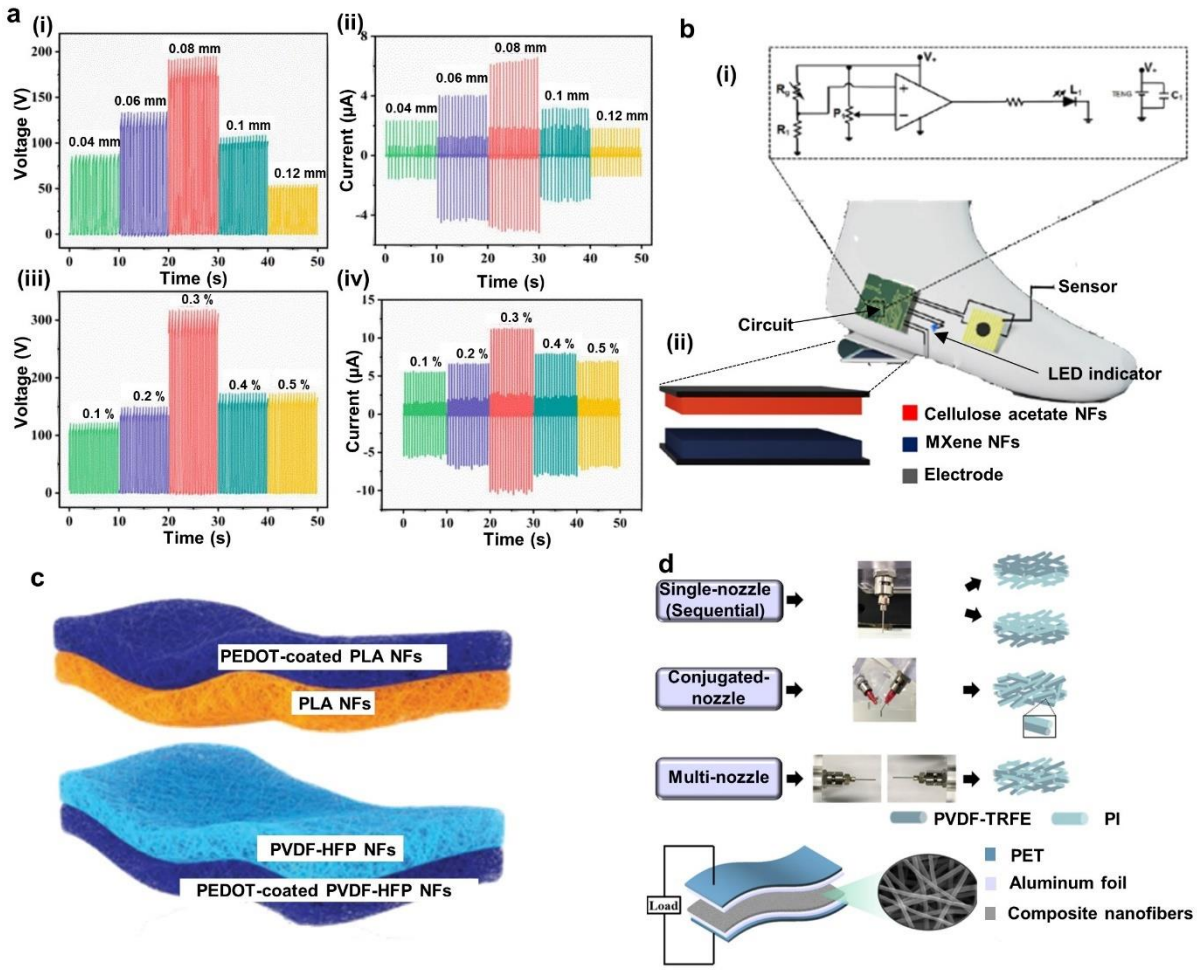


Figure 5: Further improvements and development of composite structures for TENG applications using the electrospinning process.

a) Effect of electrospun PVDF layer thickness ((i)-voltage, (ii)- current behaviour) and $MoS_2$/CNT ((iii), voltage, (iv)- current) concentration over output performance reprinted from ref[159] with permission Copyright©2022, American Chemical Society, b) Schematic of electrospun TENG based self-powered $NH_3$ monitoring sensor reprinted from ref[161] with permission Copyright©2022, American Chemical Society, c) Schematic using PLA and PVDF based composite TENG device reprinted from ref[162]with permission Copyright©2019 WILEY-VCH Verlag GmbH & Co. KGaA, Weinheim, d) Schematic of single-nozzle, conjugate-nozzle and multi-nozzle needle-based electrospinning systems reprinted from ref[163] with permission Copyright©2021, American Chemical Society

Another factor to optimise power output from TENG substrate is to alter the electrospinning fabrication process parameters. Power output is one of the most important factors that will drive commercialisation of this technology. The arrangement of the electrospinning system has a significant impact on the power output of TENG devices. Kim et al. observed the effect of power output based on the single nozzle, conjugated nozzle and multi-nozzle electrospinning system (Figure 5d). A PI/ PVDF-TRFE composite nanofibre membrane was developed during the experiment using all three techniques. Previous experiments provide evidence that PI has ability to retain more induced charges and higher electrical properties. Evidence from energy dispersive spectroscopy and SEM shows that using a single nozzle produces a layer-by-layer structure for PI and PVDF-TRFE separately. On the other hand, employing conjugate and multi-nozzle techniques results in a mixture of PI/PVDF-TRFE nanofibres throughout the material, enabling both components to be present and contribute. Based on the results, there was an increase in the power output when using conjugate or multi nozzles rather than single nozzles, concluding that conjugate or multi nozzles are a better alternative in the preparation of composite nanofibres. In addition, using a rotary collector instead of a planer collector during multi-nozzle electrospinning can further enhance the power output of composite material-based TENG devices.[163]

### 2.3.3. Electrospinning based Triboelectric self-powered sensing.

A number of studies have developed sensors to monitor physiological signals from the human body, both in vivo and in vitro using electrospun membranes. The advantage of not relying on a separate power supply means that self-powered sensing with TENGs is a highly investigated area in the field of wearable electronics.[3,164] Alagumalai et al. have provided a comprehensive review on the possibility of combining machine learning and self-powered sensing, providing more pathways for future research.[165] In the rest of this section, some examples of electrospun wearable TENG self-powered sensors will be discussed in detail.

Jian et al. have developed a TENG sensor for detecting human biomechanics using $TiO_2$@PAN electrospun membrane and nylon film as tribonegative and tribopositive layers respectively and a AgNW/TPU composite electrospun layer as the electrode. In addition to these layers, the polytetrafluoroethylene (PTFE) sandwiched layer is used between the electrospun electrode and the tribonegative membrane to safeguard the electrode from moisture. The uppermost layer containing the $TiO_2$ nanoparticles can absorb ultraviolet light and act as a self-cleaning, antibacterial agent. Furthermore, electrospinning is a highly efficient production method and provides homogeneous nature for $TiO_2$ over the PAN network, which is quite challenging with other fabrication methods. The device had a sensitivity of 5.2 mV $Pa^{-1}$ in the region of 0-4 kPa and 0.6 mV $Pa^{-1}$ for pressure >4 kPa. Furthermore, the device could detect and distinguish human motions such as walking, running, squatting and skipping, as shown in figure 6a. Moreover, the device could detect signals required for a self-powered pedometer system.[166]

Security is becoming one of the significant areas of focus worldwide due to the advancement of technology. Pressure sensing-based user authentication is highly desirable in intelligent home and appliance control systems. The advance of smart devices and wearable technologies for authentication signal indicate the potential of embedding such functionality into sophisticated garments. Primarily static pressure sensing may be achieved through capacitive, resistive and piezoresistive, while dynamic pressure sensing information such as press time and hold time is challenging to measure with those techniques. Advanced approaches are needed to address these challenges in the future. One approach investigated by Bhatta et al. uses hybridized composite nanofibre-based TENG and capacitive pressure sensors to measure dynamic and static pressure. In this experiment, siloxane and PVDF are used in the same precursor to produce an electrospun tribonegative layer, while the nylon 66 electrospun layer is used as a tribopositive layer. High charge density propagation due to siloxane and high surface area due to electrospinning provided conditions to miniaturize the

sensor down to the standard sensor size of 5 mm × 5 mm and hybridize with the capacitive technique with a maximum sensitivity of 12.062 $kPa^{-1}$ in 0 - 3.5 kPa region and 2.58 V $kPa^{-1}$ in 3.5 – 25 kPa range. The rectified output of the TENG can be used to charge a capacitor in a self-powered approach. Finally, the sensor integrated into an AI system was demonstrated to identify individual user with 98% accuracy(Figure 6b).[35]

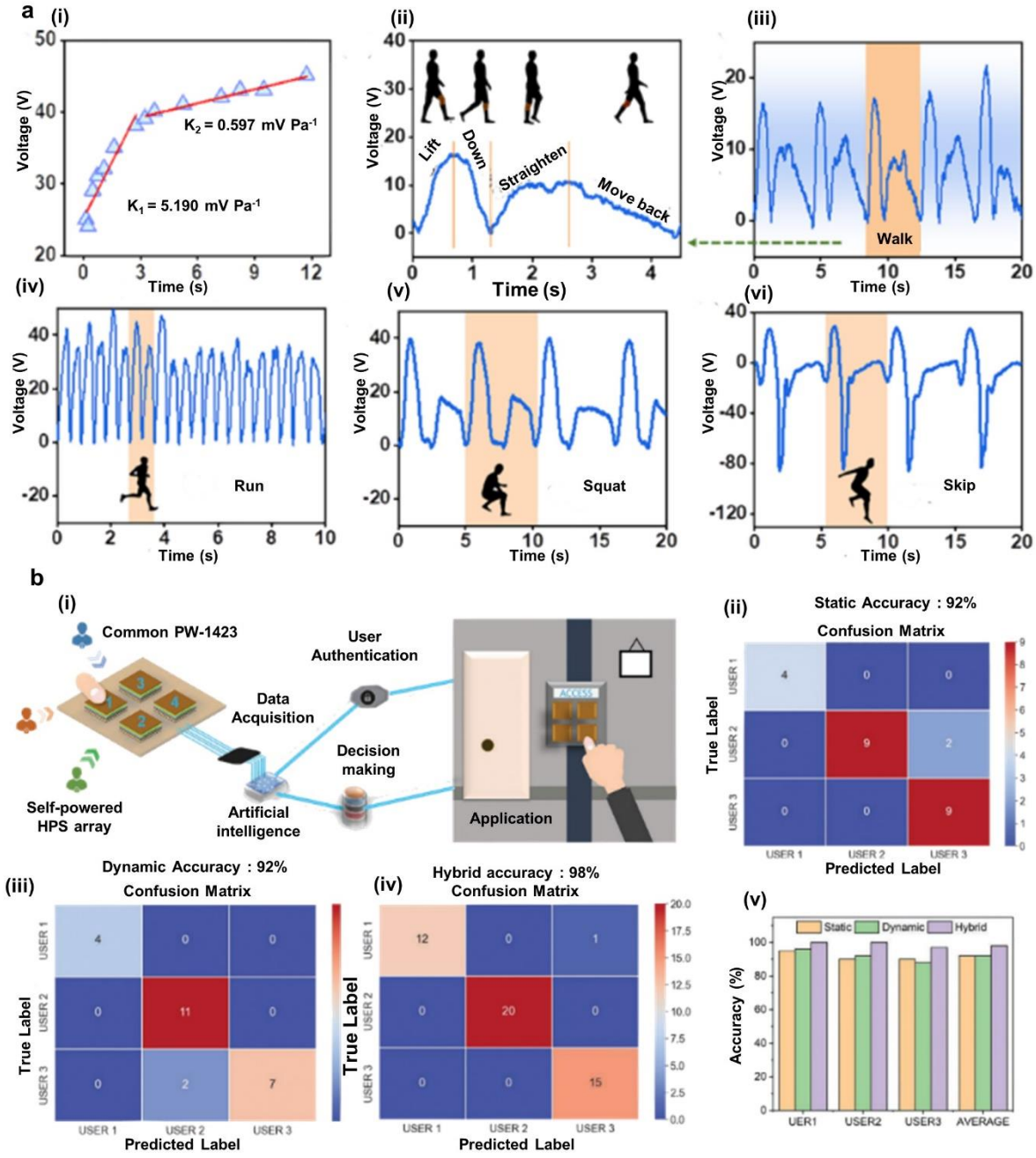


Figure 6: Applications of electrospinning modified TENG based self-powered sensing.

a) Ultraviolet-protective, self-cleaning, and antibacterial nanofibre-based TENG sensor, output voltage vs applied pressure (i), different leg actions and corresponding results of the device (ii), Sensitivity with walking(iii), running(iv), squatting(v) and skipping(vi), reprinted from ref[166] with permission Copyright©2021, American Chemical Society , b) Neural network based self-authentication system, schematic and architecture of the system (i), accuracy matrix for capacitive based pressure sensor (ii), accuracy matrix for TENG based pressure sensor (iii), accuracy matrix for hybrid pressure sensor (iv) and comparison of static, dynamic and hybrid techniques (v) reprinted from ref[35] with permission Copyright©2022 Wiley-VCH GmbH

### 2.3.4. Use of Electrospinning in PENG technology

The piezoelectric property is a natural phenomenon of generating an electric field due to the linear coupling between a specific material's stress or strain state and its electrical polarisation, which is inherently reversible. In 1880 Jacques and Pierre Curie observed the piezoelectric property of certain inorganic crystals. In the 1950s, lead zirconate titanate and barium titanate ($BaTiO_3$) were used for industrial and commercialisation purposes for piezoelectric technology.[67] Even though the piezoelectric property is prominent in ceramic crystalline materials, it is also inherent to some polymer materials such as ferroelectric polymers (PVDF), PA, polypeptides and polyesters. The electric charge generated per unit area (in C) as a result of applied mechanical force (in N) is recognised as the piezoelectric coefficient, $d_{ij}$ , of piezoelectric materials, where i is the direction of electric field propagation and j is the direction of applied force.[67,164,167] Sun et al. have derived equations from understanding the charge density, capacity, and maximum voltage resulting from the external force over piezoelectric nanostructures.[168] Furthermore, Smith and Kar-Narayan have provided detailed information on the symmetry requirements, underlying mechanism and further processing related to piezoelectric materials in ref[169]. However, a theoretical understanding of the piezoelectric material is an essential factor in optimising the PENG

concept. Wang has derived equations using Maxwell's equations to calculate to output power through an external load(P) and total output energy($E_0$) of PENG devises as given bellow.[170]

$$P = \left\{\frac{zd_{ij}s}{R\varepsilon} exp\left(-\frac{z}{RA\varepsilon}t\right)\right\}^2 R \quad \text{(E5)}$$

$$E_0 = \frac{Az(d_{ij}s)^2}{2\varepsilon} \quad \text{(E6)}$$

In equation 5 and 6; $z$ is the thickness, $s$ is the strain, $R$ is the external load, $A$ is the surface area, $t$ is the time and $\varepsilon$ is the permittivity of the material. Based on the equations increase of $d_{ij}$ can drastically enhance the power output of PENG devises. In addition, Xu et al, provide evidence that surface nanostructures can distribute the piezoelectric potential over the cross section of the surface thus favourable for final outcome.[171] In wearable applications, polymer materials are favourable due to the mix of crystalline and amorphous regions. However in comparison to ceramic materials which have a $d_{ij}$ of 500 $pCN^{-1}$, the initial polymer material's coefficient is around 1/20th of popular ceramic materials.[169] Interestingly, electrospun PVDF nanofibres have resulted in $d_{33}$ of 57.6 $pCN^{-1}$, while PVDF film exhibits 15 $pCN^{-1}$, showing a significant improvement by electrospinning.[67] Even though PVDF material has α, β, γ, δ phases, the β phase is the most prominent phase with the highest spontaneous polarisation yielding high piezoelectric power outputs.[109,172] Electrospinning can be used as a poling mechanism to improve the β phase content resulting in higher power output. [109,121,169]

Among the most prominent polymers used to create piezoelectric active layers for wearable applications are PVDF and its copolymers, PAN, Cellulose and PLA, which are compatible with electrospinning, thereby providing a balance between electrical and wearable performance[121]. Additionally, a high voltage field in the electrospinning process can further enhance and adjust the electric poling of PENG materials. Mirjalali et al. have

comprehensively reviewed electrospun PENG for energy harvesting and self-powered sensing[121] and Yu et al. have provided a review on electrospun organic nanofibres for bio applications.[67] In this section, foremost consideration is given to developing PENG with electrospun nanofibres and composite PENG structures with electrospinning. The following section discusses the advantage of the electrospinning approach and how the device performance can be further improved with chemical and mechanical modifications.

Recent advancements in PENG devices mostly use composite materials in PVDF electrospinning precursors to increase the power output of PENG devices. For example, Eun et al. added multi-walled carbon nanotubes (MWCNT) to the electrospun precursor and observed tensile and piezoelectric performance. Electrospun fibres were oriented using a bespoke linear conveyor-based collection mechanism, increasing the β phase, tenacity and initial modules of elasticity. The increase of MWCNT up to 0.008 wt.% can increase the F(β) by 46%, tenacity of 0.70 ± 0.01 g/d and initial modulus of 1.76 ± 0.19 g/d. These results are based on tensile testing carried out with ASTM D2256 standard with 250 mm gauge length and 300 mm/min crosshead speed. It was observed that increasing MWCNT percentage beyond 0.008 wt.% performance was reduced. While the sample was attached to a piezoelectric tester(Figure 7a), 0.01 wt.% MWCNT sample resulted in $V_{OC}$ of 0.71 V, which is a 343% increase compared with pristine randomly oriented PVDF nanofibres.[173]

An example of such a device was developed by Su et al., where a PENG-based self-powered sensor was used for gait pattern monitoring, identification of walking habits, and determining metatarsalgia complications. In device fabrication, Samarium-doped Lead Magnesium Niobate/Lead Titanate based PVDF (Sm-PMN-PT/PVDF) was used to produce the electrospinning precursor. 2.5 wt.% loading of $Ti_3C_2T_x$ (MXene lamellae) to the precursor has increased the piezoelectricity of the Sm-PMN-PT/PVDF by 160%. X-ray diffraction analysis (XRD) spectrometry on a sample provided evidence that the final sample had a polycrystalline perovskite structure and at 2.5% load of MXene has provided the

highest peak related to β phase. The incorporation of MXene at the precursor had minimal impact on the morphology of the electrospun sample, thus providing favourable wearable characteristics. Increasing applied force from 1 to 9 N increased voltage and current from ~7 V to ~12 V and ~0.25 μA to ~1.2 μA, respectively. The developed sensor was attached to a shoe insole in five different positions, as depicted in Figure 7b(i). Interestingly, there was a distinguished difference in signal output related to jumping, walking, running, falling backwards and falling forward (Figure 7b(ii)). In addition, the sensor system could detect posture abnormalities such as pigeon-toed or splayfooted (Figure 7b(iii)) and was shown to be suitable for the clinical prognosis of metatarsalgia conditions (Figure 7b(iv)).[174]

## 2.4. Electrospinning Applications in Wearable Electronics Beyond mechanical energy harvesting

While this thesis focuses on electrospinning application in TENG it is important to acknowledge the broader utility of this technique across all building blocks of wearable electronics domains. The inherent properties of electrospinning making is one of the most suitable methods among all energy applications.

### 2.4.1. Energy harvesting applications

**Solar energy harvesting**: Harvesting energy from sunlight using the photoelectric effect is another sustainable approach to generating clean energy. The photoelectric effect occurs by irradiating sunlight or other suitable light source upon a semiconductor device that results in the release of sufficient free electrons to generate current in an external circuit[55]. Third-generation photovoltaic techniques, namely DSSC,[71,175,176] PSC[177] and OSC[58] are prominent in wearable electronic applications. Into fabricate parts of the DSSC, OSC and PSC SEHG device structures, electrospinning has many advantages. Blachowicz and Ehrmann have provided a comprehensive review on the optical properties that can be

enhanced by using electrospun nanofibres due to high surface area and natural pore structure[178].

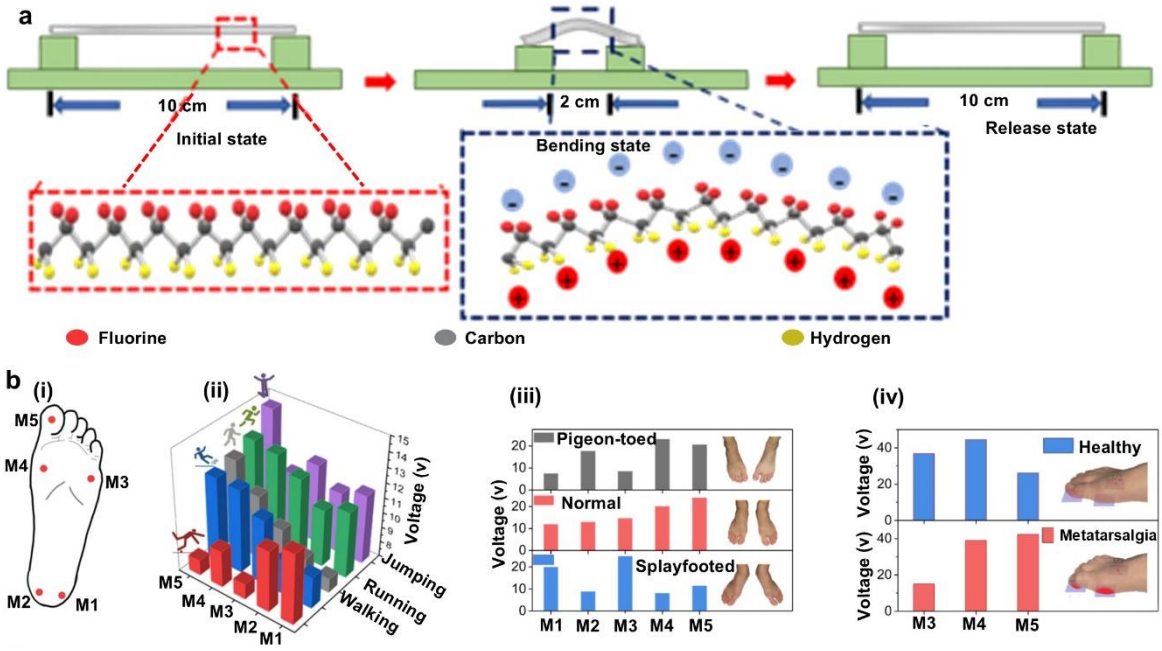


Figure 7: Electrospinning modified PENG based energy harvesting and self-powered sensing devices.

a) Schematic of MWCNT loaded PENG device electrical performance characterization reprinted from ref.[173] published with CC BY Copyright©2021, The Authors, b) High performance piezoelectric composite based PENG sensor, schematic of integration in smart insole (i), identification of gait monitoring (ii), posture abnormalities (iii) and metatarsalgia complication prognosis (iv) reprinted from ref. [174] published with CC BY Copyright©2022, The Authors.

Electrospinning provides promising results for DSSC in areas such as flexible semi-transparent electrode development,[71] highly flexible, biocompatible, eco-friendly, highly conductive electrode development and semi-solid state electrolyte layer development.[122,175] Furthermore, due to the perovskite material's composite nature, it can be embedded into garments as yarns using a single-step electrospinning process.[39,177] Wearable SEHG is prominent with techniques such as DSSC, OSC and most widely with PSC devices.

Electrospinning can be used to develop photoanodes, CEs and electrolyte layers of wearable SEHG targeting higher outputs. For example, Li et al. developed a highly flexible PSC with average weight (0.89 mg $cm^{-1}$) and high active lifetime (>216 h) by electrospinning perovskite material [126].

**Thermoelectric energy harvesting:** The natural phenomena of maintaining human body core temperature at 37 $^0$C and 60 – 180 W heat dissipation from the human body based on the activity level causes the use of thermoelectric energy harvesting concepts for powering wearable electronic applications. The discovery of the Seebeck effect in 1821 by Thomas Seebeck, followed by the Peltier effect in 1834 by Jean Peltier, and the Seebeck voltage in 1851 by Gustav Magnus, were fundamentals that led to the development of the concept of TEGs[57,179,180]. However, since long-term efficiency of such TEG devices decreases due to wearing and abrading, Ewaldz et al. suggest that electrospinning is a better alternative. In addition to their flexibility and stretchability, materials produced through the electrospinning technique possess naturally high surface area and porosity, leading to significantly reduced thermal conductivity and ultimately higher zT values.[181]

For example, He et al. developed stretchable TEG yarns using coagulation bath electrospinning with poly(ethylene imine)/PU precursors doped with PEDOT:PSS. The fibres were collected in a CNT/PEDOT:PSS bath (optimal ratio 4:6), achieving 44 μV $K^{-1}$ Seebeck coefficient, 10× improved conductivity, and 350% stretchability suitable for textile integration [182].

**Moisture Energy Generation:** Wearable energy harvesting techniques have been advancing rapidly, and MEG is one of the concepts that shows great potential. Electrospinning has been used as a fabrication technique to optimize these devices, making them more efficient and effective [183,184]. Materials that are active and contain oxygen-functional groups, such as hydroxy (-OH), carboxyl (-COOH), and sulfonic acid (-$SO_3H$), are capable of capturing

moisture molecules when prompted by an environmental stimulus. Once these functional groups are ionized by the moisture, they can release free protons due to their asymmetric structure. This flow of protons from an area of high concentration to an area of low concentration creates a current flow, which serves as the foundation of MEG devices.[185,186] In order to enhance MEG devices, it is necessary to improve the inner gradient structure of the hygroscopic material through techniques such as nano/microfabrication or chemical modifications.[187] Zhang et al. found that the MEG device's output is closely tied to its structural characteristics, including hydrophilicity, porosity, and specific surface area. To address these aspects, the authors have created a cost-effective wearable MEG device that uses tetra butyl ammonium bromide (TBAB) mixed with CA electrospun nanofibres. Electrospinning TBAB into CA creates a membrane with excellent hydrophilic properties (pristine electrospun CA - contact angle $132^0$ reduced to $26^0$ with the addition of 2% TBAB), enabling water molecule transport and ion migration. The surface area increases, resulting in better moisture absorption and higher output. The output can be further enhanced by decreasing pore size by changing nanofibre diameter and increasing interwind structures. By controlling these parameters, the device's output has improved from 110 mV (pristine CA) to 700 mV with a maximum power of 2.45 μW $cm^{-2}$ at 90% relative humidity.[184]

### 2.4.2. Wearable energy storages

**Supercapacitors:** Supercapacitors play a pivotal role among wearable energy storage devices with excellent cycle lifetime, fast charging/discharging rates and high-power density.[188] Supercapacitors are currently categorised into three main techniques: Electric Double-Layer Capacitors (EDLC), pseudocapacitors and a hybrid of these two approaches. Typical EDLC architecture consists of a thin layer of separator sandwiched between inner electrolyte-coated carbon form electrodes(Activated carbon, CNT and graphene). [188,189] The separator must serve as both an insulator and a conduit for electrolyte ion transfer in these devices.[190] The energy storage mechanism of EDLC occurs when a potential difference is

applied between the electrodes, creating double-layer electrostatic charging at the electrode/electrolyte interface without Faradic reaction.[88] In contrast to EDLC, pseudocapacitors have used metal oxides such as $MnO_2$, $V_2O_5$, and $RuO_2$ or conductive polymers such as PANI, PP, PEDOT.[189,191] With these materials, a rapid Faradaic reaction is prominent in the electrode and electrolyte interface (charging- electrode reduction with adsorption cations from the electrolyte, discharging-reverse process) in pseudocapacitors resulting in higher energy density and reduction in cycle life than EDLC[189]. Ariyamparambil and Kandasubramanian have explained that electrospinning can enhance the porosity and specific surface area of metal oxide polymers aimed at flexible electrodes for supercapacitor applications[192]. In addition, Prasannakumar et al. have provided a comprehensive review on the importance of using electrospinning for tuning conductive polymers for supercapacitor application[74].

**Flexible batteries:** In addition, flexible Li-ion batteries are prominent among storage devices for wearable applications due to scalability, mechanical robustness and electrochemical sustainability.[87,128] The anode of Li-ion batteries typically contains carbonaceous materials and electrolytes. Other than traditional materials, PEDOT: PSS, Polydopamine, PP and carbon nanofiller reinforced cellulose, PLA, PVDF, and PVA are notable in Li-ion and supercapacitor applications[128]. However, the performance of supercapacitors and Li-ion batteries noticeably depends on the porosity and surface properties of electrode materials.[188] Interestingly, most of these materials are electrospinnable polymers and provide high surface area, porosity and flexibility required by each device.

### 2.5. From Origami to Fabrigami: Smart Morphing Structures for Wearables

The performance of TENG sensors is not solely dependent on the material development but also highly influenced by the mechanical excitation between triboelectric layers. Numerous

structural engineering strategies have been introduced to precisely control device geometries, thereby enabling tailored mechanical compliance, scalability and multifunctionality. Specifically, 3D structuring approaches such as porous foams[193], multilayer stacking[194], interlocked geometries[195], spring-based damping mechanisms[196], 3D printing[197], and textile engineering techniques [3,56,198] have been widely employed to improve interfacial contact and triboelectric performance.

Among these techniques, origami-inspired patterns have been recently investigated to overcome the limitations arising within planner and rigid structures. By incorporating foldable geometries, origami designs enable large deformation, an enhanced contact area, and improved mechanical adaptability, all of which directly contribute to higher triboelectric output and durability in such sensors. Considering these advantages, this section provides a summary of origami-inspired approaches for wearable energy harvesting and sensing applications. Initially, the role of origami as a design tool in functional materials, the challenges posed by traditional origami substrates, and the evolution toward fabric-based origami (fabrigami) have been clearly described. Thereafter, the integration of electrospinning techniques and structural and material considerations for use in conjunction with the origami morphing technique is clearly described. Finally, a synergy for a practically wearable JBM with TENG and Fabrigami has been introduced.

### 2.5.1. Origami as a Design Tool in Functional Materials

Origami is an ancient Japanese art form that involves folding of 2D papers or sheets into complex 3D geometries, traditionally practiced for recreational and religious activities. Some literature suggests that this technique dates back to the 1$^{st}$ century, when papermaking was invented in China, which later influenced the development of folding practices in Japan[43,199]. Kirigami structures, as a variant of origami, provide additional degrees of freedom by incorporating strategic cuts into the material. However, with advancements in

fields such as civil engineering, aerospace engineering, biomedical engineering, robotics, metamaterials, and energy harvesting, scientists worldwide have explored various structural innovations inspired by origami to enhance functionality across different media with greater precision and a more sustainable approach. Among recent discoveries, Miura fold use by NASA for compacting solar panels[200]; Kirigami-inspired stent developed for biomedical applications[201] (Figure 8a); Origami inspired foldable shelters and architectures[202](Figure 8b); Self folding robots[203] (Figure 8c); and origami inspired metamaterials[204] are pioneering developments. Moreover, origami principles can be applied to design unconventional structures at both the macroscale and micro/nanoscale levels[205].

Traditional wearable electronic devices are often rigid and bulky, making them uncomfortable for the wearer and limiting long-term use. In contrast, the intrinsic contraction and expansion behaviour of origami structures enables the development of lightweight, conformal wearable electronics that better adapt to body movement. In particular, origami-inspired designs can be used to develop prosthetics, exoskeleton devices, joint biomechanics monitoring sensors, and shape-memory-based actuators.

### 2.5.2. Limitations of Traditional Origami Materials

Even though origami-inspired designs have shown significant promise in wearable electronics and other engineering applications, traditional materials such as paper or rigid films present notable limitations for practical use. These materials are often rigid and fragile, especially paper, making them unsuitable for repeated deformation. In addition, their lack of breathability and flexibility can cause discomfort during long-term wear. Wearable electronic systems also require the integration of sensors, processing units, communication modules, and power sources, all interconnected via conductive pathways. Traditional origami materials are generally incompatible with such integration. Consequently, there is

growing interest in developing advanced material systems that retain the geometric versatility of origami while overcoming these material-level constraints.

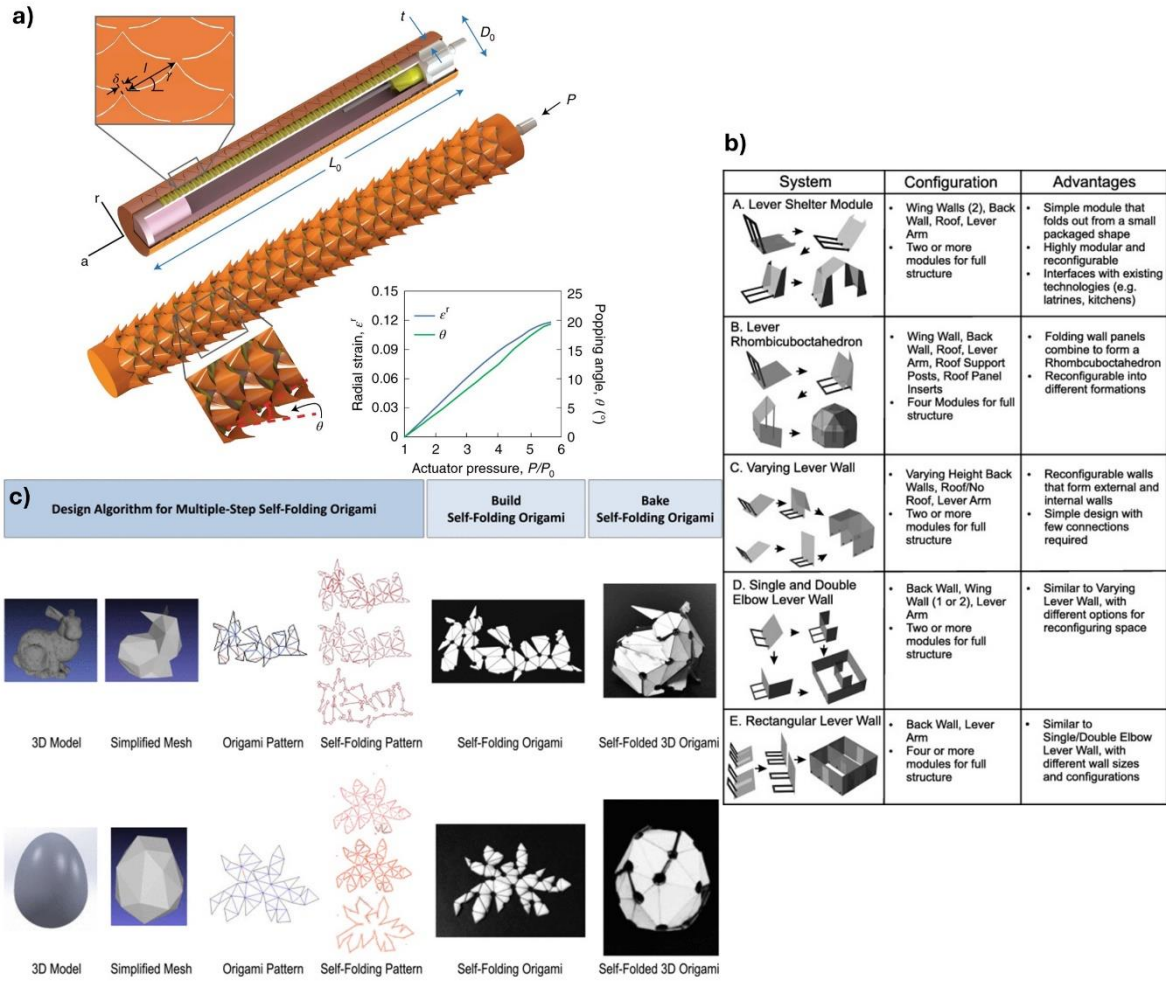


Figure 8: Origami inspired recent discoveries.

a) Kirigami-inspired stent developed for biomedical applications reprinted from ref [201] with permission Copyright©2021, The Author(s), under exclusive licence to Springer Nature Limited, b)Origami inspired foldable architecture designs reprinted from ref [202] with permission Copyright©2014 Elsevier Ltd., c) Origami inspired Self folding robots reprinted with permission from ref [203] with permission Copyright©2018, IEEE.

### 2.5.3. Fabrigami: The Evolution Toward Fabric-Based Origami

For thousands of years, fabric has served as the closest functional layer to the human body, making it an ideal platform for wearable electronic integration. Advances in textile

engineering have further enabled the incorporation of electronic functionality at various stages of textile production, from fibre spinning to fabric finishing. Next-generation textiles can sense environmental stimuli and adapt accordingly, while maintaining their primary roles in protection, comfort, and aesthetics. Furthermore, integrating energy harvesting technologies into body-worn electronics through fabrics is gaining increasing attention. This is mainly due to the favourable properties of textiles, such as flexibility, drapability, elasticity, light weight, and washability, which make them ideal for wearable energy systems[206]. By leveraging these properties, fabric-based origami structures can undergo complex folding and unfolding motions while maintaining mechanical integrity and user comfort.

Historically, civilizations such as the Romans and Egyptians utilized fabric folding techniques, particularly in pleating (Figure 9a), within the textile and fashion industries. Early methods of fabric folding involved tying or knotting fabrics in randomly oriented patterns, followed by heat pressing to permanently transfer the design onto the fabric. While this approach introduced a three-dimensional structure, it lacked precise control, as the final outcome was entirely dependent on the knotting pattern[207]. In Europe, the smocking technique (Figure 9b) was traditionally used to impart three-dimensional patterns onto fabric through thermal and mechanical processing[208]. More recently, Stovall, Stern, and Temko introduced the term fabrigami (Figure 9c) to describe the transformation of fabrics into 3D forms using origami-inspired techniques[44]. Because of the mechanical versatility of textile substrates, this approach often requires the application of a stiffening agent to help fabrics hold their folded shapes. Fabrigami has been successfully applied in the creation of card holders, decorative fabric designs, and jewellery boxes. However, the limited breathability and reduced drapability associated with stiffened textiles have restricted its applicability in wearable electronic systems.

Rutzky and Palmer introduced a technique known as shadowfolds, which applies origami-inspired geometric patterns to fabric surfaces. In this method, a dot matrix pattern is first transferred onto the fabric, then specific pairs of adjacent points are stitched or gathered together. This controlled manipulation creates complex three-dimensional structures through tension and compression within the textile. Shadowfolds have been applied to create artistic and functional items such as window hangings, room dividers, tablecloths, and fashion pieces. Also, fabrigami was used for garments that grow with you, as they would expand(e.g. as a child grows up)[209]. However, wearable electronic systems often require precise patterning to ensure accurate sensing or actuation. [208]

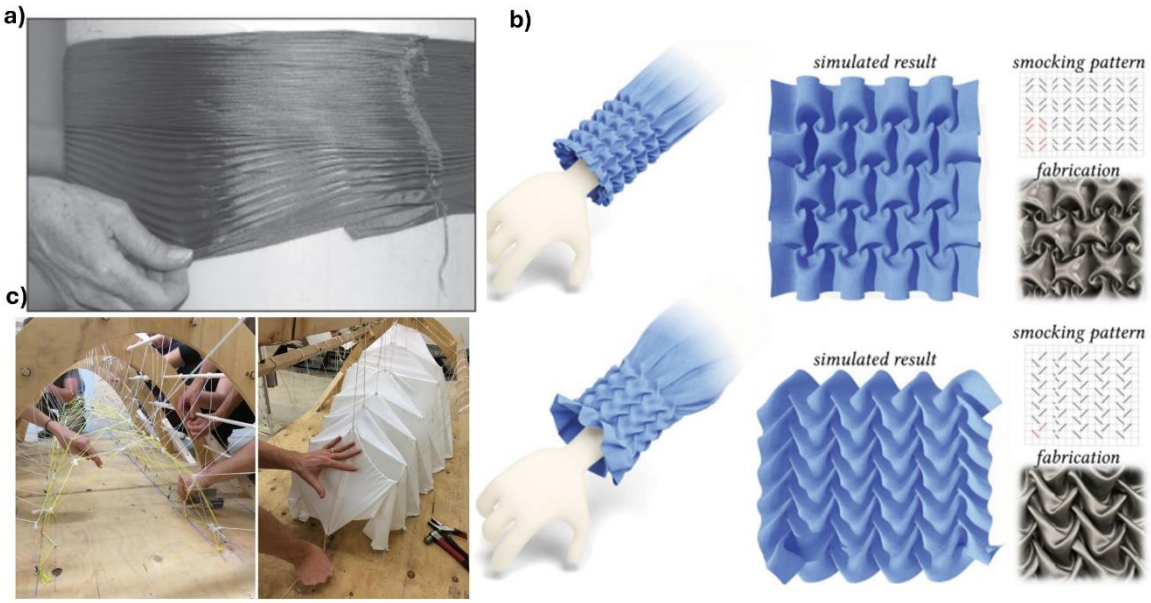


Figure 9: Fabric 3D geometry development techniques.

Fabric a)plating reprinted from ref [210] with permission Copyright©2004, Sage Publications and b)smocking reprinted from ref [211] published with CC BY 4.0 Copyright©2024, Authors technique, c) Fabrigami structure for string model for ice shell reprinted from ref [212] with permission Copyright©2021, Sage Publications.

Recent advancements in fabric-based origami highlight a blend of traditional folding techniques and cutting-edge material engineering. Initially, these techniques were focused

on aesthetics and visual appeal. However, due to the demand for smart textile technology, today's fabrigami methods are transforming to address the intricate needs of wearable electronics. This evolution allows for flexible, dynamic, and smartly integrated creations with technology.

### 2.5.4. Electrospinning and Fabrigami Integration

As outlined in Section 2, electrospinning has emerged as a versatile technique for producing nanofibrous scaffolds with high surface area, tunable porosity, and excellent conformability, which are highly desirable attributes for wearable electronic applications. The present work focuses on developing a self-powered textile-based sensor for monitoring joint biomechanics, employing TENG technology as the core sensing mechanism.

Although electrospun membranes offer ideal material properties for energy harvesting, the performance of a TENG system is significantly influenced by the contact–separation mechanism between the active layers. In this context, fabrigami, an origami-inspired approach applied to fabric-based substrates, is a practical design strategy to enable controlled mechanical motion. By incorporating electrospun layers into the fabrigami structures , a passive and repeatable contact–separation interface can be achieved, enhancing the sensitivity and output of the TENG system.

Integrating electrospun nanofibres with fabrigami folding enables better mechanical deformation during joint movement and improves overall wearability, stability, and functionality. Such a hybrid design represents a promising direction for creating efficient, flexible, and integrable self-powered sensors for next-generation wearable systems, suitable for placement in multiple body locations, conforming to the body's contours and movements.

### 2.5.5. Structural and Material Considerations

Designing a fabric-based TENG system requires careful consideration of several structural and material parameters. Factors such as biocompatibility, long-term durability, and

performance under repeated mechanical deformations (such as folding and unfolding) are critical. Additionally, materials that can be treated for heat-setting to ensure fold memory while maintaining flexibility and integrity over time must be selected.

**Mechanical Behaviour Under Folding/Unfolding**: One of the primary challenges in selecting material for fabrigami folds is understanding their mechanical behaviour under cyclic loading, which includes both elastic recovery and fatigue resistance. The material experiences stress and strain during folding and unfolding, leading to deformation and potential failure if not properly engineered. Due to the nature of the fabrigami structure, the material must recover to its original state after deformation, maintain the following contact and separation cycle. However, repeated folding cycles can also lead to fatigue, where the material gradually loses its mechanical properties and ability to recover, resulting in wear or even failure of the folds. To address this, careful selection of materials with optimal elasticity, flexibility, and durability is necessary.

**Integration of Conductive/Functional Materials into Folds:** Integrating conductive materials into the folds of electrospun nanofibres adds another layer of complexity to fabrigami systems. For wearable electronics, these conductive materials must maintain their performance under mechanical deformation, ensuring consistent electrical conductivity even after multiple cycles of folding and unfolding. It is required to carefully select flexible conductive pathways with minimal impact to the natural movement of the fabrigami structure. A key consideration in this integration is the distribution and stability of the conductive materials within the folds. The conductive layers must remain intact and effective in various deformation states, without breaking or losing conductivity during folding. This requires careful design of the material composition and incorporating conductive materials in the optimal locations to support mechanical and electrical performance.

**Careful design of the fabrigami folding pattern**: Given the complexity of material and mechanical interactions in fabrigami-based systems, the selection of an appropriate folding pattern and the respective angles is crucial for simulating and optimizing the behaviour of these structures. The folding pattern influences the mechanical performance and the functional integration of conductive materials and thermal/electrical properties in the system. Properly chosen folds ensure that the TENG system operates efficiently by maintaining contact and separation during repeated deformation cycles, optimizing the mechanical and electrical outputs of the device.

### 2.5.6. Synergy Between Origami Structure and Triboelectric Mechanism

Since the introduction of TENGs in 2012, researchers have explored various strategies to enhance their performance, including the integration of origami-inspired structures. One notable example is the work by Higoshi et al., who developed a smart cushioning device based on an origami-corrugated TENG architecture (Figure 10a(i)). The origami-based TENG uses paper as a self-folding substrate, copper electrodes for conductivity, and PTFE as the triboelectric material. The paper folds autonomously upon printing a specific solution with inkjet printing, forming a hinge that enables cyclic deformation under external force. This folding angle, controlled by the printed line width, allows the creation of compressive or tensile soft sensors. The soft, elastic hinge bends under pressure, bringing TENG layers into contact and generating electricity through electrostatic induction. Upon release, stored elastic energy restores the structure, completing a full energy harvesting cycle. In this development, the confusion matrix shows that the developed sensor can successfully identify few dropped objects (Figure 10a(ii, iii)) with 98.9% accuracy[213].

In another example, Yang et al. developed a TENG and self-powered pressure sensor using a slinky and doodlebug-shaped structure fabricated from printed paper[214]. As illustrated in figure 10b, a stiff paper substrate was folded into an origami-inspired slinky architecture,

where the paper itself and a PTFE layer functioned as the two triboelectric materials. The sensor exhibited distinct electrical signal patterns under various mechanical deformations such as stretching, twisting, and lifting. Moreover, when different coins were dropped onto the sensor, it produced unique signal outputs corresponding to each coin, demonstrating its capability to detect pressure variations and identify different applied forces. In another example, Hu et al. employed a similar slinky-inspired structure (Figure 10c) to develop a TENG capable of lighting up 28 LEDs and generating sufficient energy to power a programmable IoT sensor node[215].

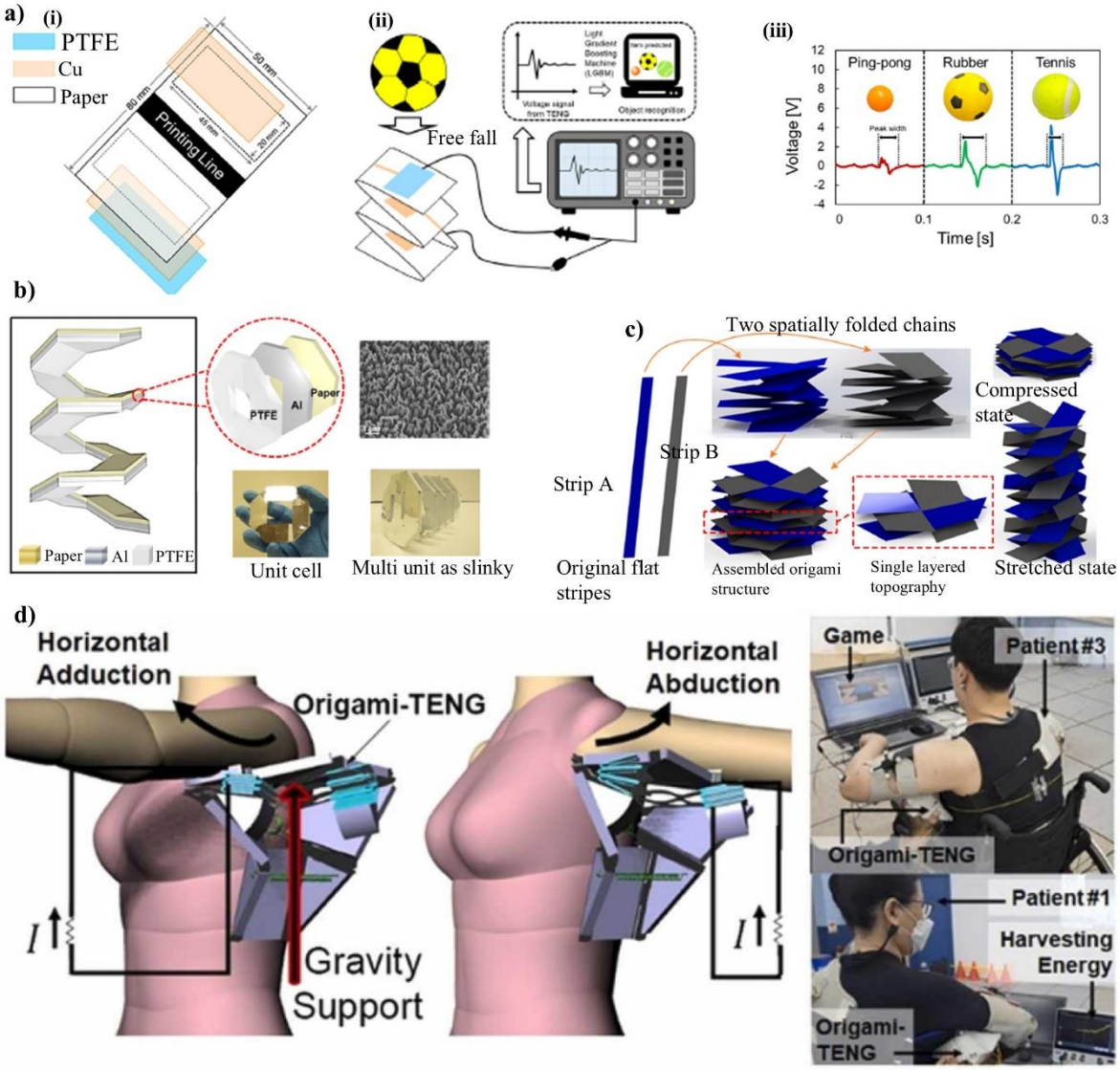


Figure 10: Use of Origami for TENG sensor developments.

a) Construction process of a PTFE-laminated paper and copper-based TENG: (i) fabrication steps, (ii) experimental setup with various object drops, (iii) corresponding voltage patterns adapted from ref [213] published with CC BY Copyright©2025, The Author(s). b) Fabrication of a slinky-type TENG architecture, showing both unit-cell and multi-unit configurations adapted from ref [214] with permission Copyright©2015, American Chemical Society. c) Implementation of a spatially arranged TENG structure adapted from ref[215] with permission Copyright©2021 Elsevier Ltd. d) TENG integrated into an origami-based gravity-support device for shoulder rehabilitation adapted from ref [24] with permission Copyright©2022 Elsevier Ltd.

Unlike the previous single-slinky design, their approach utilized two long, narrow paper strips alternately and repeatedly folded to enhance structural complexity and mechanical deformation. This design improved energy harvesting performance through increased contact-separation cycles and surface area interaction.

Bhatia et al. developed an origami-integrated TENG sensor system to support shoulder rehabilitation through interactive gaming [24]. The system utilized a poly vinyl chloride frame as the structural base for the origami mechanism, with PTFE and aluminium serving as the tribonegative and tribopositive layers, respectively (Figure 10d(i)). Two sensors were used to detect adduction and abduction movements of the left shoulder while playing the game. The origami structure, enhanced with adjustable torsion springs, provided gravity-assisted support to facilitate horizontal shoulder motion (Figure 10d(ii, iii)). Participants engaged in a simplified table tennis game that encouraged physical activity with minimal cognitive load, enhancing engagement. The energy harvested by the TENGs enabled the device to operate as a self-powered rehabilitation platform. Feedback from a pilot study indicated positive user acceptance, with patients expressing a willingness to adopt the system for home-based recovery.

### 2.5.7. Toward Self-Powered Joint Biomechanics Monitoring

Quantitative analysis of human kinematics through biomechanical measurements serves as a crucial tool for human health and performance evaluation. The assessment of JBM enables healthcare providers to create personalized treatment and rehabilitation programs for patients whose movement patterns are impacted by osteoarthritis or injury recovery or post-surgical conditions of the knee or hip. In addition to clinical applications, evaluating biomechanics is essential for sports science. Understanding and analysing body mechanics can improve techniques, enhance athletic performance, and reduce injury risks.

Despite their recognized importance, conventional biomechanical monitoring technologies are constrained by bulkiness, rigid form factors, limited wearability, and dependency on external power supplies or frequent battery replacements. These limitations have created a void in long-term and real-time settings where continuous monitoring is most valuable. Addressing this unmet need requires new research on conformable, wireless, and self-powered sensing platforms that can easily integrate into daily life while maintaining biomechanical accuracy.

In this context, origami-inspired TENGs represent a transformative class of smart, energy-autonomous systems. By synergistically combining textile engineering with origami-inspired foldable geometries, fabrigami-TENGs conform intimately following anatomical curvatures and movement, accommodating the multiaxial and nonlinear deformations typical of knee and hip articulations. Unlike rigid electronics, these soft, foldable devices maintain mechanical integrity and functional stability over thousands of motion cycles, ideally suited for dynamic biomechanical environments.

Crucially, fabrigami-TENGs offer dual-mode functionality: they sense mechanical movements with high accuracy and harvest biomechanical energy through the TENG. This self-powered capability eliminates the reliance on batteries or external power, enabling

uninterrupted, long-duration monitoring in real-world scenarios. By converting otherwise wasted biomechanical energy into usable electrical signals, fabrigami-TENGs lay the foundation for a new generation of wearable electronics capable of continuously monitoring joint dynamics in real time, seamlessly blending into the user's daily activities.

Integrating these systems into JBM platforms holds profound implications for personalized medicine, remote rehabilitation, elderly care, prosthetic design, and next-generation sports analytics. As the field moves toward smart, self-sufficient biointerfaces, fabrigami-based TENGs are a compelling solution at the intersection of biomechanics, materials science, and wearable electronics.

## 2.6. Integration Strategies and System-Level Considerations

### 2.6.1. Fabrication and Assembly

Typically, developments have focused solely on improving power generation, storage and communication aspects rather than mechanical and aesthetic performances. Considering all these factors, the use of electrospinning along with traditional textile engineering concepts can fulfil the requirements of performance optimization as well as improving wearable characteristics.[3,88] Electrospinning-based systems can be seamlessly integrated into garments through meticulous selection at every stage of the manufacturing process, from fibre to fabric[42].

From a textile engineering perspective, these TENG devices can be grouped into two main categories depending on the production stage; fibre/yarn-based systems (converted into fabrics using weaving, knitting, braiding, sewing or embroidery techniques) and fabric-based systems which are produced by electrospun layers. In textile engineering, fibre is considered as the fundamental building block, and all the mechanical and aesthetic improvements start at this stage. Conversion of fibre into yarn can be achieved through the process of spinning followed by twisting or plying. Traditionally ring spinning has been used

as the primary spinning technique, and recently air jet, rotor, wrap and friction spinning have become popular, providing additional functionalities such as extensibility, uniformness, strength and comfortability.[216]

Self-powered wearable systems mainly use commercial yarns that are already twisted as the core and adding a functional polymer sheath using electrospinning techniques.[3,42,73,217,218] As an example, Dai et al. created a piezoelectric yarn by electrospinning P(VDF-TRFE) onto a copper wire. This yarn was then used as the weft and warp yarn in woven fabric, resulting in a final product that exhibited exceptional gas permeability (1041.4 mm/s) when compared to cotton, polyester, and wool fabrics. The device also exhibited a higher β phase, achieving a $V_{OC}$ of 2.7 V and an $I_{SC}$ of 38 nA under 15 N force. Additionally, this electrospun sheath-based yarn offered excellent drapability and sufficient tensile properties, making it ideal for practical use.[219]

In contrast, some recent developments have focused on using electrospinning to directly produce yarns targeting wearable electronic applications.[220,221] Nan et al. have developed highly stretchable and conductive nanofibre yarn by using a double conjugate electrospinning technique. By inverting and tapering graphene oxide-doped PAN electrospun fibres into a hollow nanoweb on a funnel and then twisting them, a yarn was formed. To increase conductivity, the yarn was coated with Polypropylene using in situ polymerization, resulting in an increase from 94.37 S $cm^{-1}$ to 10.5 S $cm^{-1}$. The electrospinning technique not only increased pressure sensitivity by increasing (gauge factor of 4.08) contact points and cumulative contact area but also allowed the yarn to detect strains from 0.1% to 100% and repeatable up to 10,000 cycles with minimal deterioration.[220]

Targeting specific post-fabric manufacturing techniques, it is essential to maintain sufficient twist or plying, yarn thickness, yarn tenacity (breaking load as a fraction of unit length), stretchability and length. In weaving and knitting there is always a minimum length required

to produce a fabric. Some of these parameters have been highlighted in a previous publication related to this work.[3] For example, Zhi et al. emphasized that the amount of twist per meter affects both the geometry of fabric manufacturing and the formation of the β-phase in specific materials. This has implications for increasing output in energy harvesting and self-powered sensing applications.[42,222]

Weaving is a process of manufacturing fabrics by interlacing two sets of yarns, known as warp and weft, at the right angle. Plain, twill, sateen and satin are prominent weaving structures in textile engineering. Traditionally, air jet, water jet, rapier, and projectile machines produce such structures with single-phase or multiphase techniques. Recently, 3D weaving techniques have gained attention to produce highly mechanically stable fabrics with different functionalities.[223] When there is a requirement to interlace two types of functional yarns to produce the final device for wearable electronic application, weaving can be used as a prominent technique due to ease of fabrication and cost effectiveness.[3,70,224,225] Furthermore, the interlacing points and crimp can be controlled using weaving structures such as plain and twill. Based on the application, the active surface area can be increased or decreased using satin and sateen structures.[3,222] Unless the yarn is coated with a secure material, it is advisable to use it as weft yarns rather than warp yarns when manufacturing woven fabrics. This suggestion is based on the delaminating nature of electrospun sheath-based yarns. During weaving, warp yarns experience high tension and friction, which could damage the electrospun coating.

In contrast, the knitting technique uses single yarn with interloping to produce a warp or weft knitted fabric. Structurally, weft-knitted fabrics are highly extensible in one direction, while warp-knitted fabrics are mostly balanced in both directions.[226] Compared with woven fabrics, knitted fabrics can take the human body's shape, making it a more suitable technique for manufacturing intelligent garments. Specifically, TENG and PENG sensors can be closely embedded into the targeted area using knitting techniques with advanced

electrospinning-modified yarns. In addition, the rib knitting structure has higher stretchability making it suitable for energy-harvesting applications.[227] Furthermore, using techniques such as intarsia (a knitting technique that incorporates separate yarn selections to create distinct colour areas without strand carrying) and seamless knitting (Develop complete garment in one step) , the devices can be localized in the structure with minimal impact on the wearable and aesthetic performance of the fabric.[228,229] Due to high frictional force in circular and flatbed higher gauge (number of needles per inch in the knitting machine) it can lead to delamination of directly electrospun yarns without a binder. Hand knitting or lower gauge flatbed knitting[3] techniques are more suitable for electrospinning yarn-based devices. Moreover, overcoming the delamination nature (using suitable binder) of electrospun yarns by producing the complete yarn with electrospinning will lead to high-speed seamless knitting to produce these types of intelligent garments.

Contrary to knitting and weaving, sewing and embroidery techniques can finely localize complete functioning yarns made with an electrospinning process based on the applications. These techniques require high tenacity for the yarns which are subjected to rigorous motions during the fabrication process. Furthermore, if the sheath is producing solely by electrospinning it may be challenging while travelling through the needle heads. If twist exists after developing the yarn, then twist direction (Z direction for single and double needle lock stitch) is an important parameter for sewing to prevent snarling and kinking while preparing the functional device.[230]

The electrospun layer can be used as the functional or passive layer (substrate for specific functional material fabrication) based on the application. Due to the factors such as ease of fabrication, ease of characterization and fewer post-treatment processes, the use of the traditional plate, drum or conveyor-based electrospinning arrangements enables layer preparation techniques for fabric-based systems. Sun et al. have demonstrated that MEGs can be created using polymeric materials, including PVA, ethyl cellulose, silk fibroin, and

polyethylene oxide. Their electrospun fabric-based system yielded superior results compared to counter casted films of the same materials, with polyethylene oxide achieving up to 0.83 V. By adjusting the thickness, pore size, and surface area of the fabric, the power output can be further enhanced by increasing the absorption gradient between electrodes. [183]

All these examples discussed above in the previous sections have used either material selection or post-fabrication chemical treatments to optimize the results. Specifically, in TENG, PENG and SEHG developments, optimising the thickness parameters to increase the sensitivity or power outputs is essential. Furthermore, facial fabrication techniques (fabricating two functional materials into the same electrospun sample front and back side) make it suitable for developing electrodes and functional material in one step. Electrospun layer-based systems are mostly required to comply with traditional woven or knitted fabric substrates in order to maintain the required smart functionalities.[222]

From an application perspective, mechanical properties are vital to electrospun yarns or membranes. Rashid et al. thoroughly examined the relationship between mechanical properties and application of electrospun materials.[75] To improve these properties based on the end application's requirements, various techniques can be used, such as adding inorganic or organic fillers. For instance, MWCNT can be added to poly (l-lactic acid),[231] or interwind nanofibre matrices can be created from polymer blends, such as adding TBAB to CA and creating a tree-like structure with TBAB branches.[184] Polymer structures can also be modified, such as electrospun PAN peroxidation and copolymerization.[232] Han et al. have also demonstrated that post-treatments like annealing, stretching, twisting, solvent steam treatment, post compounding and cross-linking can enhance the mechanical properties of electrospun membranes.[233]

### 2.6.2. Communication and Power Management

Communication and power management remain critical challenges in developing self-powered wearable sensor systems. Bulathsinghala et al. comprehensively reviewed system-level architectures in TENG-based wearable sensing platforms. According to their analysis, the sensing process can be categorized into four key stages: data acquisition, communication, processing, and decision-making. As previously discussed, TENG devices typically generate high voltage outputs, often in the range of hundreds of volts, while producing only nano-micro ampere level currents. In contrast, most commercial microelectronic components operate within a much lower voltage range (0–9 V) and require current in the microampere to milliamperes range. This mismatch poses significant integration challenges, particularly in terms of rectification, voltage regulation, and efficient power transfer to the processing and communication modules[234].

When TENG devices are employed for energy harvesting, several strategies, including power management modules, have been developed to enhance efficiency. For example, Cheng et al. successfully integrated an inductor-capacitor (LC) oscillating circuit, which significantly improved charge transfer. In their experiments, this approach demonstrated a charge transfer increase of up to 2600 times compared to a conventional full-wave rectifier circuit[235]. Xi et al. employed a buck converter to the output of TENG device through step down the rectified voltage with comparator and a metal oxide semiconductor field effect transistor. They effectively matched the system's impedance from 35 MΩ to 1 MΩ, achieving approximately 80% energy transfer efficiency. This approach enabled charging a one mF capacitor with a performance improvement of 128 times compared to a standard rectifier setup, under a 1 Hz mechanical input frequency from the TENG.

This research project focuses on developing a TENG-based system for self-powered sensing rather than energy harvesting. For example, Jeon et al. developed a wearable TENG-based

fabric keyboard using a 12-cell text input architecture. The device was constructed with a cotton substrate, Ni-coated fabric as the conductive layer, and a wool fabric cover (Figure 11a(i)). A data acquisition board (NI PCI-6220) was used to read signals from the individual unit cells, with the detected output shown in Figure 11a(ii). The data was sampled at a rate of 100 Hz, and the pressed key was identified by analysing the absolute maximum value from the sampled signals (Figure 11a(iii)). The system successfully detected different key presses and demonstrated potential as a wearable input device for various applications[236]. This system required a connection to the PC for power supply and that creates challenges with powering and long-term use.

Arduino microcontrollers are widely used in sensor-based research and prototyping due to their ease of use, open-source ecosystem, and compatibility with a wide range of sensors. Zhang et al. developed a bionic artificial nerve using TENG and an Arduino mega based system was used to detect and communicate the signal acquired. 5 V separate power source was used to power the Arduino board and during operation the board consumed 11.85 mA. A lookup table in the microcontroller mapped digital signals to mechanical stimulation locations. The development board had a USB interface for PC communication, allowing it to send commands based on output voltage, enabling custom PC applications to execute actions[237].

# CHAPTER 2

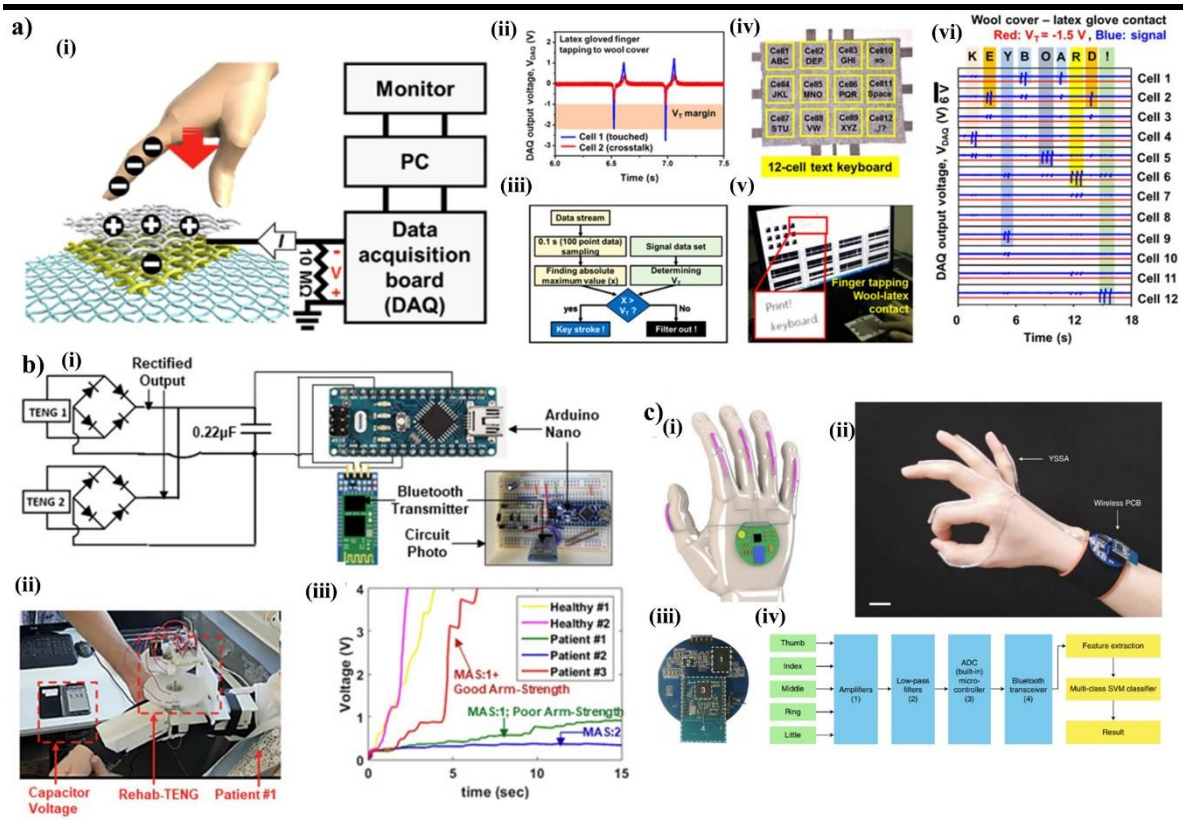


Figure 11: Communication and power management systems for TENG-based self-powered sensing.

a) Wearable fabric-based keyboard. (i) Unit cell fabrication process, (ii) typical signal output captured via a data acquisition (DAQ) system, (iii) flowchart illustrating key-press decision-making logic, (iv) 12-cell keyboard layout, (v) photograph of the keyboard interface output on a PC, and (vi) detection results of all 12 signals through the DAQ system. Adapted from Ref[236] with permission Copyright©2018 Elsevier Ltd. b) Upper limb rehabilitation exercise system. (i) Circuit diagram for signal acquisition and communication from TENG sensors, (ii) experimental setup showing sensor application for rehabilitation, and (iii) capacitor charging curves for different patients, indicating varying levels of impairment adapted from ref [21] published with CC BY Copyright©2020 The Authors. c) Sign language recognition system integrated with TENG and wireless communication. (i) Circuit schematic, (ii) photograph of the assembled system, and (iii) system-level block diagram incorporating the TENG sensor, wireless transmission, and machine learning algorithm adapted from ref [238]

For wearable TENG devices, maintaining a stable wireless connection is essential to ensure smooth data transmission to processing and collection units. Bhatia et al. developed a wearable TENG based exercise system for upper limb rehabilitation. In this experiment, each TENG signal was first fed through an op-amp configured as a comparator for motor function testing. The comparator outputs were connected to Arduino digital pins, allowing the Arduino to detect the activation of each TENG. A 9V battery powered the Arduino Nano, and Bluetooth (BLE) communicated between the circuit and the computer (Figure 11b (i)). It used a counter variable to track movements: counting up when one TENG was triggered and counting down with the other. This counter data was transmitted wirelessly via an HC-06 Bluetooth module to a laptop, where a modified Python-based game interface used the data to control on-screen elements. Furthermore, the output of TENG was passed through a rectifier and them used to charge a capacitor. The voltage of the capacitor was also monitored through the Arduino and the information sent via the BLE setup (Figure 11b(ii, iii))[21].

In another example, Zhou et al. developed a machine learning-assisted TENG sensor array to detect sign language gestures (Figure 11c(i, ii)). In this work, the output from the TENG was first passed through an amplifier (TS2712) and a low-pass filter (TLV2422) to enhance the signal and eliminate environmental noise and interference. The processed signal was then fed into the ADC integrated within a microcontroller, which was powered by a dedicated power management chip (TSP65133). Subsequently, the digitized data was transmitted wirelessly via BLE using a CC2640 chip (Figure 11c(iii)). The system operated at a sampling rate of 500 Hz and, with battery power, was capable of continuous operation for up to 23.6 hours[238].

# CHAPTER 2

## 2.7. Testing and Validation

The scaling and commercialization of electrospinning-based self-powered systems must be thoroughly investigated. Based on Technology Readiness Levels (TRL), most of the devices are either in level 3 (applied research and/or laboratory test completed) or level 4 (small-scale prototype ready in a laboratory environment).[239] Therefore, most prototype developments must be improved with standard test procedures in order for these devices to be accepted as commercially viable products. In textile testing, main bodies such as ASTM (American Society for Testing and Materials), British Standard Institution, ISO (International Organization for Standardization) and AATCC (American Association of Textile Chemists and Colourists) are responsible for developing standard procedures.[3] Furthermore, International Electrotechnical Commission (IEC) and Institute of Printed Circuits (IPC) provide some additional standards related to wearable E-textiles.[240] Following these standards to validate properties such as safety, structure, comfort, durability, and aesthetics will provide more opportunities for future steps in TRLs.

Shak Sadi and Kumpikaite have provided a comprehensive review of standard testing procedures on durability testing, namely, stability and washability related to wearable applications. Interestingly, there is positive evidence for using some testing procedures to measure the washability and stability performance of wearable electrospinning-based sensors.[240–243] In most cases, stability testing was done based on repeating performance with contact separation based architecture or lateral sliding architecture (applying constant force with constant frequency for few cycles.) for several cycles, while washability was performed in a container/beaker by stirring/ultrasonication. Therefore, it is recommended to follow standard procedures such as AATCC 61-2006, ISO 6330 A7 or AATCC 135 to test the washability of functional devices for end-user reliability. In addition, AATCC TM 210 (evaluation of resistance before and after exposure to some conditions), IEC 63203-406-1

(measure surface temperature, especially wrist-worn wearable sensors), IPC 8921 A (specifications for wearable electronic with conductive yarns based woven knitted and braided fabrics) and IPC 8981 (quality and reliability related assessment) are some of the more recently developed testing standards for wearable sensors.[240]

Humidity and temperature conditions can have an adverse impact on the performance of certain electrospinning-based devices.[244] Surface coating or nanomaterial fabrication over electrospinning substrates can favourably improve the performance of such devices to address the influence of variable environmental conditions.[240] Some materials used in these sensors or modules have been restricted or limited to wearable applications. Appendix A provided a summary of textile testing that can be performed on wearable electronics to produce market ready product. The review provided by Patra and Pariti on restricted and limited substances related to fabrics and wearable applications provides a complete insight to researchers to select a wider variety of materials for possible scalable applications[245] (Appendix B) For example, electrospinning solvents such as DMF, DMM and certain acids must be fully evaporated and ensure that devices are free of those substances to use for the purpose of wearable applications.

Furthermore, when characterizing the performance of TENGs, several fundamental measurements must be carried out. The first step involves selecting the appropriate TENG architecture. All samples should then be cut to the exact dimensions, and a precise linear actuation system must be used to mimic human motion. Gunawardhana et al. previously used the Arkibis XMGV voice coil setup, which includes a 2-micron precision encoder[56]. This system is suitable for contact–separation-based TENG architectures, offering a maximum amplitude of 150 mm and operational frequencies up to 10 Hz. It also enables sinusoidal contact–separation motion profile simulation, which can be helpful in validating theoretical models.

Rasel et al. employed an IMADA force gauge to measure the contact force, which can measure forces up to 50 N with a precision of ±0.01 N [92]. Keithley 6514 and 6517B electrometers are commonly used for electrical output characterization to measure short-circuit current and charge density due to their high input impedance and sensitivity. Some researchers have also used these electrometers for open-circuit voltage measurements. However, measuring voltages above ±200 V with these instruments is challenging due to their voltage limitations, and alternative equipment is recommended for such high-voltage measurements.

### 2.8. Overview of Literature review

This literature review summarizes the use of electrospinning in self-powered sensor systems, with particular emphasis on its applications in mechanical energy conversion techniques such as TENG and PENG. To provide a broader context, the review has also examined electrospinning-based approaches in other energy harvesting methods, as well as in energy storage and communication devices. Collectively, this body of literature highlights the versatility of electrospinning and identifies key opportunities to leverage its unique material and structural advantages to enhance the performance of wearable self-powered sensing systems.

However, despite these advancements, significant gaps remain in the development of highly sensitive, lightweight, and comfortable wearable sensor systems. The existing literature indicates a clear need for combined approaches that integrate material-level innovations with structural design strategies to enhance both mechanical adaptability and device performance. As highlighted in the latter part of this review, the incorporation of origami-inspired structures into fabrics (fabrigami) offers promising morphing capabilities that can overcome the limitations of previous bulky and rigid methods.

The synthesis of these insights makes it evident that bridging electrospinning with fabrigami holds the potential to transform wearable sensing systems. Such an approach can deliver structures that are not only mechanically adaptable and lightweight but also capable of significantly enhancing triboelectric performance. More importantly, this convergence directly addresses the pressing demand for unobtrusive, self-powered, and reliable sensors in healthcare monitoring. Thus, the literature strongly supports the need for research into electrospinning–fabrigami integration as a pathway toward the realization of truly next-generation wearable technologies.

### 2.9. Methodology and Objectives

This project aims to develop a TENG technology based self-powered sensor for joint biomechanics monitoring. After carefully carrying out a literature review the methodology, and objectives are casted as described in this section. The core methodology combines electrospinning for functional substrate fabrication with origami-inspired fabrigami structures for mechanical excitation in contact-separation TENG devices. The approach is designed to achieve high-performance, wearable, and sustainable sensing systems. The benefits of these TENG-based sensors are listed below:

- Converting body movements into electrical signals or pulses without an external power source will provide an opportunity to reduce the burden of the upcoming energy demand challenge.
- Using biodegradable materials for the fabrication will reduce the carbon footprint and enhance sustainable practices.
- Continuous monitoring of body movement will provide an opportunity to identify possible posture-related abnormalities in the early stages, improving the quality of life.

- Improving the wearable and aesthetic characteristics of the sensors will provide a comfortable and easy experience for wearers.

The field of wearable self-powered sensing has seen a surge of interest in recent times due to the emergence of biodegradable TENG. Various materials have been explored and researched for developing such devices. Among them, Cellulose acetate (CA), Chitosan, Poly lactic acid (PLA), polycaprolactone (PCL), and silk fibrions have emerged as the leading biocompatible and biodegradable solutions for incorporation in wearable textiles within the TENG and PENG sector. However, despite the immense potential, there has been little progress in developing systematic approaches for creating self-powered sensors that possess excellent wearable characteristics, which are critical for smart textile-based wearable electronic devices. Given these factors, this thesis has identified the following objectives.

- Perform a literature review and feasibility analysis of electrospinning techniques to achieve a higher triboelectric performance with biodegradable and biocompatible materials.
- Analyse the feasibility of using electrospinning to enhance the self-powered sensing performance of the selected triboelectric materials.
- Characterize and optimize the triboelectric, morphological and mechanical properties of the developed electrospun samples.
- Research textile origami structures for actuation and develop a human movement prototype with the developed sensors.
- Conduct a pilot study to evaluate the performance of the developed sensors and make necessary adjustments.

This thesis evaluates a self-powered TENG sensor with enhanced sensitivity and stable electrical outputs for wearable sensing applications. While TENGs have shown promise for energy harvesting and self-powered sensing, they often suffer from limited sensitivity under

low-pressure stimuli and challenges in adapting to dynamic biomechanical motions. To address these limitations, this work explores two key strategies. Firstly, the development of highly sensitive triboelectric layers for detecting low-force, low-frequency movements. Secondly, the introduction of a novel fabrigami-inspired TENG structure designed to efficiently capture joint biomechanics during knee movement through enhanced contact–separation mechanisms.

Chapter 2 of this thesis presented an extensive literature review, beginning with the fundamentals of electrospinning and its role in energy harvesting and self-powered sensing architectures. It also discusses recent advances and the evolution of state-of-the-art TENGs in the past few years. Particular emphasis is placed on material selection, fabrication strategies, and the choice of mechanical stimuli to enhance TENG output, with a focus on applications for monitoring human joint movements.

Chapters 3, 4, and 5 describe the development of electrospun materials tailored for highly sensitive TENG-based devices to detect joint biomechanics. These chapters introduce a wide range of material characterization methods and evaluate the suitability of the developed materials for wearable applications by examining their morphological, chemical, and mechanical properties. In parallel, the electrical performance of the devices is critically assessed using advanced testing procedures and setups.

Chapter 6 introduces a novel “fabrigami” approach that integrates origami-inspired structural design with TENG technology to more accurately capture joint biomechanics. This represents a departure from conventional TENG configurations by coupling advanced material design with innovative mechanical architectures to achieve enhanced sensitivity and functionality.

Finally, this thesis lays the groundwork for the development of sustainable wearable electronic products. Beyond advancing the scientific understanding of TENG design and

performance, the outcomes have direct relevance to applications in health monitoring, soft robotics, and the Internet of Things. With the smart textiles market projected to reach a value of approximately USD 7.2 billon by 2035, this research highlights the potential for next-generation wearable energy harvesters and sensors to make a meaningful technological and societal impact.[53,246].

# CHAPTER 3

## 3. TRIBOELECTRIC PERFORMANCE ANALYSIS OF ELECTROSPUN CA AND PCL MATERIALS

**Publication status: Published as a conference paper**

**Part of this chapter is published at IEEE 20th International conference on Body Sensor Networks from 15-17 October 2024 in Chicago, IL, USA**

S. D. G. Karnasooriya Ragalage, H. Qadeer, G. B. McGuinness, T. E. Ward, and S. M. Coyle, "Self-Powered Breath Monitoring Using Electrospun Biodegradable and Biocompatible Textile Sensors," in 2024 IEEE 20th International Conference on Body Sensor Networks (BSN), Oct. 2024, pp. 1–4. Doi: 10.1109/BSN63547.2024.10780630.

# CHAPTER 3

Building on the gaps and opportunities identified in the literature review, this chapter focuses on the selection and evaluation of electrospun materials for TENG development. The selection of suitable materials for electrospinning is critical in the development of highly sensitive TENGs. In line with future demands for sustainable technologies, this study emphasizes the use of biodegradable and biocompatible materials. Accordingly, CA and PCL were selected as the primary tribopositive and tribonegative substrates, respectively. This chapter systematically evaluates the triboelectric output characteristics of electrospun CA and PCL nanofibre mats to assess their potential as active layers in TENGs. In addition, it outlines the methodologies employed to characterize these materials for TENG development. Finally, as a practical demonstration of application, the chapter presents the design and fabrication of a self-powered breath monitoring sensor based on electrospun CA and PCL fibres.

## 3.1. Initial material screening process

### 3.1.1. Introduction to CA

CA was first discovered by Paul Schützenberger in 1865 and later developed by Franchimont and Miles in 1879 and 1903, respectively. The primary raw material for CA is cellulose, which is extracted from natural sources such as wood pulp (from species like pine and eucalyptus), cotton linters (a by-product of cotton processing), bamboo, and other plant-based biomass.

To produce CA, cellulose is typically reacted with acetic anhydride in the presence of acetic acid as a solvent and sulfuric acid as a catalyst. Sulfuric acid reacts with acetic anhydride to form acetyl sulfuric acid, and both acids react with cellulose to produce cellulose sulphate acid ester. During the acetylation process, many sulphate groups are replaced with acetyl groups. A subsequent hydrolysis step under controlled conditions of time, temperature, and

acidity removes the remaining acetyl and sulphate groups, thereby improving the physical and thermal stability of the final CA product[247].

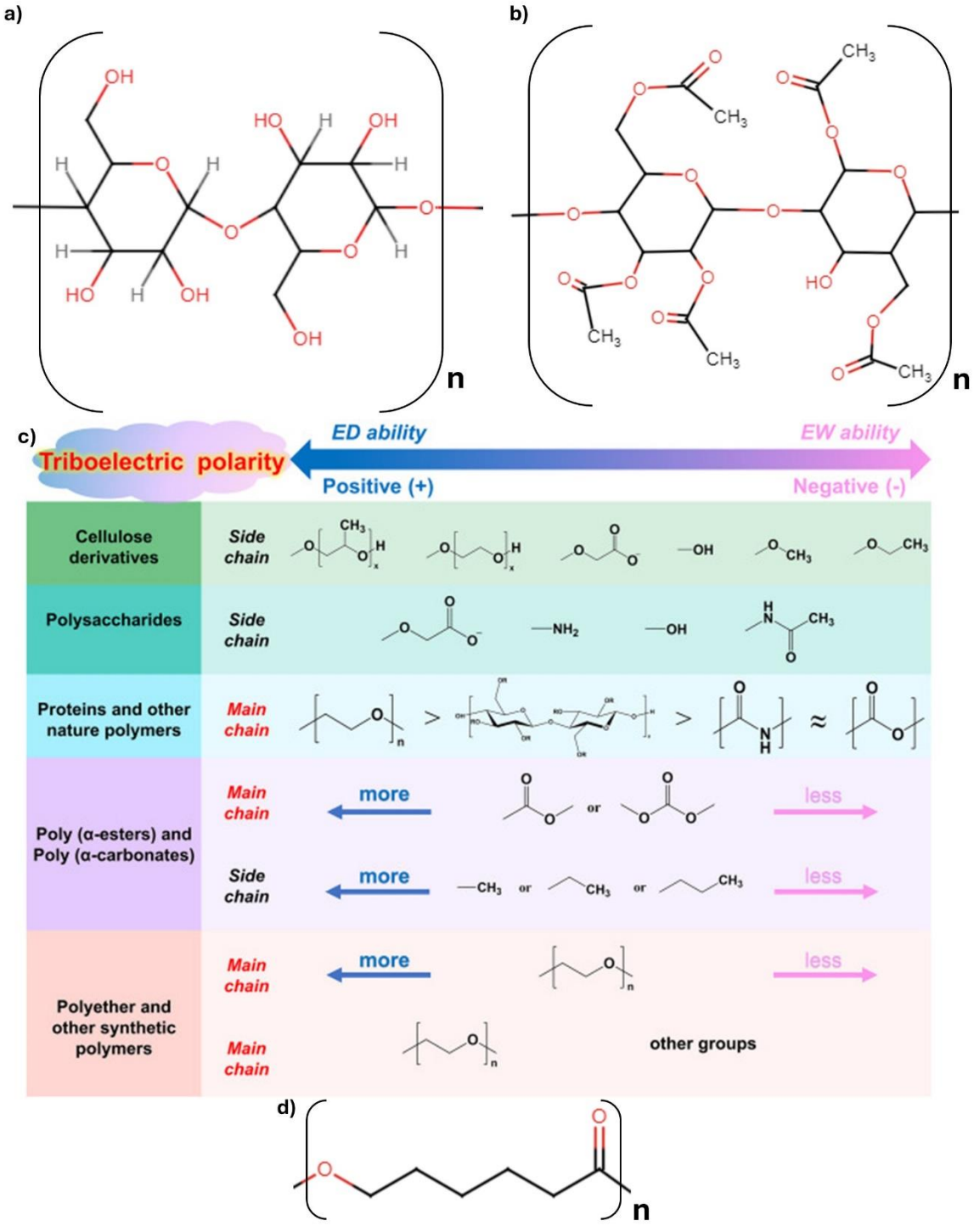


Figure 12: Chemical structures and triboelectric properties of the CA and PCL materials.

a) Chemical structure of cellulose, b) Chemical structure of CA, c) Triboelectric polarity of based on the chemical structure (adapted from Ref. [248] with permission Copyright©2023 Elsevier Inc.), d) Chemical structure of PCL.

As shown in figure 12a and b most of the H groups in the cellulose has replaced with acetyl groups in CA. Meng et al. have provided a comprehensive review on the triboelectric performance of the biodegradable polymers[248]. In cellulose derivatives if the side chain is OH group the triboelectric polarity is neutral to slightly negative while if the side chain is acetyl group the polarity tends to be slightly more negative than the OH group (Figure 12c).

### 3.1.2. Introduction to PCL

PCL is a biodegradable and biocompatible polymer, first introduced in the 1930s and widely used in packaging and tissue engineering applications. It is typically synthesized via the ring-opening polymerization of ε-caprolactone. Due to the presence of polar ester and non-polar methylene groups in its structure (Figure 12d), PCL exhibits good mechanical strength and hydrophobicity. Its physical and mechanical properties are influenced by molecular weight and crystallinity. Additionally, surface functionalization can enhance its hydrophilicity, adhesion, and biocompatibility, making it more suitable for biomedical applications.

According to Meng et al., PCL lies on the negative side of the triboelectric series [248]. The presence of ester groups, consisting of polar carbonyl and ether-like oxygen atoms, allows the PCL surface to stabilize its negative charge when in contact and separation with more tribopositive materials.

### 3.1.3. Hypothesis

A TENG constructed using CA and PCL will generate a measurable and sustainable triboelectric output due to their opposite charge transfer tendencies, with CA acting as a tribopositive and PCL as a tribonegative material. This biodegradable TENG will

demonstrate potential for use in wearable or biomedical energy-harvesting systems, with performance influenced by surface morphology and increased contact area.

### 3.1.4. Electrospinning set up

All electrospinning experiments were conducted using a custom-built (bespoke) electrospinning apparatus housed within a laboratory fume hood to ensure adequate ventilation and safety. A high-voltage power supply (Gamma High Voltage Research, USA), capable of delivering up to 30 kV DC, was configured with the positive terminal grounded, resulting in the application of –30 kV to the spinneret, while the collector was maintained at ground potential. The polymer solution was dispensed at a controlled rate using a KDS200P programmable syringe pump (KD Scientific, USA) (Figure 13a).

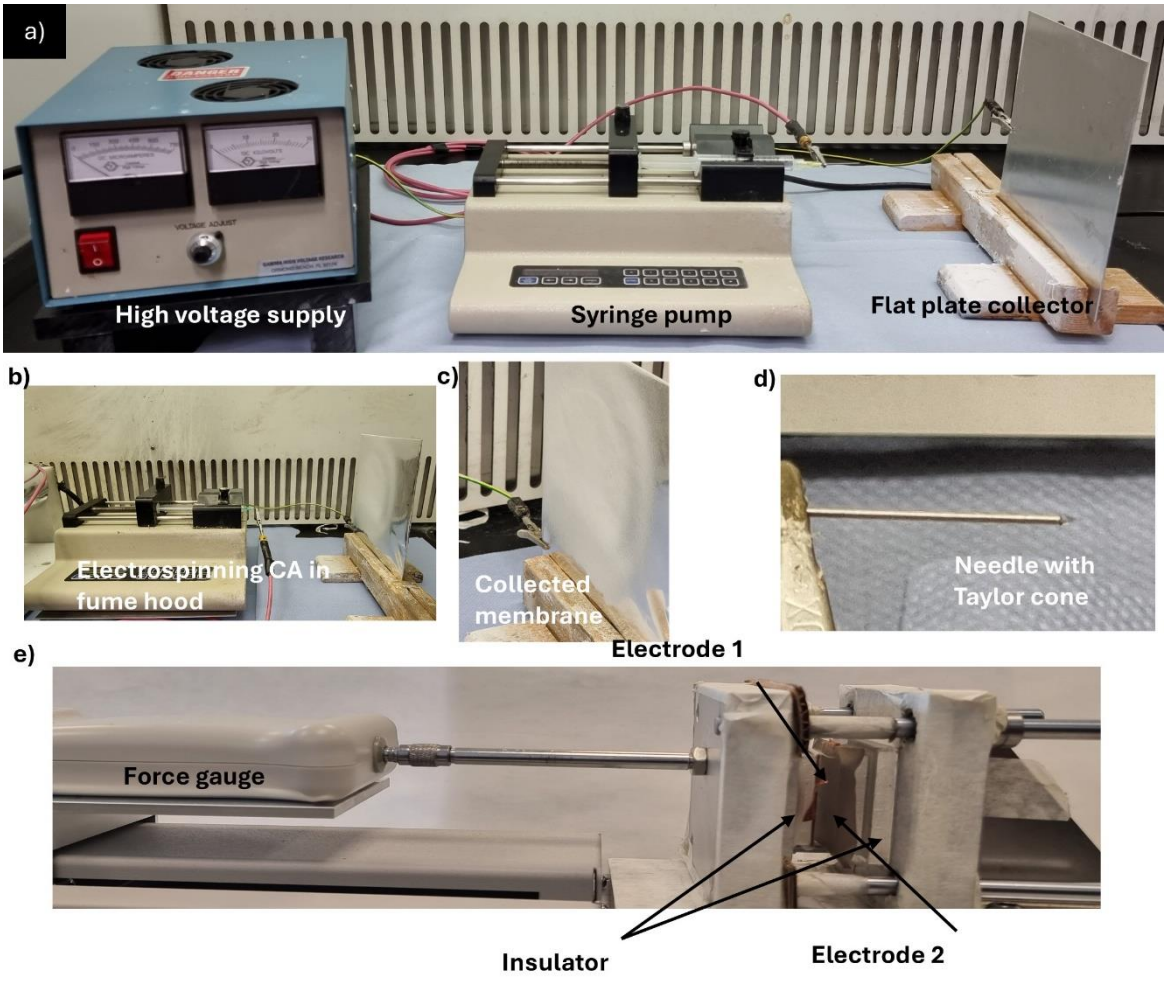


Figure 13: Electrospinning process and setup configurations for experiments.

a) Flat plate-based electrospinning setup, b) Electrospinning of CA in progress, c) Electrospun CA nanofibre mat deposited on the flat collector, d) Formation of a Taylor cone at the spinneret tip during electrospinning, e) bespoke contact and separation mechanism.

Initially, a flat plate collector configuration was used, consisting of a 250 × 250 mm aluminium plate to facilitate uniform nanofibre deposition (Figure 13b, c). During sample fabrication, an aluminium foil with a thickness of 30 μm was placed on the collector to facilitate the easy removal and handling of the electrospun membranes for subsequent characterization and testing.

### 3.1.5. Electrospinning of CA

CA (molecular weight (MW) 30,000, Sigma-Aldrich®), acetone, and DMF were procured and utilized as received for the preparation of the CA precursor. A quantity of X g (summarized in table 3) of CA was dissolved in a 10 g solution of DMF: Acetone (2:3 ratio), and the mixture was magnetically stirred for 4 hours at room temperature to create a series of solutions with concentrations ranging from 18-22%. The solution was loaded into a syringe with a 20 G blunt needle for electrospinning at a flow rate of 2 mL/h (stable Taylor cone was visible at this level figure 13d), with a 15 cm TCD and 15 kV applied voltage for 1 hour. Initially samples were collected onto the flat plate attached with aluminium foil. All samples were dried inside the fume hood for 48 hrs until the solvents evaporated. Samples were kept inside the desiccator cabinet nearly 1 week before characterizing TENG performance.

Table 3: CA weight dissolved in a DMF:acetone solvent mixture to prepare solutions with concentrations ranging from 18% to 22% (w/w).

| Solution weight | CA weight for 18% | CA weight for 19% | CA weight for 20% | CA weight for 21% | CA weight for 22% |
|---|---|---|---|---|---|

| | | | | | |
|---|---|---|---|---|---|
| 10 g | 2.195 g | 2.345 g | 2.5 g | 2.658 g | 2.821 g |

### 3.1.6. PCL Electrospinning

PCL (MW 80,000, Sigma-Aldrich®), Formic(FA), and Acetic acid (AA) were acquired and used as received for the preparation of the PCL precursor. X g of PCL (Summarized in table 4) was dissolved in a 1:1 ratio of 10 g FA and AA solution and stirred magnetically for 8 hours at 50°C to completely dissolve the PCL pellets making samples varying concentration from 14-18%. The solution was loaded into a syringe with a 20 G blunt needle for electrospinning at a flow rate of 2 mL/h, 11 cm TCD, and 16 kV applied voltage for 1 hour. Preliminary parameters were selected from previous literature and adjusted for the setup until proper electrospinning process continued[249]. The membrane was collected in the same manner as the CA and delicately removed from the aluminium foil, then dried in a fume hood for 24 hours prior to characterization.

Table 4 : PCL weight dissolved in a FA:AA solvent mixture to prepare solutions with concentrations ranging from 14% to 18% (w/w).

| Solution weight | PCL weight for 14% | PCL weight for 15% | PCL weight for 16% | PCL weight for 17% | PCL weight for 18% |
|---|---|---|---|---|---|
| 10 g | 1.628 g | 1.765 g | 1.905 g | 2.048 g | 2.195 g |

### 3.1.7. Initial screening process for determining the best concentration

As outlined in the literature review chapter (Section 2.3.2), the triboelectric performance of TENG devices can be quantitatively evaluated using three key electrical parameters: $V_{OC}$, $I_{SC}$, and Charge. To conduct these measurements, all electrospun samples were first trimmed to uniform dimensions of 40 × 40 mm and affixed to a Cu electrode using 3M 9712XYZ conductive double-sided adhesive tape to ensure reliable electrical contact.

A custom-built experimental setup (Figure 13e) was employed to facilitate controlled contact–separation cycles between the electrospun samples and a Cu counter-electrode. This motion was actuated using an IMADA MH2-500N-V900 horizontal motorized test stand. The normal contact force during testing was precisely regulated using an integrated IMADA ZTA-50N force gauge and maintained at a constant 10 N for all measurements. Contact and separation were performed at a speed of 900 mm/min, with a separation distance of 5 mm.

Electrical outputs were characterized under ambient conditions. The $V_{OC}$ was measured using a Tektronix TBS 1052B-EDU digital oscilloscope, which enabled data export in comma-separated value (CSV) format for post-processing. The $I_{SC}$ and Charge were recorded using a Keithley 6517B electrometer, with data acquisition managed through the Kickstart software platform provided by Tektronix.

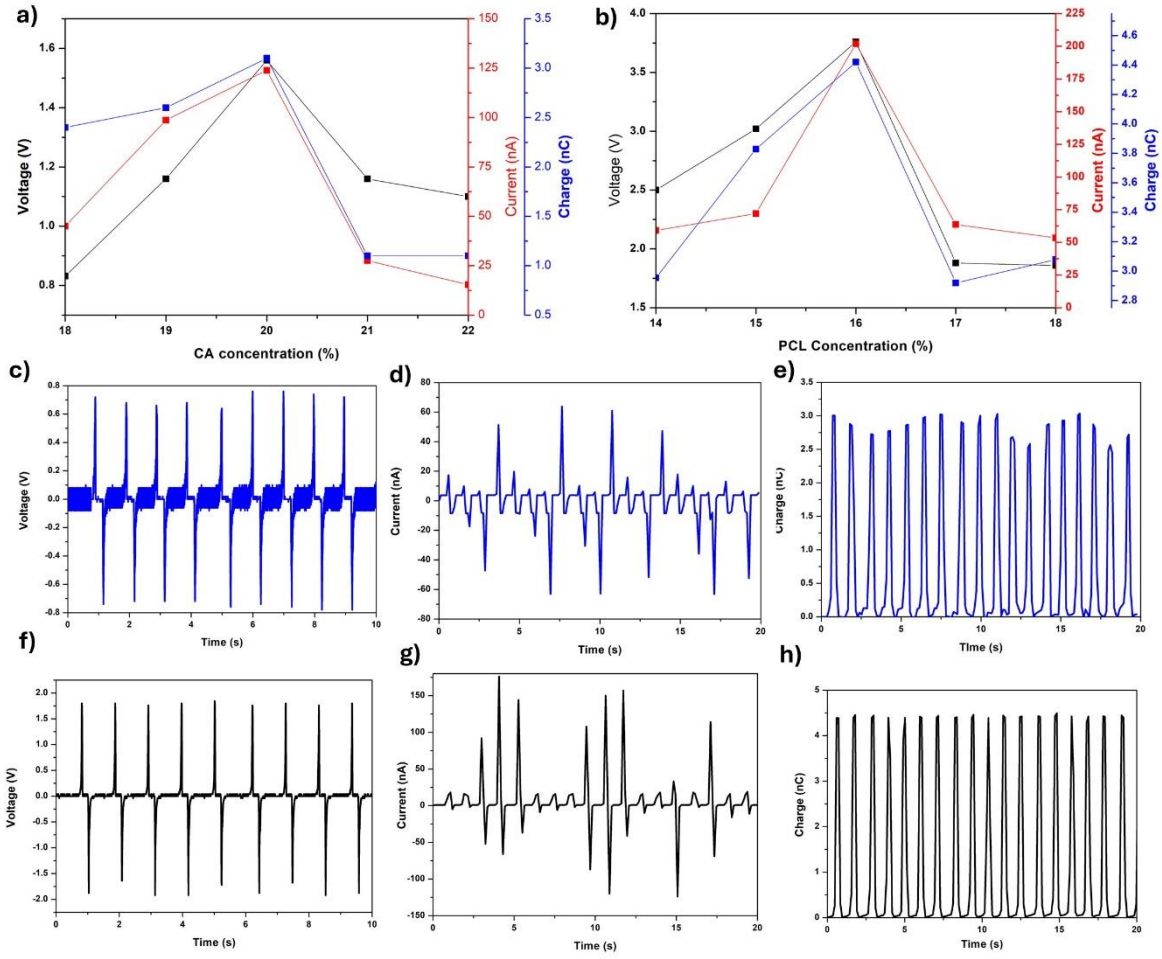


Figure 14: Output comparison of CA and PCL when changing concentration.

a) CA electrical outputs comparison for 18-22 % concentration, b) PCL electrical outputs comparison for 14-18 % concentration, c)Voltage, d) Current and e) Charge comparison for 20% CA electrospun sample, f)Voltage, g) Current and h) Charge comparison for 16% PCL electrospun sample.

As shown in Figure 14a, the highest recorded $V_{OC}$ of 1.56 V, $I_{SC}$ of 123.9 nA, and Charge of 3.1 nC were observed for the CA sample with a 20 wt.% concentration. For PCL, a $V_{OC}$ of 3.76 V, $I_{SC}$ of 103.67 nA, and Charge of 4.42 nC were recorded at 16 wt.% concentration(Figure 14b). As shown in Figure 14c-h, the current and charge outputs were not consistent, which could be attributed to poor contact and separation between layers, variations in contact-separation frequency, and limitations in data collection speed. The maximum frequency achievable with the IMADA setup is approximately 0.9–1 Hz for a 5 mm contact-separation displacement. In IMADA, the travel distance must be set manually, making it challenging to maintain constant force and amplitude. The data recording speed of KickStart with the KUSB interface and Keithley 6517B is approximately 10-12 readings per second. Since triboelectric charge separation is an instantaneous event, this recording speed presents challenges at higher frequencies. With these constraints in mind, an initial screening comparison of samples was performed under identical test conditions throughout the characterization.

Since the 20% CA and 16% PCL concentrations yielded the highest performance, all subsequent experiments and characterizations were conducted using these concentrations. In previous literature suggested that use of rotary collector (Figure 15a) can produce more finer fibre mats and that can subsequently assist with higher power generation by increasing surface area than flat-collector-based electrospinning setup. During experiment it was observed that the thickness of the flat collector based electrospun substrates to be non-uniform across the surface. As shown in Figure 15b, the thickness profile of the flat collector electrospun CA sample had an average of 0.105 mm. According to Dharmasena et al., the

thickness of the electrospun film is inversely proportional to the triboelectric output performance.

In contrast, the thickness profile of samples electrospun using a rotary collector exhibited a more uniform distribution, with an average thickness of 0.051 mm (Figure 15c). In the flat collector sample, the thickness was highest at the centre and decreased toward the edges, resulting in a broader variation across the sample. For electrical characterization and comparison, samples were selected with thicknesses in the range of 0.05–0.06 mm.

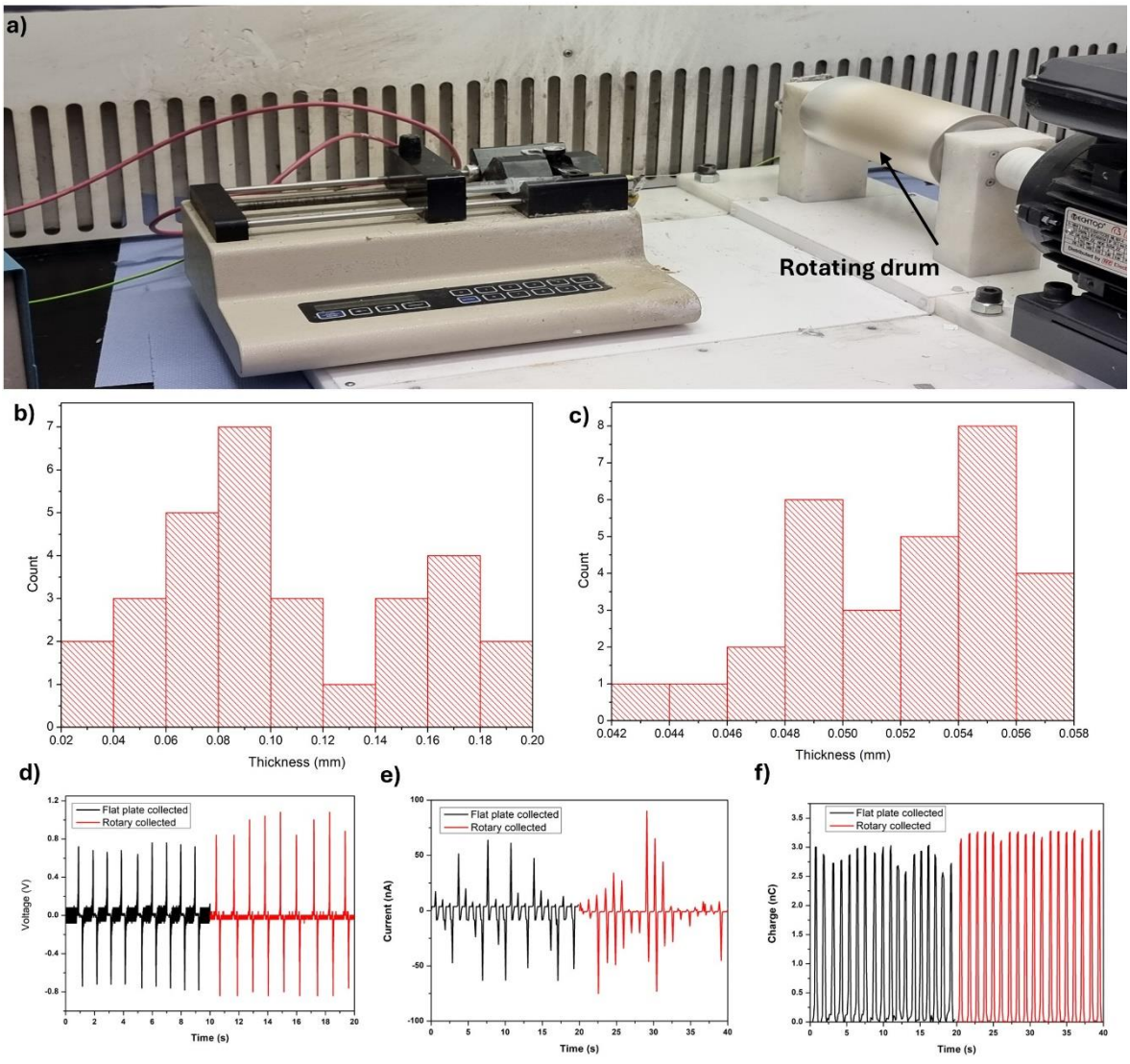


Figure 15: Thickness and electrical characterization for flat-plate and rotary collector mechanism.

a) Bespoke rotary collector mechanism. Thickness variation of b)flat plate collector mechanism, c) rotary collector mechanism collected electrospun membrane, d) Voltage, e) Current and f) Charge comparison of flat plate and rotary mechanism collected electrospun samples.

The only variable that changed between the two setups was the type of collector; all other electrospinning parameters were kept constant, as discussed earlier. A comparison of the output performance between the flat-collector and rotary-collector electrospun CA samples is presented in Figures 15d–f. The results show that $V_{OC}$, $I_{SC}$, and Charge increased by 13.96% (1.78 V), 10.57% (137 nA), and 4.45% (3.238 nC), respectively, in the rotary collector sample. Given the improved output performance and reduced thickness variation, all subsequent experiments were conducted using the rotary collector setup.

### 3.1.8. Summary and rationale for chemical modification

The initial screening of electrospun CA and PCL materials highlighted the strong influence of both polymer concentration and fibre collection method on TENG outputs. Among the concentrations tested, 20 wt.% CA and 16 wt.% PCL demonstrated the highest $V_{OC}$, $I_{SC}$, and Charge values. Furthermore, the output was further improved by changing the collector mechanism to rotary technique from flat plate. These findings established the optimal electrospinning parameters and collection strategy for the subsequent stages of this study.

While optimization of fibre morphology with concentration optimization and collection mechanism enhanced the baseline performance, the electrical output of triboelectric nanogenerators is also intrinsically governed by the surface chemistry of the studied polymers. In particular, functional groups and interfacial polarity determine the efficiency of charge generation and retention during operation ( contact separation or sliding) cycles. To further improve triboelectric performance beyond morphological control, it was therefore necessary to investigate chemical modifications that could tailor surface properties.

In the next section, NaOH treatment of CA membranes and the incorporation of chitosan with PCL are introduced as strategies to enhance TENG outputs. Furthermore, a practical application has been provided by applying such developed electrospun membranes for breath monitoring. This transition from morphology-focused optimization to surface chemistry modification provides a more comprehensive pathway toward developing high-performance, biodegradable, and biocompatible triboelectric devices.

## 3.2. Self-Powered Breath Monitoring Using Electrospun Biodegradable and Biocompatible Textile Sensors

### 3.2.1. Material development for breathing sensor

After characterizing the initial samples, new electrospun membranes with 20% CA were fabricated using a custom-built rotating mandrel setup. Electrospinning was carried out using a custom laboratory set-up in the laboratory which does not have the facility to control temperature and humidity conditions. The recorded temperature and relative humidity were $20 \pm 3\ ^{0}C$ and $50 \pm 10\%$, respectively. The electrospun membrane was collected on aluminium foil attached to a rotating mandrel (2000 rpm), then dried and annealed at 100 °C for 1 hour. (Figure 16a). NaOH solutions (0.05M to 0.25M in 0.05M increments) were prepared, and dried CA samples were cut, immersed in these solutions for 30 minutes, then thoroughly washed with deionized water and dried in a fume hood for 24 hours (Figure 16b-c).

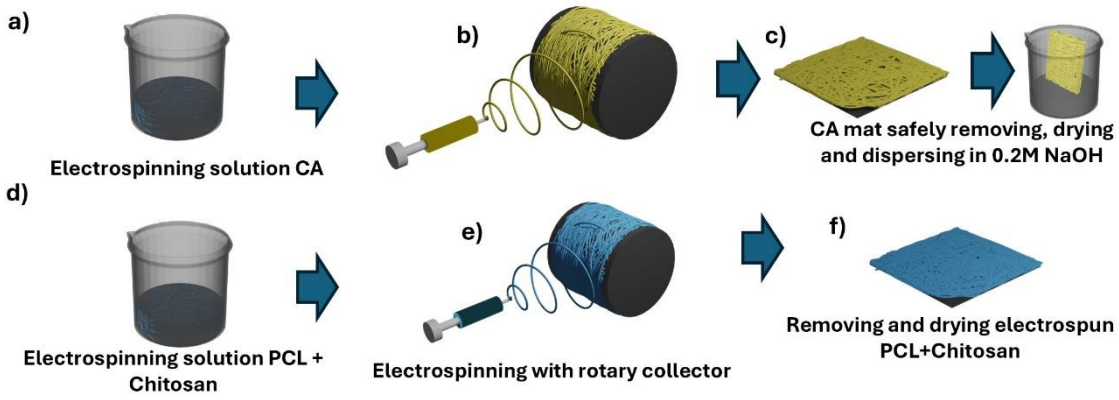


Figure 16: ) Electrospinning sample preparation for breath monitoring sensor.

a) CA precursor, b) Electrospinning process, c) Deacetylation of CA with NaOH and drying of all samples, d) PCL + chitosan precursor preparation, e) electrospinning process, f) Removal from aluminium foil and drying of PCL + chitosan samples. copied from ref[250] Copyright©2024, IEEE

PCL (MW 80,000, Sigma-Aldrich®), Formic, and Acetic acid were acquired and used as received for the preparation of the PCL precursor. 1.905 g of PCL was dissolved in a 1:1 ratio of 10 g FA and AA solution and stirred magnetically for 8 hours at 50°C to completely dissolve the PCL pellets. The solution was loaded into a syringe with a 20 G blunt needle for electrospinning at a flow rate of 2 mL/h, 11 TCD, and 16 kV applied voltage for 1 hour. The membrane was collected in the same manner as the CA and delicately removed from the aluminium foil, then dried in a fume hood for 24 hours prior to characterization.

For the second trial, Chitosan (medium MW, Sigma-Aldrich®) was procured and used in conjunction with the PCL precursor. The PCL precursor was prepared as previously described, and 0.3 g of Chitosan was mixed with 10 g of precursor and stirred thoroughly for 2 hours. After dissolution, electrospinning was carried out using the same procedure employed for PCL and dried for 24 hours before the subsequent process (Figure 16d-f).

### 3.2.2. Morphology and Chemical Modifications

The samples underwent Scanning Electron Microscopic (SEM) imaging with a Jeol JSM-IT 100 InTouchScope SEM, and Fourier-transform infrared spectroscopy (FTIR) was conducted using a PerkinElmer Spectrum Two FT-IR. SEM images of CA (Figure 17a) and NaOH-treated CA (NaOH-CA) (Figure 17b) demonstrate that the fibres retain a similar alignment post-treatment. However, there is a significant increase in the average fibre diameter, from 0.615 μm in CA to 1.208 μm in NaOH-CA. This increase in diameter is attributed to the deacetylation process, where the treatment with NaOH converts CA into cellulose II. This chemical transformation promotes fibre swelling and leads to the development of a rougher and more porous fibre surface. These morphological changes are indicative of the removal of acetyl groups and the consequent exposure of hydroxyl groups, enhancing the porosity of the fibres.

The SEM image of PCL (Figure 17c) reveals a substantial enhancement in surface area due to the formation of a micro- and nanofibre web. The fibres exhibit an average diameter of 0.501 μm, with branching nanofibres further increasing the surface area. This intricate network structure is advantageous for TENG, as the increased surface area can enhance charge generation and storage capabilities. When PCL is combined with chitosan, the average fibre diameter increases to 0.770 μm, and the fibres exhibit a more pronounced alignment in a single direction compared to PCL alone (Figure 17d). This enhanced alignment may improve the consistency and efficiency of charge transfer, making the composite material particularly suitable for high-performance TENGs.

Analysis of the FTIR spectra of CA and NaOH-CA reveals significant changes (Figure 17e). The absorption peak at 1739 $cm^{-1}$, associated with C=O stretching, and the peak at 1365 $cm^{-1}$, corresponding to C-H stretching, show a clear reduction after treatment. Furthermore,

peaks related to C-O stretching (1050-1150 $cm^{-1}$) and O-H stretching (3400-3500 $cm^{-1}$) are prominently visible in the treated sample, indicating successful deacetylation [20,251,252].

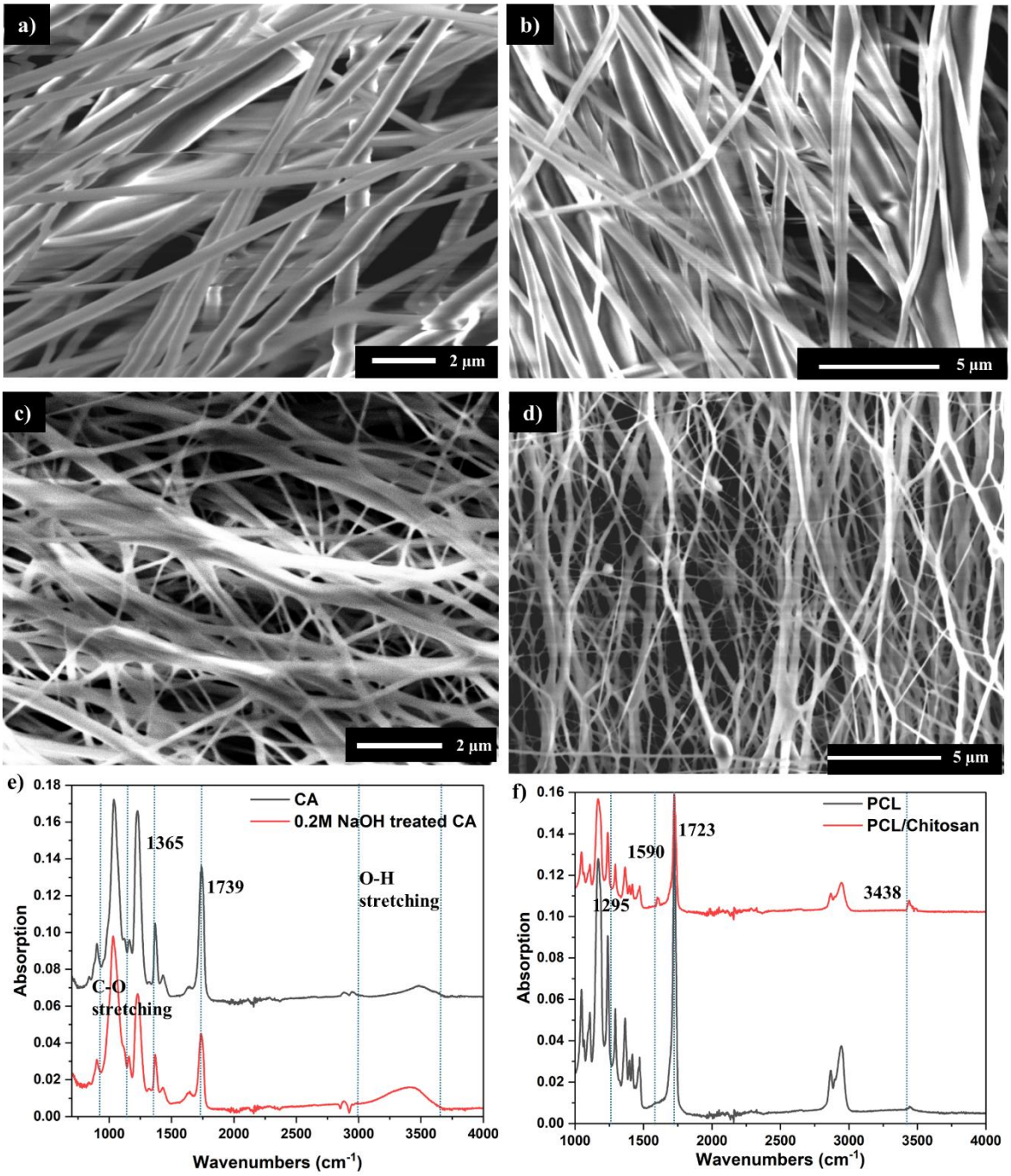


Figure 17: SEM and FTIR analysis of modified CA and PCL.

SEM images of a) CA, b) 0.2M NaOH-CA, c) PCL and d) PCL/Chitosan, FTIR analysis of e) CA and 0.2M NaOH-CA, f) PCL and PCL/chitosan. copied from ref[250] Copyright©2024, IEEE

The FTIR spectra of the PCL/chitosan blend show decreased peak intensities compared to pure PCL(Figure 17f). The interaction between the carbonyl groups of PCL and the amino groups of chitosan has reduced the peak intensity at 1723 $cm^{-1}$, while the interaction between the ester groups of PCL and chitosan has also reduced the peak at 1295 $cm^{-1}$.[253,254]

The peak at 3438 $cm^{-1}$, associated with hydrogen bonding, has broadened and become more pronounced, indicating an interaction between the hydroxyl groups of PCL and the amino groups of chitosan. Additionally, a new peak at 1590 $cm^{-1}$, characteristic of the PCL/chitosan blend, has appeared, demonstrating the effective blending of PCL and chitosan in the composite electrospun structure. [253–255]

### 3.2.3. Self-powered Sensor Performance

Initially, all NaOH-CA samples were subjected to contact and separation motion with the PCL sample. IMADA test setup maximum speed for contact separation characterization was 900 mm/min. The contact-separation cycle with the IMADA tester did not follow sinusoidal motion. Instead, a delay in separation was consistently observed following each impact force. Considering this factor, 10 N continuous contact and separation was applied manually frequency with 5 mm amplitude. Force was continuously recorded with the IMADA force gauge. The corresponding results are shown in Figure 18a, b, and c. The average $V_{OC}$ peak-to-peak values increased with NaOH concentration, peaking at 14.3 V for the 0.2M NaOH-CA sample. Similarly, the highest $I_{SC}$ and Charge were recorded for the 0.2M NaOH-CA sample, at 1.67 μA and 6.61 nC, respectively. Conversely, the lowest values were observed for the CA only sample, with a $V_{OC}$ of 4.87 V, $I_{SC}$ of 80.4 nA and a Charge of 1.5 nC.

As observed in the FTIR spectra, acetyl groups were substituted with hydroxyl groups. The introduction of hydroxyl groups in treated CA samples promotes hydrogen bonding and other interactions, enhancing the propensity to lose electrons and acquire a more positive charge compared to PCL[3]. Furthermore, the thickness of the samples has slightly reduced

from 63 µm to 57 µm, creating a more favourable environment for charge transfer. On the other hand, the swelling of fibres increases the gap between fibres and reduces the surface area. This might cause a reduction in electrical performance after a certain level of deacetylation. Further experiments are required to fully understand this phenomenon.

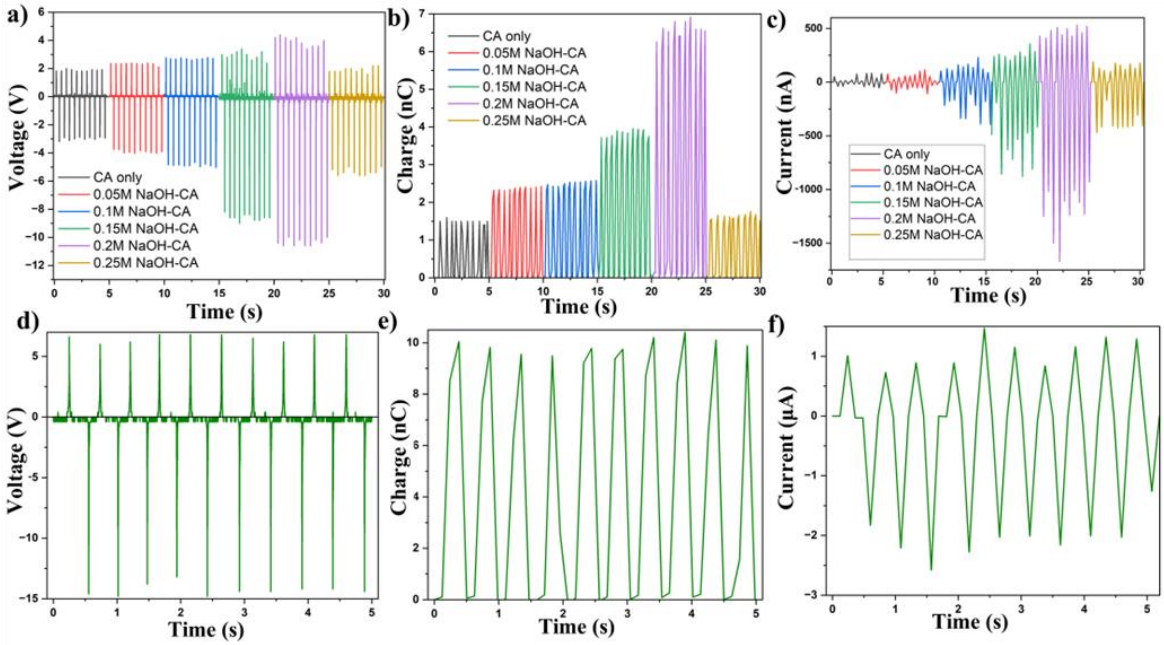


Figure 18: Triboelectric performance of modified CA and PCL samples.

Change of a) voltage, b) charge and c) current performance with the chemical modification of CA with NaOH., Output performance d) voltage, e) charge and f) current when 0.2M NaOH-CA sample contact and separated with PCL/chitosan composite electrospun sample. copied from ref[250] Copyright©2024, IEEE

After achieving peak performance with NaOH modification, another set of experiments was conducted with Chitosan modified PCL. Incorporating chitosan resulted in better improvements, with $V_{OC}$ reaching 20.8 V, $I_{SC}$ at 3.178 µA, and Charge at 9.9 nC (Figure 18 d, e, f). Although adding chitosan did not chemically alter the tribonegative properties of the PCL layer, it significantly modified the surface structure. The more textured surface with aligned fibres increased the surface area, leading to a higher charge density than pure PCL samples. Additionally, the thickness of the samples was significantly reduced from 55 µm to

34 μm (for the same electrospinning time), enhancing charge transfer and overall output[4]. This research has explored the feasibility of incorporating chitosan into PCL to improve output performance. Furthermore, the literature suggests that adding chitosan to the PCL network enhances biodegradability, offering the potential to develop sustainable devices[248,255].

In practice, it was observed that the voltage peak during the separation phase was significantly higher than during contact. According to Dharmasena, such enhanced separation peaks are caused by adhesion-induced impulsive separation, which amplifies the triboelectric output during detachment. Moreover, variations in external mechanical stimuli can have a substantial impact on TENG power generation. A consistent and uniform input motion profile is therefore critical for reliable performance. In our case, the use of manual hand tapping in initial experiments introduced variability in the motion profile, which likely contributed to the observed fluctuations and limited the effectiveness of mitigating these dynamic inconsistencies[256].

Wang et al. developed a breath monitoring TENG sensor using PTFE and Cu wire as the triboelectric materials, which could detect slow, rapid, shallow and deep breathing patterns accurately[257]. Electrospun PCL and CA fibres offer a high surface area-to-volume ratio, essential for enhancing the sensitivity and efficiency of breath monitoring sensors [7]. This study explores the potential of electrospun PCL and CA fibres for use in self-powered breath monitoring sensors. Specifically, this work investigates the effects of modifying CA by deacetylation with NaOH at concentrations ranging from 0.05M to 0.25M and combining PCL with 3% chitosan.

Final sensor samples were attached to conductive fabrics and affixed to a face mask using paper brackets (Figure 19a-b). The sensor successfully identified a range of simulated breathing patterns, demonstrating the feasibility of this technique for future wearable self-

powered sensors. This research highlights the importance of material modifications in enhancing the functionality and efficiency of self-powered sensors. By optimizing electrospinning conditions and material compositions is essential to advance the development of highly sensitive, reliable, and sustainable breath monitoring devices that can be integrated into wearable health monitoring systems. Future work may further enhance these technologies with signal processing and AI techniques for continuous breath monitoring.

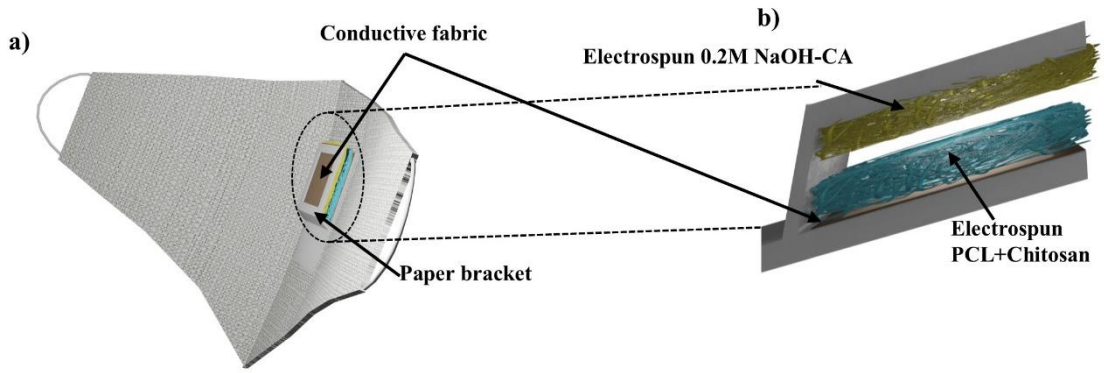


Figure 19: Breath monitoring sensor device fabrication process

a) Final prototype sensor attached to the fabric mask, b) paper bracket used for sensor attachment. copied from ref[250] Copyright©2024, IEEE

### 3.2.4. Discussion on breath monitoring

As shown in Figure 20a, during breathing, the contact and separation motions between the CA and PCL layers result in an alternating current/voltage output through the external load. This output can be used as the primary signal for determining breath patterns based on these experiments. The variation in current, corresponding to the cyclical motion of the layers, directly reflects the inhalation and exhalation phases, providing a reliable metric for analyzing respiratory activity.

A series of experiments were conducted to evaluate the sensor's sensitivity for breath monitoring applications and determine the response to applied force, response time, and

recovery time. As illustrated in Figure 20b, the sensor exhibited a peak-to-peak voltage of 9.56 V at an applied force of 1 N, with a maximum voltage of 34.6 V achieved at 20 N. Additionally, the device demonstrated a linear response ($R^2$ = 0.986) with a sensitivity of 2.209 V/kPa over a pressure range of 0.625-12.5 kPa (Figure 20c).

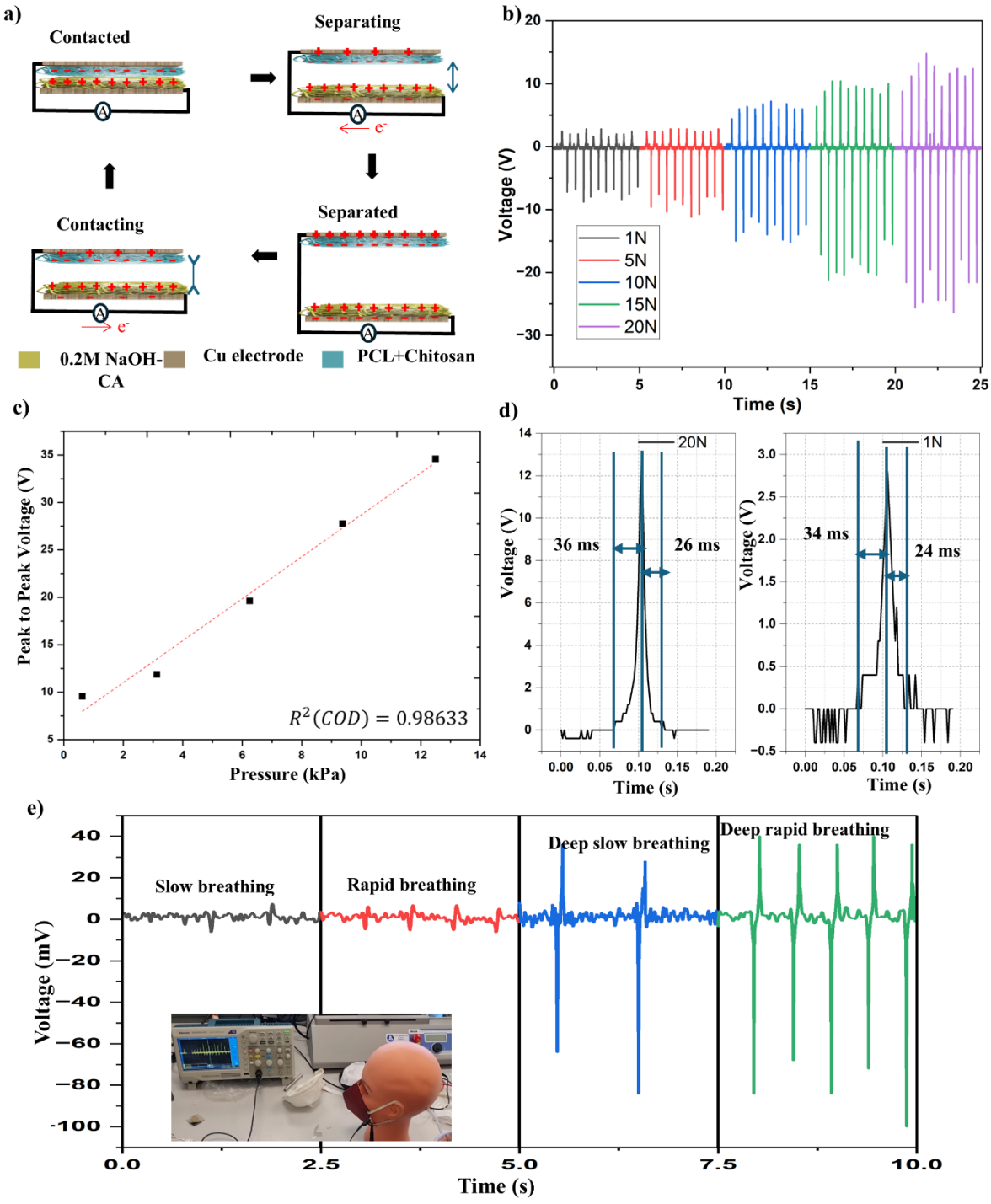


Figure 20: Sensitivity performance analysis and application development for breath monitoring sensor.

a) The working principle of the triboelectric breath monitoring sensor. b) Voltage output change with different applied force, c) Linear relationship between the voltage and pressure, d) Response and recovery time measurement for 20 N and 1 N applied force., e) Voltage response with slow, rapid, deep slow and deep rapid breathing patterns. copied from ref[250] Copyright©2024, IEEE

Practical implementations for real world applications are critical for evaluating the performance of any developed triboelectric sensor. Considering this factor, the feasibility of using CA and PCL for breath monitoring sensor development was investigated. The development of self-powered sensors for health monitoring is a significant advancement in wearable technology. Triboelectric performances of biodegradable polymers Breath monitoring sensors are particularly crucial, providing vital respiratory health information, early detection of diseases, and monitoring overall wellness. The device characteristics demonstrate the feasibility of this approach for monitoring breathing signals. Normal breathing rates range from 12 to 20 breaths per minute. Rates above this range indicate tachypnea, characterized by rapid breathing, while rates below suggest bradypnea, characterized by slow breathing. Detecting apnea, marked by the cessation of breathing, is crucial and requires high sensitivity to low pressures[258]. The sensor's response time was recorded as 34 ms to reach any given positive peak at 1N force and 36 ms at 40 N force. Recovery times were 24 ms for 1N force and 26 ms for 40 N force (Figure 20d). These results indicate that the sensor is suitable for continuous respiratory rate monitoring and is capable of detecting changes in respiration over time.

To demonstrate the feasibility of this application, the sensor was integrated into a facemask and evaluated using a model test rig, which consisted of a mannequin head with an air outlet at the mouth attached by tubing to a manual air pump. The mask was placed on the face of the mannequin head in front of the air outlet, and different breathing patterns were simulated by controlling the airflow via the manual pump. The sensor was capable of distinguishing

different signal features with slow, rapid, deep slow, and deep rapid breathing patterns, as shown in Figure 20e. Biocompatibility for long-term exposure and a feasible wireless signal detection technique need to be developed before conducting experiments with human participants.

### 3.2.5. Learning outcomes

**Literature Gap:** Our review revealed a notable absence of systematic studies on electrospun CA paired with PCL in TENGs. Both CA and PCL are well-recognized biodegradable, biocompatible polymers with triboelectric potential, but prior work typically pairs CA or PCL with other materials rather than with each other[259,260]. This identifies a clear literature gap on the CA/PCL combination.

**Concentration Effects:** Electrospun CA and PCL fibre mats were fabricated at varying polymer concentrations and assembled in a vertical contact-separation TENG configuration using a flat copper plate as the counter electrode. Varying concentrations resulted in changes in the output in the initial screening. Thus, the changes in concentration have affected the fibre morphology and strongly influenced surface contact and charge density, changing the outputs. This is consistent with the understanding that electrospinning parameters (voltage, flow rate, solution concentration, etc.) must be finely tuned to control fibre[7,261]. However, even with optimized morphology, our open-circuit voltage and short-circuit current remained very low. In all tested concentrations, the raw CA/PCL device produced only millivolt-to-volt outputs and microamp-scale current values substantially below typical literature reports.

**Performance Limitation:** The measured output from the CA/PCL TENG was found to be orders of magnitude too low for practical use. By comparison, literature reports show that optimized polymer-based TENGs can generate output voltages on the order of hundreds of volts and currents in the 10–30 μA range. For example, a PCL-based TENG with silver nanowires achieved ~800 V and 30 μA, sufficient to light hundreds of LEDs[260]. Our

CA/PCL device, by contrast, produced only a few volts and a few microamps at best. This confirms that the current biodegradable sensor output is inadequate to power even low-power modern electronics fully. In practical terms, the power density of our device is far below the milliwatt level needed by typical wearable sensors, indicating that substantial material or structural enhancements (such as surface micro-patterning or nano-additive doping) would be required before it could serve as a self-powered source[259]. Either CA or PCL needs to be replaced with a better alternative material for the development of self-powered sensor for detecting human motions.

**Dynamic Testing Requirements:** A key outcome is recognizing the importance of testing under realistic dynamic conditions. Human movements (walking, running and climbing) produce contact-separation motions over a range of frequencies (typically 1-3 Hz for slow to moderate activity)[262]. TENG output is strongly frequency-dependent: at low frequencies (~1–2 Hz), the harvested power is minimal (on the order of micro-watts), whereas higher-frequency excitation can boost the energy yield. Accordingly, future work must simulate a spectrum of motion frequencies and amplitudes. Systematic tests (e.g., at 1, 5, 10 Hz, and above) will reveal how the output scales with frequency[7,56].

**Experimental Setup Improvements:** It was found that the current test bench limits the evaluation of dynamic behaviour. To address this, future experiments require upgraded equipment, such as using an electrodynamic shaker or voice-coil actuator to drive the TENG at controlled, higher frequencies and amplitudes. Such a setup would enable reproducible, high-frequency contact-separation cycles beyond the capability of manual pressing. It would also allow precise control of contact force, displacement, and frequency, improving measurement accuracy. In summary, an improved mechanical testing rig is identified as a priority to characterize sensor output under the high-rate conditions expected in wearable applications.

**Methodological and Technical Insights:** Throughout the research process, several broader lessons were learned. First, a rigorous experimental design is essential: controlling electrospinning parameters (solution concentrations, flow rate, voltage, and collector distance) is critical to obtaining uniform, defect-free fibre mats. Handling challenges with biodegradable polymers were also noted (e.g., solvent evaporation rates, humidity control), emphasizing the need for careful environmental control during fabrication. On the measurement side, the importance of calibrating electrode alignment and contact area was recognized, as well as recording all processing variables for repeatability. In particular, next chapters to explore ways to enhance charge generation, for example, by incorporating micro- or nanoparticles for power improvements on CA surfaces or by adding functional fillers to the polymers.

# CHAPTER 4

## 4. TRIBOELECTRIC PERFORMANCE ANALYSIS OF ELECTROSPUN CA AND PVDF

**Publication status : Presented as a poster in a conference**

**Part of this chapter presented at 8th International Conference on Electrospinning 2024 at AGH University of Krakow, Krakow, Poland, 25-28th June 2024**

Flexible, biocompatible, and self-powered wearable gait monitoring and tactile sensing using parallelly electrospun CA and PVDF membranes., K. R. Sanjaya D. Gunawardhana, Garret. B. McGuinness, Tomás E. Ward, Shirley M. Coyle. at 8th International Conference on Electrospinning 2024 at AGH University of Krakow, Krakow, Poland, 25-28th June 2024.

# CHAPTER 4

Integrating sensors into intelligent garments remains challenging due to the complexity of balancing electronics, power sources, and comfort. This chapter explores electrospun PVDF and CA for self-powered sensors in gait monitoring and touch sensing. Electrospinning parameters and rotary collector optimization enhanced PVDF's β phase and CA's tribopositivity, improving performance metrics including $V_{OC}$, $I_{SC}$, Charge and pressure sensitivity. Both materials demonstrated hydrophobicity and excellent breathability, crucial for wearable applications. Mechanical testing revealed promising properties, supporting their potential for scalable, cost-effective, and biocompatible wearable sensors.

## 4.1. Introduction

In the previous chapter it was evident that CA/PCL combination output performance was below the required power levels needed for modern electronic components. Considering that finding, this chapter will explore the possibility of improving the output performance of the device by changing the PCL material with highly tribonegative PVDF material. CA was chosen over PCL due to its more sustainable origin, wide availability and biodegradability. CA is derived from naturally abundant cellulose, making it a bio-based polymer, whereas PCL is synthesized from petroleum-derived caprolactone, limiting its sustainability profile.

PVDF is a high-performance fluoropolymer discovered in the mid-20th century[263]. In 1969 Heiji Kawai discovered that PVDF has piezoelectric constants $d_{31}$, $d_{32}$, $d_{33}$, $d_{15}$ and $d_{24}$ which enabled researchers to focus on using PVDF in PENG applications since 2006[264,265]. (refer literature review section 2.3.4) Furthermore PVDF is widely used in triboelectric applications as a negatively charged material and actively being used for wearable applications due to its biocompatibility[40,266].

## 4.2. Electrospinning of PVDF Nanofibres

Previous research on piezoelectric, pyroelectric and ferroelectric materials suggested that the β phase with all-trans conformation with a dihedral angle of $180^0$ of PVDF and its copolymers shows the highest output performance. He et al. have reviewed the effect of the different electrospinning parameters on tuning the β phase and crystallinity, thus increasing the piezoelectric performance of electrospun PVDF nanofibres. An increased applied voltage between the needle tip and collector can increase the number of charges and a higher degree of molecular orientation favourable for the crystallinity of PVDF nanofibres. However, increasing beyond 20 kV can accelerate the flying time of the charger without controlling their orientation which results in a reduction of the piezoelectric properties of the material. Furthermore, TCD has a positive linear relationship between the formations of the β phase in the 9 – 15 cm region, beyond which, it is seen to decline. It is not clear whether the behaviour of the flow rate affects the piezoelectric performance, however there is evidence that up to 2 mL/hr increased flow rate increases the piezoelectric characteristic, with a decrease observed beyond this. Moreover, using a rotary collector and increasing the rotation speed up to 1500 rpm has been shown to increase the β phase and crystallinity. In addition to process parameters, solution parameters can be adapted to adjust the β phase and crystallinity. Such parameters include molecular weight (max output at 777 000 $gmol^{-1}$), concentration (lower the better, but optimum is around 16-20%) and solvent volatility ratio (moderate volatile content is required, e.g. acetone 40%). Environmental conditions also affect the characteristics, e.g. maintaining a high humidity environment at 25 $^0$C temperature can increase the percentage of β phase (F(β)) in PVDF material.[109]

### 4.2.1. PVDF in Triboelectricity

PVDF is a semi-crystalline polymer composed of repeating –($CH_2$–$CF_2$)– units, where the presence of highly electronegative fluorine atoms plays a crucial role in its triboelectric

behaviour. Fluorine's strong electron affinity causes PVDF to attract negative charges when in contact and separation with more electropositive materials, resulting in a net negative charge on its surface[7]. In the triboelectric series PVDF tends towards the negative side showing that it can charge as a tribonegative substrate when in contact with tribopositive materials [267].

Furthermore, the molecular polarity arising from the significant dipole moment between the carbon-fluorine (C–F) and carbon-hydrogen (C–H) bonds contributes to effective charge separation during triboelectric interactions. This characteristic is particularly enhanced in the electroactive β-phase of PVDF, which adopts an all-trans conformation. In this phase, the dipole moments align in the same direction, leading to an increased net polarization and superior dielectric and piezoelectric properties. These features make β-phase PVDF especially suitable for use in TENGs and self-powered sensing applications[268].

Thus, the inherent electronegativity of fluorine, combined with the polymer's polar structure and phase-dependent dipole alignment, underpins PVDF's strong negative triboelectric response and its effectiveness in wearable or fabric-based energy harvesting systems.

### 4.3. Hypothesis

A TENG constructed using CA and PVDF will generate a higher and sustainable triboelectric output compared to the CA/PCL combination due to their opposite charge transfer tendencies, with CA acting as a tribopositive and PVDF as a tribonegative material. This has the potential to deliver an output high enough for use with modern electronic components in order to develop self-powered sustainable sensors.

## 4.4. Working mechanism and theoretical simulation

### 4.4.1. Working mechanism

When the CA and PVDF layers initially come into contact, charge separation occurs due to their contrasting triboelectric properties. CA becomes positively charged, while PVDF becomes negatively charged. As an external mechanical force creates separation between these two layers, the resulting increase in distance amplifies the electric field due to charge separation, following Lenz's law. This induces a potential difference between the electrodes attached to the CA and PVDF layers.

Consequently, electrons flow from the electrode connected to CA toward the electrode connected to PVDF to balance the potential difference. When the separation reaches its maximum, the electric field stops increasing, and the electron flow ceases. During re-contact, the process reverses: as the layers approach each other, the charges on the electrodes redistribute, generating a reverse electron flow. This cyclical process of contact and separation produces an AC signal.

### 4.4.2. Theoretical simulation

To gain deeper insight into the charge transfer mechanism between PVDF and CA, a theoretical modelling approach was employed. As previously discussed in literature review section 2.3.1. the DDEF model was used for modelling as it provides opportunity to evaluate outputs with empirical modelling[134].

Simulation starts with approximating the average electric field above the midpoint of a specific surface with length L and width W along an axis perpendicular to the surface ($E_x$). Considering our experiment L=W=4 cm, surface charge density $\sigma$ which is place in a medium with permittivity $\varepsilon$ the simplified equation as given in E 7, (original equation can be found in ref[154,155])

$$E_x = \frac{\sigma}{\pi\varepsilon}\arctan\left(\frac{4\times10^{-4}}{x\sqrt{x^2+8\times10^{-4}}}\right) = \frac{\sigma}{\pi\varepsilon}f(x) \quad \text{(E7)}$$

where $x$ is the perpendicular distance with respect to the charged surface.

Considering equal positive and negative triboelectric charge of $\sigma_T$ is uniformly distributed at the surface of PVDF and CA substrates and considering electrodes are in open circuit configuration. (the charge on the electrode $\sigma_U = 0$ ) The overall electric field at the PVDF and attached electrode connecting interface was calculated using E 8.

$$E_{Total,PVDF/electrode} = \frac{\sigma_T}{\pi\varepsilon_1}((f(d_1) - f(x_0 + d_1)) \quad \text{(E8)}$$

Where, $\varepsilon_1$ and $d_1$ are permittivity and the thickness of PVDF, respectively. $x_0$ is the separation between PVDF and CA layer (Figure 21).


Figure 21: Representation of parameters for theoretical calculation with DDEF model.

Electric potential on the PVDF and attached electrode interface ($V_1$) can be calculated by integrating E7 as shown in E9

$$V_1 = \frac{\sigma_T}{\pi\varepsilon_1}\left(\int_{d_1}^{d_1+x_0} f(x)dx\right) = \frac{\sigma_T}{\pi\varepsilon_1}[Y(x)]_{d_1}^{d_1+x_0} \quad \text{(E9)}$$

Considering the analytical solution for the integration of f(x), Y(x) has developed by adapting the solution from ref[155] and modifying with parameters (in this experiment) to generate the following E10 equation.

$$Y(x) = x\,arctan\left(\frac{4\times10^{-4}}{x\sqrt{x^2+8\times10^{-4}}}\right) - 2\times10^{-2} ln\left(\frac{\sqrt{x^2+8\times10^{-4}}+2\times10^{-2}}{\sqrt{x^2+8\times10^{-4}}-2\times10^{-2}}\right) \quad \text{(E10)}$$

Considering all parameters and taking into account E10 the $V_{OC}$ can be calculated as given in E 11,

$$V_{OC} = \frac{\sigma_T}{\pi}\left(\frac{1}{\varepsilon_1}[Y(x)]_{d_1}^{d_1+x_0} - \frac{1}{\varepsilon_2}[Y(x)]_{d_2}^{d_2+x_0}\right) \quad \text{(E11)}$$

Where $\varepsilon_2$ and $d_2$ are permittivity and the thickness of CA, respectively.

Considering short circuit condition, the $J_{SC}$ can be calculated using $V_1$ and $V_2$ equations. When the attached electrodes are in short circuit condition $V_1$ -$V_2$ =0 due to free charges can move from one electrode to other electrode to neutralize any potential difference. At equilibrium state potential at the PVDF attached electrode interface can be written as E 12.

$$V_1 = \frac{\sigma_T}{\pi\varepsilon_1}\left(\int_{d_1}^{d_1+x_0} f(x)dx\right) - \frac{\sigma_U}{\pi\varepsilon_1}\left(\int_{0}^{d_1+d_2+x_0} f(x)dx\right) \quad \text{(E12)}$$

Taking the same conditions at CA and attached electrode interface equations can be derived for V2 and finally considering open circuit condition the equations for $\sigma_U$ and $J_{SC}$ can be developed as given in E 13, E 14 respectively

$$\sigma_U = \sigma_T \frac{\left(\frac{1}{\varepsilon_1}[Y(x)]_{d_1}^{d_1+x_0} + \frac{1}{\varepsilon_2}[Y(x)]_{d_2}^{d_2+x_0}\right)}{\left(\frac{1}{\varepsilon_1}+\frac{1}{\varepsilon_2}\right)[Y(x)]_0^{d_1+d_2+x_0}} \quad \text{(E13)}$$

$$J_{SC} = \frac{d\sigma_U}{dt} \quad \text{(E14)}$$

Selecting a contact and separation profile these equations can be used to simulate results for the PVDF/CA TENG development.

According to the DDEF model $\sigma_T$ needs to be experimentally evaluated before using it with the complete simulation. In order to address this requirement two samples of PVDF and CA were prepared as described in next section.

### 4.5. Sample preparation

PVDF (530,000 MW was precured from Sigma-Aldrich®(347078) and used as received. 20% of PVDF is dissolved in acetone (ACS reagent, ≥99.5%, Sigma-Aldrich®, 179124) and (HPLC, ≥99.9%, Sigma-Aldrich®, 570547) DMF (DMF: Acetone, (3:2)) solution. After adding PVDF pellets into the solution it was magnetically stirred for 4 hours at 50°C until all the pellets were fully dissolved. Once the solution reached room temperature, it was loaded into a syringe with a 21 G blunt needle. Electrospinning was conducted at room temperature (20±2 $^0$C) and relative humidity of 50±10 % (No specific measures were taken to control the environmental conditions) using a KDS200P syringe pump with a bespoke rotary collector. The flow rate of 2 ml/h, tip-to-collector distance of 15 cm and applied voltage of 18 kV was maintained during the process. Two samples were prepared based on the collection mechanism. One sample made with flat plate collector and the other PVDF mat was collected onto aluminium foil on a rotary collector at 1500 rpm. After collection, the mats were carefully removed from the aluminium foil, dried inside a fume hood for 48 h, and dried in an oven at 80 $^0$C for 1 hour to confirm the complete removal of DMF and Acetone residues.

20% CA was prepared as in the previous experiment. Since there was not much triboelectric improvement with treating CA with NaOH it was decided to use the initial CA electrospinning procedure described in chapter 3, section 3.1.5. Samples were collected onto aluminium foil at 1500 rpm with rotary collector.

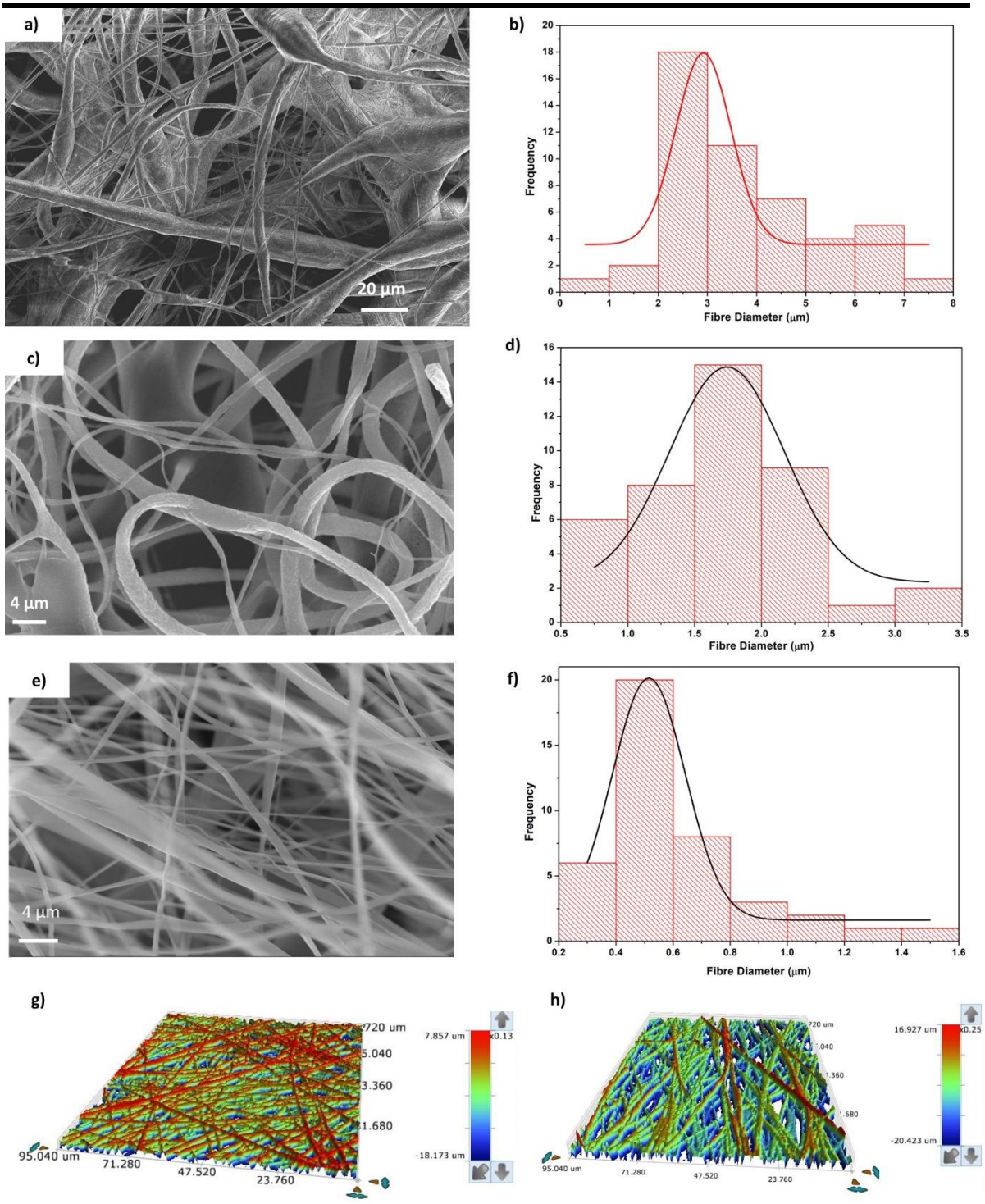


Figure 22: Sample morphology analysis of CA and PVDF.

SEM images and corresponding fibre diameter distributions of a) and b) of flat-plate-collected PVDF , c) and d) of rotary-collected PVDF, and e) and f) of rotary-collected CA, 3D surface profiles obtained using a Contour GT profilometer for g)flat-plate-collected and h) rotary-collected CA samples.

# CHAPTER 4

## 4.6. Material characterization

The morphological characteristics of the electrospun PVDF and CA fibres were initially assessed using SEM to evaluate their suitability for TENG applications. Fibres collected on a flat plate exhibited bead formation, with PVDF showing an average fibre diameter of 2.909 ± 0.21 μm (Figure 22a, b), indicating a less uniform morphology. In contrast, fibres collected using a rotary collector demonstrated significantly improved alignment.

The average fibre diameter decreased to 1.741 ± 0.103 μm (Figure 22c, d), for the rotary collector PVDF samples and the fibres appeared smoother and more continuous, suggesting enhanced electrostatic performance due to the increased surface area and reduced defect density. Similarly, CA fibres collected on the rotary collector displayed a nanoscale average diameter of 515 ± 9.39 nm (Figure 22e, f), which is desirable for maximizing surface charge generation in TENGs.

To further assess the surface topology, 3D surface profiling was performed using a Contour GT profilometer for CA samples. The flat-plate-collected CA exhibited a random fibre orientation with a surface roughness of 3.225 μm (Figure 22g). In contrast, the rotary-collected CA showed a comparable surface roughness of 3.191 μm (Figure 22h). It is confirmed visually that the fibres are arranged in a parallel order by the rotary collector compared with the flat collector. These improvements in fibre alignment and nanoscale morphology, particularly in rotary-collected samples, are critical for boosting the triboelectric output by enhancing charge separation and increasing effective contact area. Although 3D surface profiling of PVDF was attempted, the measurement was unsuccessful, possibly due to limitations in optical contrast or sample preparation.

Overall, the results confirm that the use of a rotary collector significantly improves the morphology and surface properties of both PVDF and CA fibres, making them highly

suitable for TENG applications due to their enhanced surface area, smoother fibre texture, and improved nanoscale structure.

### 4.7. Electrical characterization

For electrical characterization, CA and PVDF samples were cut into 16 $cm^2$ sections and mounted onto two copper electrodes using 3M 9713XYZ conductive adhesive tape. These copper plates were then fixed to Perspex sheets, as detailed in the previous chapter. Earlier experiments established that the maximum contact-separation frequency achievable under the initial setup was approximately 1 Hz. However, given that real-world applications such as energy harvesting from human motion often involve higher frequencies, evaluation of the materials' performance under more dynamic conditions was required.

To simulate these conditions, a manual tapping method was implemented to induce contact-separation cycles at an increased frequency. Specifically, a contact force of 10 N was applied at a frequency of 2 Hz, with a displacement amplitude of 5 mm between the triboelectric layers. This setup was designed to mimic more realistic and frequent mechanical stimuli, improving the relevance of the results for wearable and biomechanical energy harvesting applications. All other electrical measurement parameters and data acquisition systems remained consistent with those used in the previous experimental chapter.

The triboelectric performance of the rotary-collected CA and flat-plate-collected PVDF samples was evaluated under the contact-separation mode. When the rotary-collected CA film was paired with a flat-plate-collected PVDF counterpart, a Charge of 41.93 nC, an $V_{OC}$ of 28.64 V and $I_{SC}$ of 3.80 µA (Figure 23a, b, c) were initially observed. These values significantly increased following optimization of the fibre morphology and contact interface, reaching a Charge of 62.5 nC, $V_{OC}$ of 100.8 V and $I_{SC}$ of 13.67 µA. The enhancement in electrical output is attributed to improved fibre alignment, higher surface area, and better interfacial contact enabled by the rotary collection method.

# CHAPTER 4

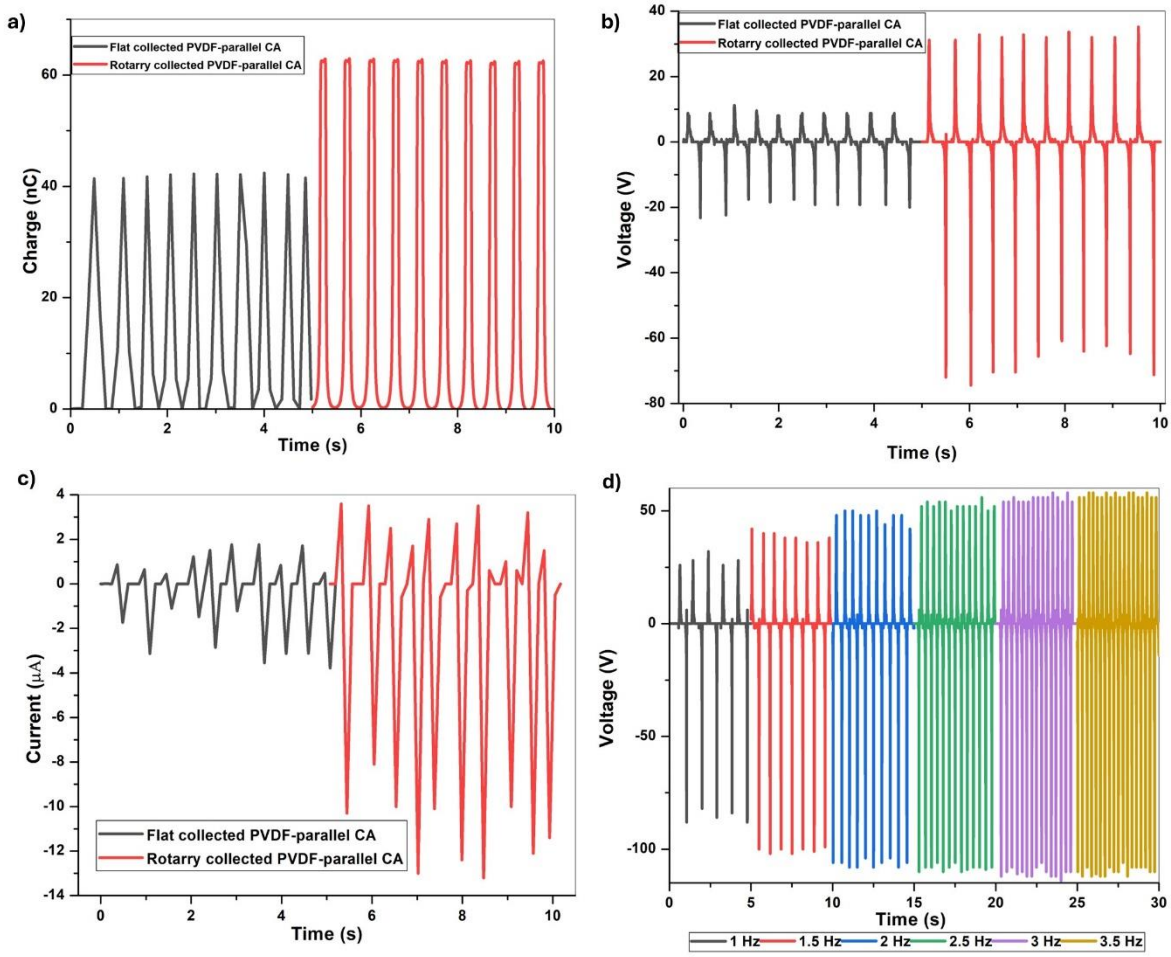


Figure 23: Triboelectric performance of CA and PVDF samples.

a) Change of charge, b) voltage and c) current performance for flat collected and rotary collected PVDF when contact separated with rotary collected CA, d) Voltage result at different frequencies for rotary collected CA-PVDF.

Additionally, the effect of contact-separation frequency on $V_{OC}$ was investigated under a constant contact force of 10 N. A clear trend of increasing $V_{OC}$ was observed with rising frequency, indicating a direct relationship between mechanical input rate and charge transfer efficiency. Specifically, $V_{OC}$ increased from 113.6 V at 1 Hz to 165.8 V at 3 Hz. Beyond 3 Hz, the $V_{OC}$ plateaued, with only marginal gains of 166.5 V at 3.5 Hz suggesting saturation in charge transfer due to limitations in effective contact time or material response. The measured $V_{OC}$ values across the tested frequencies were as follows: 1 Hz (113.6 V), 1.5 Hz (138.5 V), 2 Hz (154.0 V), 2.5 Hz (160.8 V), 3 Hz (165.8 V), and 3.5 Hz (166.5 V) (Figure

23d). These results confirm the frequency-dependent behaviour of the TENG and demonstrate the strong potential of rotary-collected CA paired with PVDF for high-performance energy harvesting applications. Due to the limitations of KickStart software and difficulty with manual contact separation mechanisms the frequency and amplitude dependence of $Q_{SC}$, $I_{SC}$, $V_{OC}$ and $J_{SC}$ was simulated with previously developed equations.

### 4.8. Theoretical modelling CA-PVDF.

Before proceeding with theoretical simulations with the DDEF model a few parameters need to be specified. These parameters are,

Assumed dielectric constant of PVDF = 10

Assumed dielectric constant of CA = 3.3

Measured thickness of the PVDF ~ 57 μm

Measured thickness of CA ~ 55 μm

Experimental charge density matched with DDEF prediction at $\sigma T$ =39.5 μC $m^{-2}$

After determining the parameters, the simulation was carried out using a python script as shown in Appendix C-F.

According to Figure 24a, a gradual increase in charge density was observed as the contact-separation frequency increased from 1 Hz to 3 Hz at a constant amplitude of 5 mm. Beyond 3 Hz, the charge density plateaued, indicating saturation in the charge transfer process. In Figure 24b, when the frequency was held constant at 2 Hz and the contact-separation amplitude was varied, the output increased steadily up to 5 mm, after which it remained relatively constant. Notably, the $I_{SC}$ increased significantly under both conditions when frequency was varied at constant amplitude and when amplitude was varied at constant frequency.

As shown in Figure 24c, simulation results for the CA–PVDF pair revealed that at 1 Hz the peak-to-peak $I_{SC}$ was approximately 2 μA, while at 5 Hz it increased to 12 μA. In comparison, when the amplitude was varied from 1 mm to 10 mm at a fixed frequency of 2 Hz, the $I_{SC}$ increased from 2 μA to 6 μA (Figure 24d). To generalize these trends, corresponding current density plots are presented in Figures 25e and 25f.

This behaviour can be attributed to the rate of charge transfer: at higher frequencies, the contact-separation cycles occur more rapidly, resulting in greater current generation due to increased charge transfer per unit time. Similarly, increasing the contact-separation amplitude leads to a larger physical displacement between the triboelectric layers, enhancing charge separation and thereby enabling more effective charge transfer. Moreover, greater amplitudes generate stronger electrostatic interactions, which enhance electrical induction between the triboelectric materials and the attached conductive electrodes, further contributing to the observed increase in output.

The open-circuit voltage remained nearly constant with increasing frequency under a fixed displacement condition (Figure 24g). However, experimental results showed a slight increase in voltage up to 2.5 Hz, after which it stabilized. This initial rise could be attributed to incomplete charge transfer or suboptimal dynamic contact quality at lower frequencies.

Additionally, it was observed that the $V_{OC}$ increased with higher amplitude of motion (Figure 24h). This can be explained by the greater mechanical energy input and increased separation distance, both of which enhance the surface charge density and the electrostatic potential difference, thereby contributing to a higher $V_{OC}$ output.

### 4.9. Mechanical and wearable characterization

In wearable applications, mechanical properties are critical to ensure both long-term durability and user comfort. To evaluate the suitability of the electrospun membranes for

such applications, a series of tests was conducted including contact angle measurements, tensile testing, and air permeability analysis.

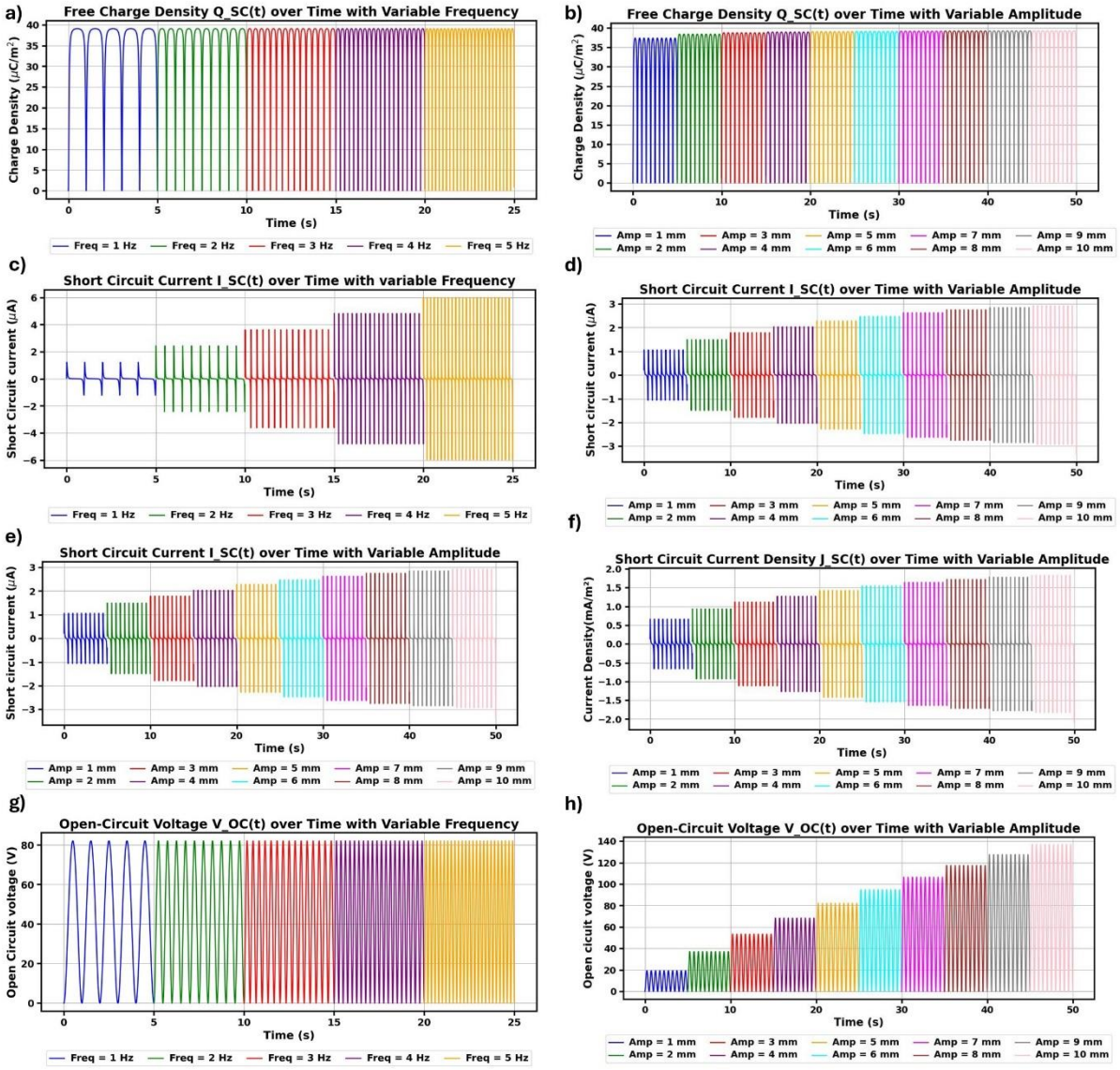


Figure 24: DDEF model simulated results for CA and PVDF.

Charge density changes with a) frequency and b) amplitude, Current density changes with c) frequency and d) amplitude, short circuit current changes with e) frequency and f) amplitude, Open circuit voltage changes with g) frequency and h) amplitude.

### 4.9.1. Contact angle measurement

According to Singh et al.[269] and Nie et al.[270] hydrophilic surfaces tend to absorb moisture from air forming a thin water layer that reduces the charge transfer, while hydrophobic

substrates are preferred for TENG applications as they prevent this moisture induced low charge retention issue. To assess the hydrophobicity of the fabricated membranes, which can influence triboelectric charge retention, static water contact angle measurements were performed using a First Ten Angstroms 200 contact angle goniometer. Prior to measurement, the electrospun membranes were carefully mounted on flat glass slides to minimize surface curvature and provide a stable measurement surface. The sessile drop method was employed, using an automated dosing system to dispense deionized water droplets at a flow rate of 4 μL/s. Contact angles were recorded immediately after droplet deposition to mitigate the effects of evaporation or absorption. The droplet baseline was manually adjusted, and the system's software calculated the contact angle using a non-spherical fitting model. To account for surface heterogeneity, multiple measurements were performed at different locations on each sample, and the average values were reported.

**Measured Static Contact Angles:**

CA membrane – 122.01° (Best triboelectric performance) (Figure 25a)

PVDF membrane – 106.02° (Best triboelectric performance) (Figure 25b)

Both materials exhibited contact angles greater than 90°, confirming their hydrophobic nature. This characteristic is beneficial for wearable triboelectric devices, as it supports effective charge retention, thereby improving the overall sensing performance during long-term use.

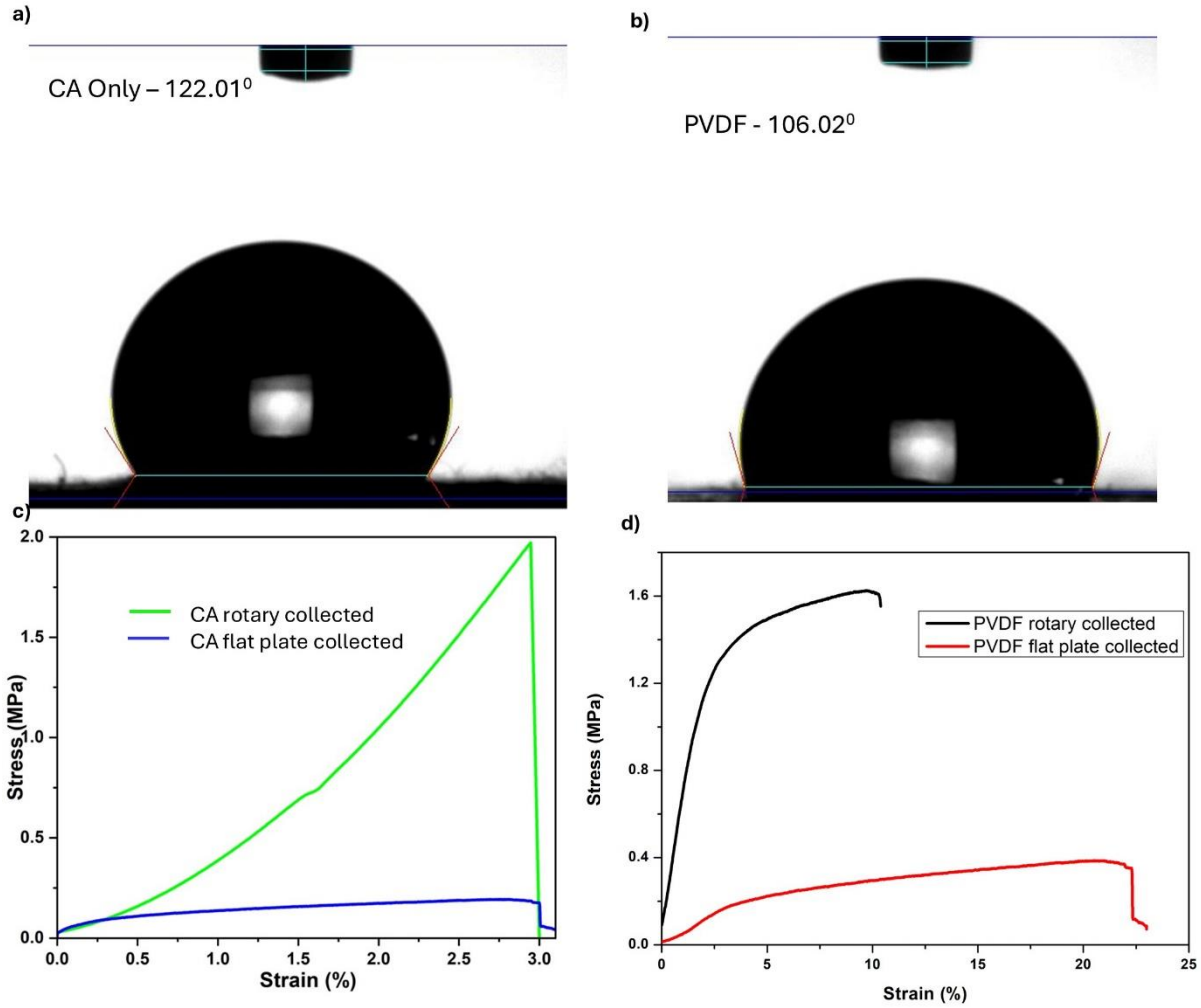


Figure 25: Contact angle and tensile results for CA and PVDF.

Contact angle results of a) CA, b) PVDF, Tensile results of c) CA, d) PVDF.

### 4.9.2. Tensile Properties

Tensile tests were conducted using a Zwick Z005 universal testing machine equipped with a 50 N load cell. The thickness of each sample was measured using a micrometre screw gauge, and the average of five measurements taken at different points was used to represent the sample thickness.

Samples were cut into strips with a length of 70 mm and width of 12.5 mm, with a gauge length set to 50 mm. To ensure secure gripping and minimize slippage during testing, sandpaper was affixed to the grips. An initial preload of 0.05 N was applied, and samples were stretched at a constant extension rate of 5 mm/min.

The test was terminated when the applied force reached 80% of the maximum force, to avoid excessive deformation that could affect repeatability and consistency across tests.

CA – Random (Maximum stress - 0.042 MPa, Maximum strain - 3.14 %), Parallel (Maximum stress -1.97 MPa, Maximum strain – 2.94 %) (Figure 25c)

PVDF - Random (Maximum stress - 0.53 MPa, Maximum strain - 23.5 %), Parallel (Maximum stress -1.815 MPa, Maximum strain – 13 %) (Figure 25d)

According to the results, CA exhibited an increase in maximum tensile stress with parallel fibre alignment compared to the random orientation. This improvement is attributed to the alignment of fibres and polymer chains along the rotation direction during electrospinning, which facilitates more efficient stress transfer and enhances mechanical strength. However, the maximum strain decreased slightly, likely because the aligned fibres restrict deformability due to a more uniform and constrained load distribution, leading to earlier structural stiffening. In contrast, the random arrangement contains longer fibres oriented in various directions, allowing them to reorient and extend during tensile loading, which contributes to higher strain.

Similarly, PVDF exhibited a significant increase in tensile stress under parallel alignment, indicating enhanced tensile strength resulting from improved molecular alignment and tighter chain packing. The exact mechanism applies as with PVDF aligned fibres limit the material's ability to elongate, whereas randomly oriented fibres can rearrange and slide, enabling greater deformation under load. As a result, while the aligned configuration enhances strength, it reduces the material's extensibility.

However, during triboelectric experiments, it was observed that CA tends to deteriorate more rapidly under repeated contact-separation cycles, likely due to its lower mechanical robustness and fatigue resistance. In contrast, PVDF retained its structural integrity over a

significantly higher number of cycles, demonstrating better durability and long-term performance in dynamic applications.

### 4.9.3. Air permeability

In addition to mechanical characterization, air permeability was characterized according to ISO 9237 using a TexTest air permeability tester. Samples with an area of 20 $cm^2$ were tested under a pressure differential of 100 Pa, and readings were directly obtained from the instrument. The results showed that CA (parallel) exhibited a significantly higher air permeability of 85.3 $m^2/s$, compared to PVDF (parallel), which recorded 40.3 $m^2/s$.

This could be attributed to the way fibres bond with each other during the electrospinning process. Due to the smaller fibre diameter as observed in SEM, CA likely forms a more porous and loosely packed fibre network. This could allow for higher air permeability, whereas PVDF forms denser, more compact structures, resulting in lower air permeability. Nevertheless, this open microstructure may contribute to its lower mechanical durability and faster degradation during triboelectric cycling, as previously observed. Conversely, PVDF's lower air permeability is indicative of a tighter fibre network, which aligns with its superior mechanical robustness and prolonged durability under dynamic triboelectric operation.

From a functional perspective, higher air permeability in CA may be advantageous for applications that require breathability or a faster response to environmental changes, such as wearable sensors, which will be considered in later parts of this thesis.

## 4.10. Sensitivity evaluation

The primary objective of this experiment was to develop and evaluate the performance of a pressure sensor based on a TENG architecture. A series of experiments was conducted to determine the voltage response to applied force.

Pressure was applied manually through tapping, and the corresponding applied force was measured using an IMADA DS2-50N digital force gauge. Initially, these experiments were carried out by manually tapping, and there were some discrepancies in maintaining the same force during the tapping. Nevertheless, measurements were systematically recorded for forces ranging from 1 N to 20 N, in 5 N intervals. The sensor's output voltage was captured for each force level and is presented in Figure 26a.

Sensor Output:

- At 1 N: Peak-to-peak voltage = 100.8 V (Vrms = 9.60 V)
- At 20 N: Maximum voltage = 416 V (Vrms = 23 V)

To assess the pressure sensitivity, 16 $cm^2$ samples were used, and the applied force values were converted to pressure (kPa). A linear regression model was used to evaluate the sensor's response, with results shown in Figure 26b.

Pressure Response Characteristics :

- Pressure range: 0.625–12.5 kPa
- Linear regression coefficient: $R^2 = 0.929$
- Sensitivity: 1.301 V/kPa

These findings demonstrate that, despite minor inconsistencies inherent in manual tapping, the TENG-based sensor exhibits a linear correlation between applied pressure and electrical output, confirming its potential as an effective pressure-sensing device. There are some deviations in the results, which will be addressed in the next chapter of this thesis.

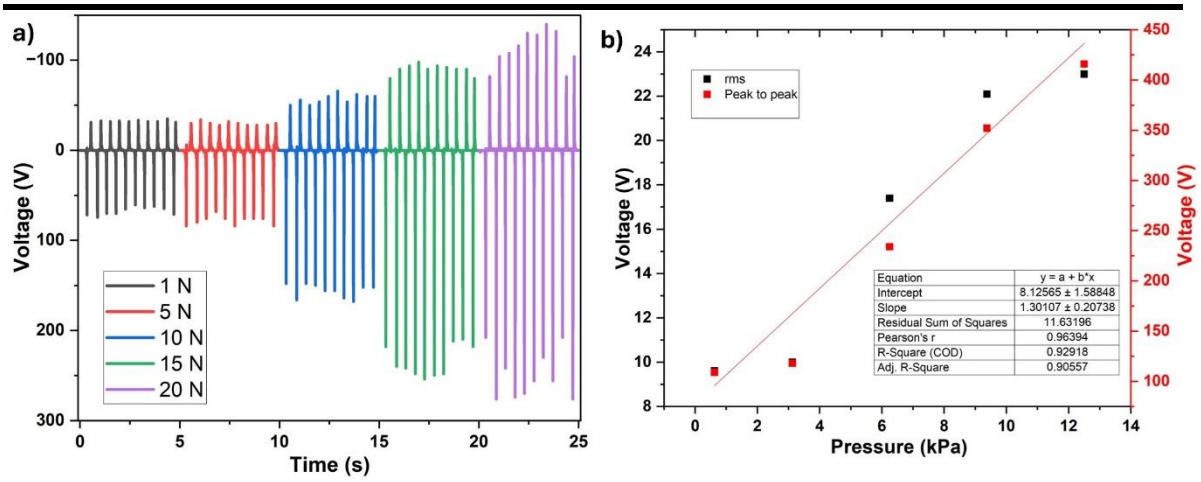


Figure 26: Sensitivity characterization of CA and PVDF samples.

a) voltage response with respect to force, b) linear regression analysis for voltage response with respect to pressure.

### 4.11. Application development

After developing the triboelectric layers, two prospective applications were tested. First, a mechanism was implemented to detect finger movement toward the palm, supporting future exosuit or rehabilitation applications involving finger flexion or hand grasp. In this setup, a CA layer was mounted on 3M 1182 conductive tape and attached to the palm section of a glove. To complete the TENG circuit, a PVDF layer was similarly mounted and placed on a corresponding finger of the same hand. When the finger made contact with the palm, a detectable electrical signal was observed using an oscilloscope. This demonstrated the potential of the system as a self-powered sensor for identifying open and closed states of a hand (Figure 27a).

The second application that was considered was for gait analysis. According to the literature, the average human walking and running speeds fall between 1 and 3 steps per second [262].Furthermore, the force acting on the foot drastically changes with the weight, size, and condition of the foot (flat or normal)[271]. Considering these factors, a foot plantar pressure

measurement system was developed utilizing the fabricated TENG-based sensors. PVDF materials were attached to the sole of the shoe, while CA samples were mounted onto a separate PET sheet. Conductive copper tape was used to create electrical pathways on both the sole and the PET sheet, as illustrated in Figure 27b. To enable effective operation of the TENG in contact–separation mode, a foam layer was introduced between the sole and the PET sheet to maintain a controllable gap. This structure allows the CA and PVDF layers to come into and out of contact during foot strikes, thereby generating measurable triboelectric signals.

The detection of signals was acquired using an Arduino Uno microcontroller, programmed using the Arduino IDE, and integrated with a Processing-based graphical user interface. The TENG sensor detects foot pressure at specific locations and generates an AC signal in response to it. This AC signal is rectified into DC using a 26MB6A full-bridge rectifier. The resulting DC voltage is then read via the Arduino's analog input pin. Depending on the magnitude of the signal, the Processing code dynamically changes the colour of a simulated foot graphic on the desktop from red (no pressure) to green (pressure detected), visually indicating the location and intensity of the footfall (Figure 27c). Relevant codes are provided in Appendix G and H.

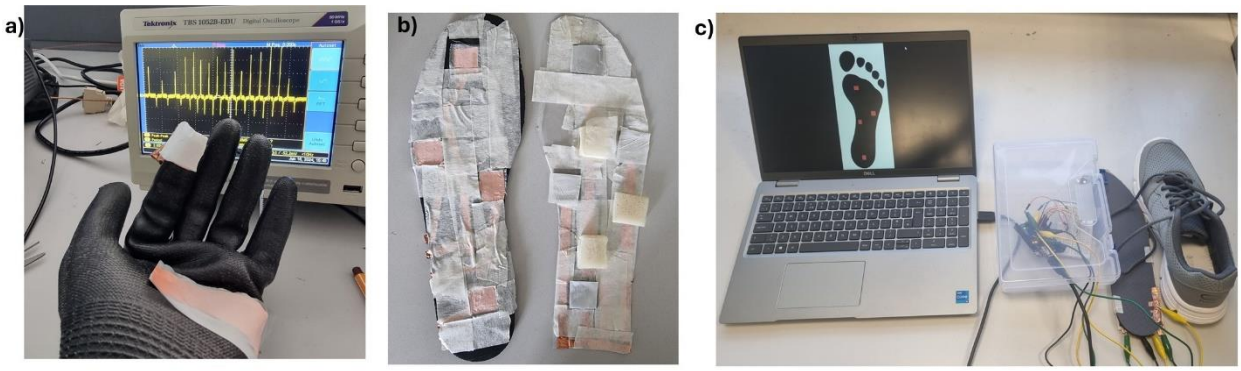


Figure 27: Application development with CA and PVDF TENG device.

a) self-powered sensor for identifying open and closed states of a hand, b) TENG sensors attached to the sole of the show and PET sheet c) Complete setup for detecting foot plantar pressure with developed TENG sensor.

## 4.12. Learning outcomes

In this chapter, the feasibility of improving TENG performance was explored by substituting PCL with PVDF while retaining CA as the tribopositive material. Several key outcomes were identified.

**Optimization of Electrospun Fibre Morphology:** Through controlled electrospinning conditions and the use of a rotary collector, both CA and PVDF nanofibres demonstrated enhanced alignment, smoother surfaces, and reduced defects. For PVDF, these conditions promoted an increase in β-phase crystallinity, which is directly correlated with improved piezoelectric and triboelectric properties as outlined in previous literature.

**Advancement in Material Selection:** The experimental results confirmed that pairing CA with PVDF produced comparatively higher $V_{OC}$ (100 V), $I_{SC}$ (13 μA) and Charge compared to the previously tested CA/PCL system. Frequency and amplitude dependent studies further confirmed that higher input dynamics directly enhance triboelectric generation. This validates the hypothesis that the contrasting triboelectric tendencies of CA (tribopositive) and PVDF (tribonegative) create a more efficient charge transfer interface.

**Modelling Validation of Device Behaviour:** The DDEF model was successfully applied to simulate device behaviour under varying frequencies and amplitudes. Simulation outputs showed strong consistency with experimental data, supporting the reliability of this theoretical framework for predicting triboelectric performance in CA/PVDF systems.

**Mechanical and Wearability Insights:** Mechanical testing revealed that aligned fibre mats improved tensile strength but reduced elasticity, underscoring the trade-off between

durability and flexibility in wearable applications. Both CA and PVDF exhibited hydrophobicity (contact angles >100°), favouring long-term charge retention. Additionally, CA demonstrated superior breathability, but lower mechanical robustness compared to PVDF, highlighting complementary roles when integrated into wearable platforms.

**Pressure Sensing Capability:** The CA/PVDF TENG device exhibited a strong linear relationship between applied pressure and voltage output, with a sensitivity of 1.301 V/kPa ($R^2 \approx 0.93$) over the range of 0.625–12.5 kPa. This validates its suitability for pressure-sensing applications relevant to human–machine interaction and wearable electronics.

**Application Demonstrations:** Proof-of-concept prototypes confirmed practical utility. A glove-mounted sensor successfully detected finger bending motions, while a shoe-integrated sensor enabled plantar pressure mapping with real-time visualization using Arduino and Processing software. These demonstrations illustrate the potential of CA/PVDF devices in both rehabilitation and gait monitoring applications.

**Challenges and Future Directions:** The study identified limitations with manual tapping methods, which introduced variability in input force and frequency, suggesting the need for more precise mechanical excitation in future testing. Furthermore, long-term durability, fatigue resistance, and the incorporation of advanced surface modification strategies remain crucial areas for future development. Also, the low force sensitivity needs to be improved to use the sensor for low force detection which could be crucial in JBM monitoring.

# CHAPTER 5

## 5. TRIBOELECTRIC PERFORMANCE ANALYSIS OF ELECTROSPUN SILVER NANOPARTICLES DOPED CA AND PVDF MICRO-NANO FIBRES

**Publication status: Published as Journal paper**

**Part of this chapter is published as a journal paper in Wiley Small Journal**

Innovative Self-Powered Sensing: Potential of Fabrigami and Electrospun Nanofibre-Based Triboelectric Nanogenerator for Joint Biomechanics Monitoring", by K. R. Sanjaya D. Gunawardhana*, Zhou Fang, Garrett B. McGuinness, Luz Alejandra Magre Colorado, Sonal Santosh Baberwal, Waseem Ahmad Wani, Brian J. Rodriguez, Robert O'Connor, Ciara Smullen, Tomás E. Ward, Shirley M. Coyle*

# CHAPTER 5

The findings from Chapter 4 demonstrated that replacing PCL with PVDF, in combination with CA, significantly enhanced triboelectric performance and yielded higher outputs. However, the results also revealed some key challenges that limit the broader application of this system in wearable sensing.

Firstly, the sensitivity of the sensor is still below expectations compared with the published papers in the literature. It is important to improve the sensitivity factor as the final goal is to use this as a sensor for JBM. Secondly, the limitation of manual tapping-based characterization and the low-speed data recording with the Keithley kickstart software needs to be resolved.

To address these challenges, the next chapter explores the incorporation of silver nanoparticles (AgNPs) into CA electrospun fibres. This approach is motivated by the dual potential of AgNPs to enhance charge density and triboelectric output by introducing localized charge trapping sites. Furthermore, improvement in the mechanical integrity of CA was observed by reinforcing the fibre network. Importantly, this strategy retains CA as the primary biodegradable component, offering a path to balance sustainability with improved functional performance. Also, a proper TENG characterization rig was introduced with a high-speed data capturing system with a Keithley 6517B to more precisely characterize our samples. This has proven that outputs can be reproducible for commercial applications in the future.

## 5.1. Introduction

The incorporation of PVDF in Chapter 4 demonstrated significant improvements in triboelectric performance compared with the CA/PCL system. CA offers a biodegradable and widely available alternative, but its intrinsic limitations in charge density and mechanical stability constrain its standalone performance in TENGs. It is vital to optimize the

performance of the CA layer to improve the sensitivity further while retaining the biodegradability aspect.

To enhance the functionality of CA, recent studies have explored the incorporation of nanomaterials into its electrospun fibres. Bai *et al.* demonstrated that CA modified with carbon nanotubes could substantially improve sensitivity in TENG configurations with PVDF, highlighting the potential of filler incorporation to overcome CA's baseline weaknesses [272]. Among different modifiers, AgNPs are particularly promising due to their dual role in changing electrospinning dynamics favourably and contributing to sensitivity and energy harvesting enhancement. AgNPs increase precursor solution conductivity, which promotes the formation of finer, more uniform fibres, while simultaneously introducing localized charge-trapping sites that can enhance triboelectric charge density. Moreover, their presence within the fibre network can improve mechanical properties, a critical factor for wearable device durability.

## 5.2. Hypothesis

A TENG constructed using AgNPs doped CA and PVDF will generate a higher and sustainable triboelectric output than pristine CA/PVDF combination due to their opposite charge transfer tendencies. Furthermore, the doping of Ag nanoparticles will increase precursor solution conductivity, promote finer fibre formation, and introduce localized charge-trapping sites. This could potentially deliver higher output sufficient to use with modern electronic components to develop self-powered sustainable sensor.

## 5.3. Material fabrication and characterization

### 5.3.1. Ag-cellulose acetate electrospinning

CA with MW 30 000 (Sigma-Aldrich®, 180955) and Ag nanoparticles ink (50 wt.%, dispersion in tripropylene glycol monomethyl ether, Sigma-Aldrich®, 796042) were used to

prepare Ag-doped CA (Ag-CA) precursor. 20 wt.% CA was mixed in DMF: Acetone (2:3) solution and magnetically stirred for 4 hours at room temperature. A series of solutions (0%, 0.5%, 1%, 1.5%, 2%, 2.5% Ag wt./wt. in CA precursor) were prepared to add Ag nanoparticle solution and stirred for 1 hr for a homogenous solution.

The precursor was loaded into a 5 ml syringe with a 21G blunt needle, and electrospinning was carried out with a flow rate of 2 ml $h^{-1}$, TCD of 15 cm and applied voltage of 15 kV. The fibres were collected on a rotating drum collector operated at 1500 rpm, yielding uniform nonwoven fibrous mats. There was no additional process to control the humidity or temperature, and all samples were prepared at 20±4 $^0$C and relative humidity of 50±10%. Ag in CA mat was collected onto Aluminium foil and dried at room temperature for 48 hrs. After that, samples were further dried in an oven at 50 $^0$C for a 4-hour period.

The PVDF sample was prepared as discussed in the previous chapter.

### 5.3.2. SEM and EDS analysis of Ag-CA and PVDF nanofibres.

The morphological analysis of electrospun nanofibres is critical for evaluating surface area and structural features, both of which play a pivotal role in the output performance of TENGs. In this study, the morphology of the developed fibrous layers was examined using an EVO LS15 (Zeiss) SEM, while a Hitachi S-500 field emission SEM (FE-SEM) was employed to capture high-resolution images and energy-dispersive X-ray spectroscopy (EDS) analysis of individual fibres.

Representative SEM images of pure CA, 1.5% Ag-CA, and 2.5% Ag-CA are shown in Figure 28a (i–iii). Bead-free fibres were successfully obtained through optimized electrospinning parameters, as discussed in the previous chapter. Fibre and nanoparticle diameters were measured using ImageJ software, and the averages were calculated from ~60 data points. The distributions are shown as frequency histograms in Figure 28b, and e. Standalone Ag nanoparticles exhibited an average diameter of 53.98 ± 2.47 nm (Figure 28b i, ii) and were

randomly distributed within the CA matrix. High-magnification images further confirmed the dispersion of Ag nanoparticles within the fibres, with Figure 28c corresponding to 1.5% Ag-CA and Figure 28d to 2% Ag-CA. As the Ag doping level increased from 1.5% to 2%, a denser distribution of nanoparticles was observed throughout the fibrous structure.

The effect of Ag concentration on fibre diameter is summarized in the distribution graphs presented in Figure 28e(i-iii). Incorporation of 1.5% Ag into pure CA did not significantly alter the average fibre diameter (pure CA: 515 ± 9.39 nm; 1.5% Ag-CA: 516 ± 5.41 nm). However, further increasing the concentration to 2.5% Ag resulted in a notable reduction to 415 ± 6.61 nm. Similar trends have been reported in the literature. For instance, Son et al.[273] And Tarus et al.[274] observed systematic reductions in fibre diameter upon Ag nanoparticle doping in CA systems. According to Son et al., the addition of Ag nanoparticles increases the electrical conductivity of the electrospinning precursor solution [273]. The resulting enhancement of electrostatic repulsion and Coulombic forces at the needle tip promotes greater jet stretching and stabilizes the Taylor cone, ultimately producing finer fibres. Our findings are therefore in agreement with these studies, confirming that Ag nanoparticle incorporation effectively modulates fibre morphology by altering the electrospinning dynamics.

The improvement of the PVDF electrospinning process has been previously discussed. The SEM image in Figure 28f depicts the morphology of the electrospun PVDF sample, revealing the formation of a well-defined fibrous mat with a porous structure. The fibres exhibit an average diameter of 1.741 ± 0.103 μm, with the overall structure appearing stable and with minimal bead formation.

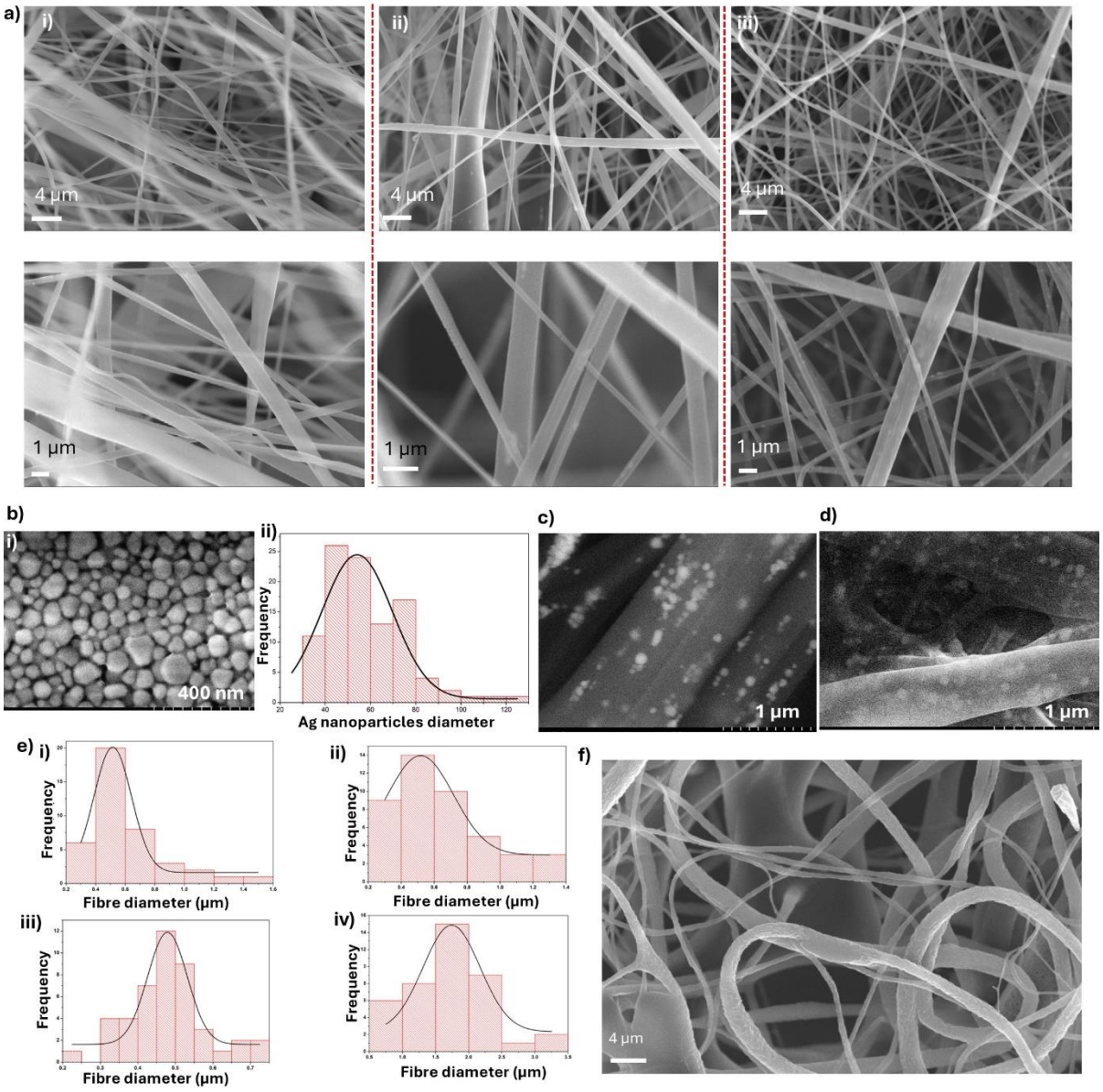


Figure 28: Material characterisation of Ag-CA and PVDF samples.

a) SEM images of electrospun pristine CA (i), Ag 1.5% in CA (ii), and Ag 2.5% in CA (iii). b) (i)SEM image of Ag nanoparticles and (ii)diameter distribution table, high magnification image of electrospun c)Ag-CA 1.5% and d) Ag-CA 2%, e) Diameter distribution graphs of electrospun (i) CA, (ii) Ag-CA 1.5%, (iii) Ag-CA 2.5% and (iv) PVDF sample, f) SEM image of PVDF electrospun sample reprinted from ref [1] published with CC BY Copyright©2025, The Authors.

In addition to the morphological analysis to observe the incorporation of Ag nanoparticles EDS analysis was performed to confirm the distribution and the presence of Ag nanoparticles on the surface of the electrospun CA.

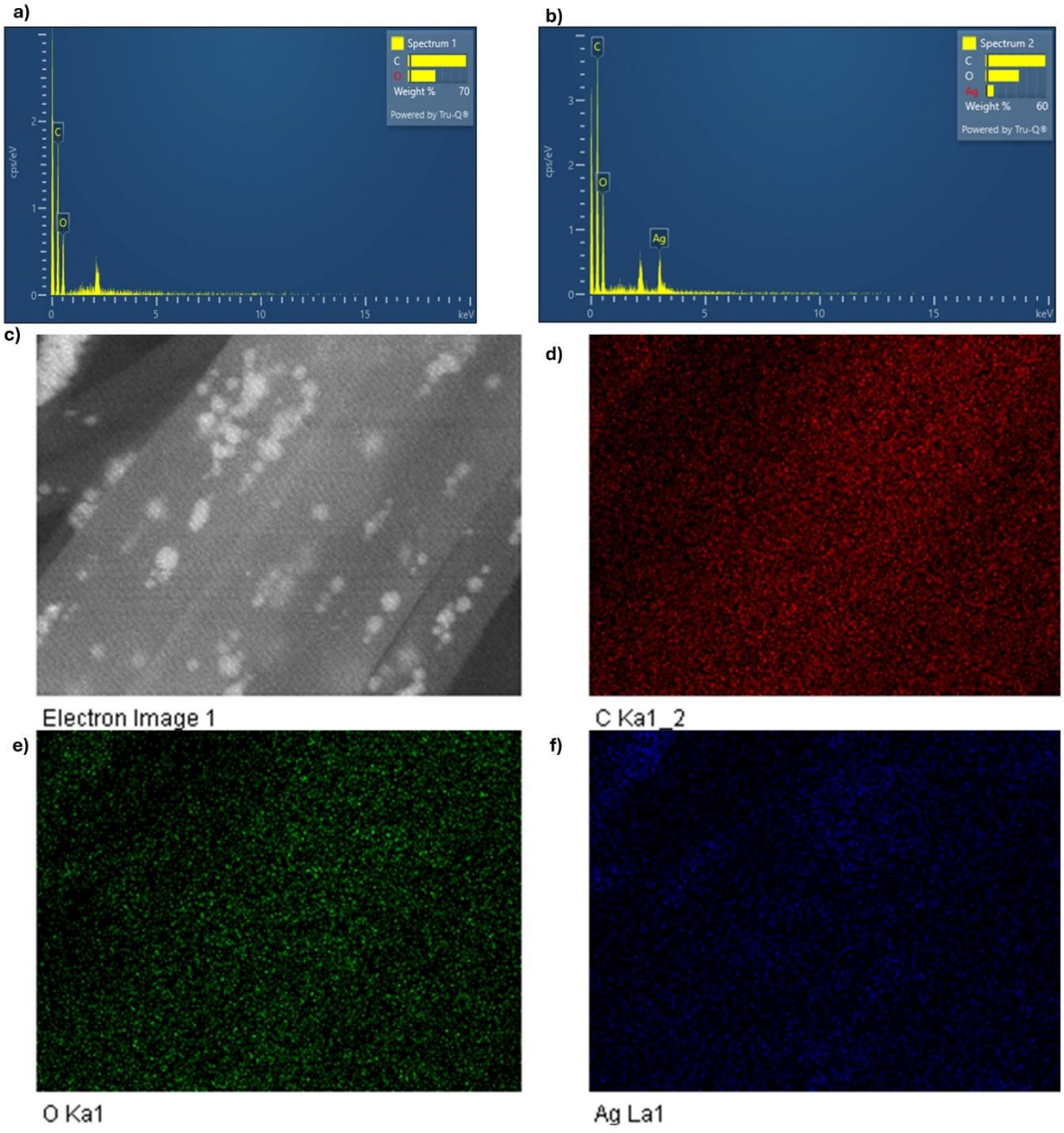


Figure 29: EDS analysis of Ag-CA samples.

EDS map of a)electrospun CA, b) Ag-CA 1.5%, c) High magnification image of Ag-CA 1.5% used for EDS colour mapping. EDS colour maps for d) Carbon (CKa1_2) , e)Oxygen (O Ka1) and Silver (Ag La1) reprinted from ref [1] published with CC BY Copyright©2025, The Authors.

Figures 29a and 29b present the EDS spectra of Pure CA and 1.5% Ag-CA samples, respectively. In 1.5% Ag loaded sample corresponding peak for Ag (Ag Lα at 3.0 keV) was observed, thereby confirming the presence of Ag nanoparticles within the fibrous matrix. Compared with pristine CA, which primarily exhibited signals from carbon (C) and oxygen (O), the Ag-doped samples displayed additional peaks that verified the successful integration of Ag.

Elemental mapping further substantiated these findings. As shown in Figures 29c–f, the spatial distribution maps highlight the random presence of Ag throughout the CA fibres, alongside the expected C and O signals from the CA backbone. The dispersion of Ag is particularly important, as seen in high-magnification images where increased concentration enhanced the distribution, potentially increasing the surface conductivity.

Figure 30 presents the EDS elemental maps of the electrospun PVDF fibres. The color-coded distribution clearly confirms the uniform presence of Fluorine (F) throughout the fibrous network, consistent with the expected chemical composition of PVDF. This uniform elemental distribution further indicates that the electrospinning process produced homogeneous fibres without phase separation or local compositional defects.

To further investigate the chemical and structural effects of Ag incorporation into CA, FTIR and XRD analyses were performed.

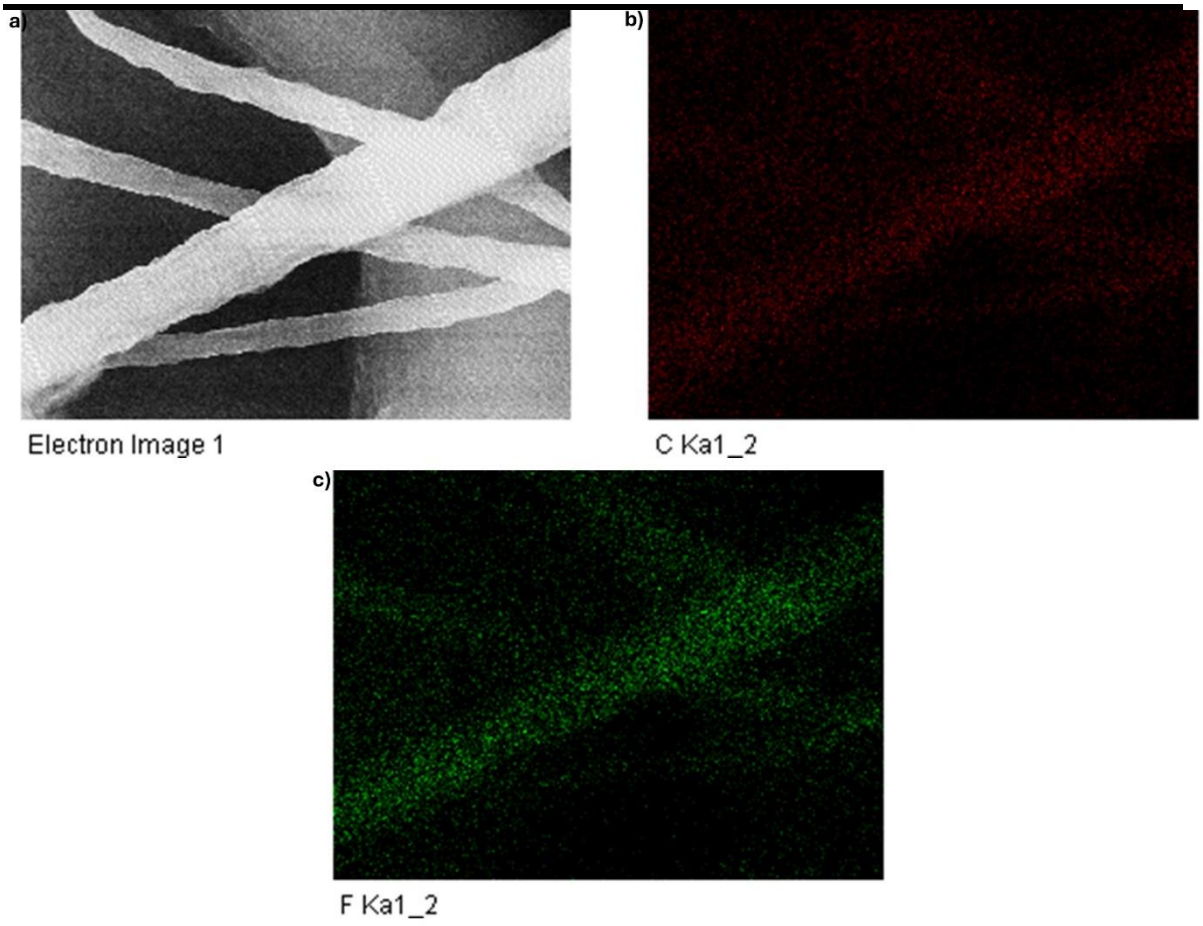


Figure 30: EDS colour maps of PVDF samples.

a) High magnification image of PVDF used for EDS mapping., EDS colour maps of b) Carbon (Ka1_2) and c) Fluorine (F Ka1_2) reprinted from ref [1] published with CC BY Copyright©2025, The Authors.

### 5.3.3. FTIR Analysis of Ag-Ca and PVDF

FTIR was carried out using PerkinElmer Spectrum two FT-IR. The FTIR spectra of pure CA and Ag-doped CA are shown in Figure 31a. No significant differences were observed between the spectra of pristine CA and those of Ag-CA samples. The absence of new absorption bands or noticeable peak shifts suggests that Ag nanoparticles do not chemically interact with the functional groups of CA. In particular, the characteristic CA peaks corresponding to C=O stretching (~1739 $cm^{-1}$), C-$CH_3$ stretching (1375 $cm^{-1}$) and C-O-C stretching (1235 $cm^{-1}$) is clearly visible with all samples [251,275]. Furthermore, the small O–

H stretching (3400-3500 $cm^{-1}$) remained unchanged shows that majority of the fibres are still in acetyl state [251,275]. This indicates that Ag is not covalently bonded or strongly complexed with the polymer chains but instead is physically embedded and dispersed within the matrix.

For completeness, FTIR analysis was also performed on PVDF (Figure 31b), which had not been presented in Chapter 4. PVDF materials are known to exhibit various crystalline phases, with the polarisation properties primarily attributed to the high content of the β phase. Previous studies, such as the work by Singh et al., have demonstrated that optimising electrospinning parameters can significantly enhance the β phase content in PVDF nanofibres.[276] Building on these findings, the electrospinning parameters were selected and adjusted to align with the constraints of our setup. As shown in Figure 31b, the formation of the β phase is evident, which was quantified using the Lambert-Beer law.

Beer–Lambert law to calculate the β phase of PVDF electrospun layer is provided in E15[277].

$$F(\beta) = \frac{A_\beta}{\left(\frac{K_\beta}{K_\alpha}\right)A_\alpha + A_\beta} \qquad \text{(E15)}$$

Where $K_\beta = 7.7 \times 10^4$ and $K_\alpha = 6.1 \times 10^4$ for coefficient of absorbance at 840 $cm^{-1}$ and 762 $cm^{-1}$, respectively. $A_\beta$ and $A_\alpha$ Using the FTIR absorption results F(β) can be calculated.

| | |
|---|---|
| $A_\beta$ | 0.071 |
| $A_\alpha$ | 0.018 |

Using these parameters final value calculated F(β) = 75.75 %

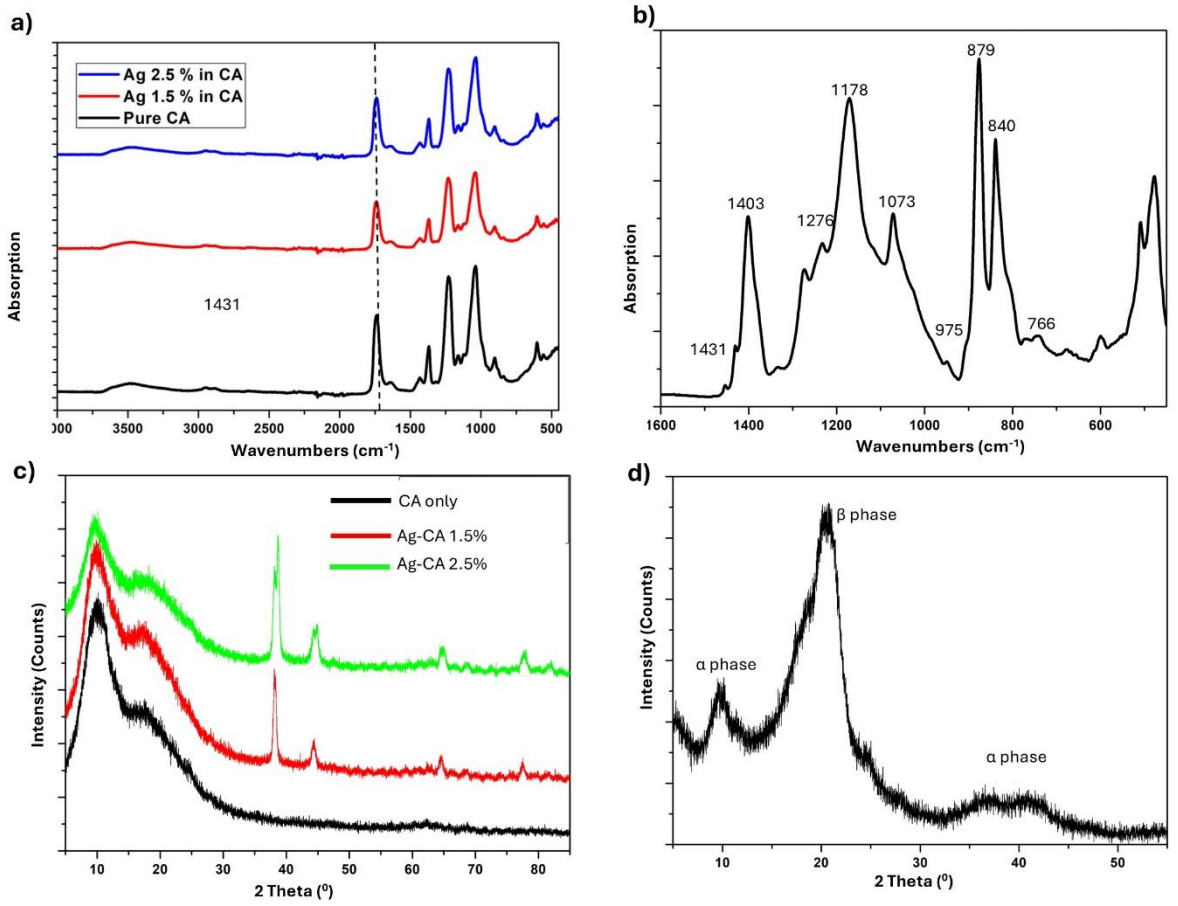


Figure 31: FTIR and XRD analysis pf Ag-CA and PVDF samples.

FTIR analysis of a)Ag-CA and b) PVDF., XRD analysis of c) Ag-CA and d) PVDF. reprinted from ref [1] published with CC BY Copyright©2025, The Authors.

By calculating the absorbance at 766 $cm^{-1}$ (Aα) and 840 $cm^{-1}$ (Aβ), the β phase fraction was determined to be 75.75%. This relatively high fraction confirms that electrospinning effectively promotes β-phase crystallization in PVDF, consistent with earlier reports[276]. The enhancement arises from the strong elongational forces and rapid solvent evaporation during electrospinning, which favour dipole alignment and β-phase stabilization reprinted from ref [1] published with CC BY Copyright©2025, The Authors.

### 5.3.4. XRD analysis of Ag-CA and PVDF

XRD was carried out with Bruker D5000 with Cu Kα radiation (λ = 1.54 $A^0$) source. The XRD analysis shown in Figure 31c reveals a clear difference in patterns between pure CA

and Ag-CA. The XRD patterns of pristine CA show the characteristic two humps centred at $\sim 2\theta = 12^0$ and $18^0$, indicative of its predominantly amorphous structure[278]. Upon silver incorporation, this amorphous profile remains, but additional sharp diffraction peaks appear at $2\theta \approx 38.2^0$, $44.5^0$, $64.8^0$, and $77.4^0$, which correspond to the (111), (200), (220), and (311) planes of face-centred cubic (fcc) metallic Ag (JCPDS No. 04-0783)[279]. The intensity of these Ag peaks increases systematically with Ag loading (1.5% → 2.5% wt.), consistent with higher nanoparticle content and corroborated by SEM/EDS mapping. While CA's amorphous phase is not converted to a crystalline phase, the incorporation of crystalline Ag NPs modifies the composite's overall diffraction profile, reflecting the dual-phase (amorphous CA + crystalline Ag) nature of the material. While FTIR results indicate that Ag does not chemically modify CA, the XRD data imply that Ag influences the physical structure and crystallinity of the material, potentially enhancing properties such as conductivity or mechanical strength in the Ag-doped samples.

Pristine PVDF typically displays diffraction peaks corresponding to both α and β phases; however, in the electrospun fibres examined here (Figure 31d), strong diffraction peaks were observed at $2\theta \approx 20.6°$, characteristic of the (110)/(200) planes of the β phase[280]. The dominance of this peak, together with the relatively weak α-phase signals, confirms the significant presence of β-phase crystallites within the fibrous mat.

These findings are in line with previous studies where electrospinning has been shown to drive β-phase crystallization, even in the absence of additional fillers or post-processing treatments. While the incorporation of nanoparticles such as LiCl, CNTs, $BaTiO_3$, or graphene has been reported to further enhance β-phase content by acting as nucleating agents [281,282], in this study pristine electrospun PVDF was deliberately used as the baseline tribonegative layer. This choice allows for a direct assessment of the performance of the Ag-CA/PVDF system without the influence of additional fillers, thereby isolating the contribution of the Ag-doped CA mat.

### 5.3.5. XPS analysis of Ag-CA

To investigate the surface chemistry of Ag and its bonding state with CA, X-ray Photoelectron Spectroscopy (XPS) analysis was conducted and provided in Figure 32. The analysis was performed on a Scienta Omicron XPS system with Argus CU multiplate detector and a monochromated Al K-alpha x-ray source with an excitation energy of 1486.6 eV. Due to charging during scanning because of the insulating nature of the CA samples, all spectra were shifted such that the maximum intensity of the C-C component of the C1s peak appeared at 284.5 eV.

No Ag signal was detected for samples with Ag loading below 2.5%, which is likely due to the detection limit of the XPS instrument. For the 2.5% Ag-loaded sample, although the signal-to-noise ratio was low reflecting the proximity of Ag content to the XPS detection limit the Ag $3d_{5/2}$ (~375 eV) and Ag $3d_{3/2}$ (~369 eV) peaks exhibited two components. These indicate that the silver at the surface is predominantly in an oxidised state (binding energy ~369 eV), with some metallic contribution (~366 eV)[283]. The C 1s spectra were broad in all cases, revealing components corresponding to C–C/C–H bonds at 284.5 eV, C–O bonds at 286 eV, and a shoulder at ~289 eV attributed to C=O functionalities[284,285]. These findings indicate that Ag nanoparticles are primarily present as physically embedded fillers within the CA matrix, with limited exposure at the fibre surface and no evidence of covalent bonding.

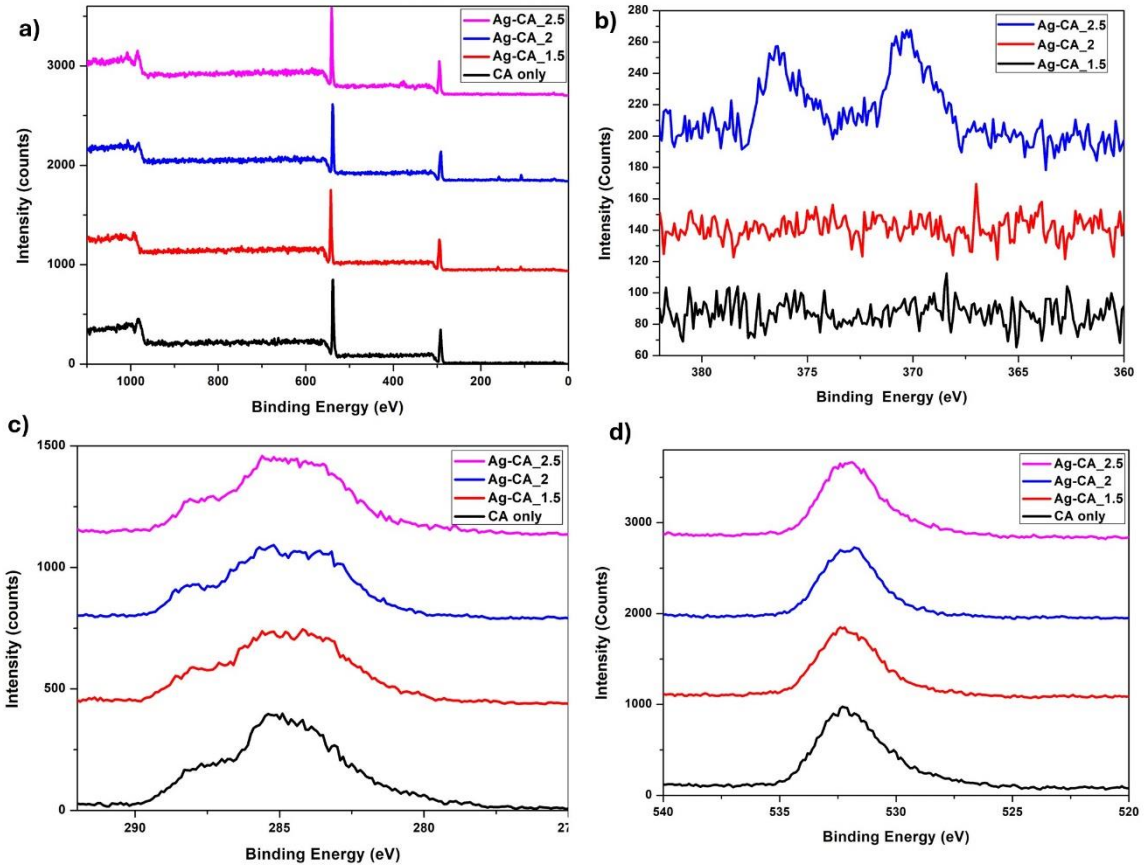


Figure 32: XPS analysis on Ag-CA samples

a) Survey scan, b) Ag 3d scan, c) C 1s scan and d) O 1s scan reprinted from ref[1] published with CC BY Copyright©2025, The Authors.

### 5.3.6. Kelvin probe force microscopy on Ag-CA samples

Kelvin Probe Force Microscopy (KPFM) measurements were conducted using an MFP-3D atomic force microscope (Oxford Instruments) with conductive PPP-EFM probes (Nanosensors) having an approximate tip radius of 20 nm and a resonance frequency of 75 kHz. KPFM was carried out in lift mode, whereby the topography was first recorded in amplitude modulation mode, followed by lifting the tip by 50 nm to measure the contact potential difference (CPD). KPFM operates through a feedback mechanism, whereby an external bias is applied to minimize the CPD between the tip and the sample during the lift pass. The tip calibration was carried out using a standard aluminium and gold sample (Bruker). To ensure the tip did not deteriorate, the standard sample was measured both before

and after the actual sample measurements. All KPFM measurements were recorded under normal ambient conditions.

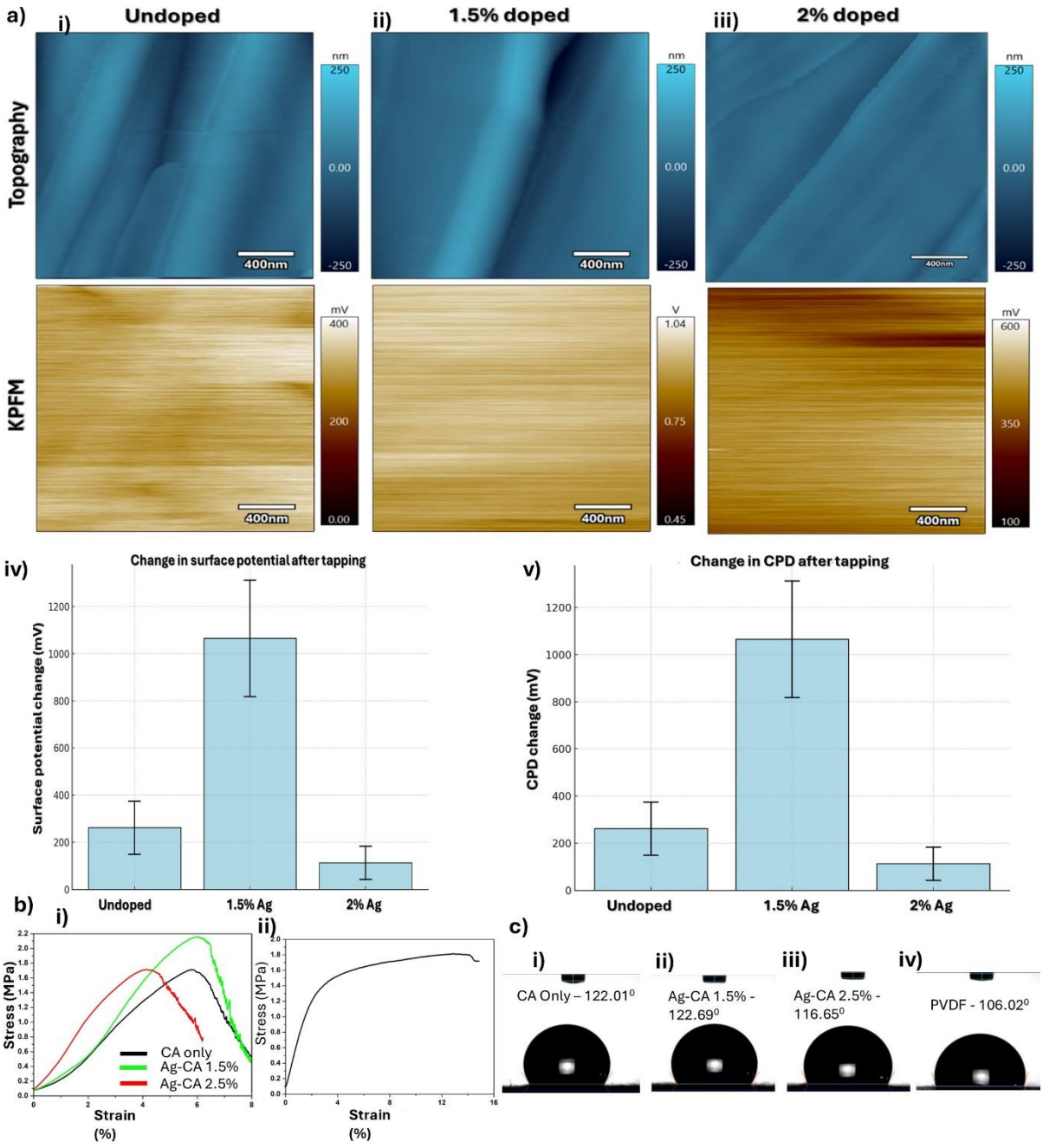


Figure 33: KPFM analysis, tensile studies and Contact angle analysis of Ag-CA and PVDF samples.

a) KPFM analysis results of i)CA only, ii) 1.5% Ag in CA and iii) 2% Ag in CA, and change in iv) Surface potential and v) CPD after tapping with PVDF sample., b) Tensile characteristics of i)Ag-CA sample and ii) PVDF, c) Contact angle analysis of i) CA only, ii)

Ag-CA 1.5%, iii) Ag-CA 2.5% and iv) PVDF samples reprinted from ref [1] published with CC BY Copyright©2025, The Authors.

Figure 33a (i-iii) shows the topography and the CPD value of the undoped, 1.5% Ag-doped, and 2% Ag-doped samples. Although the topography appears to be quite similar between samples, their CPD values showed significant differences. For the undoped sample, the CPD of the fibre was measured to be 423 ± 46 mV. In contrast, the 1.5% Ag-doped sample exhibited a significantly higher CPD of 856 ± 102 mV.

To get further insights about the influence of Ag doping on the triboelectric effect, the samples were manually tapped with PVDF, and then KPFM measurements were retaken. The variations in CPD after tapping are presented in Figure 33 a(iv,v). Interestingly, after tapping, the 1.5% Ag-doped sample showed the highest CPD, whereas the CPDs of the undoped and 2% Ag-doped samples remained within the standard deviation after tapping. This trend aligns well with the results obtained from bulk triboelectric measurements. However, after tapping, the surface charge was observed to decay rapidly over time, with a decay of more than 70% in 24 minutes. This suggests that although doping enhances the initial surface potential, long-term stability of the generated charge remains a challenge.

Based on KPFM results and high-magnification SEM/EDS imaging, the behaviour at and above 2.0 wt.% Ag is interpreted as approaching the percolation threshold of Ag within the CA matrix. Ag nanoparticle doping is expected to increase the effective permittivity of the composite due to enhanced interfacial polarization (Maxwell–Wagner–Sillars) effects,[286] which can improve surface charge storage under contact electrification. However, beyond a certain loading threshold, the formation of conductive pathways may result in increased leakage current and dielectric loss, as predicted by percolation theory which reduces effective dielectric response and triboelectric output. Similar behaviour has been observed in silver–cellulose composites: for example, a cellulose nanofibril sponge with only ~0.1 vol

% Ag nanowires exhibits percolation-driven electrical conductivity of ~1.5 S/cm[287] , supporting our interpretation that the ~2 wt. % Ag content in our CA fibres (~0.2–0.3 vol%) approaches a percolation threshold that reduces effective dielectric and triboelectric performance. Although percolation thresholds depend on filler shape and dispersion Ag nanowires can percolate at lower vol% than spherical nanoparticles This correlates with our observed decrease in open-circuit voltage and transferred charge at higher Ag concentrations (2%>) (Section 5.4.), suggesting that the percolation threshold may have been approached.

### 5.3.7. Mechanical property characterization

The tensile properties of electrospun samples were characterised by a Zwick Z005 tensile tester, and the wetting angle was analysed using the FTA200 dynamic contact angle analyser. All testing procedures are same as discussed in Chapter 4 section 4.9.

The mechanical properties of pristine CA and CA with 1.5% and 2.5% Ag are characterised in Figure 33b. An initial increase in maximum tensile stress is observed in 1.5% Ag-CA than pristine, reaching 2.104 MPa at 6.3% strain,[288] likely due to the formation of smoother, more directional fibres with the incorporation of Ag nanoparticles. However, as the Ag content increases, the maximum tensile stress decreases to 1.633 MPa at 4.2% strain. This reduction in mechanical strength can be attributed to the agglomeration of Ag nanoparticles at higher concentrations, which disrupts the uniformity of the fibre structure, leading to stress concentration points and a subsequent decrease in tensile strength. In contrast, the PVDF sample exhibits a maximum tensile strength of 1.815 MPa at approximately 13% strain. The contact angle measurements (Figure 33c) for pristine CA, 1.5%, and 2.5% Ag-CA were determined to be 122.01°, 122.69°, and 116.65°, respectively. Pristine CA exhibits a high contact angle of 122.01°, reflecting its inherently hydrophobic surface. Upon the incorporation of 1.5% Ag nanoparticles, a slight increase in the contact angle to 122.69° is

observed. However, further increasing the Ag concentration to 2.5% results in a decrease in the contact angle to 116.65°, indicating a reduction in hydrophobicity.

### 5.4. TENG Energy harvesting and self-powered sensing characterisation

The contact and separation between CA and PVDF result in CA acquiring a positive charge and PVDF a negative charge, driving electron flow between the attached electrodes and generating an alternating current. In the triboelectric series, Ag is positioned towards the negative side, and with the presence of Ag in the composite, the triboelectric contrast between Ag-CA and PVDF will decrease because the composite becomes more negative due to the influence of Ag.

#### 5.4.1. New testing mechanism development

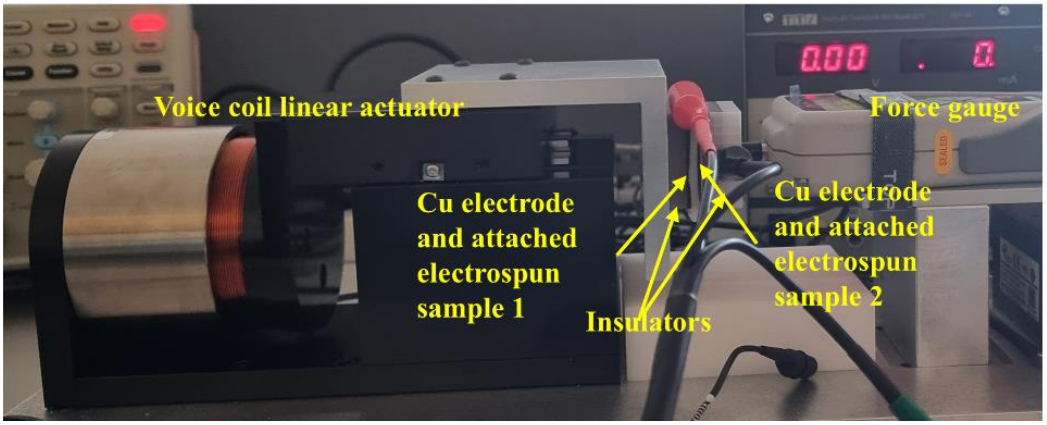


Figure 34: Bespoke setup used for contact and separation motion

reprinted from ref[1] published with CC BY Copyright©2025, The Authors.

Figure 34 illustrates the bespoke contact–separation test rig developed to overcome the limitations of manual tapping used in earlier chapters. A voice-coil linear stage (Akribis XMGV90-T30-A0G4-A1), controlled via Akribis Agito software, served as the actuator. The stage provides a maximum travel of 150 mm, supports periodic contact–separation motions up to 10 Hz, and offers ~2 µm positioning precision. These capabilities enabled us to apply

identical motion profiles across all samples, minimizing operator-dependent variability and improving run-to-run reproducibility.

Two copper electrodes of 40 mm × 40 mm were mounted on insulating plates. The insulators were centrally aligned to ensure consistent sample placement and uniform contact over the samples. During testing, electrical signals from the devices were collected using standard probe leads connected to a Keithley 6517B electrometer or the oscilloscope depending on the reading.

Earlier measurements using Keithley KickStart software were limited to approximately 10–15 data points per second, which proved insufficient for accurately capturing higher-frequency movements. Because human joint motions often occur around 2–3 Hz, a PyVISA-based Python acquisition workflow is implemented on the Keithley 6517B. The relevant charge and current recording python scripts have been provided as appendix I and J. By operating at NPLC = 0.01 (reducing the integration aperture to increase throughput), the system achieved ~440 data points per second.

In summary, the actuator-driven platform (i) standardizes the contact–separation motion with controlled amplitude and frequency, (ii) improves alignment and contact uniformity through a TENG geometry, and (iii) upgrades electrical data capture from low-rate logging to high-speed acquisition suitable for 2–10 Hz testing. This combination substantially enhances measurement repeatability and supports robust comparison across material variants presented in this chapter.

### 5.4.2. TENG characterization

A contact-separation mode TENG architecture was employed, applying a contact and separation force of 10 N, with a 5 mm amplitude and a frequency of 2 Hz sinusoidal motion. The initial electrical performance of the samples was characterised by measuring the $V_{OC}$, $Q_{SC}$ and $J_{SC}$, as shown in Figures 35a, 35b, and 35c, respectively. It was noted that the

ascending (contact) cycle output is lower than the descending (separation) cycle output. The reasons for this behaviour have been previously discussed in section 4.8. To reduce the effect of environmental conditions all samples were characterized on the same day at normal room temperature and humidity. When paired with PVDF, the pristine CA exhibited a Peak-to-peak $V_{OC}$ of 46.4 V, a $J_{SC}$ of 2.668 mA $m^{-2}$, and a $Q_{SC}$ of 39.051 μC $m^{-2}$. Notably, the highest average peak-to-peak performance was observed with the 1.5% Ag-CA sample in contact with PVDF, achieving a $V_{OC}$ of 155.9 V, a $J_{SC}$ of 8.134 mA $m^{-2}$, and a $Q_{SC}$ of 65.622 μC $m^{-2}$. This significant enhancement can be attributed to the optimised incorporation of Ag nanoparticles, which likely improved the surface charge transfer efficiency and enhanced the overall triboelectric performance. However, a further increase in Ag content to 2-2.5% resulted in a reduction in output, which can be attributed to the agglomeration of Ag nanoparticles reaching the percolation threshold at higher concentrations. This agglomeration likely disrupted the distribution of surface charges and created charge leakages, leading to decreased efficiency in the triboelectric charge generation and transfer processes. Furthermore, an increase in conductivity might have disturbed the charge transfer mechanism, resulting in a lower outcome.[159]

Following the identification of the 1.5% Ag-CA system as exhibiting the highest performance, all subsequent experiments were conducted using this optimized composition. Theoretical simulations revealed a positive correlation between output performance and both frequency and amplitude. To experimentally validate these findings within the limitations of the characterization setup, the amplitude and frequency were systematically varied. Increasing the amplitude from 1 mm to 5 mm at a constant frequency of 2 Hz led to a notable enhancement in device performance, with the $V_{OC}$ rising from 72.2 V to 155.9 V and the $J_{SC}$ increasing from 3.093 mA $m^{-2}$ to 8.134 mA $m^{-2}$ (Figure 35d, e). Similarly, by increasing the frequency from 1 Hz to 5 Hz at a fixed amplitude of 5 mm, the $V_{OC}$ improved from 90 V to 265.28 V, while the $J_{SC}$ increased from 7.224 mA $m^{-2}$ to 23.74 mA $m^{-2}$ (Figure 35f, g). These

results support the feasibility of detecting variable frequencies and amplitudes related to human joint movements.

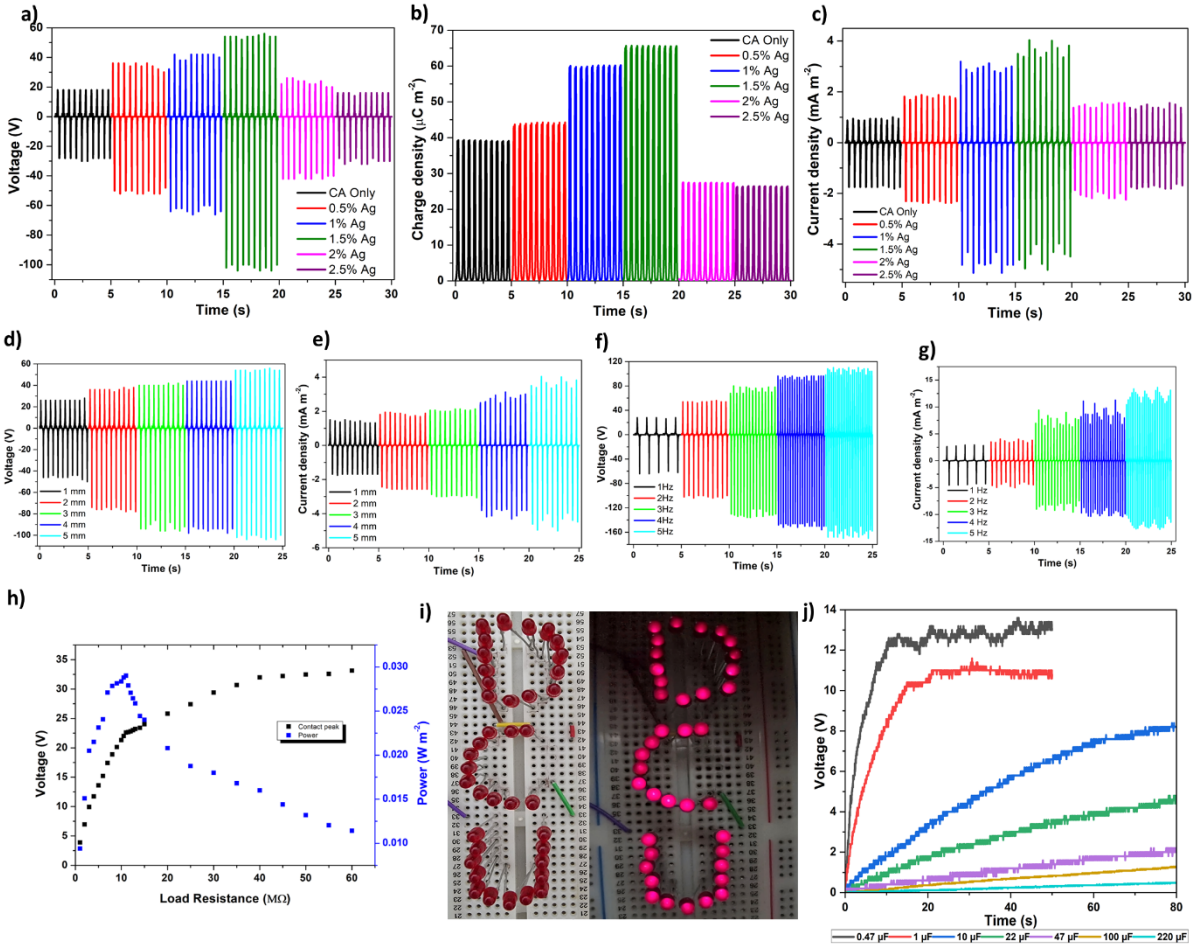


Figure 35: Energy harvesting performance evaluation of Ag- CA and PVDF samples reprinted from ref [1] published with CC BY Copyright©2025, The Authors.

a) Variation in voltage, b) charge, and c) current density concerning different Ag content in CA contact separated with PVDF. Variation of d)voltage and e) current density output with respect to change in amplitude (at constant frequency of 2Hz), Variation of f) voltage and g) current density with respect to change in frequency (constant amplitude at 5mm) h) Power generation capability of the optimised TENG as a function of external impedance. i) Demonstration of LED lighting, and j) Charging performance of various capacitors using hand tapping with the developed Ag-CA and PVDF-based TENG

To accurately determine the internal impedance, a range of load resistors were connected in a closed-loop circuit, with voltage measured across the resistor terminals. Considering the average of contact cycle voltage (V) maximum instantaneous power density was calculated using $V^2/(R*A)$, where R is the load resistance and A is the surface area of TENG device. Instantaneous peak power of 0.029 W $m^{-2}$ was observed through an 11 MΩ resistor (Figure 35h). Bai et al. previously demonstrated the incorporation of CNTs into CA and PVDF electrospun membranes for TENG applications, achieving a maximum power density of 0.74 W $m^{-2}$ with an 80 MΩ external resistor.[272] Although our power density is lower, the reduced internal impedance achieved in our study enhances compatibility with modern electronic circuits, representing a significant step toward practical application.

To further examine the energy harvesting capability of the developed TENG architecture,38 light-emitting diodes (LEDs) were powered enabling contact and separation of the TENG layers by tapping the device by hand (Figure 35i). Additionally, a circuit incorporating a full-bridge rectifier was designed to charge a series of capacitors with different capacitances. Using the developed TENG and hand tapping, capacitors with values of 0.47 μF, 1 μF, 10 μF, 22 μF, 47 μF, 100 μF, and 220 μF were charged to 12.6 V (in 10 s), 10.5 V (in 15 s), 8 V (in 69 s), 4.6 V (in 75 s), 2.2 V (in 78 s), 1.3 V (in 78 s), and 0.5 V (in 80 s), respectively(figure 35j). These results highlight that the 1.5 wt.% Ag–CA/PVDF TENG not only improves triboelectric performance but also demonstrates practical feasibility for low-power energy harvesting and storage.

### 5.4.3. Theoretical simulation with DDEF model

To interpret the experimental trends, the previously used DDEF framework was employed and updated for the Ag–CA/PVDF material pair.

For the PVDF tribonegative layer, the low-frequency permittivity is well documented: $\varepsilon_r$ values typically range between 8–12 at ~1 kHz, with datasheets reporting $\varepsilon_r$~4.5–9.5

depending on crystallinity and frequency. Peer-reviewed studies consistently confirm ≈ 10–12 for dense PVDF films. On this basis, $\varepsilon_r$ = 10 was adopted as a conservative, literature-grounded value[289,290]

For the Ag–CA tribopositive layer, neat CA films are generally reported with $\varepsilon_r$ values of 3.5–7.5 at ~1 kHz. Electrospun mats show lower effective $\varepsilon_r$ due to porosity. At the low Ag loadings used here (≈1.5 wt%), only a modest increase is expected, far below the percolation threshold. Accordingly, $\varepsilon_r$ (Ag–CA) = 5.0, was selected consistent with reported values for CA and dilute composite systems [291–294]

Measured thickness of the PVDF ~ 57 μm

Measured thickness of Ag-CA ~ 55 μm

Experimental charge density matched with DDEF prediction at $\sigma T$ =66.4 μC $m^{-2}$

According to Figure 36a, theoretically the charge density shows little change up to 3Hz. Beyond 3 Hz, the charge density reached up to 65.6 μC $m^{-2}$, indicating saturation in the charge transfer process. In Figure 36b, when the frequency was held constant at 2 Hz and the contact-separation amplitude was varied, the output increased steadily up to 5 mm, after which it remained relatively constant at 65.6 μC $m^{-2}$. These behaviours reflect sufficient contact time to achieve near-saturation charge transfer above a movement frequency and diminishing returns in electrostatic potential gain once the gap growth exceeds the effective saturation distance.

As shown in Figure 36c, simulation results for the Ag-CA/PVDF pair revealed that at 1 Hz the peak-to-peak $I_{SC}$ was approximately 3 μA, while at 5 Hz it increased to 20 μA. In comparison, when the contact-separation amplitude was varied from 1 mm to 10 mm at a fixed frequency of 2 Hz, the $I_{SC}$ increased from 2.2 μA to 6 μA (Figure 36d). To generalize these trends, corresponding current density plots are presented in Figures 36e and 36f.

The open-circuit voltage remained nearly constant with increasing frequency under a fixed displacement condition (Figure 36g). However, experimental results showed an increase in voltage when increasing the frequency. As the application is focused on the 2-3 Hz frequency detection movement, maximum testing frequency of 5Hz was selected. However, the rise in voltage with frequency could be attributed to incomplete charge transfer or suboptimal dynamic contact quality at lower frequencies. Figure 36h shows the changes of voltage with the change of amplitude at constant frequency of 2Hz. It is evident that that there is a clear increase in voltage with amplitude as observed in experimental results. To collaborate this behaviour for TENG sensor applications further experiments need to be carried out in future.

# CHAPTER 5

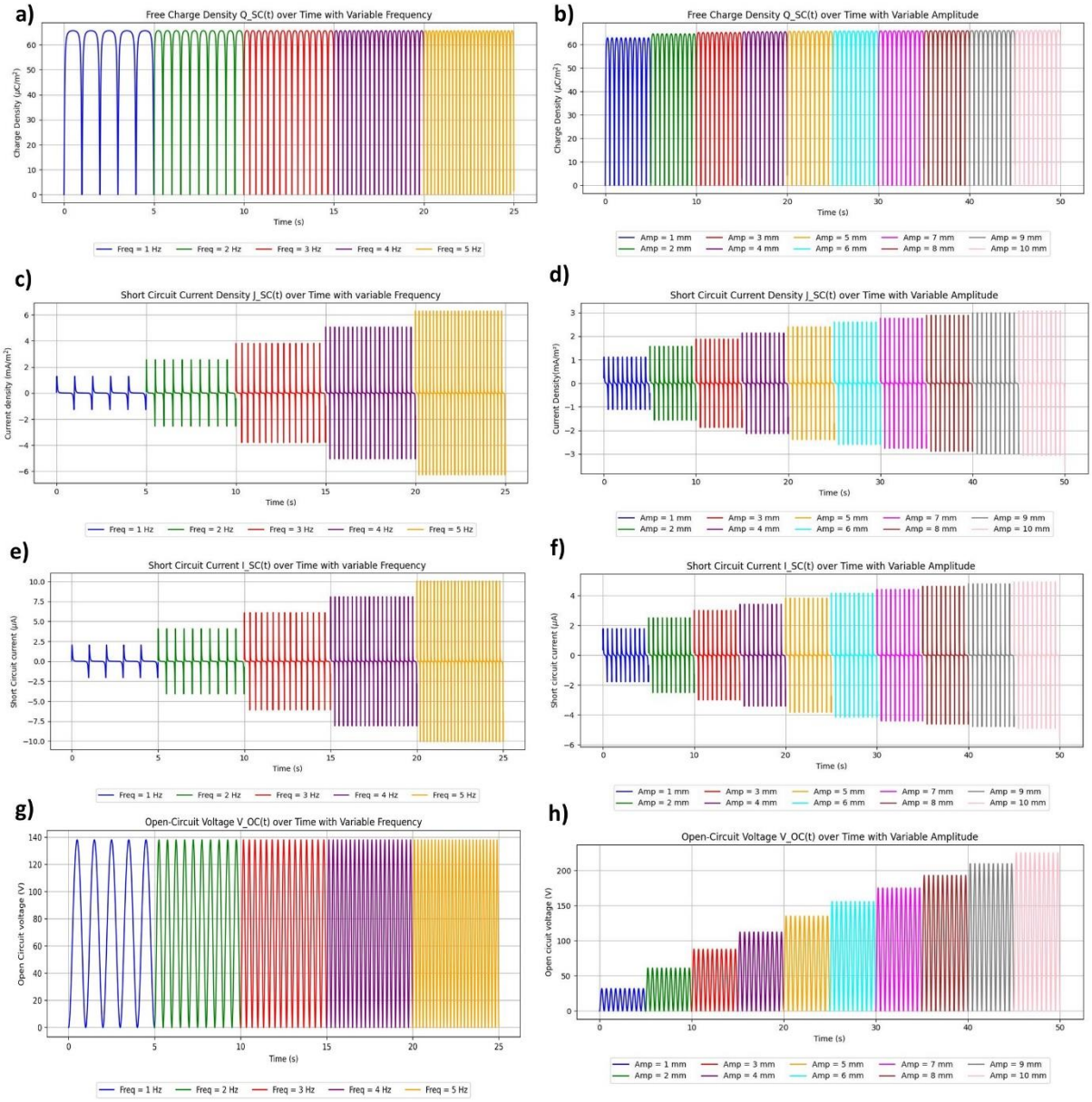


Figure 36: DDEF model simulated results for Ag-CA and PVDF samples.

Charge density changes with a) frequency and b) amplitude, Current density changes with c) frequency and d) amplitude, short circuit current changes with e) frequency and f) amplitude, Open circuit voltage changes with g) frequency and h) amplitude reprinted from ref [1] published with CC BY Copyright©2025, The Authors.

Even using the voice coil setup for contact and separation movements there is still a slight asymmetry in outputs. However, compared with manual tapping the variation in outputs are minimal and the results of experiments are very much aligned with the simulation results.

The increase in current outputs should be attributed to the increase in surface area due to the electrospinning process and improved charge trapping areas due to Ag nanoparticles inside the fibre network. The full simulation of such finer charge transfer mechanism with DDEF model is quite challenging. However, good insight into the behaviour of the device with changes in motion profile can still be obtained.

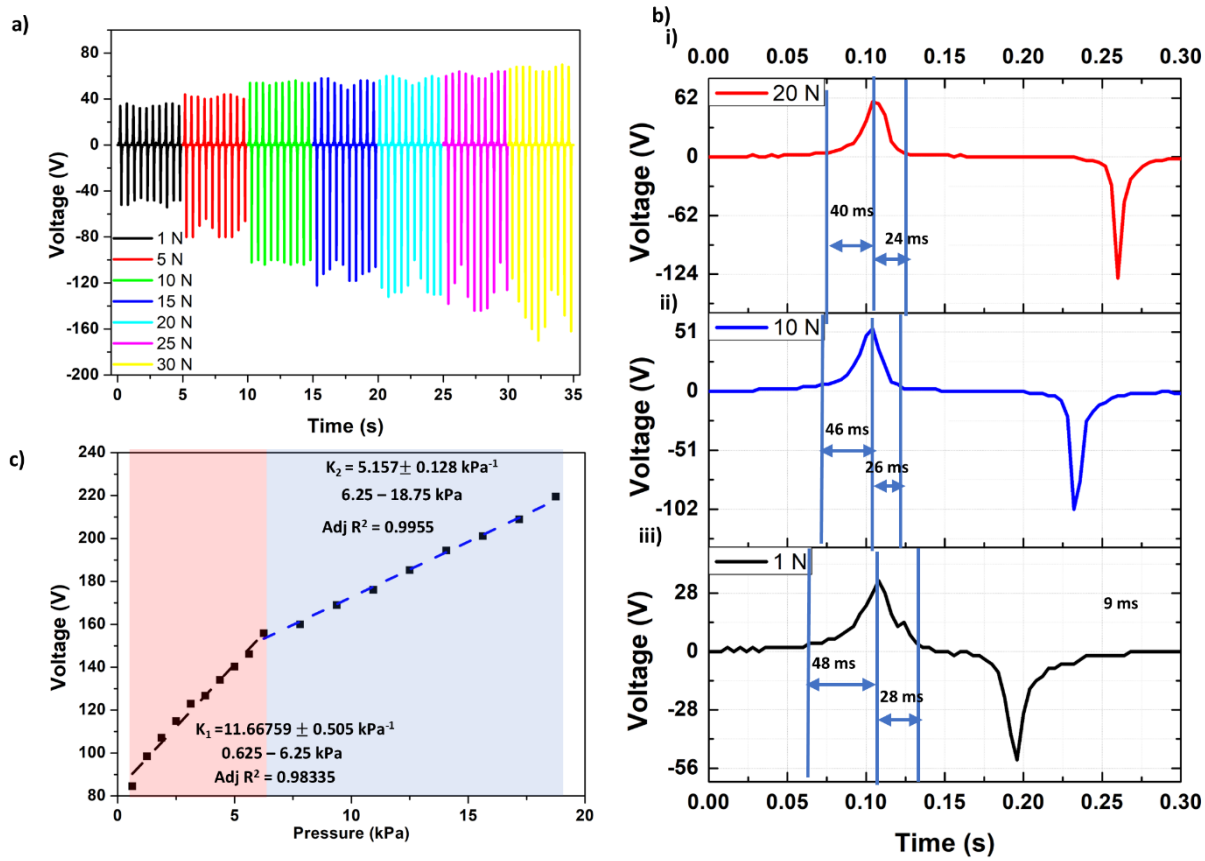


Figure 37: Self-powered sensing performance evaluation of Ag-CA and PVDF based TENG sensor.

a) Variation in peak-to-peak voltage with applied force. b) Evaluation of response time and recovery time for forces of 20 N (i), 10 N (ii) and 1 N (iii). c) Linearity of voltage with applied pressure reprinted from ref [1] published with CC BY Copyright©2025, The Authors.

### 5.4.4. Self-powered sensing evaluation

In this study, the potential of an electrospun TENG substrate for detecting low-pressure contacts with high sensitivity and accuracy was aimed. To investigate this phenomenon, a

composite substrate was utilised comprising 1.5% Ag-CA and PVDF and a series of experiments were conducted to evaluate its pressure sensitivity, as illustrated in Figure 37. Upon applying contact and separation forces ranging from 1 N to 30 N, a corresponding increase in peak-to-peak voltage was observed from 84.51 V to 219.5 V, respectively (Figure 37a). Additionally, the response times in contact at 1 N, 10 N and 20N were recorded as 48 ms, 46 ms and 40 ms, while the recovery time was 28 ms, 26ms and 24 ms (Figure 37b).

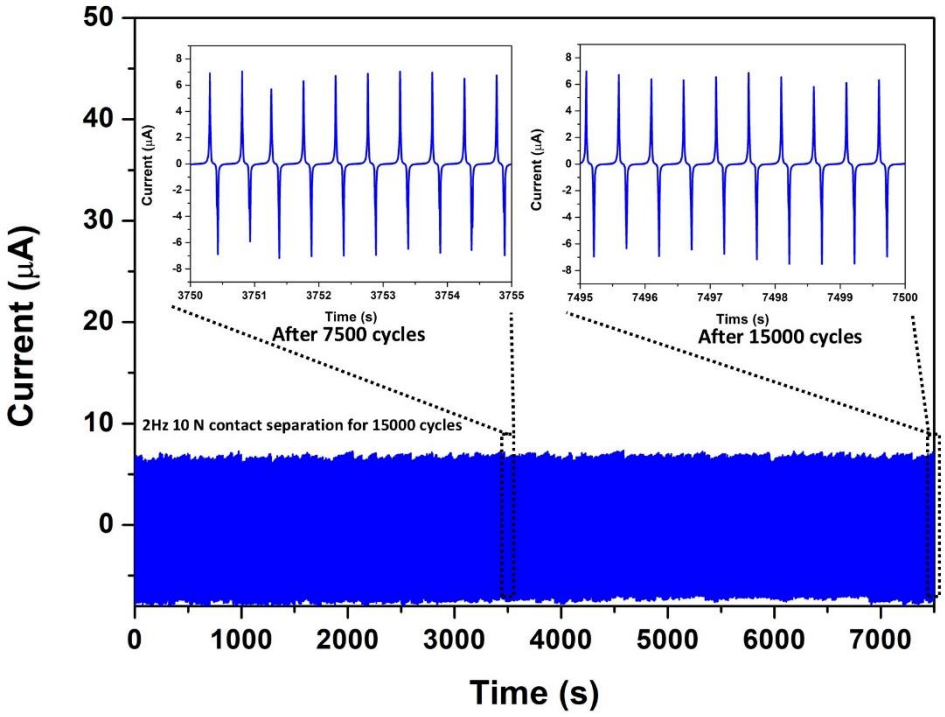


Figure 38: Ag-CA and PVDF sensor performance stability analysis

reprinted from ref[1] published with CC BY Copyright©2025, The Authors.

Further characterisation revealed that the sensor exhibits a pressure sensitivity of 11.667 ± 0.505. $kPa^{-1}$ in the 0–6.25 kPa range, which decreases to 5.157 ± 0.128 kPa-1 in the 6.25–18.75 kPa range (Figure 37c). The sensor demonstrated stable performance over 15,000 contact-separation cycles under an applied force of 10 N at a frequency of 2 Hz (Figure 38). The high sensitivity rapid response at lower pressure levels and stability for long-term use highlight the suitability of the developed sensor for JBM measurements, making it a promising candidate for applications in rehabilitation and sports injury prevention.

### 5.4.5. Learning outcomes

This chapter investigated the incorporation of AgNPs into CA as a strategy to improve TENG performance when paired with PVDF. Several key findings emerged:

**Advancement in Material Engineering:** Electrospinning produced uniform, bead-free CA fibres with controlled incorporation of AgNPs. At low concentrations (1.5 wt.%), Ag improved fibre morphology and tensile properties, while higher loadings (≥2 wt%) led to lower mechanical properties and lower TENG performance. SEM, EDS, and XRD confirmed the presence and crystalline nature of Ag within the fibres. At the same time, FTIR and XPS showed that Ag acted as a physically embedded filler providing charge trapping sites rather than chemically bonding with CA.

**Surface Potential Enhancement:** KPFM measurements demonstrated that the introduction of Ag substantially increased surface potential, with 1.5% Ag–CA exhibiting higher CPD than pristine CA. After tapping with PVDF, the higher CPD change was recorded with 1.5% Ca, and thereafter declined.

**Mechanical and Wettability Properties:** Mechanical testing revealed a modest reinforcement effect at 1.5 wt.% Ag, but deterioration at higher loadings due to nanoparticle clustering. Contact angle studies showed that hydrophobicity was largely preserved at moderate Ag contents.

**Improved Triboelectric Performance:** The 1.5%Ag–CA/PVDF device delivered significantly enhanced outputs ($V_{OC}$ of 155.9 V, a $J_{SC}$ of 8.134 mA $m^{-2}$, and a $Q_{SC}$ of 65.622 μC $m^{-2}$) compared with pristine CA/PVDF. Beyond 2 wt.% Ag, output declined, consistent with percolation-driven charge leakage. Power density peaked at 0.029 W $m^{-2}$, sufficient to drive small electronics, demonstrated through LED lighting and capacitor charging experiments.

**Validation Through Modelling:** DDEF simulations, based on realistic permittivity values and measured thicknesses, predicted charge density trends consistent with experimental results. While simulations underestimated the voltage increase with frequency, they provided a valuable framework for understanding how amplitude and frequency shape TENG performance.

**Sensing Capability:** The Ag–CA/PVDF device exhibited high pressure sensitivity in the low-pressure regime (11.67 V $kPa^{-1}$ in 0–6.25 kPa), fast response/recovery times (<50 ms), and stable operation over 15,000 cycles. These features demonstrate strong potential for applications in joint biomechanics monitoring, where low-force detection is critical.

**Challenges and Future Work:** Despite the improvements, charge stability remains an issue due to rapid decay, and high Ag contents approach the percolation threshold. Future efforts may focus on stabilizing trapped charges through other methods such as sandwiching with charge trapping layers, optimizing filler distribution, or combining Ag with secondary modifiers. Building on these findings, the next chapter will examine how structural design, particularly fabric-inspired architectures, can be leveraged to amplify sensitivity and expand the functional performance of TENGs for JBM.

# CHAPTER 6

## 6. DEVELOPMENT OF FABRIGAMI STRUCTURE FOR JBM

**Publication status: Published as a journal paper and patent**

**Part of this chapter is published as a journal paper in Wiley Small Journal**

Innovative Self-Powered Sensing: Potential of Fabrigami and Electrospun Nanofibre-Based Triboelectric Nanogenerator for Joint Biomechanics Monitoring", by K. R. Sanjaya D. Gunawardhana*, Zhou Fang, Garrett B. McGuinness, Luz Alejandra Magre Colorado, Sonal Santosh Baberwal, Waseem Ahmad Wani, Brian J. Rodriguez, Robert O'Connor, Ciara Smullen, Tomás E. Ward, Shirley M. Coyle*

**Part of this chapter filed as patent – UK patent filled no. 2505562.5**

Fabrigami Sensor by Sanjaya Dinuwan Gunawardhana Karnasooriya Ragalage, Zhou Fang, Garrett B McGuinness, Shirley M Coyle

# CHAPTER 6

The previous chapter discussed the use of Ag-modified CA and PVDF as TENG layers for highly sensitive sensor development. This work has optimized the materials for higher TENG performance ($V_{OC}$ and $I_{SC}$) and high sensitivity for low pressure. The next critical challenge is to transforms this improved performance into a wearable system capable of capturing low-force, low-frequency movements that are typical of joint biomechanics during human movement.

This chapter introduces the concept of Fabrigami as the smart textile structure for developing TENG based self-powered sensors. Fabrigami is an origami-inspired fabric folding technology which has been used to create an architecture that can seamlessly incorporate the developed electrospun sensor for wearable applications. In addition to material modification, this technique can amplify the sensitivity of TENG devices by enhancing contact–separation efficiency and mechanically coupling joint movements to the active sensing area.

This chapter describes the design and fabrication of a thermally imprinted fabrigami structure, along with the integration of electrospun nanofibres with conductive fabrics. A geometrical model of the fabrigami folds has provided to rationalize the mechanical amplification effect. Also, the development of a compact electronic interface is described which comprises rectifiers, a Serial Peripheral Interface(SPI)-based multi- ADC, and a BLE-enabled microcontroller for wireless data acquisition. The sensor's capability is evaluated through a series of experiments involving knee flexion, squatting, walking, running, and stair climbing, with its performance benchmarked against commercial angle sensors.

Finally, this chapter demonstrates how structural design and material innovation can converge to enable self-powered, wearable monitoring platforms.

# CHAPTER 6

## 6.1. Introduction

The development of the fabrigami structure commenced with the design of a 2D paper mould specifically tailored to capture the knee's movement. The goal was to translate the intricate movements of the knee into a responsive fabrigami structure capable of enhancing the TENG's performance. The figure 39 comprises two main components: (a) the fabrication process and (b) the application and data collection mechanism design. The electrospun membranes of Ag-CA and PVDF have been employed as the tribopositive and tribonegative layers, respectively. Six sensors made with Ag-CA and PVDF and attached via fabric electrodes, as detailed in section 6.4. These six sensors within the folded structure are positioned behind the knee. Knee flexion causes the mountains of the fabrigami structure to close sequentially from top to bottom creating contact of the TENG layers, while knee extension causes them to open and separate the TENG layers. This progressive contact-separation mechanism generates electrical signal output in a pattern that correlates with the specific angle of knee flexion, enabling precise angle detection through the sensor activation sequence.

The results of this fabrication process demonstrate the successful integration of the materials into the fabrigami structure, leading to a functional device capable of efficiently monitoring JBM. The use of Ag-CA and PVDF electrospun membranes provided enhanced triboelectric performance, evident from the electrical characterisation and self-powered sensing data collected during the application. The findings also indicate that the choice of materials and the structural design play a crucial role in optimising the device’s performance, aligning with similar trends observed in previous studies (see Appendix K for comparative analysis of results from previous literature). These results underscore the potential of our approach in advancing the development of flexible and efficient triboelectric devices. Further discussion

on the implications of these findings and their comparison with existing literature is provided in subsequent sections.

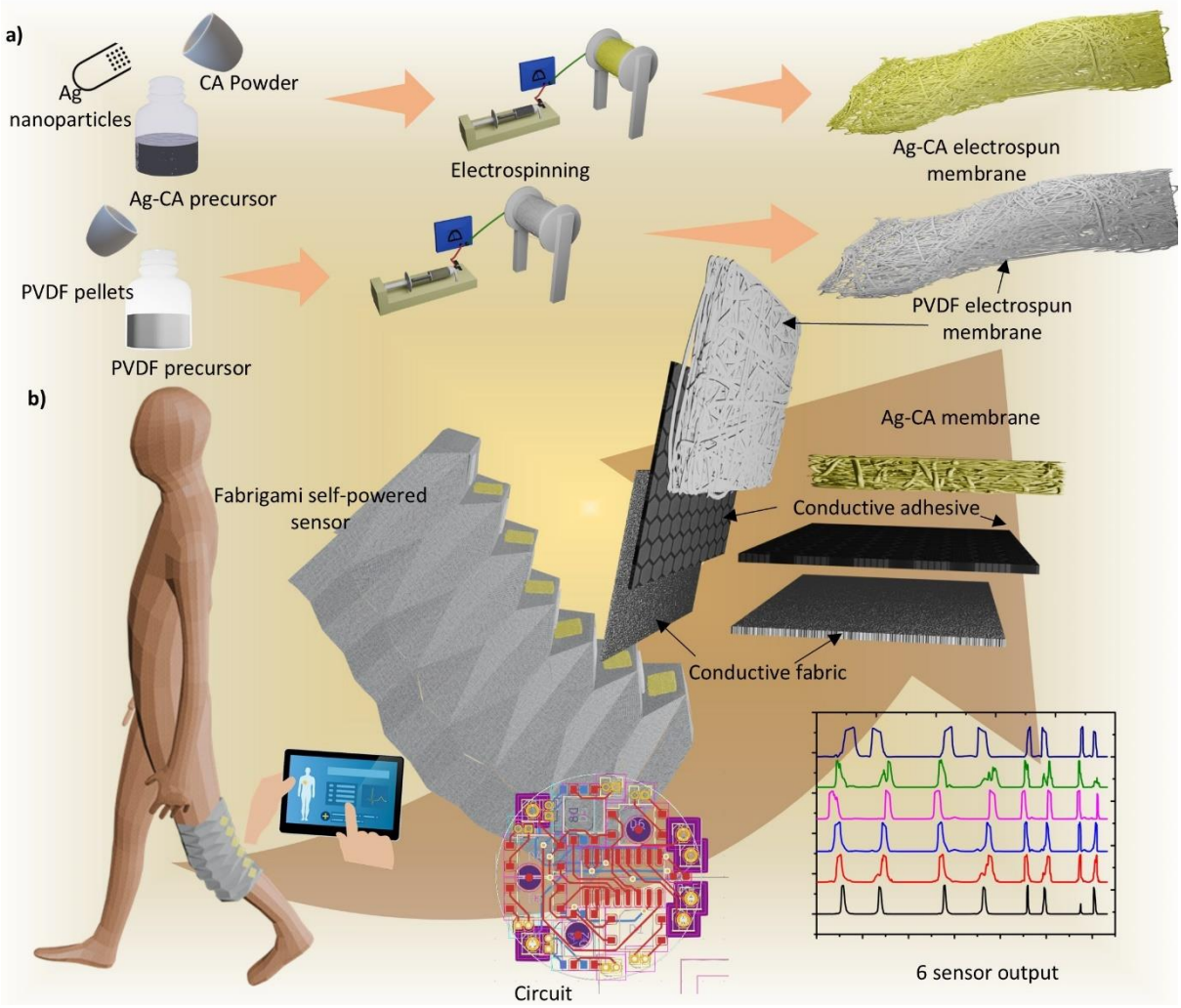


Figure 39: Fabrigami JBM monitoring sensor architecture.

a) Fabrication process of electrospun membranes, and b) Application and data collection mechanism reprinted from ref [1] published with CC BY Copyright©2025, The Authors.

### 6.2. Fabrigami structure geometry

To translate the geometry of the knee to the paper, the knee was considered to have a semicircular cross-section. As shown in Figure 40a(i), the top view of the semi-circle represents the knee and the horizontal part of the fabrigami structure is designed to be placed posterior to the knee. To maintain the position of the sensor, the overall structure wraps

around the knee, which is achieved by incorporating two bends at each side of the knee. Firstly, side panel 1 was folded at an angle of 2α with respect to the horizontal panel under the knee. Then, side panel 2 is folded so that it is vertical with respect to the horizontal panel, resulting in an angle of ($180^0$-2β) with respect to side panel 1 as shown in Figure40a.

The description of each label used in Figure 40a(i) is as follows:

- R – Radius of the knee (approximated as a semi-circle)
- $W_1$ – Width of the fabric ridge panel
- $A_1$ – Half-distance of the central panel
- $A_2$ – Distance of the first bending
- $A_3$ – Distance of the side panel 1
- $A_4$ – Distance of the side bending between side panel 1 and 2
- $A_5$ – Vertical side panel 2 distance

These parameters form the basis for the subsequent geometric relationships and equations that define the fabrigami structure.

By geometry the equation E16 can be developed.

$$\beta = \frac{\pi}{4} - \alpha \qquad \text{(E16)}$$

In this R and W are considered as constants for a given design.

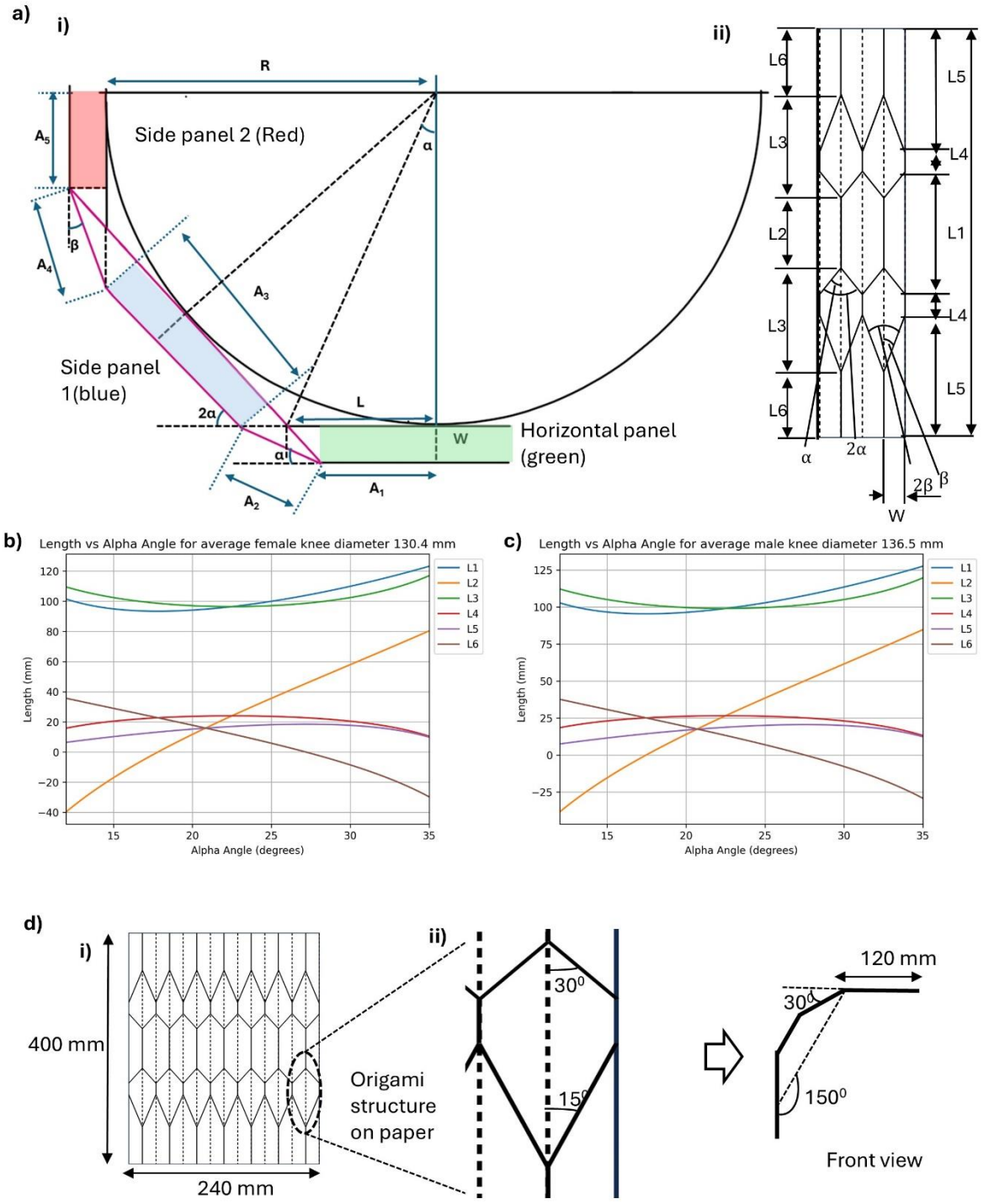


Figure 40: Model used to develop angles for fabrigami sensor

reprinted from ref[1] published with CC BY Copyright©2025, The Authors.

a) i) Knee model (taking semicircular architecture. and related bending parts of the fabrigami sensor. ii) relevant length, width and angle notations with respect to the fabrigami sensor on the paper. Change of length in fabrigami structure with respect to α angle for b)Female and

c) male average knee diameters. d) i) Fabrication of the paper mould structure; ii) Explanation of different angles in the structure from front view before and after folding.

Based on that E17 to E26 can be used to find $A_1$ to $A_5$ with respect to the R, W and α.

$$A_2 = \frac{W_1}{\sin\propto} \quad \text{(E17)}$$

$$A_4 = \frac{W_1}{\sin\beta} \quad \text{(E18)}$$

$$A_4 = \frac{W_1}{\sin\left(\frac{\pi}{4}-\alpha\right)} \quad \text{(E19)}$$

$$A_1 = L - \frac{W_1}{\tan 2\alpha} \quad \text{(E20)}$$

$$L = R\tan\alpha \quad \text{(E21)}$$

$$A_1 = R\tan\alpha - W_1\cot 2\alpha \quad \text{(E22)}$$

$$R = A_1 + A_2\cos\alpha + A_3\cos 2\alpha = R\tan\alpha - W_1\cot 2\alpha + W_1\cot\alpha + A_3\cos 2\alpha \quad \text{(E23)}$$

$$A_3 = \frac{R-(R\tan\alpha - W_1\cot 2\alpha + W_1\cot\alpha)}{\cos 2\alpha} \quad \text{(E24)}$$

$$A_5 = R - A_4\cos\beta - A_3\sin 2\alpha \quad \text{(E25)}$$

$$A_5 = R - W_1\cot\left(\frac{\pi}{4}-\alpha\right) - (R - (R\tan\alpha - W_1\cot 2\alpha + W_1\cot\alpha))\tan 2\alpha \quad \text{(E26)}$$

After finding these values the next step is translating these distances to the 2D plane to create the related structure for paper mould.

Based on the Figure 40a(ii) relationships with $L_1$ to $L_6$ with already established parameters can be developed using E27 to E37.

$$L1 = 2A_1 + 2A_2\cos\alpha \quad \text{(E27)}$$

$$L1 = 2(R\tan\alpha - W_1\cot 2\alpha) + 2W_1\cot\alpha \quad \text{(E28)}$$

$$L2 = 2A_1 \quad \text{(E29)}$$

$$L2 = 2(R\tan\alpha - W_1\cot 2\alpha) \quad \text{(E30)}$$

$$L3 = A_4\cos\beta + A_3 + A_2\cos\alpha \quad \text{(E31)}$$

$$L3 = W_1\cot\left(\frac{\pi}{4} - \alpha\right) + \frac{R-(R\tan\alpha - W_1\cot 2\alpha + W_1\cot\alpha)}{\cos 2\alpha} + W_1\cot\alpha \quad \text{(E32)}$$

$$L4 = A_3 \quad \text{(E33)}$$

$$L4 = \frac{R-(R\tan\alpha - W_1\cot 2\alpha + W_1\cot\alpha)}{\cos 2\alpha} \quad \text{(E34)}$$

$$L5 = R - (R - (R\tan\alpha - W_1\cot 2\alpha + W_1\cot\alpha))\tan 2\alpha \quad \text{(E35)}$$

$$L6 = A_5 \quad \text{(E36)}$$

$$L6 = R - W_1\cot\left(\frac{\pi}{4} - \alpha\right) - (R - (R\tan\alpha - W_1\cot 2\alpha + W_1\cot\alpha))\tan 2\alpha \quad \text{(E37)}$$

Since the design wraps around the knee with two side panels, the constraint $\alpha < \pi/4$ must be satisfied to maintain structural integrity. Based on the geometry of the joint, α can be determined. A parametric simulation was performed to investigate the effect of varying α on the derived parameters ($L_1$–$L_6$), using W = 15 mm and the average knee diameter reported in Ref. [295] for male and female subjects (Figure 40b-c).

During the initial stages of designing, several values of α were examined to balance structural geometry with functional performance. From the derived equations and simulations, it resulted that when $\sim\alpha < 17.5°$, the parameter $L_2$ becomes negative, removing the horizontal panel. It is vital to maintain the central panel for sensor attachment. Conversely, when $\sim\alpha > 28°$, the parameter $L_6$ becomes negative, making the vertical side panel 2 impractical.

Although the knee was initially approximated as a semi-circular arc, anatomical considerations revealed that the geometry is more complex[296]. In particular, the biceps

femoris tendon protrudes beyond the simplified semi-circular profile when the knee is flexed. This anatomical feature necessitates additional clearance in the design to prevent interference with the fabrigami folds.

For this reason, $\alpha = 30°$ was selected despite exceeding the purely geometric limit derived from the idealised semi-circular model. At this angle, the mid-panel length ($2L_1$) is sufficiently large to maintain a functional central panel, while also allowing space for the tendon to move during knee flexion. This configuration provides an effective compromise between theoretical geometry and practical anatomical requirements. The final paper mould is presented in Figure 40d. where all the distances are made based on the previous equation with w=15 mm and $\alpha = 30°$.

It is acknowledged that further optimisation of α may be necessary in future work. However, the current selection ensures both structural stability of the fabrigami device and improved conformity with knee biomechanics, thereby supporting its application in joint monitoring.

### 6.3. Development of fabric-based structure

Translation of the geometry to the fabric required careful selection of the material, as discussed in section 6.2. In particular, the material should have sufficient flexibility to accommodate repeated folding and unfolding motion without being fatigued. Furthermore, wearable properties and adequate stiffness to maintain fold definitions with applies heat is a prerequisite.

Commercial white polyester fabric with 167.4 grams per square meter was selected to create the fabric-based origami structure. This material was plain woven with a low thread count of 102, ensuring that the fabric possessed both the flexibility required for dynamic folding and the structural integrity needed to maintain the origami form under repeated stress.[297] Polyester was chosen for its well-documented mechanical properties, including high tensile

strength, thermal stability, and resistance to environmental degradation. These properties make polyester an ideal candidate for applications where durability and resilience are paramount, particularly in wearable technologies. The 3D origami structure was formed by folding two pieces of paper into a complex configuration, as shown in Figure 41a. The folding process utilised a pattern with solid lines on one side representing mountain folds and dotted lines on the other side indicating valley folds (Figure 40d). The mountain folds are the sharp ascending points on the structure while valley fold are the sharp descending points in the structure as shown in figure 41b.

After extensive experimental trials with paper-based moulds, the final configuration was chosen, consisting of seven mountain folds and six valley folds. This arrangement consistently produced distinct and repeatable contact–separation cycles, optimising the triboelectric response. The final design, depicted in Figure 41a, was selected for its ability to consistently produce distinct and efficient contact-separation events, a key factor in optimising the triboelectric effect. Thermal processing method was employed to imprint the origami pattern onto the polyester fabric permanently. The fabric, sandwiched between the folded paper moulds, was subjected to a controlled heating process at 140°C for 20 minutes. This temperature was deliberately chosen to exceed the glass transition temperature of polyester, which is 68°C, ensuring that the fabric could be softened sufficiently to conform to the mould's intricate folds. Upon cooling, the fabric retained the 3D origami structure, a result corroborated by previous studies showing that thermal imprinting at temperatures of 130-150 $^{0}$C can permanently alter the morphology of polymeric materials.[298–300]

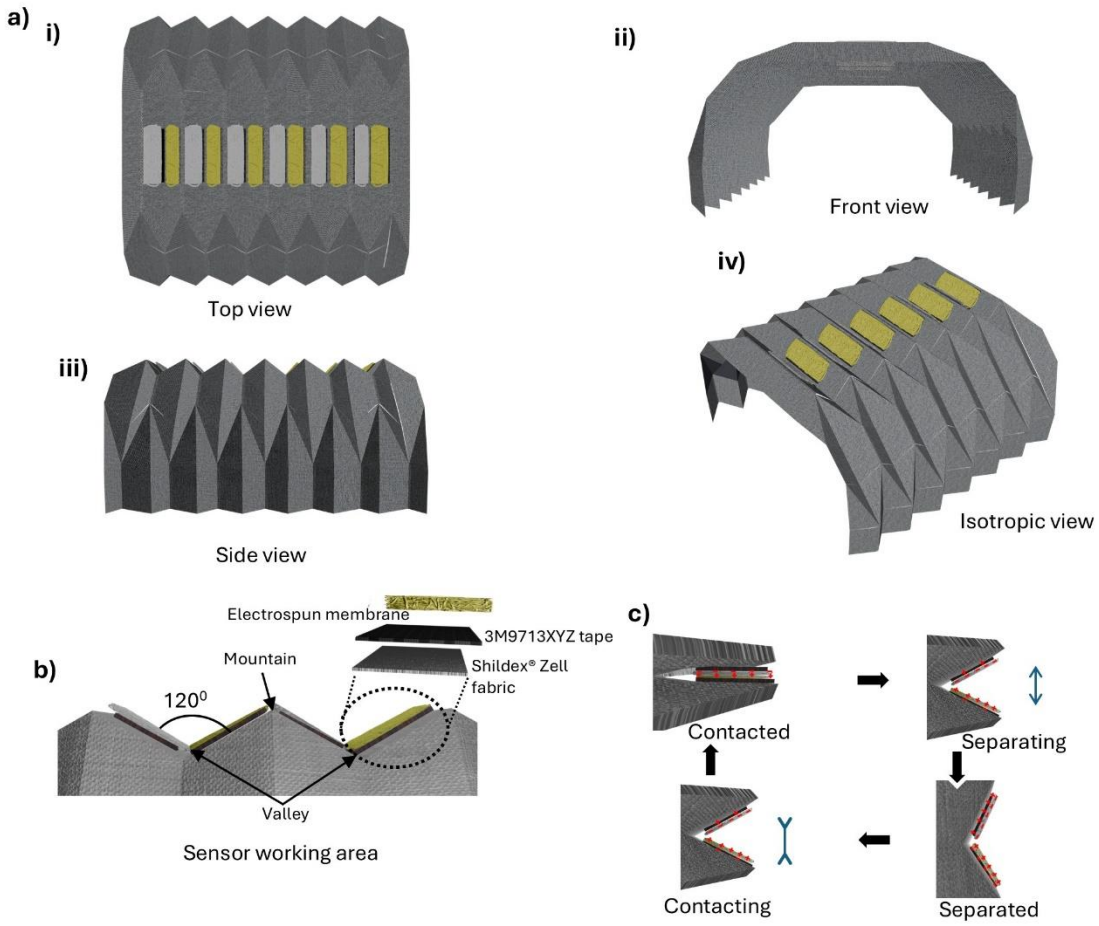


Figure 41: a) Schematic view of the finalized fabrigami structure.

a)top view (i), front view (ii), side view (iii) and isotropic view (iv); b) Schematic of the sensor working area; c) Working principle of the newly developed sensor reprinted from ref [1] published with CC BY Copyright©2025, The Authors.

### 6.4. Fabrigami sensor development for JBM

#### 6.4.1. TENG sensor attachment to the fabrigami structure

After development of the fabrigami substrate the next step was attaching TENG sensors to determine the JBM. The mountain folds were chosen as the primary attachment sites, since they undergo pronounced closure during knee flexion, thereby maximizing contact–separation events. As illustrated in Figure 41b, one sensor was placed on either side of each mountain fold, except for the first and last folds, where a single sensor was attached. This

arrangement provided a total of six functional sensors distributed along the structure, numbered sequentially from bottom (Sensor 1) to top (Sensor 6).

An additional conductive layer was applied between the electrospun substrate and polyester fabric using Shieldex® Zell RS fabric (0.02 Ω/□), known for its excellent conductivity and flexibility to enhance electrostatic induction. The Ag-CA layer was applied onto the conductive fabric with 3M9713XYZ tape to ensure robust and reliable electrical connections. On the opposite side of each Ag-CA layer, a sample of PVDF was attached using a similar technique. A conductive yarn (0.04 Ω/cm) created connections from the Shieldex fabric and the conductive connectors to the circuit within the fabric substrate. At rest, the sensor's active area encompassed 300 mm², providing a substantial surface for the contact-separation interactions critical to the TENG's operation.

As shown in Figure 41c, the developed fabrigami structure facilitated consistent and effective contact-separation cycles, crucial for the TENG's reliable performance during dynamic knee movement.

### 6.4.2. Circuit development

The data acquisition process for the fabrigami sensor system is illustrated in Figure 42a. Analog outputs from the six sensors are first processed through individual bridge rectifiers and then fed into an 8-channel, 10-bit ADC with SPI (MCP3008), effectively mapping the signal within the 0–3.3 V input range. The digitized signals are transmitted via a Bluetooth enabled microcontroller unit (BLE-MCU) (nRF52840), which integrates an onboard LSM6 6-axis IMU and RGB LED, and communicates with a mobile app (Figure 42b).

# CHAPTER 6

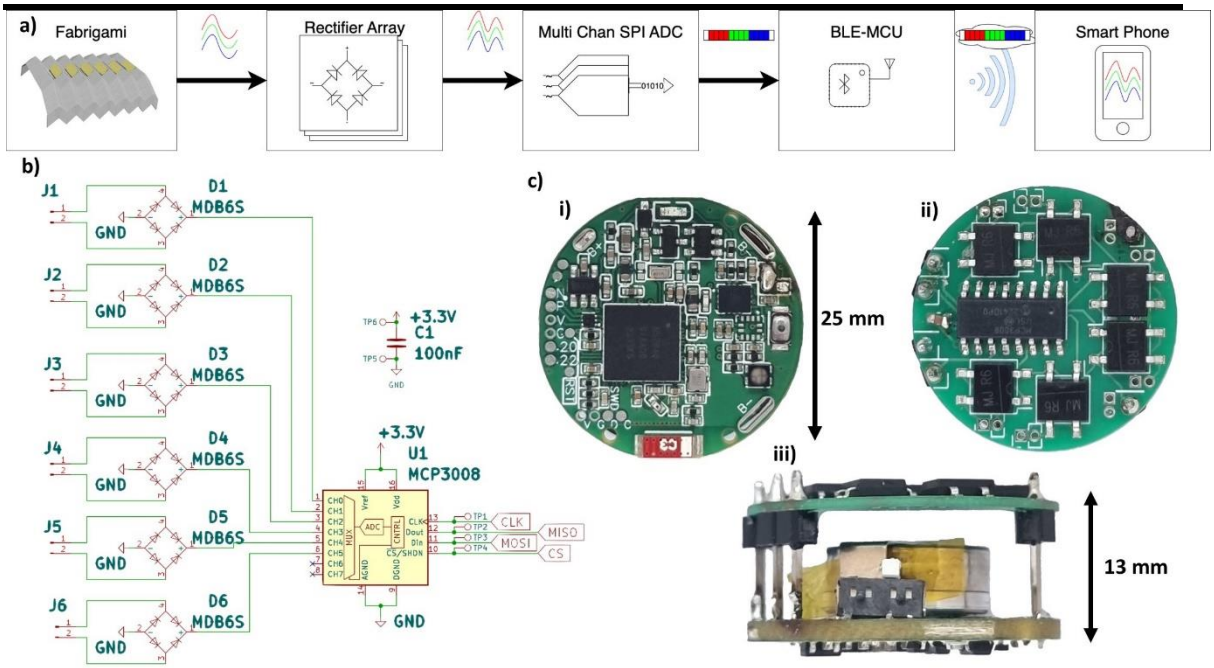


Figure 42: Flow chart of the data collection mechanism with the developed sensor.

a)including the fabrigami sensor, rectified array, multi-channel SPI ADC, BLE-MCU, and data collection with the smartphone, b) Schematic diagram of rectified array and multi-channel SPI ADC., c) Images of final circuit i) top, ii) Bottom and iii)side view reprinted from ref [1] published with CC BY Copyright©2025, The Authors.

The hardware is arranged in a compact, sandwich-style configuration comprising two stacked PCBs with a VARTA 1454 rechargeable battery (0.3 Wh, 14 × 5.4 mm) embedded between them(Figure 42c). Board 1 contains the BLE MCU and battery management circuitry, while Board 2 contains the ADC, six MDB6S bridge rectifiers, and lead pairs connecting to the fabric sensor. Communication between the two boards is facilitated by a 6-pin interface: four SPI lines (MOSI, MISO, SCK, CS), ground, and 3.3 V power.

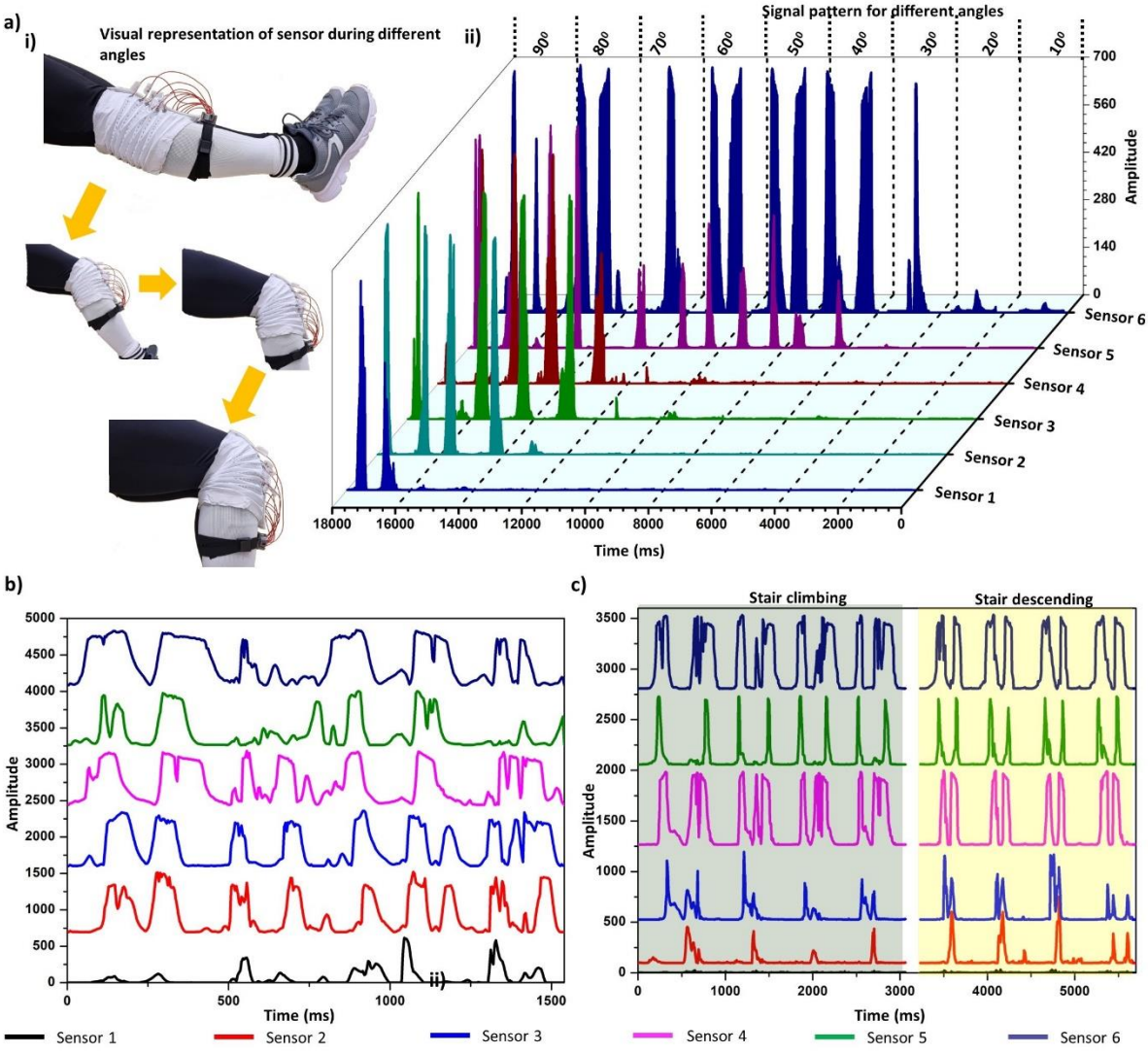


Figure 43: Application development by evaluating fabrigami sensor sensitivity performance.

a) (i) visual representation of knee bending, and (ii) sensors response at different bending angles. Sensor measurements during b) running, c) climbing and descending stairs reprinted from ref [1] published with CC BY Copyright©2025, The Authors.

The system operated at a sampling rate of 250 Hz per channel, providing sufficient temporal resolution to capture dynamic knee movements. Data were transmitted via BLE UART in a text-based format for straightforward visualization and post-processing. For proof-of-concept demonstrations, data were received on iOS and Android devices using the Adafruit Bluefruit Connect app, which supports UART monitoring, real-time plotting, and CSV

export.[301] The code used for the sensor can be found via the repositor https://doi.org/10.5281/zenodo.16749138.

It is important to note that the circuit was designed as an enabling platform to demonstrate the feasibility of real-time, wireless data collection from the fabrigami TENG sensor, rather than as the primary focus of this research. The modular design provided adequate performance for wearable demonstrations, while leaving scope for future optimization in terms of power efficiency, miniaturization, and advanced signal processing.

### 6.5. Assessing JBM using the fabrigami TENG sensor

The primary objective of the developed sensor is to detect the JBM of the knee. In daily practice, runners and athletes often experience variations in their JBM due to changes in body posture or the initiation and conclusion of joint movements during various exercises.[302] Six sensors were employed to detect angles ranging from 10° to 90° with 10° intervals. This represents the first development of a sensor using the TENG concept combined with a fabrigami structure. Once the device was assembled, it was attached to the knee, as shown in Figure 43a, where the fabrigami TENGs are positioned posterior to the knee joint and signal detection was performed at different angles. A commercial angle detection sensor (Bend Labs 1-Axis Flex Sensor Evaluation Kit) was used to monitor the actual knee angle, and the responses of the various sensors at different angles are depicted in Figure 43a(ii). Notably, up to 30°, there is a distinct change in pressure sensitivity for Sensor 6, and beyond this angle, all sensors are activated to provide different signal patterns corresponding to various angles. Additionally, fast movements such as running (Figure 43b), climbing and descending stairs (Figure 43c) were tracked to get an overall idea about the sensor's limitations. It was evident that the sensor can successfully detect slow and fast movements accurately, providing real-time angle measurements with temporal information to determine the time taken to reach a set angle allowing analysis of the wearer's

performance of repeated exercises, this allows the identification of the knee angle and movement frequency throughout the activity.

To further understand the signal patterns, half-squat exercises were conducted, i.e. targeting the top half range of motion during a squat (Figure 44a) and walking (Figure 44b). During the squatting process, it was observed that the sensors are activated in a characteristic pattern as the knee bends and the folds are compressed. As the knee bends, each sensor responds in sequence after the topmost sensor, i.e. sensor 6, is activated, in correspondence with the knee flexion which increases the knee flexion angle, e.g. sensor 5 has a 92ms time delay after sensor 1, corresponding to bending by $30\text{-}40^0$. Combining these results, insight into different exercises and movement patterns can be gained. The developed sensor proved particularly effective in monitoring exercises like squatting, offering detailed insights into knee movement. Moreover, the activation of sensor 1 when the person reaches the bottom position during squatting indicates the knee angle reaching up to 90°.

Walking is composed of two primary phases: the stance phase and the swing phase. As depicted in Figure 44b(i), key moments include standing, initiating a left step while preparing for right heel-off, right leg swing forward, and right toe-down.[303,304] In this experiment, the sensor was attached to the right knee, and the corresponding signal profile was recorded, as shown in Figure 44b(ii). The knee demonstrates a characteristic flexion-extension pattern during the gait cycle, with peak flexion occurring during the initial swing phase, followed by extension before foot contact. Lower flexion angles are typically maintained during most of the stance phase. The sensor amplitude shown in the graph corresponds to these angle changes, with higher amplitude signals correlating with increased knee flexion. Although the sensor did not fully distinguish between the stance and swing phases, it successfully captured the maximum knee flexion angle during the gait cycle. These results offer promising insights into providing a more detailed understanding of knee JBM.

With future improvements, this sensor could evolve into a self-powered, sustainable tool for monitoring exercise and therapeutic performance for sports and health.

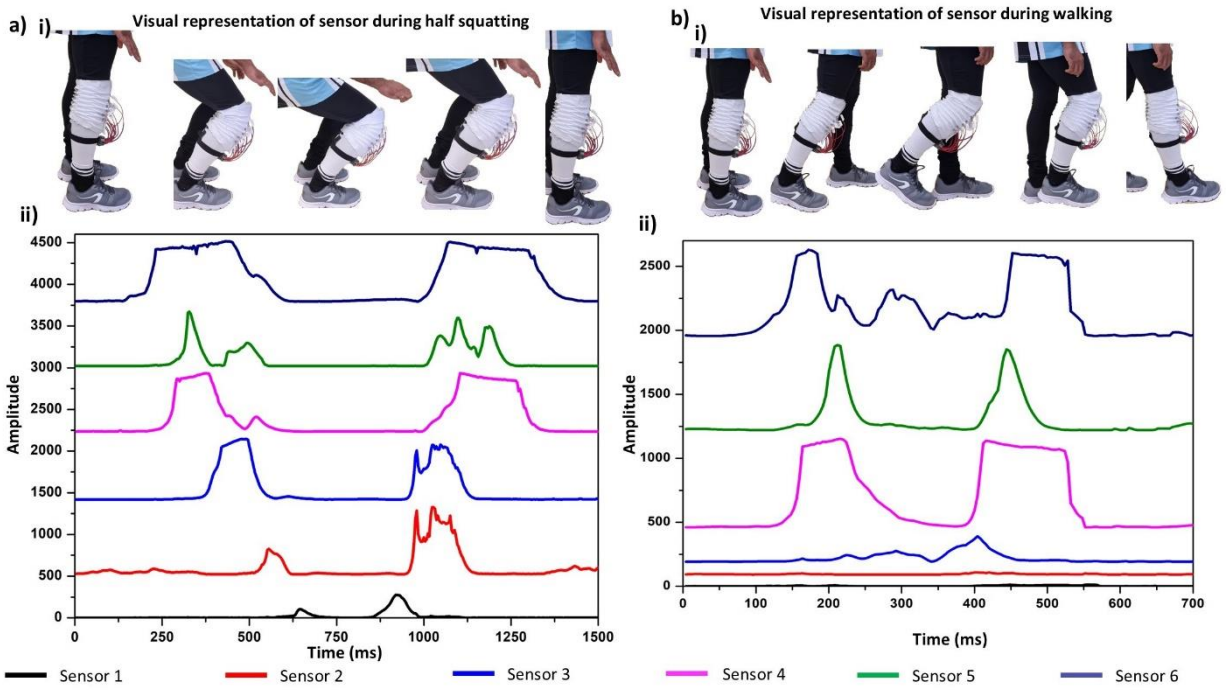


Figure 44: Further clarification on-body performance of the fabrigami sensor.

a) visual representation(i) and signal pattern(ii) during half squatting, b) visual representation(i) and signal pattern(ii) during walking reprinted from ref [1] published with CC BY Copyright©2025, The Authors.

### 6.6. Learning outcomes

In this chapter, the feasibility of integrating Ag-CA/PVDF TENG materials into a fabrigami structure for knee JBM monitoring was explored. Several key outcomes were identified.

**Translation of Knee Geometry into Fabrigami Design:** By approximating the knee as a semicircle, geometric equations were developed to define folding angles and panel lengths of the fabrigami structure. Experimental adjustments, such as increasing $\alpha=30^0$ to accommodate subdural features of the knee, validated the balance between structural fit,

mid-panel length, and biomechanical freedom. This demonstrated the importance of geometry-driven design in wearable origami sensors.

**Development of Fabric-Based Origami Structure:** A polyester fabric substrate was successfully transformed into a stable 3D origami structure through thermal imprinting at 140 $^0$C. The chosen material and processing conditions ensured both mechanical durability and fold fidelity, aligning with requirements for long-term wearable applications. The final structure comprised seven mountain folds and six valley folds, optimised to produce repeatable contact–separation events.

**Integration of TENG Sensors within Fabrigami:** Six Ag-CA/PVDF-based triboelectric sensor units were integrated into the mountain folds of the origami design using Shieldex® conductive fabric and conductive yarn interconnections. The sensor arrangement provided sequential activation during knee bending, enabling mapping of specific flexion angles through distinct contact–separation patterns.

**Wireless Data Acquisition and Circuit Development:** A compact two-board circuit system incorporating bridge rectifiers, an MCP3008 ADC, and a nRF52840 BLE microcontroller was implemented for wireless data collection. The FreeRTOS-based firmware enabled synchronized sampling at 250 Hz and stable BLE transmission, demonstrating the feasibility of a lightweight, mobile-compatible acquisition platform.

**JBM Monitoring and Application Demonstrations:** The fabrigami sensor system effectively detected knee flexion angles from $10^0$ to $90^0$ with $10^0$ interval and captured dynamic movements such as squatting, stair climbing, running, and walking. Distinct activation patterns across the six sensors enabled both angular resolution and temporal tracking of motion, validating the sensor's capability for real-time JBM monitoring.

**Implications for Wearable Technologies:** The study highlighted the synergy between origami-inspired geometry and triboelectric sensing. The successful demonstration of a self-

powered fabrigami TENG device underscores its potential for deployment in sports performance monitoring, rehabilitation, and broader wearable health applications.

# CHAPTER 7

## 7. CONCLUSION AND FUTURE WORK

### 7.1. Conclusion

This thesis focused on developing practically wearable sensor for JBM using TENG technology. After the development of TENG technology in 2012 there has been vast development which shows the promising future of this technology particularly in self-powered sensing and energy harvesting applications. When developing TENG based self-powered sensor selection of materials, fabrication technique, selection of mechanical excitation techniques and interface development are key areas that need to be focused.

The aim and objectives of this thesis have clearly been explained in Chapter 1. According to Chapter 1, the aim of this project was to develop a TENG-based self-powered sensor for joint biomechanics monitoring by combining electrospinning for functional substrate fabrication with origami-inspired fabrigami structures for mechanical excitation. To achieve this, the thesis pursued five key objectives: assessing the feasibility of electrospinning with biodegradable and biocompatible materials for enhanced triboelectric performance; investigating the potential of electrospinning to improve self-powered sensing capabilities; characterizing and optimizing triboelectric, morphological and mechanical properties of electrospun samples; exploring textile origami structures for actuation and developing a human movement prototype; and finally, conducting a pilot study to evaluate sensor performance and refine the design. Together, these objectives established a systematic approach to bridging material science, sustainable design, electronic textiles and sensing technology in the development of next-generation self-powered wearable sensors for physiological measurement.

Chapter 2 presents an extensive literature review that underpins the problem statement and objectives of this thesis, providing the foundation by identifying both the opportunities and limitations of current approaches in wearable self-powered sensing. It highlighted the

advantage of electrospinning in fabricating functional substrates and its potential to enhance triboelectric performance, while also revealing persistent gaps in achieving lightweight, flexible, and user-friendly devices. Furthermore, the review emphasized that the integration of structural design strategies such as fabrigami can provide the mechanical adaptability needed to overcome the shortcomings of rigid and bulky systems. These insights collectively justified the research direction of this thesis, which sought to bridge electrospinning with origami-inspired textile structures to advance the development of next-generation, sustainable, and continuous self-powered sensors for healthcare monitoring.

Building on the literature review, the experimental investigations in Chapter 3 provided critical methodological and technical insights into material selection, device fabrication, and performance characterization. Initial studies on electrospun CA/PCL demonstrated the feasibility of combining biodegradable polymers for TENG fabrication but also revealed their severe output limitations compared with literature benchmarks. This highlighted the need for material modification and structural enhancement to achieve practical self-powered sensing. Subsequent experimental work addressed this gap by chemically modifying CA with NaOH and incorporating chitosan into PCL, which significantly improved triboelectric performance. The optimized samples achieved output voltages up to 20.8 V and currents of 3.178 μA, alongside moderate sensitivity and rapid response times for respiratory monitoring applications. These findings confirmed that targeted material engineering through surface modification and polymer blending can overcome some of the limitations of raw biodegradable polymers and provide a pathway toward sustainable, high-performance wearable sensors.

Chapter 4 advanced the research by substituting PCL with PVDF while retaining CA as the tribopositive layer, resulting in a considerable improvement in TENG performance. Optimized electrospinning conditions enhanced fibre alignment and β phase which is highly regarded in PENG performance. This directly contributed to superior $V_{OC}$, $I_{SC}$, and $Q_{SC}$

outputs compared with the CA/PCL system. Experimental results have been supported by DDEF modelling and have validated the strong frequency and amplitude dependent behaviour of the CA/PVDF devices. Furthermore, the device confirmed the suitability of the optimised materials for pressure sensing with a sensitivity of 1.301 V/kPa. Application-oriented prototypes, including a glove-mounted sensor for finger bending detection and a shoe-integrated system for plantar pressure mapping, further demonstrated the practical potential of this material combination for rehabilitation and gait monitoring. At the same time, important limitations were identified, such as variability in manual tapping methods, the trade-off between durability and flexibility, and relatively low force sensitivity for body movement detection. These insights not only highlighted the strengths of the CA/PVDF approach but also outlined key directions for the optimizations achieved in chapter 5.

In chapter 5 material engineering strategies were further enhanced by incorporating AgNPs into CA to enhance tribopositive performance when paired with PVDF. Electrospinning produced uniform, bead-free fibres, and at an optimal loading of 1.5 wt.%, AgNPs improved fibre morphology, tensile strength, and charge-trapping capacity without compromising hydrophobicity. This translated into significant performance gains, with the Ag–CA/PVDF device achieving outputs of 155.9 V and a power density of 0.029 W $m^{-2}$, sufficient to drive small electronic devices as demonstrated by LED lighting and capacitor charging. KPFM, XPS, FTIR and XRD provided valuable insight on the Ag doping process on CA. According to the characterization it was evident that Ag provided charge trapping areas within the CA nanofibre network while enhancing overall TENG performance.

Furthermore, DDEF modelling provided valuable validation of charge distribution and device behaviour, reinforcing the experimental outcomes. Importantly, the device exhibited strong sensing capabilities, including high pressure sensitivity of 11.667 V/kPa in the low-pressure regime of 0-6.25 kPa. Fast response/recovery times, and stable cycling performance, making it particularly relevant for JBM where subtle force detection is

essential. Furthermore, overcoming the challenges in chapter 4 the new sample characterization technique including bespoke linear actuation system and Pyvisa based data acquisition with Keithley 6517B electrometer has provided the opportunity to develop an advanced sample characterization system.

The final experimental chapter, of this thesis, chapter 6, demonstrated the feasibility of integrating Ag–CA/PVDF based TENG materials into a fabrigami structure for JBM. For the first time the use of fabrigami for such delicate measurement is introduced and characterized with the knee used as a representative case study. By translating knee geometry into foldable designs and fabricating stable polyester-based origami structures through thermal imprinting, the research established a robust mechanism for geometry-modified contact separation based TENG wearable sensors. Six triboelectric pairs made with Ag-CA and PVDF were embedded into either side of each mountain fold, with conductive textiles enabling sequential activation that corresponded to knee flexion angles and dynamic movements. A compact wireless acquisition circuit, built on an nRF52840 BLE microcontroller, further enabled real-time data capture and mobile Bluetooth data transmission. Pilot demonstrations confirmed that the fabrigami sensor system could successfully monitor knee bending angles with 10-degree resolution, squatting, stair climbing, running, and walking, producing distinct activation patterns that resolved angle, frequency and speed measurements. These outcomes highlight the power of combining material-level development with structural design strategies, establishing a proof-of-concept for self-powered, wearable, and wireless JBM monitoring technologies with potential applications in rehabilitation, sports performance, and healthcare.

Table 5 has summarized some of the recent developments used for JBM with different techniques. Based on the comparison it is evident that the fabrigami device is the first device which has the ability to get a complete idea about the full joint flexion with 10-degree

resolution. Furthermore, the complete sensor is lightweight and comfortable to wear compared with rigid and bulky architectures typically found in recent developments.

Table 5: Comparison of fabrigami sensor with relevant range of motion detection-based literature.

| **Sensor type** | **Materials and methods** | **Sensing principle** | **Range of motion** |
|---|---|---|---|
| Textile resistive sensor (2019)[305] | Silver-coated yarn Agposs T1 sewn into denim fabric which attached to commercial elastic band | Resistance changes with the stretch | Activities such as walking and squatting with $30^0$ motion range |
| Origami-inspired electret-based triboelectric generator (2020)[306] | Two strips made from thick copper/LCP/copper sandwiched composite-with origami structure | Triboelectric self-powered sensing | Elbow bending movement at 90°, 120° and 150°.<br>Arm swinging movement at 30°, 60° and 90°.<br>Hand squeezing<br>Knee bending movement at 90°, 120° and 150° |
| Embroidered yarn for self-powered sensing and human machine interaction(2022).[307] | Plasma etched copper enamelled with polyurethane yarn and PTFE fabric.<br>Embroidered onto denim fabric | Triboelectric self-powered sensing | Can distinguish walking, running and jumping motions. |
| Low-hysteresis strain sensors using origami-inspired 3D mesostructured (2023)[308] | Origami-inspired foldable 3D mesoscale electrodes, featuring triangular multi-panel thin film on stretchable dielectric substrate with two electrodes | Capacitive field change due to electrode deformation. | Relative capacitances change at 0°, 45°, and 90° with respect to a uniaxial stretching of 70% strain. |
| Kirigami triboelectric spider fibroin microneedle patches for comprehensive joint management (2024)[309] | Spider fibroin microneedles with PU backing and transformed into Kirigami cuts. | Triboelectric with microneedles generate signals with bending. | Finger, wrist and elbow bending.<br>Nodding and twisting of head, walking and full flexion of knee |
| Strain Sensor Using Kirigami and Corrugated Structures (2025)[310] | Hydrothermal lead zirconate titanate layers on flexible substrate (embedded in silicone) elastic behaviour | Piezoelectric strain sensor | Full squat detection, full flexion of knee |

| | | | |
|---|---|---|---|
| | achieved with corrugated shape | | |
| Fabrigami sensor, 2025 (our work) | Ag-CA electrospun - tribopositive<br>PVDF electrospun – tribonegative<br>Attached onto fabrigami substrate | Triboelectric self-powered sensing | Full joint flexion (e.g. 0–90° knee) with $10^0$ movement detection.<br>Distinguishing speed, frequency of different angles, distinguishing different movements, walking, running, squatting and stair climbing. |

In summary, this thesis has systematically advanced the development of self-powered wearable sensors by bridging material innovation with structural design. Starting from the identification of literature gaps, the research progressed through feasibility studies on CA/PCL systems, material modification with chitosan and NaOH, improving output with replacing PCL with PVDF, and Ag nanoparticle reform for CA electrospun membrane to improve the sensitivity factor. Each stage provided critical methodological and technical insights, culminating in the integration of optimized Ag–CA/PVDF materials into a fabric-based origami architecture for real-time knee JBM. The pilot demonstrations of walking, running, stair climbing, squatting, and knee bending confirmed the feasibility of continuous, wireless, and self-powered wearable sensing. Collectively, these findings establish a proof-of-concept pathway for sustainable, biocompatible, and high-performance sensors with promising applications in rehabilitation, healthcare monitoring, and sports performance.

At the same time, the research acknowledges several limitations. The pilot study was restricted to a single participant, and while it successfully demonstrated device feasibility, broader trials involving around 20 participants will be required to validate statistical robustness and long-term wearability. Similarly, despite substantial material and structural improvements, challenges remain in enhancing low-force sensitivity, stabilizing charge

retention, and ensuring durability under repeated use. The next section of this chapter highlights on the overcoming procedures and future research avenues for this research area for advancing commercial level wearable JBM devices with TENG technology.

### 1.1. Future work recommendations

The thesis has overall justified self-powered sensing for JBM with advanced fabrigami and electrospun membranes-based systems. While the findings confirm strong potential, several limitations were identified during experimentation. Addressing these limitations presents a pathway toward the development of next-generation, robust, and sustainable TENG systems. This section outlines detailed recommendations for future work, structured as a research roadmap that expands on material, fabrication, characterization, structural, and application-level improvements.

**Sustainable Materials and Green Electrospinning**

One of the most pressing limitations identified in this study is the reliance on solvents, such as DMF, and polymers, such as PVDF. DMF is toxic, volatile, and environmentally hazardous, raising concerns about scalability and environmental impact. Similarly, PVDF, while an excellent tribonegative material due to its high dielectric constant and β-phase piezoelectricity, is a fluoropolymer. This class of materials is facing increasing inquiry due to concerns about their persistence in the environment and potential biocompatibility issues for long-term wearable applications.

Future work should prioritize the development of sustainable and eco-friendly solvent systems and polymers. For instance, water-based electrospinning has gained momentum, with several studies demonstrating the feasibility of using biopolymers such as chitosan, cellulose acetate, and polyvinyl alcohol. Furthermore, during the experiments, it was noticed that acetone can be used for CA electrospinning. On the material side, further investigation

into biopolymers with strong electron-donating or electron-withdrawing characteristics (e.g., silk fibroin, gelatine, alginate, or polypeptides) could identify substitutes for PVDF. A dual approach of developing both green solvents and biodegradable tribonegative counterparts will be necessary to ensure that future wearable sensors meet sustainability and regulatory expectations.

**Controlling environmental conditions during electrospinning**

Electrospun nanofibres are highly sensitive to subtle variations in ambient temperature and humidity, which can significantly influence fibre morphology, entanglement, and porosity. In some cases, even nanoscale and microscale surface structures can be induced by fluctuations in environmental conditions. During the experiments presented in this thesis, a bespoke electrospinning setup, located inside a fume hood, was used; however, the constant airflow within the hood altered the fibre deposition pathways and affected fibre morphology. As a result, considerable batch-to-batch variations were observed, and changes in seasonal weather patterns further amplified inconsistencies across experimental runs. To mitigate these issues, samples were fabricated on the same day under comparable conditions, but this approach offered only a partial solution.

Future research should therefore prioritise the use of closed-chamber electrospinning systems with precise control of humidity and temperature. Such systems would enable reproducible fibre morphologies and minimize uncontrolled environmental effects. Additionally, incorporating in situ monitoring technologies, such as motion-detection or high-speed camera systems, can provide valuable feedback for detecting morphological variations in real-time. Exploring alternative approaches, such as needleless electrospinning or advanced techniques outlined in Chapter 2, such as centrifugal or wet electrospinning, may also improve throughput while reducing variability. Together, these advancements

would enhance reproducibility, scalability, and ultimately the reliability of electrospun nanofibres for wearable triboelectric applications.

**Advanced surface and dielectric characterization**

The use of KPFM to measure the CPD before and after tapping was extremely challenging. Due to the changes in surface can create artifacts in the surface morphology figure thus resulting in changes in CPD values. In this thesis amplitude modulation based KPFM technique was used for the characterization and some research group has suggested that frequency modulation based KPFM provide more accurate CPD data. Considering that factor it is recommended to use frequency modulation based KPFM characterization for future research to get more accurate and better results for CPD and surface potential analysis.

A key limitation encountered in this work was the inability to perform reliable dielectric constant ($\varepsilon_r$) and dielectric loss measurements on electrospun films within the 1Hz–10 MHz range. Electrospun PVDF and Ag–CA samples are inherently porous, rough, and compressible, meaning that capacitance values are strongly affected by trapped air, surface roughness, moisture uptake, and imperfect electrode dielectric interfaces. According to IEC 62631-2-1 (Dielectric and resistive properties of solid insulating materials – Part 2-1: Relative permittivity and dissipation factor, 0.1 Hz–10 MHz), accurate dielectric spectroscopy requires guarded electrodes, metallized sample surfaces, and precise control of pressure and humidity during measurement[311]. Without this specialized setup, the production of capacitance vs frequency curves are prone to artifacts that reflect interface effects rather than the intrinsic dielectric response of the material. At present, such instrumentation was unavailable in our facility, and therefore dielectric characterization was not included in the reported results. Instead, the DDEF simulations used in this thesis were parameterized with well-documented $\varepsilon_r$ values for PVDF and Ag-CA from the literature,

following a transparent and widely accepted practice in the triboelectric nanogenerator community.

Moving forward, developing a dedicated test bench for low-frequency capacitance and dielectric spectroscopy of fibrous, porous films is a critical recommendation. Guard-ring electrode systems combined with humidity- and pressure-controlled chambers would allow the measurement of true dielectric constants in conditions that mimic wearable environments. Pairing dielectric measurements with surface potential mapping (via advanced frequency modulated KPFM or scanning surface potential microscopy) would allow for a multi-scale correlation of nanoscale charge storage with bulk dielectric response. Such approaches would not only validate the assumptions used in current simulations but also reveal how porosity, filler distribution, and interfacial polarization contribute to overall TENG performance.

**Development of standard testing protocol for TENG characterization**

The lack of a universal standard testing procedure for TENG characterization creates significant discrepancies when comparing the reported performance metrics across different research groups. As highlighted in the comprehensive review by Mulvihill et al., the need for such a standardization mechanism is both timely and urgent[312]. Specific attention must be given to controlling and reporting key variables, including applied mechanical excitation parameters (applied force, contact mechanism, frequency, and amplitude of motion), and the material fabrication method, surface topography, thickness and effective surface area of the substrates.

Furthermore, it is increasingly evident that atmospheric conditions have a strong influence on TENG output. As demonstrated in prior studies, moisture can alter surface charge density and dielectric behaviour, while temperature variations can affect polymer crystallinity and charge transport mechanisms. To ensure reproducibility and comparability of results, future

power characterization experiments must be conducted under standardized environmental conditions, in alignment with wearable electronic standards. Developing a test protocol that explicitly defines these parameters will reduce inconsistencies between laboratories and accelerate progress toward reliable benchmarks for wearable TENG devices.

**Comprehensive power and efficiency evaluation**

In this thesis, the electrical performance of the TENG was characterized primarily through open-circuit voltage measurements and by estimating power output using the $V^2/R$ relationship across different resistive loads. While this method is widely used and accepted in the literature, it only provides instantaneous peak power values, which may not accurately represent the average or continuous power generation capability of the device. Due to the pulsed, intermittent, and nonlinear nature of TENG power output, such an approach can lead to an overestimation of energy harvesting potential, especially when translating laboratory-scale results into practical, real-world applications.

For future work, simultaneous measurement of both voltage and current waveforms across a range of load resistances should be adopted. By capturing time resolved current and voltage data, it becomes possible to calculate the true instantaneous power = $Voltage(V) \times Current(t)$ and subsequently derive average power and energy density metrics over multiple cycles. This approach would provide a more realistic understanding of the effective energy harvesting capability of TENGs, particularly under dynamic human motion conditions where loading is nonuniform.

A related challenge lies in the quantification of power conversion efficiency. TENG devices efficiency characterization remains difficult to standardize because of the interplay between mechanical input energy, triboelectric charge transfer, and electrostatic energy storage. Reported methods in the field vary significantly, with some groups focusing on output-to-input energy ratios and others employing normalized power densities. Establishing a

consistent methodology for PCE measurement is crucial for comparing different material systems and device architectures. Future studies should therefore aim to couple electrical power output measurements with mechanical input energy quantification, for example, by measuring applied force, displacement, and frequency using a tribometer or dynamic mechanical analyser targeting actual power conversion efficiency.

**Fabrigami structure optimization**

The fabrigami approach introduced in this thesis demonstrates a promising pathway for incorporating foldable, fabric-based origami designs into JBM applications. However, several critical structural parameters, including damping behaviour, pressure distribution between folds, and characterization of folding fatigue, remain inadequate. These mechanical factors directly influence the quality of contact–separation events, as well as the sensitivity and durability of the device.

Future research should prioritize systematic mechanical characterization of fabrigami folds to better understand their dynamic behaviour. This includes conducting force–displacement analyses, determining damping coefficients, and measuring fold contact pressures during dynamic bending cycles. Finite element modelling can provide valuable insights by simulating fold stresses and enabling the optimization of key design parameters, such as panel lengths, fold angles, and material layering configurations.

Furthermore, there is considerable potential in translating origami folding principles into textile manufacturing-compatible processes, such as knitting, weaving, or jacquard patterning. This approach could enable the scalable production of fabrigami structures that retain their geometric tunability while simultaneously offering improved comfort, washability, and long-term durability, which are necessary for practical wearable applications.

Furthermore, it is vital to carryout wearable testing such as washability, breathability, abrasion resistance, biocompatibility, durability and moisture management properties for TENG sensor and attached fabric substrates to promote practically wearable sensor system.

**Large scale statistical validation**

The current pilot study for evaluating sensor performance is statistically insignificant, as it involves only one participant. Human biomechanics changes across individuals due to factors such as age, gender, fitness level, weight, and height. Considering these factors, it is essential to conduct extensive clinical trials with a more diverse range of ages, genders, fitness levels, heights, weights, and ethnic backgrounds to develop real-world, commercially viable applications. This sensor characterization should be compared with a gold standard technique, such as motion capture using Vicon or inertial measurement units.

Furthermore, the current device is designed for monitoring knee JBM, and this functionality needs to be extended to other joints in the human body. These will provide more realistic applications for the future wearable market.

**Integration with energy storage and hybrid systems**

While this work primarily targeted sensing, a self-powered wearable system ultimately requires integration with energy management and storage system. With the current scenario, a battery powered circuit has been employed for processing and sending data via Bluetooth technology. Small-scale storage elements, such as supercapacitors or flexible batteries could be directly coupled to the fabrigami TENG to buffer the harvested energy.

Future work should investigate hybrid systems that combine TENGs with complementary harvesting technologies such as PENG, TEG, or SEG devices. Such hybrid systems could ensure a more continuous energy supply by leveraging different forms of biomechanical and

environmental energy. Integration with energy management circuits capable of rectification, step-up conversion, and regulated output would further expand practical applicability.

**Biocompatibility and toxicity analysis**

The literature review section 2.7 and appendix B highlighted that there are materials that need to be minimally used or carefully controlled to ensure the sensors remain biocompatible and nontoxic. Materials such as PVDF (due to excessive use of harmful solvents such as DMF, DMAc) and Ag (if concentration is too high) are currently under debate as cytotoxic in nature if used in excessive amounts and subjected to prolonged contact with human skin[313,314]. Considering those factors, it is important to carry out biocompatibility tests, including cytotoxicity, irritation, and sensitization, to check if the device is harmful for living cells. The ISO 10993 is the standard testing procedure that covers these aspects of biocompatibility testing, and in future, all samples developed should undergo this procedure before carrying out large-scale clinical trials[315].

**Recommendations for next generation of TENG researchers**

TENG related Research into TENGs is becoming increasingly prominent, targeting energy harvesting and self-powered sensing applications. This thesis will provide the initial step for anyone who is willing to integrate TENG with traditional textile manufacturing. The findings of this research strongly suggest that TENG holds a more promising future in self-powered sensing applications than in large-scale energy harvesting. Furthermore, the integration of TENG sensors into daily-wear fabrics presents an excellent opportunity to monitor human kinematics while achieving a necessary balance between wearability and functional performance. Given that the textile engineering field is a well-established discipline, the incorporation of TENG architectures with modified, scalable textile manufacturing concepts offers the most rapid pathway to industrial solutions for the ever-growing wearable electronics market.

**APPENDIX A**

**Standard testing procedure for wearable characterization recommended for wearable electronics**

| Category | Type | Required property | Testing standard |
|---|---|---|---|
| Structure related testing | Fibre/yarn | Linear density (weight) | ASTM D1577 - 07(2018) |
| | | Evenness | ASTM D1425 / D1425M - 14(2020) |
| | Fabric | Area density | ASTM D3776 / D3776M - 09a (2017), ISO 3801:1977 |
| | | Thickness | ASTM D1777 - 96(2019) |
| | | Drapability | Pierce's cantilever method/ Rotrakote CISICK drape tester /3D body scanner techniques |
| Durability related testing | Fibre/yarn | Tensile strength | ASTM D2256 / D2256M - 10(2015) |
| | Fabric | Tensile strength | ISO 13934-1:1999/ ASTM D5035-95/ AS 4878.6-2001(specifically used when external coating is applied) |
| | | Tearing strength (specifically woven) | ISO 4674-1998 /ASTM D1423-83/ BS 3424 standard (for coated fabrics) |
| | | Bursting strength (specifically knitted) | ISO 3303-1995/ BS 3424/ ASTM D3787 |
| | | Abrasion resistance | ISO 13934-1:2013/, ASTM D5035 - 11(2019) |
| | | Dimensional stability after washing | BS EN ISO 3759:1995 /, BS EN ISO 6330:2001 |
| | | Conductivity after washing or laundering | ASTM (ASTM WK61480) (new test) |
| Comfort and aesthetic related testing | Fabric | Air permeability | BS 5636, ASTM D 7534. |
| | | Moisture management [+] | AATCC 195 |
| | | Thermal comfort | ASTM D7140 /, D7140M - 13(2017) |
| | | Colour fastness | ISO-105 |
| Safety related properties | Fabric | Flammability [++] | BS 5438/ EN ISO 6941/, BS EN ISO 15025:2002/, BS EN 367:1992 (ISO 9151) |
| Specific property testing | Fabric | Shape memory effect of fabric [+++] | AATCC 66-1998 |
| | | Superhydrophobic property | AATCC 195 |
| | | Conductivity of textile | BS EN IEC 63203-201-1/ BS EN IEC 63203-201-3 |

Adopted from ref [3,240,316–325]

**APPENDIX B**

**Maximum allowable limit and testing standards for certain materials used in wearable self-powered wireless communications systems.**

| Material | Maximum allowable level in finished product | Potential use in textile processing | Testing standard |
|---|---|---|---|
| Acetophenone | 50 ppm | - | Extraction with MeOH / GC-MS |
| 2-Phenyl-2-Propanol | 50 ppm | - | Extraction with MeOH/GC-MS |
| Extractable Antimony | 60 ppm | Textile, leather, polymers (R.F.A.) | DIN EN ISO 105-E04 (2013) (acid sweat solution)// ISO 17294-2 (2003) or DIN EN ISO 11885 (2009) |
| Extractable Arsenic | 25 ppm | Textile, leather, polymers (R.F.A.) | DIN EN ISO 105-E04 (2013) (acid sweat solution)// ISO 17294-2 (2003) or DIN EN ISO 11885 (2009) |
| Extractable Barium | 1000 ppm | Textile, leather, polymers (R.F.A.) | EN 71-3<br>CNS 4797-4 |
| Total Cadmium | Adults: 75 ppm<br>Children: 40 ppm | Textile, leather, polymers (R.F.A.) | EN 1122 (2001)/<br>ISO 17294-2 (2003) or DIN EN ISO 11885 (2009)<br>Total digestion /<br>ISO 17294-2 (2003) or DIN EN ISO 11885 (2009) |
| Extractable Chromium | 60 ppm | Textile, leather, polymers (R.F.A.) | Textile: DIN EN ISO 105-E04 (2013) (acid sweat solution) // ICP<br>Leather: 17075 (2008) |
| Extractable Cobalt | Adults: 4 ppm<br>Children: 1 ppm | Textile, leather, polymers (R.F.A.) | DIN EN ISO 105-E04 (2013) (acid sweat solution)// ISO 17294-2 (2003) or DIN EN ISO 11885 (2009) |
| Extractable Copper | Adults: 50 ppm<br>Children: 25 ppm | Textile, leather, polymers (R.F.A.) | DIN EN ISO 105-E04 (2013) (acid sweat solution)// ISO 17294-2 (2003) or DIN EN ISO 11885 (2009) |
| Total Lead | 90 ppm | Textile, leather, polymers (R.F.A.) | Total digestion /<br>ISO 17294-2 (2003) or DIN EN ISO 11885 (2009) |
| Extractable Lead | Total: 90 ppm<br>Adults and children: 1 ppm<br>Babies: 0.2 ppm | Textile, leather, polymers (R.F.A.) | DIN EN ISO 105-E04 (2013) (acid sweat solution)// ISO 17294-2 (2003) or DIN EN ISO 11885 (2009) |

| | | | |
|---|---|---|---|
| Fluorene | 10 ppm | Textile, leather, polymers (R.F.A.) | |
| DMF | 500 ppm | Candidate list* | |
| Formamide | 1000 ppm | - | |
| Dimethylacetamide (DMAC) | 1000 ppm | Candidate list* | Headspace /GC-MS or Textile: Extraction with MeOH / GC-MS or LC-MS, Plastic: 2-step Extraction with THF and MeOH / GC-MS or LC-MS |
| N-Methyl-2-pyrrolidone (NMP) | 1000 ppm | Candidate list* | |
| 2-methoxypropanol | - | Candidate list* | |
| Toluene | - | Candidate list* | Headspace /GC-MS |
| Methanol | - | Candidate list* | |
| Ethylbenzene | - | Candidate list* | |
| 2-(2-methoxyethoxy)-ethanol | - | Candidate list* | |
| Methylene chloride | - | Textile, leather, polymers (R.F.A.) | |
| Benzene | 5 ppm | Textile, leather, polymers (R.F.A.) | Headspace /GC-MS |
| Carbon Disulfide/Carbon Tetrachloride/Chloroform/Cyclohexanone | 1000 ppm | - | |
| 1,2-Dichloroethane and Tetrachloroethylene (PERC) | 1000 ppm | Textile, leather, polymers (R.F.A.) | Headspace GC-MS |
| Ethylbenzene and Toluene | 1000 ppm | Candidate list* | |
| Trichloroethylene | 1000 ppm | Textile, leather, polymers (R.F.A.) | Headspace /GC-MS |

Adopted from ref [245,326]*Candidate list comprises chemical substances that may pose a hazard, but the evidence is not conclusive. Therefore, these items are not yet included in the Manufacturing Restricted Substances List

**APPENDIX C**

**Current and charge modelling with the change of frequency in constant amplitude**

```
import numpy as np
from scipy.integrate import quad
import matplotlib.pyplot as plt

# Constants for the test condition
permittivity = 8.85418782e-12
epsilon_1 = 3.3* permittivity
epsilon_2 = 10 * permittivity
charge_density = 75.85e-6
d_1 = 57e-6
d_2 = 55e-6
amplitude = 5e-3

# To draft figure with 5s interval for each frequency
intervals = [(0, 5, 1), (5, 10, 2), (10, 15, 3), (15, 20, 4), (20, 25, 5)]
t_val = np.concatenate([np.arange(start, end, (end - start) / 5000) for start, end, _ in intervals])
frequencies = np.concatenate([[freq] * 5000 for _, _, freq in intervals])

# Define the function Y(x)
def Y(x):
    return x*np.arctan((4*1e-4)/(x*np.sqrt((x**2)+8*1e-4)))-2*1e 2*np.log((np.sqrt((x**2)+8*1e-4)+2*1e-2)/(np.sqrt((x**2)+8*1e-4)-2*1e-2))

# Define Q_SC (Charge density)_at_time function with variable frequency
def Q_SC_at_time(t, frequency):
    # x_0 changes with time
    d = amplitude * np.sin(2 * np.pi * frequency * t + 1.5 * np.pi) + amplitude  # mm
    # Perform the integrals with time-dependent x_0
    integral_1, _ = quad(Y, d_1, d_1 + d)
    integral_2, _ = quad(Y, d_2, d_2 + d)
    integral_3, _ = quad(Y, 0, d_1 + d_2 + d)
```

```
    # Calculate Q_OC at time t
    return charge_density * (((1 / epsilon_1) * integral_1) + ((1 / epsilon_2) * integral_2)) / (((1 / epsilon_1) + (1 / epsilon_2)) * integral_3) * 1e6


# Calculate Q_SC for all time points with variable frequencies
Q_SC_values = np.array([Q_SC_at_time(t, freq) for t, freq in zip(t_val, frequencies)])
tstep = (t_val[-1] - t_val[0]) / len(t_val)


colors = ['blue', 'green', 'red', 'purple', 'orange']


# Plot Q_SC over time with color segments
plt.figure(figsize=(10, 6))
for i, (start, end, freq) in enumerate(intervals):
    mask = (t_val >= start) & (t_val < end)
    plt.plot(t_val[mask], Q_SC_values[mask], color=colors[i], label=f'Freq = {freq} Hz')


plt.xlabel('Time (s)')
plt.ylabel('Charge Density ($\mu$C/m$^2$)')
plt.title('Free Charge Density Q_SC(t) over Time with Variable Frequency')
plt.legend(loc='upper center', bbox_to_anchor=(0.5, -0.2), ncol=5)
plt.grid(True)
plt.tight_layout(rect=[0, 0.15, 1, 1])
plt.savefig("E:/python examples/results/Q_SC(CA).jpg",bbox_inches='tight', pad_inches=0.2)
plt.show()


# Calculate and plot J_SC (Short circuit current density)
dQ_SC_dt = np.gradient(Q_SC_values, tstep)
J_SC_mili = dQ_SC_dt * 1e-3  # convert to mA/cm^2


# Plot J_SC over time with color segments
plt.figure(figsize=(10, 6))
for i, (start, end, freq) in enumerate(intervals):
    mask = (t_val >= start) & (t_val < end)
```

```
    plt.plot(t_val[mask], J_SC_mili[mask], color=colors[i], label=f'Freq = {freq} Hz')


plt.xlabel('Time (s)')
plt.ylabel('Current density (mA/m$^2$)')
plt.title('Short Circuit Current Density J_SC(t) over Time with variable Frequency')
plt.legend(loc='upper center', bbox_to_anchor=(0.5, -0.2), ncol=5)
plt.grid(True)
plt.tight_layout(rect=[0, 0.15, 1, 1])
plt.savefig("E:/python examples/results/J_SC(CA).jpg",bbox_inches='tight',
pad_inches=0.2)
plt.show()


# Calculate and plot I_SC (Short circuit current)
I_SC_values = dQ_SC_dt * 1600 * 1e-6  # convert to A/cm^2


# Plot I_SC (Short circuit current) over time with color segments
plt.figure(figsize=(10, 6))
for i, (start, end, freq) in enumerate(intervals):
    mask = (t_val >= start) & (t_val < end)
    plt.plot(t_val[mask], I_SC_values[mask], color=colors[i], label=f'Freq = {freq} Hz')


plt.xlabel('Time (s)')
plt.ylabel('Short Circuit current ($\mu$A)')
plt.title('Short Circuit Current I_SC(t) over Time with variable Frequency')
plt.legend(loc='upper center', bbox_to_anchor=(0.5, -0.2), ncol=5)
plt.grid(True)
plt.tight_layout(rect=[0, 0.15, 1, 1])
plt.savefig("E:/python examples/results/I_SC(CA).jpg",bbox_inches='tight',
pad_inches=0.2)
plt.show()
```

**APPENDIX D**

**Current and charge modelling with the change of amplitude in constant frequency**

```
import numpy as np
from scipy.integrate import quad
import matplotlib.pyplot as plt


# Constants
permittivity = 8.85418782e-12
epsilon_1 = 3.3 * permittivity
epsilon_2 = 10 * permittivity
charge_density = 39.5*1e-6
d_1 = 57e-6
d_2 = 55e-6
frequency = 2


# Define time intervals and amplitudes
intervals = [    (0, 5, 1e-3), (5, 10, 2e-3), (10, 15, 3e-3), (15, 20, 4e-3),
   (20, 25, 5e-3), (25, 30, 6e-3), (30, 35, 7e-3), (35, 40, 8e-3),
   (40, 45, 9e-3), (45, 50, 10e-3)]


t_val = np.concatenate([np.arange(start, end, (end - start) / 1000) for start, end, _ in
intervals])


amplitudes = np.concatenate([[amp] * 1000 for _, _, amp in intervals])



# Define the function Y(x)
def Y(x):
   return x*np.arctan((4*1e-4)/(x*np.sqrt((x**2)+8*1e-4)))-2*1e-
2*np.log((np.sqrt((x**2)+8*1e-4)+2*1e-2)/(np.sqrt((x**2)+8*1e-4)-2*1e-2))


# Define Q_SC_at_time function with variable amplitude
def Q_SC_at_time(t, amplitude):
   d = amplitude * np.sin(2 * np.pi * frequency * t + 1.5 * np.pi) + amplitude  # mm
```

```
    integral_1, _ = quad(Y, d_1, d_1 + d)
    integral_2, _ = quad(Y, d_2, d_2 + d)
    integral_3, _ = quad(Y, 0, d_1 + d_2 + d)
    return charge_density * (((1 / epsilon_1) * integral_1) + ((1 / epsilon_2) * integral_2)) / (((1 / epsilon_1) + (1 / epsilon_2)) * integral_3) * 1e6


# Calculate Q_SC for all time points with variable amplitudes
Q_SC_values = np.array([Q_SC_at_time(t, amp) for t, amp in zip(t_val, amplitudes)])
tstep = (t_val[-1] - t_val[0]) / len(t_val)


# Colors for each interval
colors = ['blue', 'green', 'red', 'purple', 'orange', 'cyan', 'magenta', 'brown', 'gray', 'pink']


# Plot Q_SC over time with color segments and legend
plt.figure(figsize=(10, 6))
for i, (start, end, amp) in enumerate(intervals):
    mask = (t_val >= start) & (t_val < end)
    plt.plot(t_val[mask], Q_SC_values[mask], color=colors[i], label=f'Amp = {amp*1e3:.0f} mm')


plt.xlabel('Time (s)')
plt.ylabel(r'Charge Density ($\mu$C/m$^2$)')
plt.title('Free Charge Density Q_SC(t) over Time with Variable Amplitude')
plt.legend(loc='upper center', bbox_to_anchor=(0.5, -0.2), ncol=5)
plt.grid(True)
plt.tight_layout(rect=[0, 0.15, 1, 1])
plt.savefig("E:/python examples/results/Q_SC_amp(CA).jpg",bbox_inches='tight', pad_inches=0.2)
plt.show()


# Calculate the derivative of Q_SC over time to get J_SC
dQ_SC_dt = np.gradient(Q_SC_values, tstep)
J_SC_mili = dQ_SC_dt * 1e-3  # Convert to mA/m² for plotting
I_SC_values = dQ_SC_dt * 1600 * 1e-6  # Convert to A for plotting
```

```
# Plot J_SC over time with color segments and legend
plt.figure(figsize=(10, 6))
for i, (start, end, amp) in enumerate(intervals):
    mask = (t_val >= start) & (t_val < end)
    plt.plot(t_val[mask], J_SC_mili[mask], color=colors[i], label=f'Amp = {amp*1e3:.0f} mm')
plt.xlabel('Time (s)')
plt.ylabel(r'Current Density(mA/m²)')
plt.title('Short Circuit Current Density J_SC(t) over Time with Variable Amplitude')
plt.legend(loc='upper center', bbox_to_anchor=(0.5, -0.2), ncol=5)
plt.grid(True)
plt.tight_layout(rect=[0, 0.15, 1, 1])
plt.savefig("E:/python examples/results/J_SC_amp(CA).jpg",bbox_inches='tight', pad_inches=0.2)
plt.show()


# Plot I_SC over time with color segments and legend
plt.figure(figsize=(10, 6))
for i, (start, end, amp) in enumerate(intervals):
    mask = (t_val >= start) & (t_val < end)
    plt.plot(t_val[mask], I_SC_values[mask], color=colors[i], label=f'Amp = {amp*1e3:.0f} mm')
plt.xlabel('Time (s)')
plt.ylabel(r'Short circuit current ($\mu$A)')
plt.title('Short Circuit Current I_SC(t) over Time with Variable Amplitude')
plt.legend(loc='upper center', bbox_to_anchor=(0.5, -0.2), ncol=5)
plt.grid(True)
plt.tight_layout(rect=[0, 0.15, 1, 1])
plt.savefig("E:/python examples/results/I_SC_amp(CA).jpg", bbox_inches='tight', pad_inches=0.2)
plt.show()
```

**APPENDIX E**

**Voltage modelling with the change of frequency in constant amplitude**

```
import numpy as np
from scipy.integrate import quad
import matplotlib.pyplot as plt


# Constants
permittivity = 8.85418782e-12
epsilon_1 = 3.3 * permittivity
epsilon_2 = 10 * permittivity
charge_density = 39.5e-6  # Amplitude is fixed
d_1 = 57e-6
d_2 = 55e-6
amplitude = 5e-3


# Define intervals and frequencies
intervals = [    (0, 5, 1), (5, 10, 2), (10, 15, 3), (15, 20, 4), (20, 25, 5)]


t_val = np.concatenate([np.arange(start, end, (end - start) / 1000) for start, end, _ in
intervals])


frequencies = np.concatenate([[freq] * 1000 for _, _, freq in intervals])
# Define the function Y(x)
def Y(x):
    return x*np.arctan((4*1e-4)/(x*np.sqrt((x**2)+8*1e-4)))-2*1e-
2*np.log((np.sqrt((x**2)+8*1e-4)+2*1e-2)/(np.sqrt((x**2)+8*1e-4)-2*1e-2))
# Define V_OC_at_time function with variable frequency
def V_OC_at_time(t, frequency):
    x = amplitude * np.sin(2 * np.pi * frequency * t + 1.5 * np.pi) + amplitude # mm
    integral_1, _ = quad(Y, d_1, d_1 + x)
    integral_2, _ = quad(Y, d_2, d_2 + x)
    return (charge_density / np.pi) * (((1 / epsilon_2) * integral_2) - ((1 / epsilon_1) *
integral_1))
```

```
# Calculate V_OC for all time points with variable frequencies
V_OC_values = np.array([V_OC_at_time(t, freq) for t, freq in zip(t_val, frequencies)])

# Colors for each interval
colors = ['blue', 'green', 'red', 'purple', 'orange']

# Plot V_OC over time with color segments and legend
plt.figure(figsize=(10, 6))
for i, (start, end, freq) in enumerate(intervals):
    mask = (t_val >= start) & (t_val < end)
    plt.plot(t_val[mask], V_OC_values[mask], color=colors[i], label=f'Freq = {freq} Hz')

plt.xlabel('Time (s)')
plt.ylabel(r'Open Circuit voltage (V)')
plt.title('Open-Circuit Voltage V_OC(t) over Time with Variable Frequency')
plt.legend(loc='upper center', bbox_to_anchor=(0.5, -0.2), ncol=5)
plt.grid(True)
plt.tight_layout(rect=[0, 0.15, 1, 1])
plt.savefig("E:/python examples/results/V_OC_freq(CA).jpg",bbox_inches='tight',
pad_inches=0.2,dpi=300)
plt.show()
```

**APPENDIX F**

**Voltage modelling with the change of amplitude in constant frequency**

```
import numpy as np
from scipy.integrate import quad
import matplotlib.pyplot as plt


# Constants
permittivity = 8.85418782e-12
epsilon_1 = 3.3 * permittivity
epsilon_2 = 10 * permittivity
charge_density = 39.5e-6
frequency = 2
d_1 = 57e-6
d_2 = 55e-6


intervals = [    (0, 5, 1e-3), (5, 10, 2e-3), (10, 15, 3e-3), (15, 20, 4e-3),
   (20, 25, 5e-3), (25, 30, 6e-3), (30, 35, 7e-3), (35, 40, 8e-3),
   (40, 45, 9e-3), (45, 50, 10e-3)# interval definition]
t_val = np.concatenate([np.arange(start, end, (end - start) / 1000) for start, end, _ in
intervals])
amplitudes = np.concatenate([[amp] * 1000 for _, _, amp in intervals])


def Y(x):
   return x*np.arctan((4*1e-4)/(x*np.sqrt((x**2)+8*1e-4)))-2*1e-
2*np.log((np.sqrt((x**2)+8*1e-4)+2*1e-2)/(np.sqrt((x**2)+8*1e-4)-2*1e-2))
#np.arctan((4e-2) / (x * np.sqrt((x**2) + 8e-4)))
def V_OC_at_time(t, amplitude):#V_OC_at_time function with variable amplitude
   x = amplitude * np.sin(2 * np.pi * frequency * t + 1.5 * np.pi) + amplitude  # mm
   integral_1, _ = quad(Y, d_1, d_1 + x)
   integral_2, _ = quad(Y, d_2, d_2 + x)
   return (charge_density / np.pi) * ((-(1 / epsilon_1) * integral_1) + ((1 / epsilon_2) *
integral_2))


V_OC_values = np.array([V_OC_at_time(t, amp) for t, amp in zip(t_val, amplitudes)])#
V_OC for all time points with variable amplitudes
```

```
colors = ['blue', 'green', 'red', 'purple', 'orange', 'cyan', 'magenta', 'brown', 'gray', 'pink']
plt.figure(figsize=(10, 6)) #V_OC over time with color segments and legend
for i, (start, end, amp) in enumerate(intervals):
    mask = (t_val >= start) & (t_val < end)
    plt.plot(t_val[mask], V_OC_values[mask], color=colors[i], label=f'Amp = {amp*1e3:.0f} mm')


plt.xlabel('Time (s)')
plt.ylabel(r'Open cicuit voltage (V)')
plt.title('Open-Circuit Voltage V_OC(t) over Time with Variable Amplitude')
plt.legend(loc='upper center', bbox_to_anchor=(0.5, -0.2), ncol=5)
plt.grid(True)
plt.tight_layout(rect=[0, 0.15, 1, 1])
plt.savefig("E:/python examples/results/V_SC_amp(CA).jpg",bbox_inches='tight', pad_inches=0.2)
plt.show()
```

## APPENDIX G

### Arduino code for foot pressure monitoring system

```
int top = 0;
int left = 0;
int right = 0;
int bottom = 0;
String top1;
String right1;
String left1;
String bottom1;
void setup() {
  // put your setup code here, to run once:
  Serial.begin(115200);
}

void loop() {
  // put your main code here, to run repeatedly:
  top = analogRead(A2);
  right = analogRead(A4);
  left = analogRead(A3);
  bottom = analogRead(A5);
  if (top> 4) {
    top1 = "a";
    Serial.println("S1000E");
    delay(300);
  }
  if (right>4){
    right1 = "a";
    Serial.println("S0100E");
    delay(300);
  }
  if (left>5){
    left1 = "a";
    Serial.println("S0010E");
    delay(300);
```

```
  }
  if (bottom>5){
    bottom1 = "a";
    Serial.println("S0001E");
    delay(300);
  }
  String data = String("S")+top1+right1+left1+bottom1+String("E");
  Serial.println(data);
  top1="0";
  right1="0";
  bottom1="0";
  left1="0";
}
```

# APPENDIX H

## Processing code for foot pressure monitoring system

```
import processing.serial.*;

Serial myPort;
String portStream;
int top = 0;
int right = 0;
int left = 0;
int bottom = 0;
PImage bg;
void setup(){
  size (421,969);
  bg = loadImage("black-foot-imprint-smooth-vector-8635853.jpg");
  background(bg);
  //stroke (160);
  //fill (50);
  String portName=Serial.list()[0];
  myPort = new Serial(this,portName,115200);
  myPort.bufferUntil('\n');
}
void draw(){
  if(portStream!=null){
    if (portStream.length()==8 && portStream.charAt(0)=='S' && portStream.charAt(5)=='E'){
      top = int(portStream.substring(1,2));
      right = int(portStream.substring(2,3));
      left = int(portStream.substring(3,4));
      bottom = int(portStream.substring(4,5));
      if (top == 1){
        fill(0,255,0);
      }
      else{
        fill (255,0,0);
      }
      rect(180,320,50,50);
      if (right == 1){
        fill(0,255,0);
      }
      else{
        fill (255,0,0);
      }
      rect(270,530,50,50);
      if (left == 1){
        fill(0,255,0);
      }
      else{
        fill (255,0,0);
      }
      rect(150,600,50,50);
      if (bottom == 1){
        fill(0,255,0);
      }
      else{
        fill (255,0,0);
      }
      rect(150,850,50,50);
      delay(100);
    }
  }
}
void serialEvent(Serial myPort){
  portStream =myPort.readString();
}
```

**APPENDIX I**

**Charge recording with py visa using Keithley 6517B**

```
import pyvisa
import time
import numpy as np
import pandas as pd

data_points = 5000 # N value needs to update with this value
time_s = 15

# Connect to the Keithley 6517B
visa_address = 'GPIB0::27::INSTR'  # Replace with the actual address (GPIB)
rm = pyvisa.ResourceManager()
keithley = rm.open_resource(visa_address)
keithley.write('*RST')
# Check for any existing errors or status from the instrument
error_status = keithley.query('SYSTEM:ERROR?')
print('Initial Error Status:', error_status)

# Configure the instrument for current measurement
keithley.write(':SENSE:FUNC "CHAR"')  # Set to charge measurement mode
keithley.write(':SENSE:CHAR:RANGE 200E-9')  # Set charge range (e.g., 200 nC range)
keithley.write(':SENSE:CHAR:NPLC 0.01')  # Set NPLC
keithley.write(':SENS:CHAR:MED:STAT OFF')  # Turn off median filtering
keithley.write(':SYST:ZCH OFF')  # Disable zero check

# Disable the display for better performance
keithley.write(':DISP:ENABLE OFF')
keithley.write(':SYST:LSYNC:STAT 0')

# Clear the trace and set up data collection
keithley.write(':TRACe:CLEAR')
keithley.write(':TRACE:ELEM TST')
```

```
keithley.write(':TRACE:POINTS 5000')  # Collect N data points
keithley.write(':TRIG:COUNT 5000')  # Trigger N measurements
keithley.write(':TRIG:DELAY 0')  # No delay between triggers
keithley.write(':TRACE:FEED:CONTROL NEXT')  # Feed data point by point

# Initialize the measurement process
keithley.write(':INIT')
# Allow some time for measurements to be taken
time.sleep(time_s)  # Set this time based on number of data points and time

# Query the data from the trace buffer
trace_data = keithley.query("TRAC:DATA?")
buffer_array = np.array([trace_data.split('#')])

flattened_data = buffer_array.flatten()
filtered_data = [entry for entry in flattened_data if entry.strip()]  # Remove newlines or empty entries

# Extract charge (NCOUL) and time (secs) values
Charge = []
time = []

for entry in filtered_data:
    if entry[0] != ',':
        entry = ',' + entry
    parts = entry.split(',')
    NCOUL_value = parts[1].replace('NCOUL', '').strip()
    secs_value = parts[2].replace('secs', '').strip()
   Charge.append(float(NCOUL_value))  # Convert to float
    time.append(float(secs_value))  # Convert to float

# Create a DataFrame
df = pd.DataFrame({    'Time(s)': time, 'Charge(C)': Charge})
```

```
# Save the DataFrame to an Excel file
output_file = 'Charge_new.xlsx'
df.to_excel(output_file, index=False)
print(f"Data saved to {output_file}")
keithley.write(':SYST:ZCH ON')
keithley.write(':DISP:ENABLE ON')

# Check the status of the instrument after the measurement
final_error_status = keithley.query('SYSTEM:ERROR?')
print('Final Error Status:', final_error_status)

# Close the connection to the instrument
keithley.close()
```

**APPENDIX J**

**Current recoding modification for the code with pyvisa for Keithley 6517B**

```
# Configure the instrument for current measurement
keithley.write(':SENSE:FUNC "CURR"')  # Set to current measurement mode
keithley.write(':SENSE:CURR:RANGE 20E-6')  # Set current range (e.g., 2uA range)
keithley.write(':SENSE:CURR:NPLC 0.01')  # Set NPLC for averaging (default to 1)
keithley.write(':SENS:CURR:MED:STAT OFF')  # Turn off median filtering
keithley.write(':SYST:ZCH OFF')  # Disable zero check

# Disable the display for better performance (if needed)
keithley.write(':DISP:ENABLE OFF')
keithley.write(':SYST:LSYNC:STAT 0')

# Clear the trace and set up data collection
keithley.write(':TRACe:CLEAR')
keithley.write(':TRACE:ELEM TST')
keithley.write(':TRACE:POINTS 5000')  # Collect N data points
keithley.write(':TRIG:COUNT 5000')  # Trigger N measurements
keithley.write(':TRIG:DELAY 0')  # No delay between triggers
keithley.write(':TRACE:FEED:CONTROL NEXT')  # Feed data point by point

# Initialize the measurement process
keithley.write(':INIT')
# Allow some time for measurements to be taken
time.sleep(time_s)  # Set this time based on number of data points and time

# Query the data from the trace buffer
trace_data = keithley.query("TRAC:DATA?")
buffer_array = np.array([trace_data.split('#')])

flattened_data = buffer_array.flatten()
filtered_data = [entry for entry in flattened_data if entry.strip()]  # Remove newlines or empty entries
```

```
# Extract current (NADC) and time (secs) values
current = []
time = []

for entry in filtered_data:
    if entry[0] != ',':
        entry = ',' + entry
    parts = entry.split(',')
    nadc_value = parts[1].replace('NADC', '').strip()
    secs_value = parts[2].replace('secs', '').strip()
    current.append(float(nadc_value))  # Convert to float
    time.append(float(secs_value))  # Convert to float

# Create a DataFrame
df = pd.DataFrame({ 'Time(s)': time, 'Current(A)': current})

# Save the DataFrame to an Excel file
output_file = 'Current_new.xlsx'
df.to_excel(output_file, index=False)
print(f"Data saved to {output_file}")
```

**APPENDIX K**

For comparing the sensor performance with previously published results (Table S1) a literature surway was conducted using following criteriars.

Material fabrication – at least one triboelectric layer is modified via electrospinning

Applicaton – Wearable signal monitoring or related pressure sensitivty

Pressure sensitivty – V $kPa^{-1}$

Summarization of previously developed electrospun layer based wearable sensors.

| Year | Materials | Energy harvesting performance | Self-powered sensing performance | Application |
|---|---|---|---|---|
| 2018[327] | Ag nanoparticles ink – tribopositive<br>PVDF nanofibres – tribonegative | $V_{OC}$ ~ 25 V<br>$I_{SC}$ ~ 320 nA<br>Power ~ 0.12 mW | 0.385 V $kPa^{-1}$<br>Approximately 0-40 kPa range | Identification of breathing patterns normal and rapid. |
| 2018[328] | PDMS core-shell PDMS ion gel / PVDF-HFP nanofibre – tribonegative<br>Kapton film – tribopositive | $V_{OC}$ ~ 75 V<br>$I_{SC}$ ~ 10 μA $cm^{-2}$<br>Power ~ 0.9 W $m^{-2}$ | 0.43 V $kPa^{-1}$<br>0-1.6 kPa<br>0.068 V $kPa^{-1}$<br>0-700 kPa | NA |
| 2019[329] | PVDF/Ag NW, nanofibres- tribonegative<br>ethyl cellulose nanofibres- tribopositive | $V_{OC}$ -62.73 V<br>$I_{SC}$ – 490.7 nA<br>Charge– 22.35 nC<br>power density – 7.2 mW $m^{-2}$ | 1.67 V·$kPa^{-1}$<br>0–3 kPa<br>0.20 V·$kPa^{-1}$<br>3–32 kPa | Joint movement detection (elbow, knee ancles) |
| 2020[68] | PLGA/AgNW/PVA facial electrospun layer – tribonegative<br>PTFE – tribopositive-Middle sandwiched AgNW work as the electrode for tribonegative layer. | $V_{OC}$ ~90 V<br>$I_{SC}$ ~ 2.5 μA<br>Charge ~ 30 nC<br>power density - 130 mW $m^{-2}$ through 500 mΩ | 0.011 V $kPa^{-1}$<br>0-40 kPa | Frown movements, eye blinking, breathing behaviour monitoring |
| 2020[330] | PVDF nanofibres – tribonegative<br>human skin – tribopositive | $V_{OC}$ ~30 V | 0.18 V $kPa^{-1}$<br>0-175 kPa | Curvature or bending of the wrist |
| 2021[166] | $TiO_2$@PAN electrospun coated with PTFE – tribonegative<br>Nylon film – tribopositive | $V_{OC}$ ~58 V<br>$I_{SC}$ ~ 100nA<br>Charge ~ 25 nC<br>Power density - 48.6 mW $m^{-2}$ through 4160 MΩ | 5.2 V $kPa^{-1}$<br>0–4 kPa<br>0.6 V $kPa^{-1}$<br>>4 kPa | distinguish human motions such as walking, running, squatting, and skipping |

| | | | | |
|---|---|---|---|---|
| 2021[331] | Single electrode mode TPU electrospun – tribonegative layer Ag NW on PVA/CS electrospun layer as electrode | $V_{OC}$ ~12 V $I_{SC}$ ~ 200 nA Charge ~ 5 nC | 0.3086 V $kPa^{-1}$ 6.65–19.21 kPa. | Impact of volleyball on skin during practice. |
| 2021[332] | poly-DADMAC/nylon-11 nanofibre mat) – tribopositive PVDF-TrFE nanofibre mat – tribonegative | $V_{OC}$ - 380 V $I_{SC}$ - 80 µA Charge – 200 nC power density - 7.6 W $m^{-2}$ Through 4 MΩ | 1.01 V $kPa^{-1}$ 0-16 kPa 0.355 V $kPa^{-1}$ 16-36 kPa | Distinguish walking patterns (slow, fast jogging etc) |
| 2022[333] | Core sheath yarn electrospinning PCL -tribopositive PVDF/PTFE – tribonegative | $V_{OC}$ - 20 V $I_{SC}$ – 2.26 µA Charge – 6.3 nC power density – 2.2 mW $m^{-2}$ Through 20 MΩ | 0.367 V $kPa^{-1}$ 0-35 kPa range | Lying and standing up can be distinguished. |
| 2022[334] | Co-NPC/PVDF composite NFs – tribonegative layer Nylon 11 nanofibres – tribopositive layer | $V_{OC}$ – 710 V $J_{SC}$ – 210.96 mA $m^{-2}$ Charge density – 392 µC $m^{-2}$ power density – 19.24 W $m^{-2}$ Through 5 MΩ | 6.39 V $kPa^{-1}$ 1.5-16 kPa 0.36 V $kPa^{-1}$ 16-65 kPa | Walking, slow running, jumping, fall down can be distinguished |
| 2022[35] | Nylon 66 electrospun – tribopositive Siloxane – PVDF - tribonegative | $V_{OC}$ – 645.65 V $I_{SC}$ – 276 µA Charge – 212 nC power density – 13.25W $m^{-2}$ Through 1 MΩ | 12.062 V $kPa^{-1}$ 0-3 kPa 2.58 V $kPa^{-1}$ 3-25 kPa | Dynamic pressure can be measured on a wearable application |
| 2023[335] | TPU electrospun – tribopositive Ecoflex film - tribonegative | $V_{OC}$ – 123 V $I_{SC}$ – 1.7 µA Charge – 41.5 nC power density – 122 mW $m^{-2}$ Through 500 MΩ | 15.94 V $kPa^{-1}$ 0-3 kPa 3.70 V $kPa^{-1}$ 3-15.63 kPa | Detecting pulses at different sites (the radial, superficial temporal, and carotid artery) |
| 2023[272] | CNT incorporated CA electrospun – tribopositive PVDF electrospun - tribonegative | $V_{OC}$ ~ 112.8 V $I_{SC}$ ~ 29.9 µA Charge – 35.5 nC power density – 0.74 W $m^{-2}$ Through 80 MΩ | 3.03 V $kPa^{-1}$ 0-6.8 kPa 0.11 V $kPa^{-1}$ 6.8-65 kPa | Finger, wrist and arm bending angle was measured using this device |

| | | | | |
|---|---|---|---|---|
| 2024[336] | polarized polyvinylidene fluoride-barium titanate electrospun – tribonegative<br>Ni fabric - tribonegative | $V_{OC}$ ~ 240 V<br>$I_{SC}$ ~ 11 μA<br>Charge – 80 nC<br>power density – 4.62 W $m^{-2}$<br>Through 50 MΩ | 2.62 V $kPa^{-1}$<br>1-10 kPa | Getting - 30°, 60°, 90° degrees of knee, elbow and finger |
| 2024[337] | PEO@Poly-DADMAC electrospun composite – tribopositive<br>PVDF electrospun - tribonegative | $V_{OC}$ ~ 980 V<br>$I_{SC}$ ~ 30 μA<br>Charge – 145 nC<br>power density – 5.6 W $m^{-2}$<br>Through 10 MΩ | 8.923 V $kPa^{-1}$<br>1-25 kPa<br>2.265 V $kPa^{-1}$<br>25-87 kPa | Differentiate walking, running, jumping, cycling (both straight and with bending shoulders), sitting, and reseating |
| 2025 (our work) | Ag-CA electrospun - tribopositive<br>PVDF electrospun – tribonegative | $V_{OC}$ -155.9 V<br>$J_{SC}$ – 8.134 mA $m^{-2}$<br>$Q_{SC}$ – 65.622 nC $m^{-2}$<br>power density – 0.029 W $m^{-2}$ | 11.667 V $kPa^{-1}$<br>0-6.25 kPa<br>5.157 V $kPa^{-1}$<br>6.25-18.75 kPa | Detecting knee biomechanics targeting rehabilitation and exercise (running, walking, squatting etc) |

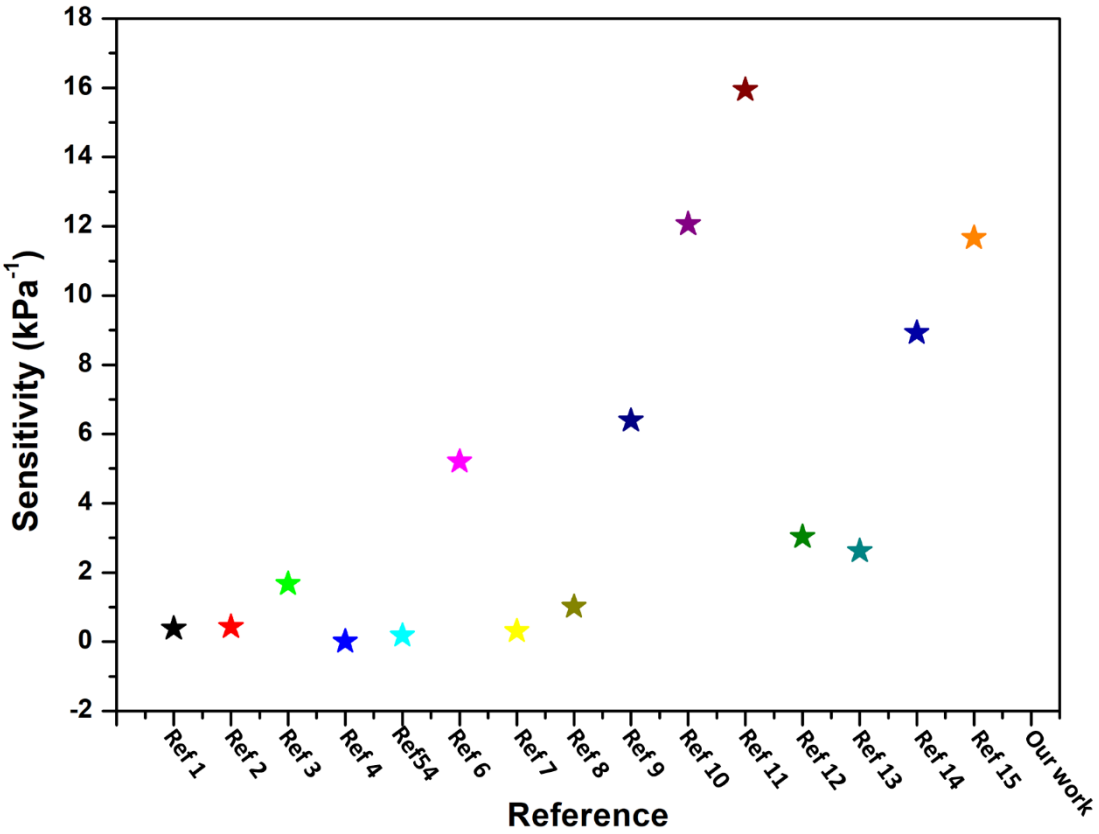


*Figure S1: Comparison of sensitivity of different literature results with newly developed sensor.*

## REFERENCES


[1] K. R. S. D. Gunawardhana, Z. Fang, G. B. McGuinness, L. A. M. Colorado, S. S. Baberwal, W. A. Wani, B. J. Rodriguez, R. O'Connor, C. Smullen, T. E. Ward, S. M. Coyle, *Small* 2025, e06363.

[2] E. van der Kruk, M. M. Reijne, *Eur J Sport Sci* 2018, *18*, 806.

[3] K. R. S. D. Gunawardhana, N. D. Wanasekara, R. D. I. G. Dharmasena, *iScience* 2020, *23*, 101360.

[4] Q. Shi, B. Dong, T. He, Z. Sun, J. Zhu, Z. Zhang, C. Lee, *InfoMat* 2020, *2*, 1131.

[5] G. Zubi, R. Dufo-López, M. Carvalho, G. Pasaoglu, *Renewable and Sustainable Energy Reviews* 2018, *89*, 292.

[6] Y. Ling, T. An, L. W. Yap, B. Zhu, S. Gong, W. Cheng, *Advanced Materials* 2020, *32*, 1904664.

[7] K. R. S. Gunawardhana, R. B. V. B. Simorangkir, G. B. Mcguinness, M. S. Rasel, L. A. M. Colorado, S. S. Baberwal, T. E. Ward, B. O'flynn, S. M. Coyle, *ACS Nano* 2024, *18*, 2649.

[8] W. He, X. Fu, D. Zhang, Q. Zhang, K. Zhuo, Z. Yuan, R. Ma, *Nano Energy* 2021, *84*, 105880.

[9] M. Munoz-Organero, J. Parker, L. Powell, S. Mawson, *Sensors* 2016, *16*, 1631.

[10] Y. Wang, P. Zhu, Y. Sun, P. Li, Y. Mao, *Biodes Manuf* 2024, *7*, 566.

[11] S. Zhang, X. Lin, J. Wan, C. Xu, M. Han, *Adv Mater Technol* 2024, 2301895.

[12] P. Pandey, P. Maharjan, M.-K. K. Seo, K. Thapa, J. I. Sohn, *Int J Energy Res* 2024, *2024*, 5572736.

[13] Z. Lin, Z. Wu, B. Zhang, Y. Wang, H. Guo, G. Liu, C. Chen, Y. Chen, J. Yang, Z. L. Wang, *Adv Mater Technol* 2019, *4*, 1800360.

[14] D. Vera Anaya, M. R. Yuce, *Med Devices Sens* 2021, *4*, e10154.

[15] W. Choi, I. Yun, J. Jeung, Y. S. Park, S. Cho, D. W. Kim, I. S. Kang, Y. Chung, U. Jeong, *Nano Energy* 2019, *56*, 347.

[16] Y. Zeng, H. Xiang, N. Zheng, X. Cao, N. Wang, Z. L. Wang, *Nano Energy* 2022, *91*, 106601.

[17] M. Zhu, Q. Shi, T. He, Z. Yi, Y. Ma, B. Yang, T. Chen, C. Lee, *ACS Nano* 2019, *13*, 1940.

[18] W. Li, L. Lu, A. G. P. Kottapalli, Y. Pei, *Nano Energy* 2022, *95*, 107018.

[19] Z. Lin, J. Chen, X. Li, Z. Zhou, K. Meng, W. Wei, J. Yang, Z. L. Wang, *ACS Nano* 2017, *11*, 8830.

[20] S. Shen, X. Xiao, X. Xiao, J. Chen, *ACS Appl Energy Mater* 2022, *5*, 3952.

[21] D. Bhatia, S. H. Jo, Y. Ryu, Y. Kim, D. H. Kim, H.-S. S. Park, *Nano Energy* 2021, *80*, 105508.

[22] J. Wang, H. Wang, T. He, B. He, N. V Thakor, C. Lee, *Advanced Science* 2019, *6*, 1900149.

[23] Q. Xu, Y. Fang, Q. Jing, N. Hu, K. Lin, Y. Pan, L. Xu, H. Gao, M. Yuan, L. Chu, Y. Ma, Y. Xie, J. Chen, L. Wang, *Biosens Bioelectron* 2021, *187*, 113329.

[24] D. Bhatia, K. S. Lee, M. U. K. Niazi, H. S. Park, *Nano Energy* 2022, *97*, 107179.

[25] Ö. Erdem, E. Derin, S. Zeibi Shirejini, K. Sagdic, E. G. Yilmaz, S. Yildiz, G. A. Akceoglu, F. Inci, *Adv Mater Technol* 2022, *7*, 2100572.

[26] Y. Zhang, Z. Huo, X. Wang, X. Han, W. Wu, B. Wan, H. Wang, J. Zhai, J. Tao, C. Pan, Z. L. Wang, *Nat Commun* 2020, *11*, 5629.

[27] Y. Hu, X. Wang, H. Li, H. Li, Z. Li, *Nano Energy* 2020, *71*, 104640.

[28] R. K. Cheedarala, J. Il Song, *Frontiers in Nanotechnology* 2021, *3*, 1.

[29] Z. Bai, Y. Xu, J. Li, J. Zhu, C. Gao, Y. Zhang, J. Wang, J. Guo, *ACS Appl Mater Interfaces* 2020, *12*, 42880.

[30] D. G. Dassanayaka, T. M. Alves, N. D. Wanasekara, I. G. Dharmasena, J. Ventura, *Adv Funct Mater* 2022, *32*, 2205438.
[31] A. Garkal, D. Kulkarni, S. Musale, T. Mehta, P. Giram, *New Journal of Chemistry* 2021, *45*, 21508.
[32] I. Partheniadis, I. Nikolakakis, I. Laidmäe, J. Heinämäki, *Processes* 2020, *8*, 673.
[33] T. A. Arica, T. Isık, T. Guner, N. Horzum, M. M. Demir, *Macromol Mater Eng* 2021, *306*, DOI 10.1002/mame.202100143.
[34] A. Babu, I. Aazem, R. Walden, S. Bairagi, D. M. Mulvihill, S. C. Pillai, *Chemical Engineering Journal* 2023, *452*, 139060.
[35] T. Bhatta, S. Sharma, K. Shrestha, Y. Shin, S. Seonu, S. Lee, D. Kim, Md. Sharifuzzaman, S. S. Rana, J. Y. Park, *Adv Funct Mater* 2022, *32*, 2202145.
[36] J.-H. Zhang, Y. Li, J. Du, X. Hao, Q. Wang, *Nano Energy* 2019, *61*, 486.
[37] M. Venkatesan, W.-C. Chen, C.-J. Cho, L. Veeramuthu, L.-G. Chen, K.-Y. Li, M.-L. Tsai, Y.-C. Lai, W.-Y. Lee, W.-C. Chen, C.-C. Kuo, *Chemical Engineering Journal* 2022, *433*, 133620.
[38] S. A. Hosseini Ravandi, M. Sadrjahani, A. Valipouri, F. Dabirian, F. K. Ko, *Textile Research Journal* 2022, *92*, 5130.
[39] C. Bohr, K. Lê, T. Fischer, S. Mathur, *Adv Eng Mater* 2022, *24*, 2100773.
[40] J. H. Zhang, Y. Li, J. Du, X. Hao, H. Huang, *J Mater Chem A Mater* 2019, *7*, 11724.
[41] R. Das, W. Zeng, C. Asci, R. Del-Rio-Ruiz, S. Sonkusale, *APL Bioeng* 2022, *6*, 021505.
[42] C. Zhi, S. Shi, Y. Si, B. Fei, H. Huang, J. Hu, *Adv Mater Technol* 2023, *8*, 2201161.
[43] M. Meloni, J. Cai, Q. Zhang, D. Sang-Hoon Lee, M. Li, R. Ma, T. E. Parashkevov, J. Feng, *Advanced Science* 2021, *8*, 1.
[44] J. Stovall, Scott Wasserman Stern, F. Temako, *Fabrigami: The Origami Art of Folding Cloth to Create Decorative and Useful Objects (Furoshiki - The Japanese Art of Wrapping)*, Tuttle Publishing, 2013.
[45] C. T. O'Neill, N. S. Phipps, L. Cappello, S. Paganoni, C. J. Walsh, in *2017 International Conference on Rehabilitation Robotics (ICORR)*, IEEE, 2017, pp. 1672–1678.
[46] S. Seo, W. Park, D. Lee, J. Bae, *IEEE Robot Autom Lett* 2021, *6*, 5239.
[47] S. Liu, Y. Zhu, Z. Zhang, Z. Fang, J. Tan, J. Peng, C. Song, H. H. Asada, Z. Wang, *IEEE/ASME Transactions on Mechatronics* 2021, *26*, 2747.
[48] X. Chen, Y. Li, X. Wang, H. Yu, *ACS Appl Mater Interfaces* 2022, *14*, 36227.
[49] D. J. Yao, Z. Tang, L. Zhang, Z. G. Liu, Q. J. Sun, S. C. Hu, Q. X. Liu, X. G. Tang, J. Ouyang, *J Mater Chem C Mater* 2021, *9*, 12642.
[50] J. Chen, H. Zhang, H. Ji, F. Wang, H. Xiao, *Compos Part A Appl Sci Manuf* 2023, *164*, 107257.
[51] S. Alharbi, S. Chaudhari, A. Inshaar, H. Shah, C. Zou, R. L. Harne, A. Kiourti, *IEEE Antennas Wirel Propag Lett* 2018, *17*, 2218.
[52] J. Zhu, S. Ji, J. Yu, H. Shao, H. Wen, H. Zhang, Z. Xia, Z. Zhang, C. Lee, *Nano Energy* 2022, *103*, 107766.
[53] "Wearable Sensors Market 2025-2035: Technologies, Trends, Players, Forecasts: IDTechEx," can be found under https://www.idtechex.com/en/research-report/wearable-sensors-market-2025-2035-technologies-trends-players-forecasts/1051, 2025.
[54] J. Zhao, J. Zha, Z. Zeng, C. Tan, *J Mater Chem A Mater* 2021, *9*, 18887.
[55] A. Satharasinghe, T. Hughes-Riley, T. Dias, *Sensors* 2020, *20*, 5938.
[56] K. R. S. Gunawardhana, N. D. Wanasekara, K. G. Wijayantha, R. D. I. Dharmasena, *ACS Appl Electron Mater* 2022, *4*, 678.

[57] A. Nozariasbmarz, H. Collins, K. Dsouza, M. H. Polash, M. Hosseini, M. Hyland, J. Liu, A. Malhotra, F. M. Ortiz, F. Mohaddes, V. P. Ramesh, Y. Sargolzaeiaval, N. Snouwaert, M. C. Özturk, D. Vashaee, *Appl Energy* 2020, *258*, 114069.
[58] Chunyi. Zhi, L. Dai, *Flexible Energy Conversion and Storage Devices*, Wiley, Weinheim, Germany, 2018.
[59] M. Zhang, T. Gao, J. Wang, J. Liao, Y. Qiu, Q. Yang, H. Xue, Z. Shi, Y. Zhao, Z. Xiong, L. Chen, *Nano Energy* 2015, *13*, 298.
[60] T. F. O'Connor, A. V. Zaretski, S. Savagatrup, A. D. Printz, C. D. Wilkes, M. I. Diaz, E. J. Sawyer, D. J. Lipomi, *Solar Energy Materials and Solar Cells* 2016, *144*, 438.
[61] R. Li, X. Xiang, X. Tong, J. Zou, Q. Li, *Advanced Materials* 2015, *27*, 3831.
[62] Z. Li, J. Shen, I. Abdalla, J. Yu, B. Ding, *Nano Energy* 2017, *36*, 341.
[63] M. J. Yun, S. I. Cha, S. H. Seo, H. S. Kim, D. Y. Lee, *Sci Rep* 2015, *5*, 11022.
[64] S. Selvam, J.-H. Yim, *J Energy Storage* 2023, *58*, 106340.
[65] R. B. V. B. Simorangkir, Y. Yang, K. P. Esselle, B. A. Zeb, *IEEE Trans Antennas Propag* 2018, *66*, 50.
[66] S. Praveen, P. Santhoshkumar, Y. C. Joe, C. Senthil, C. W. Lee, *Appl Mater Today* 2020, *20*, 100688.
[67] S. Yu, Y. Tai, J. Milam-Guerrero, J. Nam, N. V. Myung, *Nano Energy* 2022, *97*, 107174.
[68] X. Peng, K. Dong, C. Ye, Y. Jiang, S. Zhai, R. Cheng, D. Liu, X. Gao, J. Wang, Z. L. Wang, *Sci Adv* 2020, *6*, DOI 10.1126/sciadv.aba9624.
[69] M. Kim, Y. Wu, E. Kan, J. Fan, *Polymers (Basel)* 2018, *10*, 745.
[70] X. Guan, B. Xu, M. Wu, T. Jing, Y. Yang, Y. Gao, *Nano Energy* 2021, *80*, 105549.
[71] R. Zhou, W. Guo, R. Yu, C. Pan, *J Mater Chem A Mater* 2015, *3*, 23028.
[72] W. Zhou, S. Yao, H. Wang, Q. Du, Y. Ma, Y. Zhu, *ACS Nano* 2020, *14*, 5798.
[73] J. Xue, T. Wu, Y. Dai, Y. Xia, *Chem Rev* 2019, *119*, 5298.
[74] A. Thejas Prasannakumar, R. R. Mohan, R. R, M. V, S. J. Varma, *ChemistrySelect* 2023, *8*, DOI 10.1002/slct.202203564.
[75] T. U. Rashid, R. E. Gorga, W. E. Krause, *Adv Eng Mater* 2021, *23*, DOI 10.1002/adem.202100153.
[76] J. Kim, J. Park, Y.-G. Park, E. Cha, M. Ku, H. S. An, K.-P. Lee, M.-I. Huh, J. Kim, T.-S. Kim, D. W. Kim, H. K. Kim, J.-U. Park, *Nat Biomed Eng* 2021, *5*, 772.
[77] E. S. Medeiros, G. M. Glenn, A. P. Klamczynski, W. J. Orts, L. H. C. Mattoso, *J Appl Polym Sci* 2009, *113*, 2322.
[78] J. E. Oliveira, E. A. Moraes, R. G. F. Costa, A. S. Afonso, L. H. C. Mattoso, W. J. Orts, E. S. Medeiros, *J Appl Polym Sci* 2011, *122*, 3396.
[79] K. H. Lim, H. Kweon, H. Kim, *J Electrochem Soc* 2019, *166*, A3425.
[80] A. Shaker, A. H. Hassanin, N. M. Shaalan, M. A. Hassan, A. A. El-Moneim, *Smart Mater Struct* 2019, *28*, 075029.
[81] H. T. H. Shi, S. Jang, A. Reza-Ugalde, H. E. Naguib, *ACS Appl Energy Mater* 2020, *3*, 987.
[82] H. Niu, H. Zhou, H. Wang, in *Energy Harvesting Properties of Electrospun Nanofibers*, IOP Publishing, 2019, pp. 1-1-1–44.
[83] C. Liu, J. Shen, K. W. K. Yeung, S. C. Tjong, *ACS Biomater Sci Eng* 2017, *3*, 471.
[84] W. Liu, J. Zhang, H. Liu, *Polymers (Basel)* 2019, *11*, 954.
[85] S. S. Ojha, D. R. Stevens, K. Stano, T. Hoffman, L. I. Clarke, R. E. Gorga, *Macromolecules* 2008, *41*, 2509.
[86] Z. Song, X. Hou, L. Zhang, S. Wu, *Materials* 2010, *4*, 621.
[87] M. Gong, L. Zhang, P. Wan, *Prog Polym Sci* 2020, *107*, 101279.
[88] B. Joshi, E. Samuel, Y. il Kim, A. L. Yarin, M. T. Swihart, S. S. Yoon, *Coord Chem Rev* 2022, *460*, 214466.

[89] S. N. Mahmood, A. J. Ishak, T. Saeidi, H. Alsariera, S. Alani, A. Ismail, A. C. Soh, *Progress In Electromagnetics Research B* 2020, *89*, 1.
[90] K. Xiao, W. Wang, K. Wang, H. Zhang, S. Dong, J. Li, *Adv Funct Mater* 2024, 2404744.
[91] X. Cui, Y. Zhang, *Nano Select* 2020, *1*, 461.
[92] M. S. Rasel, P. Maharjan, M. Salauddin, M. T. Rahman, H. O. Cho, J. W. Kim, J. Y. Park, *Nano Energy* 2018, *49*, 603.
[93] B. Sun, X. Guo, Y. Zhang, Z. L. Wang, J. Shao, *Nano Energy* 2024, *126*, 109637.
[94] Z. Liu, T. Zhao, H. Guan, T. Zhong, H. He, L. Xing, X. Xue, *J Mater Sci Technol* 2019, *35*, 2187.
[95] D. H. Reneker, I. Chun, *Nanotechnology* 1996, *7*, 216.
[96] D. H. Reneker, H. Fong, *Polymeric Nanofibers*, American Chemical Society, Washington, DC, 2006.
[97] H. Niu, T. Lin, *J Nanomater* 2012, *2012*, 1.
[98] H. J. Nieminen, I. Laidmäe, A. Salmi, T. Rauhala, T. Paulin, J. Heinämäki, E. Hæggström, *Sci Rep* 2018, *8*, 4437.
[99] S. Shi, Y. Si, Y. Han, T. Wu, M. I. Iqbal, B. Fei, R. K. Y. Y. Li, J. Hu, J. Qu, *Advanced Materials* 2022, *34*, 2107938.
[100] Y. Li, S. Xiao, Y. Luo, S. Tian, J. Tang, X. Zhang, J. Xiong, *Nano Energy* 2022, *104*, 107884.
[101] W.-F. Lai, Ed., *Systemic Delivery Technologies in Anti-Aging Medicine: Methods and Applications*, Springer International Publishing, Cham, 2020.
[102] G. Taylor, P. R. S. L. A, *Proceedings of the Royal Society of London. A. Mathematical and Physical Sciences* 1969, *313*, 453.
[103] Lord Rayleigh, *The London, Edinburgh, and Dublin Philosophical Magazine and Journal of Science* 1882, *14*, 184.
[104] C. J. Luo, E. Stride, M. Edirisinghe, *Macromolecules* 2012, *45*, 4669.
[105] A. Koski, K. Yim, S. Shivkumar, *Mater Lett* 2004, *58*, 493.
[106] A. H. Hekmati, A. Rashidi, R. Ghazisaeidi, J.-Y. Drean, *Textile Research Journal* 2013, *83*, 1452.
[107] B. Tarus, N. Fadel, A. Al-Oufy, M. El-Messiry, *Alexandria Engineering Journal* 2016, *55*, 2975.
[108] A. Dodero, E. Brunengo, M. Alloisio, A. Sionkowska, S. Vicini, M. Castellano, *Carbohydr Polym* 2020, *235*, 115976.
[109] Z. He, F. Rault, M. Lewandowski, E. Mohsenzadeh, F. Salaün, *Polymers (Basel)* 2021, *13*, 174.
[110] L. Persano, A. Camposeo, C. Tekmen, D. Pisignano, *Macromol Mater Eng* 2013, *298*, 504.
[111] W. Yang, R. Li, C. Fang, W. Hao, *Prog Org Coat* 2019, *131*, 67.
[112] D. Bassyouni, M. Mohamed, E. S. El-Ashtoukhy, M. A. El-Latif, A. Zaatout, H. Hamad, *Microchemical Journal* 2019, *149*, 103998.
[113] A. Haider, S. Haider, I.-K. K. Kang, *Arabian Journal of Chemistry* 2018, *11*, 1165.
[114] E. S. Cozza, O. Monticelli, E. Marsano, P. Cebe, *Polym Int* 2013, *62*, 41.
[115] D. Kamireddi, R. M. Street, C. L. Schauer, *Polym Eng Sci* 2023, 1.
[116] W. Serrano-Garcia, S. Ramakrishna, S. W. Thomas, *Polymers (Basel)* 2022, *14*, 5073.
[117] C. Jiang, C. Wu, X. Li, Y. Yao, L. Lan, F. Zhao, Z. Ye, Y. Ying, J. Ping, *Nano Energy* 2019, *59*, 268.
[118] X. Peng, K. Dong, Z. Wu, J. Wang, Z. L. Wang, *J Mater Sci* 2021, *56*, 16765.
[119] Y. Kim, X. Wu, J. H. Oh, *Sci Rep* 2020, *10*, 2742.
[120] J. P. Lee, J. W. Lee, J. M. Baik, *Micromachines (Basel)* 2018, *9*, 532.
[121] S. Mirjalali, A. Mahdavi Varposhti, S. Abrishami, R. Bagherzadeh, M. Asadnia, S. Huang, S. Peng, C. Wang, S. Wu, *Macromol Mater Eng* 2023, *308*, 2200442.

[122] S. S. Mali, P. S. Patil, C. K. Hong, *ACS Appl Mater Interfaces* 2014, *6*, 1688.
[123] M. A. Haghighat Bayan, F. Afshar Taromi, M. Lanzi, F. Pierini, *Sci Rep* 2021, *11*, 21144.
[124] K. Seo, J. Lee, J. Jo, C. Cho, J. Lee, *Advanced Materials* 2019, *31*, 1902447.
[125] N. M. Bedford, M. B. Dickerson, L. F. Drummy, H. Koerner, K. M. Singh, M. C. Vasudev, M. F. Durstock, R. R. Naik, A. J. Steckl, *Adv Energy Mater* 2012, *2*, 1136.
[126] Q. Li, A. Balilonda, A. Ali, R. Jose, F. Zabihi, S. Yang, S. Ramakrishna, M. Zhu, *Solar RRL* 2020, *4*, 2000269.
[127] Y. Cao, W. Zhang, F. Shi, T. Chen, P. Du, L. Song, J. Xiong, *Textile Research Journal* 2023, 004051752311545.
[128] S. Lage-Rivera, A. Ares-Pernas, M. Abad, *Int J Energy Res* 2022, *46*, 10475.
[129] Y. Liu, J. Tan, S. Yu, M. Yousefzadeh, T. Lyu, Z. Jiao, H. Li, S. Ramakrishna, *J Appl Polym Sci* 2020, *137*, 48299.
[130] B. Zaarour, L. Zhu, C. Huang, X. Jin, *Polym Adv Technol* 2020, *31*, 1449.
[131] D. H. Ho, S. Cheon, P. Hong, J. H. Park, J. W. Suk, D. H. Kim, J. T. Han, J. H. Cho, *Adv Funct Mater* 2019, *29*, 1.
[132] M. B. Taskin, L. H. Klausen, M. Dong, M. Chen, *Nano Res* 2020, *13*, 315.
[133] A. Keirouz, M. Chung, J. Kwon, G. Fortunato, N. Radacsi, *WIREs Nanomedicine and Nanobiotechnology* 2020, *12*, 1.
[134] R. D. I. G. Dharmasena, S. R. P. Silva, *Nano Energy* 2019, *62*, 530.
[135] P. Basset, S. P. Beeby, C. Bowen, Z. J. Chew, A. Delbani, R. D. I. G. Dharmasena, B. Dudem, F. R. Fan, D. Galayko, H. Guo, J. Hao, Y. Hou, C. Hu, Q. Jing, Y. H. Jung, S. K. Karan, S. Kar-Narayan, M. Kim, S.-W. Kim, Y. Kuang, K. J. Lee, J. Li, Z. Li, Y. Long, S. Priya, X. Pu, T. Ruan, S. R. P. Silva, H. S. Wang, K. Wang, X. Wang, Z. L. Wang, W. Wu, W. Xu, H. Zhang, Y. Zhang, M. Zhu, *APL Mater* 2022, *10*, 109201.
[136] R. D. I. G. Dharmasena, J. H. B. Deane, S. R. P. Silva, *Adv Energy Mater* 2018, *8*, 1802190.
[137] Z. L. Wang, J. Song, *Science (1979)* 2006, *312*, 242.
[138] Y.-M. Choi, M. Lee, Y. Jeon, *Energies (Basel)* 2017, *10*, 1483.
[139] C. Zhang, W. Tang, L. Zhang, C. Han, Z. L. Wang, *ACS Nano* 2014, *8*, 8702.
[140] F.-R. Fan, Z.-Q. Tian, Z. Lin Wang, *Nano Energy* 2012, *1*, 328.
[141] C. Fang, T. Tong, T. Bu, Y. Cao, S. Xu, Y. Qi, C. Zhang, *Advanced Intelligent Systems* 2020, *2*, 1900129.
[142] X. Cheng, W. Tang, Y. Song, H. Chen, H. Zhang, Z. L. Wang, *Nano Energy* 2019, *61*, 517.
[143] Y. Guo, X.-S. S. Zhang, Y. Wang, W. Gong, Q. Zhang, H. Wang, J. Brugger, *Nano Energy* 2018, *48*, 152.
[144] J.-H. Zhang, Z. Zhou, J. Li, B. Shen, T. Zhu, X. Gao, R. Tao, X. Guo, X. Hu, Y. Shi, L. Pan, *ACS Mater Lett* 2022, *4*, 847.
[145] C. Zhang, W. Fan, S. Wang, Q. Wang, Y. Zhang, K. Dong, *ACS Appl Electron Mater* 2021, *3*, 2449.
[146] C. Xu, Y. Zi, A. C. Wang, H. Zou, Y. Dai, X. He, P. Wang, Y. C. Wang, P. Feng, D. Li, Z. L. Wang, *Advanced Materials* 2018, *30*, 1706790.
[147] H. T. Baytekin, B. Baytekin, J. T. Incorvati, B. A. Grzybowski, *Angewandte Chemie* 2012, *124*, 4927.
[148] F. Galembeck, T. A. L. Burgo, L. B. S. Balestrin, R. F. Gouveia, C. A. Silva, A. Galembeck, *RSC Adv.* 2014, *4*, 64280.
[149] H. Ko, Y. Lim, S. Han, C. K. Jeong, S. B. Cho, *ACS Energy Lett* 2021, *6*, 2792.
[150] H. Zou, Y. Zhang, L. Guo, P. Wang, X. He, G. Dai, H. Zheng, C. Chen, A. C. Wang, C. Xu, Z. L. Wang, *Nat Commun* 2019, *10*, 1427.
[151] Z. L. Wang, *Materials Today* 2017, *20*, 74.
[152] J. Wen, H. He, C. Niu, M. Rong, Y. Huang, Y. Wu, *Nano Energy* 2022, *96*, 107070.

[153] Q. Xu, Y. Qin, *APL Mater* 2017, *5*, 74101.
[154] R. D. I. G. Dharmasena, K. D. G. I. Jayawardena, C. A. Mills, R. A. Dorey, S. R. P. Silva, *Nano Energy* 2018, *48*, 391.
[155] R. D. I. G. I. G. Dharmasena, K. D. G. I. G. I. Jayawardena, C. A. Mills, J. H. B. B. Deane, J. V. Anguita, R. A. Dorey, S. R. P. P. Silva, *Energy Environ Sci* 2017, *10*, 1801.
[156] N. Wang, X.-X. X. Wang, K. Yan, W. Song, Z. Fan, M. Yu, Y.-Z. Z. Long, *ACS Appl Mater Interfaces* 2020, *12*, 46205.
[157] Y. Song, J. Bao, Y. Hu, H. Cai, C. Xiong, Q. Yang, H. Tian, Z. Shi, *Sustain Energy Fuels* 2022, *6*, 2377.
[158] K. Dong, X. Peng, R. Cheng, Z. L. Wang, *Nanoenergy Advances* 2022, *2*, 133.
[159] C. Sun, G. Zu, Y. Wei, X. Song, X. Yang, *Langmuir* 2022, *38*, 1479.
[160] J. Huang, Y. Hao, M. Zhao, W. Li, F. Huang, Q. Wei, *ACS Appl Mater Interfaces* 2021, *13*, 24774.
[161] S. Sardana, H. Kaur, B. Arora, D. K. Aswal, A. Mahajan, *ACS Sens* 2022, *7*, 312.
[162] Z. Qin, X. Chen, Y. Yin, G. Ma, Y. Jia, J. Deng, K. Pan, *Adv Mater Technol* 2020, *5*, 1.
[163] Y. Kim, X. Wu, C. Lee, J. H. Oh, *ACS Appl Mater Interfaces* 2021, *13*, 36967.
[164] M. R. Gomes, F. Castelo Ferreira, P. Sanjuan-Alberte, *Biomaterials Advances* 2022, *137*, 212808.
[165] A. Alagumalai, W. Shou, O. Mahian, M. Aghbashlo, M. Tabatabaei, S. Wongwises, Y. Liu, J. Zhan, A. Torralba, J. Chen, Z. Wang, W. Matusik, *Joule* 2022, *6*, 1475.
[166] Y. Jiang, K. Dong, J. An, F. Liang, J. Yi, X. Peng, C. Ning, C. Ye, Z. L. Wang, *ACS Appl Mater Interfaces* 2021, *13*, 11205.
[167] A. Mondal, M. Faraz, N. Khare, *Appl Phys Lett* 2022, *121*, 103901.
[168] C. Sun, J. Shi, X. Wang, *J Appl Phys* 2010, *108*, 034309.
[169] M. Smith, S. Kar-Narayan, *International Materials Reviews* 2022, *67*, 65.
[170] Z. L. Wang, *Nano Energy* 2020, *68*, 104272.
[171] Q. Xu, J. Wen, Y. Qin, *Nano Energy* 2021, *86*, 106080.
[172] O. Gryshkov, F. AL Halabi, A. I. Kuhn, S. Leal-Marin, L. J. Freund, M. Förthmann, N. Meier, S.-A. Barker, K. Haastert-Talini, B. Glasmacher, *Int J Mol Sci* 2021, *22*, 11373.
[173] J. H. Eun, S. M. Sung, M. S. Kim, B. K. Choi, J. S. Lee, *Mater Des* 2021, *206*, 109785.
[174] Y. Su, W. Li, X. Cheng, Y. Zhou, S. Yang, X. Zhang, C. Chen, T. Yang, H. Pan, G. Xie, G. Chen, X. Zhao, X. Xiao, B. Li, H. Tai, Y. Jiang, L.-Q. Chen, F. Li, J. Chen, *Nat Commun* 2022, *13*, 4867.
[175] L. Song, T. Wang, W. Jing, X. Xie, P. Du, J. Xiong, *Mater Res Bull* 2019, *118*, 110522.
[176] J. S. Shaikh, N. S. Shaikh, S. S. Mali, J. V. Patil, K. K. Pawar, P. Kanjanaboos, C. K. Hong, J. H. Kim, P. S. Patil, *Nanoscale* 2018, *10*, 4987.
[177] A. Balilonda, Z. Li, Y. Fu, F. Zabihi, S. Yang, X. Huang, X. Tao, W. Chen, *J Mater Chem C Mater* 2022, *10*, 6957.
[178] T. Blachowicz, A. Ehrmann, *Membranes (Basel)* 2023, *13*, 441.
[179] Z. Soleimani, S. Zoras, B. Ceranic, Y. Cui, S. Shahzad, *Nano Energy* 2021, *89*, 106325.
[180] F. J. DiSalvo, *Science (1979)* 1999, *285*, 703.
[181] E. Ewaldz, J. M. Rinehart, M. Miller, B. Brettmann, *ACS Omega* 2023, *8*, 30239.
[182] X. He, J. Gu, Y. Hao, M. Zheng, L. Wang, J. Yu, X. Qin, *Chemical Engineering Journal* 2022, *450*, 137937.
[183] Z. Sun, L. Feng, C. Xiong, X. He, L. Wang, X. Qin, J. Yu, *J Mater Chem A Mater* 2021, *9*, 7085.
[184] J. Zhang, Y. Hou, L. Lei, S. Hu, *J Memb Sci* 2022, *662*, 120962.

[185] W. He, H. Wang, Y. Huang, T. He, F. Chi, H. Cheng, D. Liu, L. Dai, L. Qu, *Nano Energy* 2022, *95*, 107017.
[186] T. Tabrizizadeh, J. Wang, R. Kumar, S. Chaurasia, K. Stamplecoskie, G. Liu, *ACS Appl Mater Interfaces* 2021, *13*, 50900.
[187] Y. Huang, H. Cheng, C. Yang, P. Zhang, Q. Liao, H. Yao, G. Shi, L. Qu, *Nat Commun* 2018, *9*, 1.
[188] D. B. Basha, S. Ahmed, A. Ahmed, M. A. Gondal, *J Energy Storage* 2023, *60*, 106581.
[189] M. R. Islam, S. Afroj, K. S. Novoselov, N. Karim, *Advanced Science* 2022, *9*, 2203856.
[190] K. D. Verma, P. Sinha, S. Banerjee, K. K. Kar, M. K. Ghorai, in *Springer Series in Materials Science*, Springer, 2020, pp. 315–326.
[191] K. Joseph, H. Kasparian, V. Shanov, *Energies (Basel)* 2022, *15*, 6506.
[192] V. J. Ariyamparambil, B. Kandasubramanian, *Chemical Engineering Journal Advances* 2022, *11*, 100355.
[193] M. Wu, Z. Gao, K. Yao, S. Hou, Y. Liu, D. Li, J. He, X. Huang, E. Song, J. Yu, X. Yu, *Mater Today Energy* 2021, *20*, 100657.
[194] H. Zhou, X. Wei, B. Wang, E. Zhang, Z. Wu, Z. L. Wang, *Adv Funct Mater* 2023, *33*, 2210920.
[195] S. Si, C. Sun, Y. Wu, J. Li, H. Wang, Y. Lin, J. Yang, Z. L. Wang, *Nano Res* 2024, *17*, 1923.
[196] R. K. Gupta, Q. Shi, L. Dhakar, T. Wang, C. H. Heng, C. Lee, *Sci Rep* 2017, *7*, 1.
[197] M. A. P. Mahmud, A. Zolfagharian, S. Gharaie, A. Kaynak, S. H. Farjana, A. V. Ellis, J. Chen, A. Z. Kouzani, *Advanced Energy and Sustainability Research* 2021, *2*, 2000045.
[198] K. R. S. D. Gunawardhana, Development of a Triboelectric Nanogenerator Using Nylon-Hybrid Yarn, Master by Research, University of Moratuwa, 2021.
[199] S. Leanza, S. Wu, X. Sun, H. J. Qi, R. R. Zhao, *Advanced Materials* 2024, *36*, 1.
[200] In *Origami 4*, A K Peters/CRC Press, 2011, pp. 99–112.
[201] S. Babaee, Y. Shi, S. Abbasalizadeh, S. Tamang, K. Hess, J. E. Collins, K. Ishida, A. Lopes, M. Williams, M. Albaghdadi, A. M. Hayward, G. Traverso, *Nat Mater* 2021, *20*, 1085.
[202] C. P. Quaglia, A. J. Dascanio, A. P. Thrall, *Eng Struct* 2014, *75*, 276.
[203] B. An, S. Miyashita, A. Ong, M. T. Tolley, M. L. Demaine, E. D. Demaine, R. J. Wood, D. Rus, *IEEE Transactions on Robotics* 2018, *34*, 1409.
[204] X. Ning, X. Wang, Y. Zhang, X. Yu, D. Choi, N. Zheng, D. S. Kim, Y. Huang, Y. Zhang, J. A. Rogers, *Adv Mater Interfaces* 2018, *5*, 1.
[205] Z. Song, C. Lv, M. Liang, V. Sanphuang, K. Wu, B. Chen, Z. Zhao, J. Bai, X. Wang, J. L. Volakis, L. Wang, X. He, Y. Yao, S. Tongay, H. Jiang, *Small* 2016, *12*, 5401.
[206] N. A. Choudhry, L. Arnold, A. Rasheed, I. A. Khan, L. Wang, *Adv Eng Mater* 2021, *23*, DOI 10.1002/adem.202100469.
[207] J. Wu, in *Bridges Aalto*, 2022, pp. 375–378.
[208] Jeffrey. Rutzky, C. K. Palmer, *Shadowfolds : Surprisingly Easy-to-Make Geometric Designs in Fabric*, Kodansha International, 2011.
[209] R. Smithers, "Origami-inspired clothing range that grows with your child wins Dyson award," can be found under https://www.theguardian.com/environment/2017/sep/07/origami-inspired-clothing-range-that-grows-with-your-child-wins-dyson-award, 2017.
[210] D. Sparks, *Clothing and Textiles Research Journal* 2004, *22*, 38.
[211] J. Ren, A. Segall, O. Sorkine-Hornung, *ACM Trans Graph* 2024, *43*, DOI 10.1145/3631945.
[212] L. Coar, J. Hare, L. De Laet, Y. J. Cha, G. Suh, J. Piper, V. Jiang, *International Journal of Space Structures* 2021, *36*, 13.

[213] H. Higoshi, D. Naritomi, S. Kamiyauchi, H. Minamide, K. Yamashita, S. Ueno, Y. Fukatsu, K. Nakane, H. Shigemune, *Adv Mater Technol* 2025, 2500032.
[214] P. K. Yang, Z. H. Lin, K. C. Pradel, L. Lin, X. Li, X. Wen, J. H. He, Z. L. Wang, *ACS Nano* 2015, *9*, 901.
[215] G. Hu, C. Zhao, Y. Yang, X. Li, J. Liang, *Appl Energy* 2022, *306*, 118037.
[216] R. V. M. Gowda, in *Technical Textile Yarns*, Elsevier, 2010, pp. 56–90.
[217] A. Balilonda, Q. Li, X. Bian, R. Jose, S. Ramakrishna, M. Zhu, F. Zabihi, S. Yang, *Chemical Engineering Journal* 2021, *410*, 128384.
[218] L. Ma, M. Zhou, R. Wu, A. Patil, H. Gong, S. Zhu, T. Wang, Y. Zhang, S. Shen, K. Dong, L. Yang, J. Wang, W. Guo, Z. L. Wang, *ACS Nano* 2020, *14*, 4716.
[219] Z. Dai, N. Wang, Y. Yu, Y. Lu, L. Jiang, D.-A. Zhang, X. Wang, X. Yan, Y.-Z. Long, *ACS Appl Mater Interfaces* 2021, *13*, 44234.
[220] N. Nan, J. He, X. You, X. Sun, Y. Zhou, K. Qi, W. Shao, F. Liu, Y. Chu, B. Ding, *Adv Mater Technol* 2019, *4*, 1800338.
[221] P. C. Uzabakiriho, M. Wang, K. Wang, C. Ma, G. Zhao, *ACS Appl Mater Interfaces* 2022, *14*, 46068.
[222] S. Seyedin, T. Carey, A. Arbab, L. Eskandarian, S. Bohm, J. M. Kim, F. Torrisi, *Nanoscale* 2021, *13*, 12818.
[223] C. Harvey, E. Holtzman, J. Ko, B. Hagan, R. Wu, S. Marschner, D. Kessler, *Leonardo* 2019, *52*, 381.
[224] T. M. W. J. Bandara, J. M. C. Hansadi, F. Bella, *Ionics (Kiel)* 2022, *28*, 2563.
[225] J. Chen, H. Guo, X. Pu, X. Wang, Y. Xi, C. Hu, *Nano Energy* 2018, *50*, 536.
[226] D. J. Spencer, *Knitting Technology : A Comprehensive Handbook and Practical Guide*, CRC Press, 2001.
[227] S. S. Kwak, H. Kim, W. Seung, J. Kim, R. Hinchet, S. W. Kim, *ACS Nano* 2017, *11*, 10733.
[228] S. Dong, F. Xu, Y. Sheng, Z. Guo, X. Pu, Y. Liu, *Nano Energy* 2020, *78*, 105327.
[229] Li Li, Wai Man Au, Yi Li, Kam Man Wan, Sai Ho Wan, Kwok Shing Wong, *Textile Research Journal* 2010, *80*, 279.
[230] S. Ahmad, A. Rasheed, A. Afzal, F. Ahmad, Eds., *Advanced Textile Testing Techniques*, CRC Press, 2017.
[231] L. Liu, Y. Ren, Y. Li, Y. Liang, *Polymer (Guildf)* 2013, *54*, 5250.
[232] Y. Zou, S. Jiang, X. Hu, W. Xu, Z. Chen, K. Liu, H. Hou, *Mater Today Commun* 2021, *26*, 102069.
[233] Y. Han, Y. Xu, S. Zhang, T. Li, S. Ramakrishna, Y. Liu, *Macromol Mater Eng* 2020, *305*, 2000230.
[234] R. L. Bulathsinghala, W. Ding, R. D. I. G. Dharmasena, *Nano Energy* 2023, *116*, 108792.
[235] X. Cheng, L. Miao, Y. Song, Z. Su, H. Chen, X. Chen, J. Zhang, H. Zhang, *Nano Energy* 2017, *38*, 438.
[236] S.-B. B. Jeon, S.-J. J. Park, W.-G. G. Kim, I.-W. W. Tcho, I.-K. K. Jin, J.-K. K. Han, D. Kim, Y.-K. K. Choi, *Nano Energy* 2018, *53*, 596.
[237] Q. Zhang, Z. Zhang, Q. Liang, Q. Shi, M. Zhu, C. Lee, *Advanced Science* 2021, *8*, 2004727.
[238] Z. Zhou, K. Chen, X. Li, S. Zhang, Y. Wu, Y. Zhou, K. Meng, C. Sun, Q. He, W. Fan, E. Fan, Z. Lin, X. Tan, W. Deng, J. Yang, J. Chen, *Nat Electron* 2020, *3*, 571.
[239] B. Östlund, M. Malvezzi, S. Frennert, M. Funk, J. Gonzalez-Vargas, K. Baur, D. Alimisis, F. Thorsteinsson, A. Alonso-Cepeda, G. Fau, F. Haufe, M. Di Pardo, J. C. Moreno, *Front Public Health* 2023, *11*, DOI 10.3389/fpubh.2023.979225.
[240] M. Shak Sadi, E. Kumpikaitė, *Nanomaterials* 2022, *12*, 2039.
[241] N. Sun, G.-G. Wang, H.-X. Zhao, Y.-W. Cai, J.-Z. Li, G.-Z. Li, X.-N. Zhang, B.-L. Wang, J.-C. Han, Y. Wang, Y. Yang, *Nano Energy* 2021, *90*, 106639.

[242] Q. Qiu, M. Zhu, Z. Li, K. Qiu, X. Liu, J. Yu, B. Ding, *Nano Energy* 2019, *58*, 750.
[243] T. Busolo, P. K. Szewczyk, M. Nair, U. Stachewicz, S. Kar-Narayan, *ACS Appl Mater Interfaces* 2021, *13*, 16876.
[244] J. Shen, Z. Li, J. Yu, B. Ding, *Nano Energy* 2017, *40*, 282.
[245] A. K. Patra, S. R. K. Pariti, *Textile Progress* 2022, *54*, 1.
[246] "Wearable Sensors 2018-2028: Technologies, Markets & Players: IDTechEx," can be found under https://www.idtechex.com/en/research-report/wearable-sensors-2018-2028-technologies-markets-and-players/555, 2018.
[247] S. A. Ashter, in *Technology and Applications of Polymers Derived from Biomass*, William Andrew Publishing, 2018, pp. 57–74.
[248] H. Meng, Q. Yu, Z. Liu, Y. Gai, J. Xue, Y. Bai, X. Qu, P. Tan, D. Luo, W. Huang, K. Nie, W. Bai, Z. Hou, R. Tang, H. Xu, Y. Zhang, Q. Cai, X. Yang, Z. L. Wang, Z. Li, *Matter* 2023, *6*, 4274.
[249] R. Ghobeira, M. Asadian, C. Vercruysse, H. Declercq, N. De Geyter, R. Morent, *Polymer (Guildf)* 2018, *157*, 19.
[250] S. D. G. Karnasooriya Ragalage, H. Qadeer, G. B. McGuinness, T. E. Ward, S. M. Coyle, in *2024 IEEE 20th International Conference on Body Sensor Networks (BSN)*, IEEE, 2024, pp. 1–4.
[251] J. Song, N. L. Birbach, J. P. Hinestroza, *Cellulose* 2012, *19*, 411.
[252] N. Tulos, D. Harbottle, A. Hebden, P. Goswami, R. S. Blackburn, *ACS Omega* 2019, *4*, 4936.
[253] M. Pantić, G. Horvat, M. Berk Bevc, Ž. Knez, Z. Novak, *Journal of CO2 Utilization* 2024, *80*, 102697.
[254] S. Jana, M. Leung, J. Chang, M. Zhang, *Biofabrication* 2014, *6*, 035012.
[255] L. Van der Schueren, I. Steyaert, B. De Schoenmaker, K. De Clerck, *Carbohydr Polym* 2012, *88*, 1221.
[256] R. D. I. G. Dharmasena, *Nano Energy* 2020, *76*, 105045.
[257] M. Wang, J. Zhang, Y. Tang, J. Li, B. Zhang, E. Liang, Y. Mao, X. Wang, *ACS Nano* 2018, *12*, 6156.
[258] M. Ali, A. Elsayed, A. Mendez, Y. Savaria, M. Sawan, *IEEE Sens J* 2021, *21*, 14569.
[259] H. Varghese, H. M. A. Hakkeem, K. Chauhan, E. Thouti, S. Pillai, A. Chandran, *Nano Energy* 2022, *98*, 107339.
[260] N. Luo, Y. Feng, D. Wang, Y. Zheng, Q. Ye, F. Zhou, W. Liu, *ACS Appl Mater Interfaces* 2020, *12*, 30390.
[261] D. Tao, P. Su, A. Chen, D. Gu, M. Eginligil, W. Huang, *npj Flexible Electronics* 2025, *9*, 1.
[262] N. Saunders, K. R. S. D. Gunawardhana, L. A. Magre Colorado, S. S. Baberwal, S. Coyle, *Engineering Proceedings* 2023, *30*, 6.
[263] L. F. Brown, *IEEE Trans Ultrason Ferroelectr Freq Control* 2000, *47*.
[264] B. H. Moghadam, M. Hasanzadeh, A. Simchi, *ACS Appl Nano Mater* 2020, *3*, 8742.
[265] J. Li, J. Yin, M. G. V. Wee, A. Chinnappan, S. Ramakrishna, *Advanced Fiber Materials* 2023, *5*, 1417.
[266] R. Dallaev, T. Pisarenko, D. Sobola, F. Orudzhev, S. Ramazanov, T. Trčka, *Polymers (Basel)* 2022, *14*, 4793.
[267] P. Tofel, K. Částková, D. Říha, D. Sobola, N. Papež, J. Kaštyl, Ş. Ţălu, Z. Hadaš, *Nanomaterials* 2022, *12*, 349.
[268] J. Lin, M. Gende, Y. Zhan, Y. Zhao, G. Zheng, A. Jaworski, C. Cui, H. Cao, *Polymer (Guildf)* 2025, *325*, 128232.
[269] H. H. Singh, N. Khare, *Energy* 2019, *178*, 765.
[270] S. Nie, Q. Fu, X. Lin, C. Zhang, Y. Lu, S. Wang, *Chemical Engineering Journal* 2021, *404*, 126512.

[271] D. Ohlendorf, K. Kerth, W. Osiander, F. Holzgreve, L. Fraeulin, H. Ackermann, D. A. Groneberg, *J Physiol Anthropol* 2020, *39*, 1.
[272] Y. Bai, Z. Zhou, Q. Zhu, S. Lu, Y. Li, L. Ionov, *Carbohydr Polym* 2023, *313*, 120868.
[273] W. K. Son, J. H. Youk, T. S. Lee, W. H. Park, *Macromol Rapid Commun* 2004, *25*, 1632.
[274] B. K. Tarus, J. I. Mwasiagi, N. Fadel, A. Al-Oufy, M. Elmessiry, *SN Appl Sci* 2019, *1*, 1.
[275] W. K. Son, J. H. Youk, T. S. Lee, W. H. Park, *J Polym Sci B Polym Phys* 2004, *42*, 5.
[276] R. K. Singh, S. W. Lye, J. Miao, *Polymer (Guildf)* 2021, *214*, 123366.
[277] M. Yasar, P. Hassett, N. Murphy, A. Ivankovic, *ACS Omega* 2024, *9*, 26020.
[278] D. Ezzat, M. Youssif, H. Elhaes, M. El-Nahass, *Opt Quantum Electron* 2024, *56*, 1.
[279] B. K. Mehta, M. Chhajlani, B. D. Shrivastava, in *J Phys Conf Ser*, 2017, p. 12050.
[280] S. M. Purushothaman, M. F. Tronco, B. Kottathodi, I. Royaud, M. Ponçot, N. Kalarikkal, S. Thomas, D. Rouxel, *Polymer (Guildf)* 2023, *283*, 126179.
[281] F. Mokhtari, M. Shamshirsaz, M. Latifi, *Polym Eng Sci* 2016, *56*, 61.
[282] H. Güçlü, H. Kasım, M. Yazici, *J Compos Mater* 2023, *57*, 409.
[283] N. Yuan, T. Su, L. Zhang, D. Li, J. Li, T. Zhu, J. Hu, H. Guo, Y. Liu, N. Liu, W. Han, D. Yao, *ChemistrySelect* 2024, *9*, e202304718.
[284] G. Greczynski, L. Hultman, *Sci Rep* 2021, *11*, 11195.
[285] A. Roy, A. K. Mukhopadhyay, S. C. Das, G. Bhattacharjee, A. Majumdar, R. Hippler, *Coatings* 2019, *9*, 551.
[286] M. Samet, V. Levchenko, G. Boiteux, G. Seytre, A. Kallel, A. Serghei, *Journal of Chemical Physics* 2015, *142*, DOI 10.1063/1.4919877.
[287] Y. Chen, L. Zhang, C. Mei, Y. Li, G. Duan, S. Agarwal, A. Greiner, C. Ma, S. Jiang, *ACS Appl Mater Interfaces* 2020, *12*, 35513.
[288] G. A. Bastida, R. J. Aguado, M. V. Galván, M. Á. Zanuttini, M. Delgado-Aguilar, Q. Tarrés, *Cellulose* 2024, *31*, 2221.
[289] M. M. Rastegardoost, O. A. Tafreshi, Z. Saadatnia, S. Ghaffari-Mosanenzadeh, C. B. Park, H. E. Naguib, *Appl Mater Today* 2023, *30*, 101732.
[290] X. Ren, N. Meng, H. Zhang, J. Wu, I. Abrahams, H. Yan, E. Bilotti, M. J. Reece, *Nano Energy* 2020, *72*, 104662.
[291] F. Zhang, X. Li, Z. yuan Lan, N. Zhang, J. hui Yang, Y. Wang, *Carbohydr Polym* 2025, *366*, 123934.
[292] Z. M. Dang, J. K. Yuan, J. W. Zha, T. Zhou, S. T. Li, G. H. Hu, *Prog Mater Sci* 2012, *57*, 660.
[293] N. Ahmadi, G. Rezazadeh, A. Rahmani, M. Ghanbari, *Heliyon* 2024, *10*, e30626.
[294] "Properties: Cellulose Acetate," can be found under https://www.azom.com/properties.aspx?ArticleID=1461, n.d.
[295] D. Sieroń, I. Jabłońska, D. Lukoszek, K. Szyluk, H. Meusburger, G. Delimpasis, M. Kostrzewa, I. Platzek, A. Christe, *Medicina (Lithuania)* 2022, *58*, 1142.
[296] "RCSI - Drawing Cross-section of the knee joint - English labels | AnatomyTOOL," can be found under https://anatomytool.org/content/rcsi-drawing-cross-section-knee-joint-english-labels, n.d.
[297] P. Samyn, *Tribol Int* 2016, *99*, 127.
[298] C. J. Jahagirdar, S. Venkatakrishnan, *Indian Journal of Textile Research* 1986, *11*, 94.
[299] Walter. Fung, Mike. Hardcastle, *Textiles in Automotive Engineering*, Woodhead Pub. ; Technomic, 2001.
[300] K. W. Hillier, *Physical Properties of Textile Fibres*, 1964.
[301] "Software: BlueFruit Pin I/O | Getting Started with the nRF8001 Bluefruit LE Breakout | Adafruit Learning System," can be found under https://learn.adafruit.com/getting-started-with-the-nrf8001-bluefruit-le-breakout/software-bluefruit-firmata, 2014.

[302] J. G. Pallarés, A. Hernández-Belmonte, A. Martínez-Cava, T. Vetrovsky, M. Steffl, J. Courel-Ibáñez, *Scand J Med Sci Sports* 2021, *31*, 1866.
[303] B. Postolka, P. Schütz, S. F. Fucentese, M. A. R. Freeman, V. Pinskerova, R. List, W. R. Taylor, *J Biomech* 2020, *110*, 109915.
[304] N. A. Borghese, L. Bianchi, F. Lacquaniti, *Journal of Physiology* 1996, *494*, 863.
[305] S. Hu, M. Dai, T. Dong, T. Liu, *Sensors (Switzerland)* 2019, *19*, 2369.
[306] K. Tao, H. Yi, Y. Yang, H. Chang, J. Wu, L. Tang, Z. Yang, N. Wang, L. Hu, Y. Fu, J. Miao, W. Yuan, *Nano Energy* 2020, *67*, 104197.
[307] Y. Chen, E. Chen, Z. Wang, Y. Ling, R. Fisher, M. Li, J. Hart, W. Mu, W. Gao, X. Tao, B. Yang, R. Yin, *Nano Energy* 2022, *104*, 107929.
[308] X. Huang, L. Liu, Y. Hsin Lin, R. Feng, Y. Shen, Y. Chang, H. Zhao, *Sci Adv* 2023, *9*, DOI 10.1126/sciadv.adh9799.
[309] S. Li, S. Cao, H. Lu, B. He, B. Gao, *Mater Today Bio* 2024, *26*, 101044.
[310] C. Das, G. H. Feng, *IEEE Sens J* 2025, *25*, 10775.
[311] "IEC 62631-2-1:2018 | IEC," can be found under https://webstore.iec.ch/en/publication/34510, n.d.
[312] D. M. Mulvihill, R. Mukherjee, Y. Xu, C. Kumar, G. Khandelwal, J. Perris, S. Bairagi, A. K. Aliyana, G. K. Stylios, S. C. Pillai, N. Gadegaard, *Adv Energy Mater* 2025, *15*, e02920.
[313] Special Chem, "Polyvinylidene Fluoride (PVDF) Plastic: Material Properties & Other Info," can be found under https://www.specialchem.com/plastics/guide/polyvinylidene-fluoride-pvdf-plastic, 2020.
[314] H. Gao, N. Jiang, Q. Niu, S. Mei, H. J. Haugen, Q. Ma, *Int J Nanomedicine* 2023, *18*, 7359.
[315] H. Kanďárová, P. Pôbiš, *Frontiers in Toxicology* 2023, *5*, 1337468.
[316] Jinlian. Hu, E. Textile Institute (Manchester, *Fabric Testing*, CRC Press, 2008.
[317] S. N. Niles, W. Dias, T. Perera, W. Vinoth, E. Wijenayake, *INTERNATIONAL JOURNAL OF SCIENTIFIC & TECHNOLOGY RESEARCH* 2017, *6*, 2.
[318] Milton Keynes: BSI, "BS EN 60601-1:2006+A12:2014 | 30 Jun 2018 | BSI Knowledge," can be found under https://knowledge.bsigroup.com/products/wearable-electronic-devices-and-technologies-electronic-textile-measurement-methods-for-basic-properties-of-conductive-yarns, 2006.
[319] AATCC, "Test Method AATCC 195 Liquid Moisture Management," can be found under https://darongtester.com/aatcc-195-liquid-moisture-management/, 2017.
[320] AATCC, "AATCC 66 : Test Method for Wrinkle Recovery of Woven Fabrics: Recovery Angle," can be found under https://standards.globalspec.com/std/14209979/aatcc-66, 2023.
[321] I. O. for Standardization, *61010-1 © Iec:2001* 2013, 12.
[322] ASTM, "Test Method for Thickness of Textile Materials," DOI 10.1520/D1777-96R19can be found under https://store.astm.org/d1777-96r19.html, 2019.
[323] ASTM-D3776/D3776M-20, *Standard Test Methods for Mass Per Unit Area (Weight) of Fabric*, ASTM International, West Conshohocken, PA, 2020.
[324] ASTM D 1425, "Standard Test Method for Unevenness of Textile Strands Using Capacitance Testing Equipment," 2020.
[325] ASTM, "Standard test methods for linear density of textile fibres," DOI 10.1520/D1577-07R18can be found under https://store.astm.org/d1577-07r18.html, 2018.
[326] G - Star Raw, 2016, 1.
[327] R. Cao, J. Wang, S. Zhao, W. Yang, Z. Yuan, Y. Yin, X. Du, N.-W. Li, X. Zhang, X. Li, Z. L. Wang, C. Li, *Nano Res* 2018, *11*, 3771.

[328] M.-F. Lin, J. Xiong, J. Wang, K. Parida, P. S. Lee, *Nano Energy* 2018, *44*, 248.
[329] M. Lou, I. Abdalla, M. Zhu, J. Yu, Z. Li, B. Ding, *ACS Appl Mater Interfaces* 2020, *12*, 1597.
[330] Z. Li, M. Zhu, J. Shen, Q. Qiu, J. Yu, B. Ding, *Adv Funct Mater* 2020, *30*, 1908411.
[331] Y. Shi, X. Wei, K. Wang, D. He, Z. Yuan, J. Xu, Z. Wu, Z. L. Wang, *ACS Appl Mater Interfaces* 2021, *13*, 50329.
[332] S. M. S. Rana, M. T. Rahman, S. Sharma, M. Salauddin, S. H. Yoon, C. Park, P. Maharjan, T. Bhatta, J. Y. Park, *Nano Energy* 2021, *88*, 106300.
[333] M. Zhou, F. Xu, L. Ma, Q. Luo, W. Ma, R. Wang, C. Lan, X. Pu, X. Qin, *Nano Energy* 2022, *104*, 107885.
[334] M. T. Rahman, S. S. Rana, M. A. Zahed, S. Lee, E. S. Yoon, J. Y. Park, *Nano Energy* 2022, *94*, 106921.
[335] M. Cui, H. Guo, W. Zhai, C. Liu, C. Shen, K. Dai, *Adv Funct Mater* 2023, *33*, 2301589.
[336] J. Yang, M. Wang, Y. Meng, Z. Niu, Y. Hao, H. Liu, W. Su, H. Zhang, Y. Qin, C. Zhang, X. Li, *ACS Appl Electron Mater* 2024, *6*, 1385.
[337] M. Robiul Islam, O. Faruk, S. M. S. Rana, G. B. Pradhan, H. Kim, M. S. Reza, T. Bhatta, J. Y. Park, *Adv Funct Mater* 2024, 2403899.

**This page intentionally left blank**